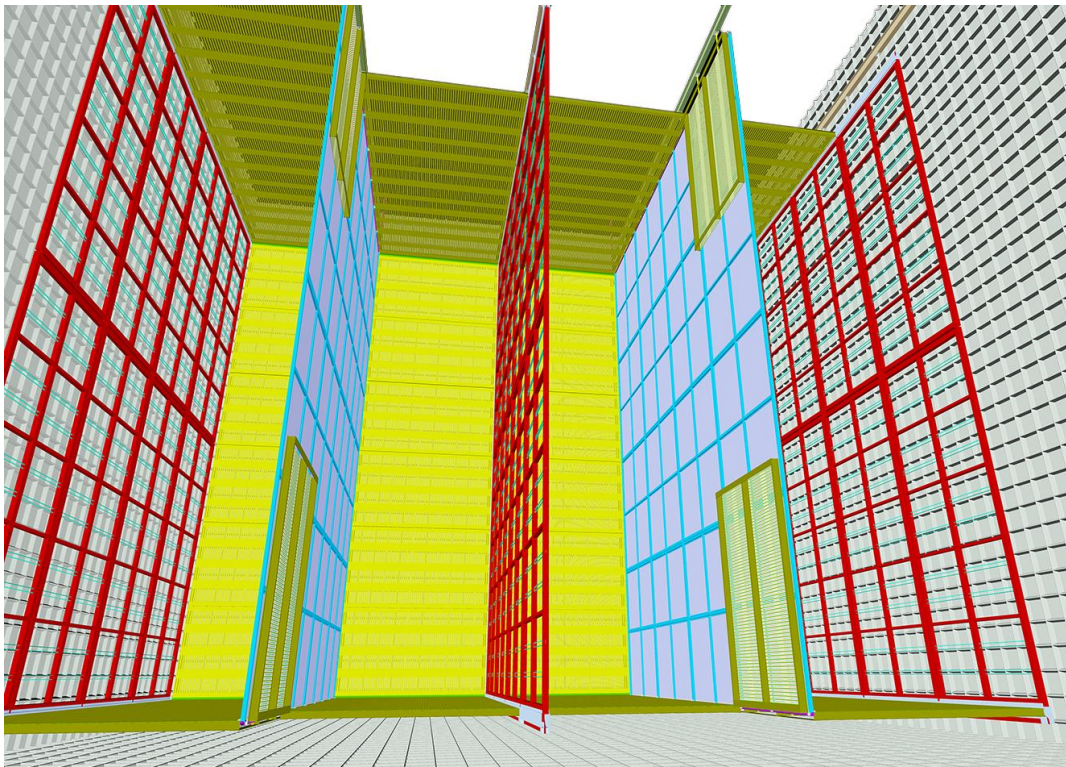


1 Long-Baseline Neutrino Facility (LBNF) and
2 Deep Underground Neutrino Experiment (DUNE)

3 Conceptual Design Report

4 Volume 4: The DUNE Detectors at LBNF



1

1 August 14, 2015

3 Contents

4	1 Overview	1
5	1.1 Introduction to LBNF and DUNE	1
6	1.2 Introduction to the DUNE Detectors	2
7	1.2.1 Far detector	2
8	1.2.2 Near detector	4
9	2 Implementation Strategy	5
10	2.1 Overview	5
11	2.2 Strategy for implementing the DUNE far detectors	5
12	2.3 Strategy for implementing the DUNE near detector(s)	8
13	3 DUNE Project Management	11
14	3.1 Overview	11
15	3.2 Work Breakdown Structure (WBS)	12
16	4 Far Detector Reference Design: Single-Phase LArTPC	15
17	4.1 Overview	15
18	4.2 Reference Design Expected Performance	16
19	4.3 The Time Projection Chamber (TPC)	17
20	4.3.1 Overview	17
21	4.3.2 Anode Plane Assemblies (APA)	20
22	4.3.3 Cathode Plane Assemblies (CPA)	24
23	4.3.4 Field Cage	25
24	4.3.5 High Voltage components	27
25	4.3.6 TPC prototyping and test	28
26	4.4 The Data Acquisition (DAQ) System and Monitoring	29
27	4.5 The Cold Electronics (CE)	33
28	4.6 The Photon Detection System	34
29	4.6.1 Reference Design	38
30	4.6.2 Alternative Designs	39
31	4.6.3 Technology Selection	40
32	4.7 Installation and Commissioning	40
33	5 Far Detector Alternative Design: Dual-Phase LArTPC	44
34	5.1 Overview	44
1	5.2 Detector Configuration	47

2	5.3	The Charge Readout System	52
3	5.3.1	The charge readout plane (CRP)	53
4	5.3.2	The LEM/Anode Sandwich (LAS)	56
5	5.4	The Field Cage and High Voltage System	58
6	5.5	The Electronics, Chimneys and DAQ	62
7	5.5.1	Front-end cryogenic amplifiers	64
8	5.5.2	Digital electronics and DAQ global architecture	67
9	5.5.3	MicroTCA standard and applications	68
10	5.5.4	Back-end and event builder	70
11	5.5.5	Timing distribution system and White Rabbit standard	70
12	5.6	The slow control system	71
13	5.7	The Light Readout System	73
14	5.8	Installation and Commissioning	76
15	5.8.1	Preparatory works	76
16	5.8.2	Detector installation sequence	77
17	5.8.3	Construction program of detector installation	78
18	6	Synergies Between FD Designs	80
19	6.1	Overview	80
20	6.2	Interface with the cryogenic system	81
21	6.3	Drift high Voltage	81
22	6.4	Photon Detection	82
23	6.5	Calibration	82
24	6.6	Underground installation strategies	83
25	6.7	Local computing infrastructure and DAQ	83
26	6.8	Detector Modelling and simulations	83
27	6.9	Further steps	83
28	7	Near Detector Reference Design	84
29	7.1	Overview	84
30	7.2	The Fine-Grained Tracker	85
31	7.2.1	Straw-Tube Tracking Detector	87
32	7.2.2	Electromagnetic Calorimeter	91
33	7.2.3	Dipole Magnet	93
34	7.2.4	Muon Identifier	95
35	7.2.5	Instrumentation	96
36	7.3	Matching the ND Requirements for DUNE/LBNF	97
37	7.3.1	Matching ND Requirements for the Oscillation Analyses	97
38	7.3.2	Matching ND Requirements for the Short Baseline Precision Measurements and Searches	99
39	7.3.3	Future Tasks to Quantitate the Systematic Errors	100
40	7.4	Addition of a Liquid Argon Detector to the NND	100
41	7.5	Beam Line Measurements	101
42	7.5.1	Design Considerations	101
43	7.5.2	Muon-Measurement Facilities	102
44	7.5.3	Installation and Operation	104
45	7.6	Hadron Production Measurements	104
1			

2	7.6.1	Introduction	104
3	7.6.2	External Hadron-Production Measurements	105
4	7.6.3	Background	105
5	7.7	The Data Acquisition System (DAQ) and Computing	106
6	7.7.1	NDS DAQ	106
7	7.7.2	NDS Computing	109
8	8	Software and Computing	110
9	8.1	Overview	110
10	8.2	Computing Infrastructure	110
11	8.2.1	Raw Data Rates	110
12	8.2.2	Processed Data	115
13	8.2.3	Computing Model	115
14	8.2.4	Computing Implications of the Alternative Design	117
15	8.3	Near Detector Physics Software	117
16	8.4	Far Detector Physics Software	118
17	8.4.1	Far Detector Simulation	118
18	8.4.2	Far Detector Reconstruction	119
19	9	Prototyping Strategy	126
20	9.1	Overview	126
21	9.2	The 35-t Prototype	127
22	9.2.1	35-t Phase-1: Cryostat Construction	127
23	9.2.2	35-t Phase-1: Operation and Performance	128
24	9.2.3	35-t Phase-1: Conclusions	129
25	9.2.4	35-t Phase-2: Installation of Active Detectors	130
26	9.2.5	35-t Phase-2: Simulation, Reconstruction and Analysis	130
27	9.3	The CERN Single-Phase Prototype	132
28	9.3.1	Detector Configuration and Components	134
29	9.4	The WA105 Prototype	137
30	9.5	Connections to the Short-Baseline Program at Fermilab	141
31	9.6	The ND Neutrino Measurements Prototyping Plan	142
32	9.6.1	Straw Tube Tracking Detector	142
33	9.6.2	ECAL Detector	146
34	9.6.3	Dipole Magnet Development	147
35	9.6.4	MuID-RPC Detector	148
36	9.7	The ND Beamline Measurements Prototyping Plan	148
37	9.7.1	Prototype Development for the Cherenkov and Ionization Detectors	148
38	9.7.2	Current Prototyping Activities	151
39	10	Summary of DUNE Detectors	152

41 List of Figures

42	1.1	3D models of the DUNE far detector designs	3
43	3.1	Near detector WBS	12
44	3.2	Far detector WBS	13
45	4.1	FD reference design	16
1	4.2	Cross section of the TPC inside the cryostat	18
2	4.3	A view of the partial assembled TPC	19
3	4.4	Illustration of the APA wire wrapping scheme	20
4	4.5	Winding machine concepts	23
5	4.6	Conceptual design of the cathode plane assembly	24
6	4.7	35-t field cage	26
7	4.8	FCA with roll-formed metal profile	27
8	4.9	Concept of new feedthrough	28
9	4.10	DAQ subsystem block diagram	30
10	4.11	DAQ time diagram	32
11	4.12	The front-end electronics as mounted on an APA	34
12	4.13	The Cold Electronics Architecture	35
13	4.14	Functional Block Diagram of the COLDATA ASIC	35
14	4.15	PD Overview	37
15	5.1	The 50-kt LBNO detector	46
16	5.2	Dual-phase detector 3D view	48
17	5.3	Dual-phase detector 3D view (partially open)	49
18	5.4	Charge Readout Plane (CRP) structure	49
19	5.5	DUNE CRP 3 m×3 m units.	50
20	5.6	Signal collection in the X and Y views by the 3 SFT chimneys.	50
21	5.7	Wires hanging comb blade.	51
22	5.8	Dual-phase readout	53
23	5.9	Side and top views of the 4 × 4 m ² CRP	54
24	5.10	3D view of the 4 × 4 m ² CRP.	55
25	5.11	Pictures of the LEM and anode along with microscope views	56
26	5.12	The 2D anode	57
27	5.13	Charge deposition as function of track angle	57
1	5.14	LEM performance vs geometry	58
1	5.15	LEM/anode sandwich metrology	59
2	5.16	Pictures of the assembly of a 3 × 1m ² CRP.	59

3	5.17	Assembly concept of the field cage	60
4	5.18	Cathode design	62
5	5.19	Dual-phase cryogenic ASIC amplifiers	65
6	5.20	Double-slope ASIC response	65
7	5.21	3D model of the signal feedthrough chimneys	66
8	5.22	Prototype of the signal feedthrough chimneys	67
9	5.23	MicroTCA crate organization	69
10	5.24	Charge readout AMC board prototype	69
11	5.25	FPGA processing board	70
12	5.26	White Rabbit network organization	71
13	5.27	Slow Control prototype rack	72
14	5.28	Dual-phase slow control sensors.	74
15	5.29	Slow control feedthroughs	74
16	5.30	Block diagram of the light readout AMC demonstrator card	76
17	7.1	A schematic drawing of the fine-grained tracker design	86
18	7.2	A schematic drawing of the straw tube tracker	88
19	7.3	Simulated distributions of dE/dx for different particles in FGT	90
20	7.4	Schematic drawing of the ECAL	92
21	7.5	Magnetic field maps	94
22	7.6	Fabrication and test of RPC prototype	96
23	7.7	Absorber conceptual design, elevation view	103
24	7.8	Energy loss in absorber	103
25	7.9	Near Detector System DAQ block diagram	107
26	7.10	A block diagram of the Near Neutrino Detector DAQ	108
27	8.1	The trajectory of a 1 GeV μ^- simulated in the near detector.	118
28	8.2	Simulated neutrino interactions in MicroBooNE	120
29	8.3	Dual-phase LArTPC reconstructed events for data and MC	121
30	8.4	PANDORA reconstruction efficiency	123
31	8.5	PANDORA vertex resolution	124
32	8.6	Reconstruction of electron neutrino energy	125
33	9.1	Cutaway view	128
34	9.2	Gas Ar Purge and Recirculation	129
35	9.3	35t Electron Lifetime	130
1	9.4	35-t with TPC	131
2	9.5	Cutaway view	135
3	9.6	Illustration of the $6 \times 6 \times 6 m^3$ with the inner detector inside the cryostat	138
4	9.7	Plan view section of the $6 \times 6 \times 6 m^3$	139
5	9.8	Vertical cross section of the $6 \times 6 \times 6 m^3$	139
6	9.9	Exploded view of the $3 \times 3 \times 1 m^3$ prototype	141
7	9.10	Basic GEANT4 Simulations of 1 cm Straws for the prototype plan	143
8	9.11	Design of the target plane with pressurized Ar gas	144
9	9.12	Wire tension measurement studies (20 μm and 30 μm)	144
10	9.13	Pulse and voltage-amplitude for the test straw chamber	145
11	9.14	Signal from single straw using the BARC preamp and source	145

12	9.15 Longitudinal view of the electromagnetic shower in the downstream ECAL by 2 GeV	
13	photons	147
14	9.16 Laboratory refurbishment plan for ECAL R&D and assembly	148
15	9.17 RPC characteristics measured during the prototype development	149
16	9.18 Muon gas Cherenkov counter	149
17	9.19 Muon detector waveforms	150

18

List of Tables

20 4.1 Far Detector Performance Expectations 17

21 4.2 Wire parameters. 21

22 4.3 Estimated data rates 32

23 4.4 Cold Electronics Device Counts 36

24 4.5 Cold Electronics Key parameters 36

25 5.1 Alternate Far Detector design parameters 45

26 5.2 Sizes and Dimensions for the 12 kt (15 kt) dual-phase LArTPC 51

27 5.3 Quantities of Items for the 12 kt (15 kt) dual-phase LArTPC 52

28 5.4 Interstage distances and electric field settings of the dual-phase readout components. . . 52

29 5.5 Numbers of components of the 4×4 m² CRP 54

30 7.1 A summary of the performance for the FGT configuration 87

31 7.2 Straw Tube Detector specifications 89

32 7.3 ECAL specifications 93

33 7.4 Dipole Magnet specifications 94

34 7.5 MuID specifications 95

35 7.6 Number of electronics channels for each of the three detector systems 96

36 8.1 Annual data volume estimations for zero-suppressed (ZS) data from various sources. . . 113

37 9.1 35-t Details and Dimensions 127

38 9.2 35-t Design Elements 131

39 9.3 Main parameters of the WA105 demonstrator 137

41 **Todo list**

42	Stephen said he didn't find this part clear, so am trying to clarify. Anne	11
43	Tom will amplify on expected performance for low and high energy events.	16
44	Michelle will describe what we know about purity and how we extrapolate to expected performance 1 in the 10-kt.	81
2	This link is broken, what is cdrsec:detectors-nd-ref-fgt supposed to refer to?	97
3	This link is broken, what is cdrsec:detectors-nd-ref-fgt supposed to refer to?	98
4	The Physics Volume, Volume 2 does not have a "Beamline at the near site chapter"	101
5	old LBNE reference	101
6	Might want to add an overview of chapter. Anne 5/7	110
1	Are you referring to something other than the reference design? If so, which configuration? If 1 not, no need to state this.	112
2	Should we mention the SBN synergy (from section 9.5) here or past ICARUS experience?	126

Chapter 1

Overview

overview

1.1 An International Physics Program

The global neutrino physics community is developing a multi-decade physics program to measure unknown parameters of the Standard Model of particle physics and search for new phenomena. The program will be carried out as an international, leading-edge, dual-site experiment for neutrino science and proton decay studies, which is known as the Deep Underground Neutrino Experiment (DUNE). The detectors for this experiment will be designed, built, commissioned and operated by the international DUNE Collaboration. The facility required to support this experiment, the Long-Baseline Neutrino Facility (LBNF), is hosted by Fermilab and its design and construction is organized as a DOE/Fermilab project incorporating international partners. Together LBNF and DUNE will comprise the world's highest-intensity neutrino beam at Fermilab, in Batavia, IL, a high-precision near detector on the Fermilab site, a massive liquid argon time-projection chamber (LArTPC) far detector installed deep underground at the Sanford Underground Research Facility (SURF) 1300 km away in Lead, SD, and all of the conventional and technical facilities necessary to support the beamline and detector systems.

The strategy for executing the experimental program presented in this Conceptual Design Report (CDR) has been developed to meet the requirements set out in the P5 report [?] and takes into account the recommendations of the European Strategy for Particle Physics [?]. It adopts a model where U.S. and international funding agencies share costs on the DUNE detectors, and CERN and other participants provide in-kind contributions to the supporting infrastructure of LBNF. LBNF and DUNE will be tightly coordinated as DUNE collaborators design the detectors and infrastructure that will carry out the scientific program.

The scope of LBNF is

- an intense neutrino beam aimed at the far site
- conventional facilities at both the near and far sites

- 7 • cryogenics infrastructure to support the DUNE detector at the far site

8 The DUNE detectors include

- 9 • a high-performance neutrino detector and beamline measurement system located a few hun-
10 dred meters downstream of the neutrino source
- 11 • a massive liquid argon time-projection chamber (LArTPC) neutrino detector located deep
12 underground at the far site

13 With the facilities provided by LBNF and the detectors provided by DUNE, the DUNE Collab-
14 oration proposes to mount a focused attack on the puzzle of neutrinos with broad sensitivity to
15 neutrino oscillation parameters in a single experiment. The focus of the scientific program is
16 the determination of the neutrino mass hierarchy and the explicit demonstration of leptonic CP
17 violation, if it exists, by precisely measuring differences between the oscillations of muon-type neu-
18 trinos and antineutrinos into electron-type neutrinos and antineutrinos, respectively. Siting the
19 far detector deep underground will provide exciting additional research opportunities in nucleon
20 decay, studies utilizing atmospheric neutrinos, and neutrino astrophysics, including measurements
21 of neutrinos from a core-collapse supernova should such an event occur in our galaxy during the
22 experiment's lifetime.

10 1.2 The LBNF/DUNE Conceptual Design Report Volumes

11 1.2.1 A Roadmap of the CDR

12 The LBNF/DUNE CDR describes the proposed physics program and technical designs at the
13 conceptual design stage. At this stage, the design is still undergoing development and the CDR
14 therefore presents a *reference design* for each element as well as *alternative designs* that are under
15 consideration.

16 The CDR is composed of four volumes and is supplemented by several annexes that provide details
17 on the physics program and technical designs. The volumes are as follows

- 18 • Volume 1: *The LBNF and DUNE Projects* provides an executive summary of and strategy
19 for the experimental program and of the CDR as a whole.
- 20 • Volume 2: *The Physics Program for DUNE at LBNF* outlines the scientific objectives and
21 describes the physics studies that the DUNE Collaboration will undertake to address them.
- 22 • Volume 3: *The Long-Baseline Neutrino Facility for DUNE* describes the LBNF Project,
23 which includes design and construction of the beamline at Fermilab, the conventional facilities
1 at both Fermilab and SURF, and the cryostat and cryogenics infrastructure required for the
2 DUNE far detector.

- Volume 4: *The DUNE Detectors at LBNF* describes the DUNE Project, which includes the design, construction and commissioning of the near and far detectors.

More detailed information for each of these volumes is provided in a set of annexes listed on the *CD-1-R Reports and Documents* page.

1.2.2 About this Volume

The first part of Volume 4: *The DUNE Detectors at LBNF* of the CDR describes the strategies for implementing the near and far detectors (Chapter 2) and outlines the DUNE management structure (Chapter 3). The next part describes the technical designs: the reference and alternative designs for the far detector and the synergies between them (Chapters 4, 5 and 6), and the near detector systems design (Chapter 7). Following this, Chapter 8 describes the designs for the computing infrastructure and physics software and Chapter 9 provides an overview of the ongoing and planned prototyping effort. The software and computing efforts, as well as some of the prototyping activities are off-project. Chapter ?? summarizes and concludes the volume.

1.3 Introduction to the DUNE Detectors

1.3.1 Far Detector

The proposed far detector (FD) will be located deep underground at the SURF 4850L with a fiducial mass of 40 kt. It consists of four cryostats instrumented with Liquid Argon Time Projection Chambers (LArTPCs). It is assumed that all four detector modules will be similar but not necessarily identical, allowing for evolution of the LArTPC technology to be implemented.

LArTPC technology provides excellent tracking and calorimetry performance. It is ideal for massive neutrino detectors that require high signal efficiency, effective background discrimination, capability to identify and precisely measure neutrino events over a wide range of energies and high resolution reconstruction of kinematic properties. The full imaging of events in the DUNE detector will allow study of neutrino interactions and other rare events with unprecedented detail. The detector's huge mass will result in data sets large enough to enable precision studies and the search for CP violation.

The mature LArTPC technology, pioneered by ICARUS, is the result of several decades of worldwide R&D. Nonetheless, the size of a single 10-kt DUNE detector module represents an extrapolation by over one order of magnitude relative to the ICARUS T600, which is the largest detector of this kind operated to date. To address this challenge, DUNE is developing both a reference and an alternative design (see Figure 1.1), and is engaged in a comprehensive prototyping effort. A list of synergies between the reference and alternative designs has been identified and is summarized in Chapter 6. Common solutions for DAQ, electronics, HV feedthroughs, and so on, will be

36 pursued and implemented, independent of the details of the TPC design choice. The development
 37 of the two detector module designs is a considerable advantage, and it is made possible by the
 1 convergence of previously separate international neutrino efforts into the DUNE Collaboration.

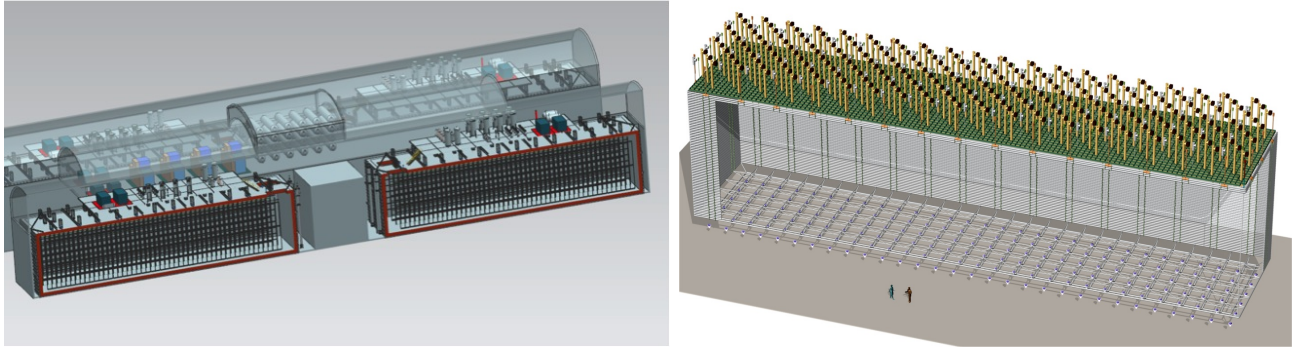


Figure 1.1: 3D models of two 10-kt detectors using the single-phase reference design (left) and the dual-phase alternate design (right) for the DUNE far detector to be located at 4850L.

fig:FarD

2 Interactions in liquid argon (LAr) produce ionization charge and scintillation light. The electrons
 3 drift in a constant electric field away from the cathode plane towards the segmented anode plane.
 4 The prompt scintillation light is observed by photodetectors that provide the absolute time of the
 5 event. The reference design, described in Chapter 4, adopts a single-phase readout, in which the
 6 readout anode is composed of wire planes in the LAr volume. The alternate design, discussed in
 7 Chapter 5, considers the dual-phase approach, where ionization charge is extracted, amplified and
 8 detected in gaseous argon above the liquid surface. The dual-phase design allows a finer readout
 9 pitch (3 mm), a lower detection-energy threshold, and better pattern reconstruction of the events.
 10 Both the reference and alternate designs include systems to collect the scintillation light.

11 A comprehensive prototyping strategy for both designs is being actively pursued, as described in
 12 Chapter 9. The reference design, closer to the original ICARUS design, is currently being validated
 13 in the 35-t prototype LAr detector at Fermilab (see Section 9.2). The novel alternative design
 14 approach has been proven on several small-scale prototypes, and a 20-t dual-phase prototype is
 15 being constructed at CERN, intended for operation in 2016. Full-scale engineering prototypes will
 16 be assembled and commissioned at the CERN neutrino platform ¹; they are expected to provide
 17 the ultimate validation of the engineered solutions for both far detector designs around the year
 18 2018.

19 A test-beam data campaign will be executed in the following years to collect a large sample of
 20 charged particle interactions to study the detector response with high precision.

21 The deployment of the four 10-kt modules at SURF will take several years and be guided by
 22 principles detailed in Chapter 2. According to this strategy, DUNE adopts the lowest-risk design
 23 that satisfies the physics and detector requirements and allows installation of the first 10-kt detector
 24 module as early as possible. Accordingly, the first 10-kt module will implement the reference design.

25 A clear and transparent decision process will be adopted for determining the design of the second

¹See CERN Bulletin article at <http://cds.cern.ch/journal/CERNBulletin/2014/51/News%20Articles/1975980?ln=en>.

26 and subsequent modules. The decision will be based on physics performance, technical and schedule
27 risks, costs and funding opportunities. Besides taking advantage of technological developments,
28 a flexible approach to the far detector design acknowledges the diversity of DUNE and offers the
29 potential to attract additional interest and resources into the Collaboration. A staged approach
30 provides access to an early science program while allowing for new developments to be implemented
1 over the relatively long installation period of the experiment.

2 1.3.2 Near Detector Systems

3 DUNE will install a near neutrino detector (NND) ~ 0.5 km downstream of the target and a
4 Beamline Measurement System (BLM) ~ 300 m upstream of the NND. These are collectively called
5 the Near Detector Systems (NDS). The NDS will allow DUNE to reduce systematic errors to match
6 the high-statistics phase precision sensitivity for the long-baseline neutrino oscillation studies. The
7 primary role of the neutrino detector is to measure the spectrum and flavor composition of the beam
8 to high precision. This detector will be magnetized so that it can charge-discriminate electrons
9 and muons produced in the neutrino charged current interactions; it will therefore be capable of
10 making separate measurements of the neutrino and antineutrino fluxes.

11 In addition, exposure to the intense neutrino flux provides the opportunity to collect neutrino in-
12 teraction data sets of unprecedented size, enabling an extended science program. The near detector
13 therefore provides an opportunity for a wealth of fundamental neutrino interaction measurements,
14 which are an important part of the ancillary scientific goals of the DUNE collaboration.

15 The reference design for the neutrino near detector (NND) design is the NOMAD-inspired fine-
16 grained tracker (FGT) and is described in Chapter 7. The NND subsystems include a central
17 straw-tube tracker and an electromagnetic calorimeter embedded in a 0.4-T dipole field. The
18 magnet yoke steel will be instrumented with muon identifiers.

1 The Beamline Measurement System (BLM), designed to measure the muon flux from hadron decay,
2 is located in the region of the beam absorber at the downstream end of the decay region. It is
3 intended to monitor the beam profile on a spill-by-spill basis and will operate for the life of the
4 experiment.

5 Chapter 2

6 Implementation Strategy

strategy

7 2.1 Overview

8 Recommendation 12 of the Report of the Particle Physics Prioritization Panel (P5) states that for a
9 Long-Baseline Neutrino Oscillation Experiment to proceed “The minimum requirements to proceed
10 are the identified capability to reach an exposure of $\text{kt} \cdot \text{MW} \cdot \text{year}$ 120 by the 2035 timeframe, the
11 far detector situated underground with cavern space for expansion to at least 40-kt LAr fiducial
12 volume, and 1.2-MW beam power upgradable to multi-megawatt power. The experiment should
13 have the demonstrated capability to search for supernova bursts and for proton decay, providing a
14 significant improvement in discovery sensitivity over current searches for the proton lifetime.” The
15 strategy presented here meets these criteria. The P5 recommendation is in line with the CERN
16 European Strategy for Particle Physics (ESPP) of 2013, which classified the long-baseline neutrino
17 program as one of the four scientific objectives with required international infrastructure.

18 2.2 Strategy for Implementing the DUNE Far Detector

ategy-FD

19 The LBNF Project will provide four cryostats at the 4850L of the Sanford Underground Re-
20 search Facility (SURF) in which the DUNE Collaboration will deploy four 10-kt (fiducial) mass
21 far detector LArTPCs. DUNE contemplates two options for the read out of the ionization signals:
22 single-phase readout, where the ionization is detected using wire planes in the liquid argon volume;
23 and dual-phase readout, where the ionization signals are amplified and detected in gaseous argon
24 above the liquid surface. An active development program for both technologies is being pursued
25 in the context of the CERN neutrino platform, as well as the the Fermilab SBN program.

26 The viability of the LArTPC technology has been proven by the ICARUS experiment with single-
1 phase wire plane LArTPC readout, where data was successfully accumulated over a period of three
2 years. An extrapolation of the observed performance and implementation of improvements in the
3 design (e.g., cold electronics) will allow the single-phase approach (see Chapter 4) to meet DUNE

ch:detectors-id-ref

4 requirements, and is hence adopted as *reference design*.

5 The reference design is already relatively advanced for the conceptual design stage. Modifications
6 of the reference design will be approved by the DUNE technical board. A preliminary design
7 review will take place as early as possible, utilizing the experience from the DUNE 35-t prototype;
8 the design review will define the baseline design that will form the basis of the TDR (CD-2). Once
9 defined, changes to the baseline will fall under a formal change-control process. An engineering
10 prototype consisting of six full-sized drift cells will be validated at the CERN neutrino platform¹.
11 This engineering prototype at CERN is a central part of the risk mitigation strategy for the first
12 10-kt FD module. Following experience at the CERN neutrino platform, the DUNE technical
13 coordinator will organize a final design review. The CERN single-phase prototype provides the
14 opportunity for production sites to validate manufacturing procedures ahead of large-scale pro-
15 duction for the far detector. Three major operational milestones are defined for this single-phase
16 prototype: 1) engineering validation — successful cool-down; 2) operational validation — success-
17 ful TPC readout with cosmic-ray muons; and 3) physics validation with test beam data. Reaching
18 milestone 2, will allow the retirement of a number of technical risks for the construction of the first
19 10-kt detector module.

20 In parallel with preparation for construction of the first 10-kt detector module, the DUNE Col-
21 laboration recognizes the potential of the dual-phase technology and strongly endorses the already
22 approved WA105 experiment at the CERN neutrino platform, which includes the operation of the
23 20-ton prototype and the $6\times 6\times 6$ m³ WA105 demonstrator. Many DUNE collaborators are partic-
24 ipants in the WA105 experiment. A concept for the dual-phase implementation of a far detector
25 module is presented in detail as an *alternative design* in Chapter 5. This alternative design, if
26 demonstrated, could form the basis of the second or subsequent 10-kt far detector modules, to
27 achieve improved detector performances in a cost-effective way.

28 The DUNE program at the CERN neutrino platform will be coordinated by a single L2 manager.
29 Common technical solutions will be adopted wherever possible. The charged-particle test-beam
30 data will provide essential calibration samples for both technologies and will enable a direct com-
31 parison of the relative physics benefits.

32 For the purposes of cost and schedule, the reference design for the first far detector module is
33 adopted as the reference design for the subsequent three modules. However, the experience with
34 the first 10-kt module and the development activities at the CERN platform are likely to lead to
35 the evolution of the TPC technology, both in terms of refinements to single-phase design and the
36 validation of the operation of the dual-phase design. The technology choice for the second and
37 subsequent LArTPCs will be based on risk, cost (including the potential benefits of additional
38 non-DOE funding) and physics performance (as established in the CERN charged-particle test
39 beam).

40 As already stated, this strategy allows flexibility with respect to international contributions and
41 provides the possibility of attracting interest and resources from a broader community with space
1 for flexibility to respond to the funding constraints from different sources.

¹The proposal for the DUNE single-phase prototype will be presented to the CERN SPSC in June 2015.

2.3 Strategy for Implementing the DUNE Near Detector Systems

Within the former LBNE collaboration the neutrino near detector (NND) design was the NOMAD-inspired fine-grained tracker (FGT), which was developed through a strong collaboration of Indian and U.S. institutions. DUNE adopts the FGT concept as the *reference design* for the NND according to the following guidelines:

- The primary design consideration of the DUNE NND is the ability to adequately constrain the systematic errors in the DUNE long-baseline oscillation analysis.
- The secondary design consideration for the DUNE NND is the self-contained non-oscillation neutrino physics program.
- It is recognized that a detailed cost-benefit study of potential NND options has yet to take place and such a study is of high priority to DUNE.

The cost and resource-loaded schedule are based on this design (see Chapter [7](#)). ch:detectors-nd-ref

The contribution of Indian institutions to the design and construction of the DUNE FGT near detector is a vital part of the strategy for the construction of the experiment. The reference design will provide a rich, self-contained physics program. From the perspective of the high-statistics phase of the long-baseline oscillation program, there may be benefits of augmenting the FGT with a relatively small LArTPC that would allow for a direct comparison with the far detector, or adding a high-pressure gaseous argon TPC. At this stage, the benefits of such options have not been studied, nor are alternative designs for the NND presented in the CDR; they will be the subject of detailed studies in the coming months.

A full end-to-end study of the impact of the reference NND design on the oscillation systematics has yet to be performed. Many of the elements of such a study are in development, for example the Monte Carlo simulation of the FGT and the adaptation of the T2K framework for implementing near detector measurements as constraints in the propagation of systematic uncertainties to the far detector. After the CD-1-R review, the DUNE Collaboration will initiate a detailed study of the optimization of the NND. To this end a task force will be set up with the charge to:

- Deliver the simulation of the reference design of the NND and possible alternatives;
- Undertake an end-to-end study to provide a quantitative understanding of the power of the NND designs to constrain the systematic uncertainties on the long-baseline oscillation measurements;
- Quantify the benefits of augmenting the reference design with a LArTPC or high-pressure gaseous argon TPC.

35 High priority will be placed on this work and the intention is to engage a broad cross section of
36 the collaboration in this process. The task force will be charged to deliver a report by July 2016.
37 Based on this report and input from the DUNE technical board, the DUNE executive board will
38 refine the DUNE strategy for the near detector.

Chapter 3

DUNE Project Management

ctors-pm

3.1 Overview

The international DUNE Project is responsible for managing all contributions to the design, construction, installation and commissioning of the DUNE near and far detectors.

As described in CDR Volume 1: *The LBNF and DUNE Projects*, the DUNE Project is integrated within the DUNE Collaboration. The collaboration, in consultation with the Fermilab director, is responsible for forming the international project team. The leaders of this team are the Technical Coordinator (TC) and Resource Coordinator (RC), who are jointly appointed by the DUNE Co-Spokespersons and the Fermilab Director. The project receives appropriate oversight from stakeholders including the Fermilab Directorate and DOE. A detailed description of the DUNE collaboration structure along with its advisory and coordinating structures is contained within Chapter 4 of CDR Volume 1: *The LBNF and DUNE Projects*.

The DUNE Project is responsible for coordinating the work packages assigned to each of the international partners contributing to the effort. These individual work packages, which are supported through independent funding agencies, have internal management structures that are responsible for satisfying the tracking and reporting requirements of the supporting agencies. However, the entire project scope (including non-DOE partner contributions) will be subject to the DOE critical decision process.

The international DUNE Project Office maintains a schedule for the entire project and tracks individual contributions through detailed sets of milestones embedded within the schedule. It is also responsible for ensuring that the interfaces between the different work package deliverables are well defined and that all of these deliverables meet safety and operational readiness requirements for installation at Fermilab and the Sanford Underground Research Facility. Project Office members including the Project Manager are appointed by the TC. The managers of the collaboration detector and prototyping organizations report to the Project Manager and provide the required interface between the DUNE project and the other members of the collaboration contributing to these efforts. As members of these organizations, they participate in all discussions related to

26 the design, construction, installation and commissioning of individual detector elements. Man-
27 agers have the primary responsibility for implementing collaboration plans developed within their
28 organizations.

29 Following this model, the DUNE-US project will have its own project office and management
30 structure. All normal DOE project management requirements will apply to the DUNE-US project.
31 In its role as host, the DOE will provide financial support for both the international DUNE
32 Project Office and the DUNE-US Project Office. The DUNE TC, who acts as Project Director
33 in the context of the international DUNE project, also serves as the DUNE-US Project Director.
34 However, each project office will have its own project manager. Other equivalent positions within
35 the project offices may be filled by the same individuals in cases where the TC believes this sharing
36 of resources to be most efficient. Some project office staff may also overlap with the LBNF project
37 office as appropriate.

38 **3.2 WBS**

39 The DUNE Project will manage all contributions to the design, construction, installation and
1 commissioning of the DUNE near and far detectors through an international Work Breakdown
2 Structure (WBS). The WBS organizes the Project's tasks and deliverables into convenient com-
3 ponents and is used to organize the cost and schedule for the DUNE project. The DUNE Project
4 consists of two major subsystems: the Near Detector (WBS 130.03), shown to WBS level 4 in
5 Figure 3.1, and the Far Detector (WBS 130.05), shown to WBS level 3 in Figure 3.2.

6 The DUNE Project organization and structure will evolve as the project becomes more fully
7 internationalized.

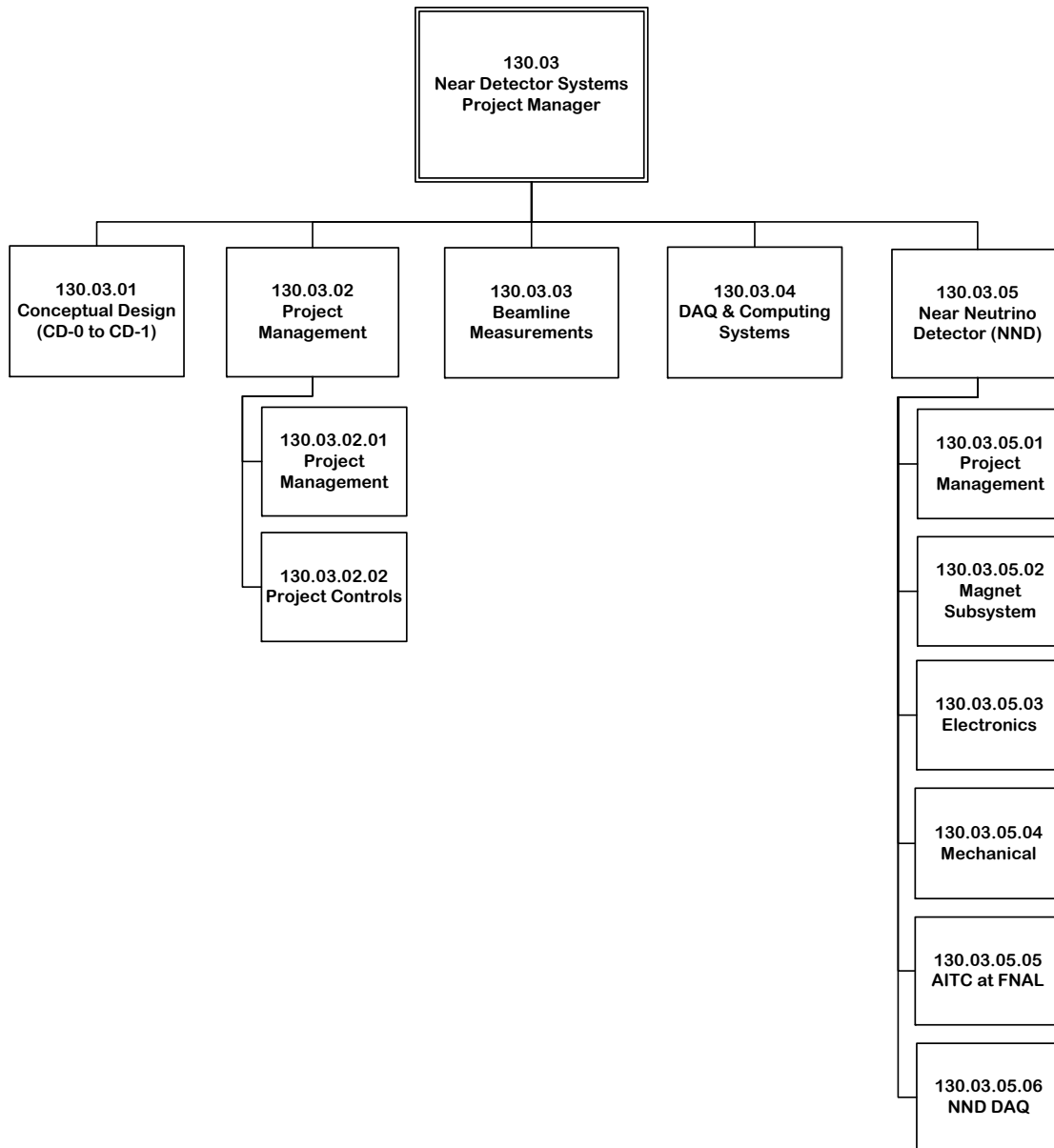


Figure 3.1: Near detector Work Breakdown Structure.

fig:ND_w

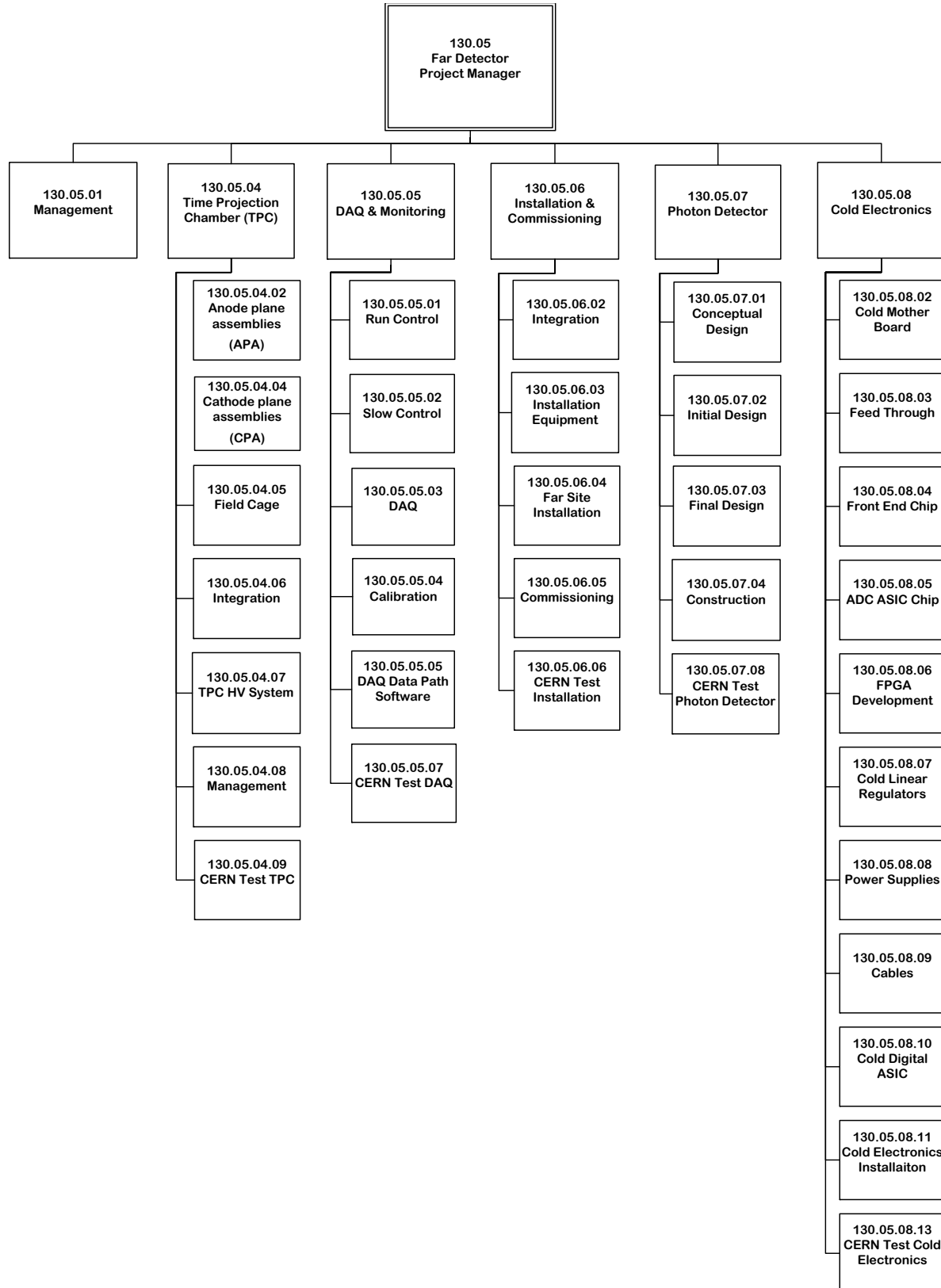


Figure 3.2: Far detector Work Breakdown Structure.

fig:FD_w

Chapter 4

Far Detector Reference Design: Single-Phase LArTPC

4.1 Overview

This chapter describes the reference design of the DUNE far detector. The reference design consists of four nominal 10-kt fiducial mass, single-phase LArTPC modules, augmented with photon detection systems. A “single-phase” detector is one in which the charge generation, drift and collection all occur in liquid argon (LAr). The scope of the far detector includes the design, procurement, fabrication, testing, delivery, installation and commissioning of the detector components:

- Time Projection Chamber (TPC)
- Data Acquisition System (DAQ)
- Cold Electronics (CE)
- Photon Detector System (PD)

The LArTPCs will be housed in cryostats provided by LBNF, described in Volume 3: *The Long-Baseline Neutrino Facility for DUNE*. The reference design is based largely on the LBNE far detector design as of January 2015, documented in Annex 4A: *The LBNE Design for a Deep Underground Single-Phase Liquid Argon TPC*. This annex provides the detailed descriptions of the systems and components that the DUNE reference design incorporates; the differences between the DUNE and LBNE designs are clearly indicated in this chapter. Important differences include detector size, APA and CPA placement, and small changes to the APA dimensions.

The detector modules will be constructed sequentially with the first module coming online as soon as possible and the rest at a regular pace thereafter. A model of the underground experimental area with the four 10-kt LArTPCs is shown in Figure 4.1.

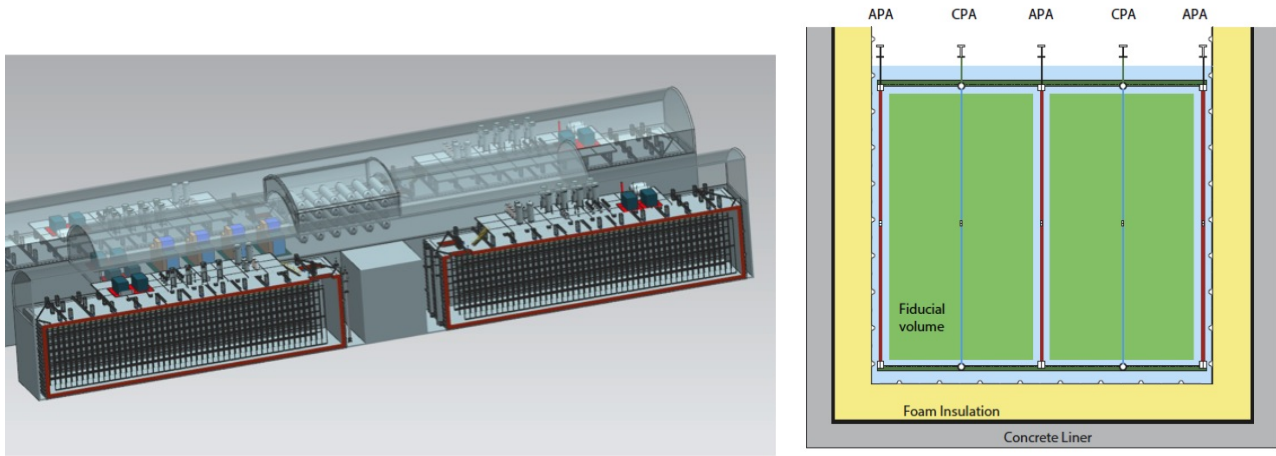


Figure 4.1: Left: 3D model of the reference design for the DUNE far detector to be located at the 4850L. Right: Schematic view of the active detector elements showing the plane ordering of the TPC inside the detector.

fig:FarD

31 Planning for the conventional facilities calls for construction of the second cryostat to be completed
 32 prior to filling the first so that it may serve initially as a liquid storage facility. The detector
 33 technology is expected to improve in the coming years with MicroBooNE, the SBN program and
 34 the CERN neutrino platform. DUNE’s staged program allows selection of optimal designs for each
 35 module as the technology evolves.

36 The reference design presented in this chapter and documented in the project cost and schedule is
 37 patterned after the successful ICARUS experiment, but adapted to the local site requirements at
 1 SURF and the scaled up detector size. The TPC configuration is shown on the right in Figure 4.1.
 2 The TPC, described in Section 4.3, is constructed by placing alternating high-voltage cathode
 3 planes and anode readout planes in a bath of ultra-pure liquid argon. Particles interacting in the
 4 argon generate electron-ion pairs and scintillation light.

fig:FarDet-over

5 The single-phase design offers the advantage that the charge is collected directly without gain,
 6 enabling precision charge calibration. However, signal levels are low, requiring the use of cold
 7 electronics (Section 4.5). The readout is based on stereo induction and collection planes, requiring
 8 a deconvolution of the induced signal. A photon detection system (Section 4.6) provides the t_0 or
 9 event time for physics processes that are uncorrelated with the LBNF neutrino beam.

10 4.2 Reference Design Expected Performance

ref-perf

11 The physics requirements are described in *Volume 2: The Physics Program for DUNE at LBNF*,
 1 for the long-baseline oscillation, atmospheric, supernova and nucleon decay physics programs. This
 2 section outlines the numerical detector performance parameters needed to meet the requirements
 3 and the ability of the far detector reference design to achieve these performance parameters.

The expected performance of the far detector reference design is based on the measured performance of the ICARUS[53] and ArgoNeuT[41] detectors, scanned Monte Carlo events[?] and newer studies with automated reconstruction, which are described in Sections 8.4.1, 8.4.2 and in Annex 4C: *Simulation and Reconstruction*. Simulation and reconstruction studies are ongoing. While many components are in place, a full end-to-end simulation, reconstruction and analysis chain does not yet exist. Many of the numerical detector performance requirements are estimates; some of them correspond to achievements by ICARUS and ArgoNeuT, although these detectors differ somewhat from the DUNE far detector. Additional parameters will be calibrated using the data from LArIAT and the two CERN prototypes, the *Full-Scale Detector Engineering Test and Test Beam Calibration of a Single-Phase LArTPC* and the *Long Baseline Neutrino Observatory Demonstration (WA105)*.

Table 4.1 lists the required performance values, achieved values (if any) and the values expected from DUNE. The rest of this section describes each parameter and its connection to the detector design and physics goals.

Table 4.1: Preliminary summary of the most important performance parameters of the DUNE reference design far detector. For each parameter, the table lists the required (reference) performance, performance achieved by other detectors and projected performance for DUNE. References are given. Notes: ¹For a MIP at the CPA, minimum in all three views, for any track angle; ²Achieved for the collection view; ³In order for the fiducial volume to be known to $\pm 1\%$, the resolution performances are reported separately in the x , y , and z directions, where z points along the neutrino beam axis; ⁴For a sample of stopping muons; ⁵For electron stubs with $E > 5$ MeV.

Parameter	Reference Performance	Achieved Elsewhere	Expected Performance
Signal/Noise Ratio ¹	9:1	10:1 [1, 2] ²	9:1
Electron Lifetime	3 ms	> 15 ms [2]	> 3 ms
Uncertainty on Charge Loss due to Lifetime	< 1%	< 1% [2]	< 1%
Dynamic Range of Hit Charge Measurement	15 MIP		15 MIP
Vertex Position Resolution ³	(2.5,2.5,2.5) cm		(1.1,1.4,1.7) cm [3, 4]
$e - \gamma$ separation ϵ_e	0.9		0.9
$e - \gamma$ separation γ rejection	0.99		0.99
Multiple Scattering Resolution on muon momentum ⁴	$\sim 18\%$	$\sim 18\%$ [5, 6]	$\sim 18\%$
Electron Energy Scale Uncertainty	5%	2.2% [7]	From LArIAT and CERN Prototype
Electron Energy Resolution	$0.15/\sqrt{E(\text{MeV})} \oplus 1\%$	$0.33/\sqrt{E(\text{MeV})} [7] + 1\%$	From LArIAT and CERN Prototype
Energy Resolution for Stopping Hadrons	1–5%		From LArIAT and CERN Prototype
Stub-Finding Efficiency ⁵	90%		> 90%

The signal-to-noise ratio requirement is motivated by the need to detect weak signals in a large detector that has a low signal rate, while limiting the required output data volume. It is set at 9:1

for a minimum-ionizing particle (MIP) in all three views, for any orientation of the track. This ratio is required for all particles in the detector, specifically those ionizing the liquid argon close to the CPA, where the reattachment effects are greatest. Since the strategy is to zero-suppress the data, it is important that the data volume from random excursions of the noise over the zero-suppression threshold compose a vanishingly small fraction of all ADC samples, and that it preserve the detector's ability to detect sub-MIP signals (e.g., signals from nuclear de-excitation photons or isolated hits on the edges of electromagnetic showers). Since the noise in the detector may vary by channel and by time, and in addition to thermal noise from the wires and the electronics, may include coherent noise sources from electromagnetic pickup and acoustical vibrations of the wires, among other sources, sufficient contingency on the signal-to-noise ratio is necessary to ensure that the detector meets the physics requirements. A value of 10:1 was achieved by ICARUS[1, 2] and even higher values were achieved by Long Bo[?]. Similar to the DUNE design, Long Bo used cold electronics, although its wires were much shorter than those planned for DUNE.

The electron lifetime requirement is set at 3 ms to preserve the signal-to-noise ratio across the entire detector volume in the presence of noise sources that are not yet foreseen. A shorter lifetime also places demands on the dynamic range of the ADCs: the gain will need to be large enough to detect weak signals at the CPA, but small enough to record strong signals near the APAs without saturation, if possible. The calorimetric energy resolution of low-energy electrons is highly sensitive to the lifetime for electrons that do not record flashes in the photon-detection system. The energy resolution is approximately 20% for electrons of energy below 50 MeV (see Section ??) without corresponding photon flashes in a detector with a 2.5 m maximum drift length, assuming only an average correction is applied for the lifetime. This resolution rapidly degrades for shorter lifetimes and longer drift lengths. For a maximum drift length of 3.6 m and an electron lifetime of 1.5 ms, the energy resolution is estimated to degrade to 44%. A lifetime of 3 ms is consistent with that achieved by the 35-t prototype. The ICARUS Collaboration has reported a much longer lifetime, >15 ms[2].

The charge loss due to lifetime effects is expected to be well measured in the DUNE far detector. In addition to the cosmic-ray muons which accumulate at a rate of 0.259 Hz (see Annex 4B: *Expected Data Rates for the DUNE Detectors*), the laser calibration system and purity monitors will provide detailed time-dependent measurements of the electron lifetime. This limit is placed at 1% in order to meet the energy-scale and resolution requirements for electrons, and to a lesser extent, to meet the requirements of dE/dx -based particle identification algorithms.

The dynamic range requirement is placed at 15 MIP in order to detect, without ADC saturation, particle ionization densities from one MIP up to the last hit on a track before a particle stops. The typical application is for protons, where data from ArgoNeuT show roughly a factor of 15 between the lowest-charge hit and the highest. Nonetheless, particles also travel along wires and dense showers may require even more dynamic range before saturation. The desire to measure sub-MIP signals also expands the desired dynamic range. MicroBooNE set a requirement of 50 on the signal dynamic range[?]. The dynamic range requirement is effectively a compound requirement on the noise level, electron lifetime and number of bits in the ADC.

The primary vertex position resolution requirement is intended to keep it from being a significant source of uncertainty on the fiducial volume determination, though this effect is mitigated if the resolution is well known. The current resolution from PANDORA easily meets this requirement.

5 The axis along which the resolution is the weakest is that of the neutrino beam direction and the
 6 asymmetry in the achieved resolution is not a result of detector anisotropy. Tighter demands on
 7 the primary vertex position resolution will be made by topological selection of $\pi^0 \rightarrow \gamma\gamma$ decays,
 8 which require pointing of the photon-induced showers back to the primary vertex.

9 In order to reduce the neutral-current background to ν_e CC events by a factor of roughly 100,
 10 information from the dE/dx of the initial ~ 2.5 cm of an electromagnetic shower must be combined
 11 with the topological $\pi^0 \rightarrow \gamma\gamma$ selection[?]. Current Monte Carlo studies indicate that, for showers
 12 with enough hits in the initial part to measure dE/dx , the performance of the ionization method
 13 is roughly 90% electron efficiency with a 90% rejection factor for single photons. A topological
 14 hand-scan indicates that a signal ν_e CC signal efficiency of $\sim 80\%$ with a 95% rejection of neutral-
 15 current background can be obtained. With optimizations to the dE/dx analysis and automating
 16 the pattern-recognition identification of π^0 decays by topology, it is anticipated that the requested
 17 level of 99% π^0 rejection can be obtained at 90% signal efficiency.

18 The momentum of muons in ν_μ CC events is an important ingredient in measuring the ν_μ energy
 19 spectrum in the far detector, which is one of the inputs to the oscillation parameter fits. Muons
 20 which stop in the detector volume will be well measured using their range. For those that are not
 1 contained the distribution of deviations of the muon track from a straight line is a function of the
 2 muon momentum. The expected performance of $\pm 18\%$ on the muon momentum was achieved by
 3 ICARUS for a sample of stopping muons, where the momentum measured by multiple scattering
 4 was compared against that obtained from the range. It is anticipated that the resolution will
 5 deteriorate for higher-energy muons because they scatter less.

6 The requirements on the electron energy-scale uncertainty and the resolution are driven by the
 7 need to analyze the reconstructed ν_e energy spectrum to extract oscillation parameters in the
 8 high-statistics phase of DUNE. A fraction of the energy of an electromagnetic shower escapes in
 1 undetected low-energy photons that can be simulated, but this fraction must be calibrated in
 2 data in order to give confidence in the uncertainty. An absolute energy scale will need to come
 3 from test-beam data — LArIAT and the CERN prototypes, the *Full-Scale Detector Engineering*
 4 *Test and Test Beam Calibration of a Single-Phase LArTPC* and the *Long Baseline Neutrino*
 5 *Observatory Demonstration (WA105)*. Analyzing $\pi^0 \rightarrow \gamma\gamma$ decays in ICARUS[7] gives an achieved
 6 $\pm 2.2\%$ uncertainty on the electromagnetic energy scale. The same data also constrain the energy
 7 resolution. The proposed data sets from the test-beam experiments will easily measure these,
 8 though the results will need to be extrapolated to the DUNE far detector geometry and readout
 9 details using a full simulation. Similarly, the detector response to hadrons — protons, charged pions
 10 and kaons — will be calibrated to the necessary precision by LArIAT and the CERN prototypes.

11 Absent from the list is a requirement on the two-hit resolution. In the direction parallel to the drift
 12 field, this resolution is expected to be very good, of the order of 2 mm, given existing ArgoNeuT
 13 data and simulations. The resolution in the other two dimensions is governed by the wire spacing.
 14 Separation of hits is important for pattern recognition, for counting tracks near the primary vertex
 15 (which is important for classifying neutrino scatters as quasi-elastic, resonant, or DIS), and for
 16 associating dense groups of tracks in showers between views. More study is required to determine
 17 the required two-hit resolution.

18 It is expected that as the software tools improve and as measurements from MicroBooNE and the

dedicated test-beam programs become available, the uncertainties on the projected performance will become smaller.

4.2.1 Expected Performance for Low-Energy Events

Low-energy (5–50 MeV) events require special consideration. Electron-type neutrino interactions appearing close together in time constitute the signature for a supernova burst event. A 5-MeV electron is expected to hit four wires in the DUNE far detector, and given the signal-to-noise requirement above, it is anticipated that this signal will be easy to separate from noise with the required 90% efficiency. (Similarly, the photon-detection system is expected to detect the energy from a proton decay event resulting in a 100-MeV kaon with high efficiency.)

Work is currently underway using the LArSoft simulation package to characterize low-energy response for realistic DUNE detector configurations. So far, most studies have been done with the MicroBooNE geometry, with the results expected to be generally applicable to the larger DUNE detector. For a preliminary understanding of achievable energy resolution, isotropic and uniform monoenergetic electrons with energies of 5–50 MeV (which should approximate the ν_e CC electron products) were simulated and reconstructed with the LArSoft package. The charge of reconstructed hits on the collection plane was used to reconstruct the energy of the primary electrons.¹ Figure ?? shows the results of a resolution study. A correction to compensate for loss of electrons during drift, $Q_{\text{collection}} = Q_{\text{production}} \times e^{-T_{\text{drift}}/T_{\text{electron}}}$ (where T_{drift} is the drift time of the ionization electrons, and T_{electron} is the electron lifetime), using Monte Carlo truth to evaluate T_{drift} , improved resolution significantly. This study indicated that photon-time information will be valuable for low-energy event reconstruction. Some of the resolution was determined to be due to imperfect hit-finding by the nominal reconstruction software. A tuned hit-finding algorithm did somewhat better (Figure ??), and further improvements for reconstruction algorithms optimized for low-energy events are expected.

Also under study is the potential for tagging ν_e CC absorption events ($\nu_e + {}^{40}\text{Ar} \rightarrow e^- + {}^{40}\text{K}^*$) using the cascade of de-excitation γ rays (that Compton-scatter in the detector); this should serve the dual purposes of rejecting background and isolating the CC component of the supernova burst signal. Reconstructing these gammas also improves the neutrino energy measurement.

4.2.2 Reference Design Optimization

Considerations of physics reach as well as cost, schedule and risk enter the optimization of the detector design parameters. Ideally one would like to estimate the asymptotic far-future performance of a full simulation, reconstruction and analysis chain, replicated for each design parameter choice and then choose the values that maximize sensitivity while minimizing the cost and producing timely physics results. While the GEANT4 simulation is fairly mature, it needs to be tuned to

¹Collection-plane hit charge gave the best resolution results compared to induction-plane and track-length-based reconstruction in this preliminary study; however, improved reconstruction based on broader information should be possible.

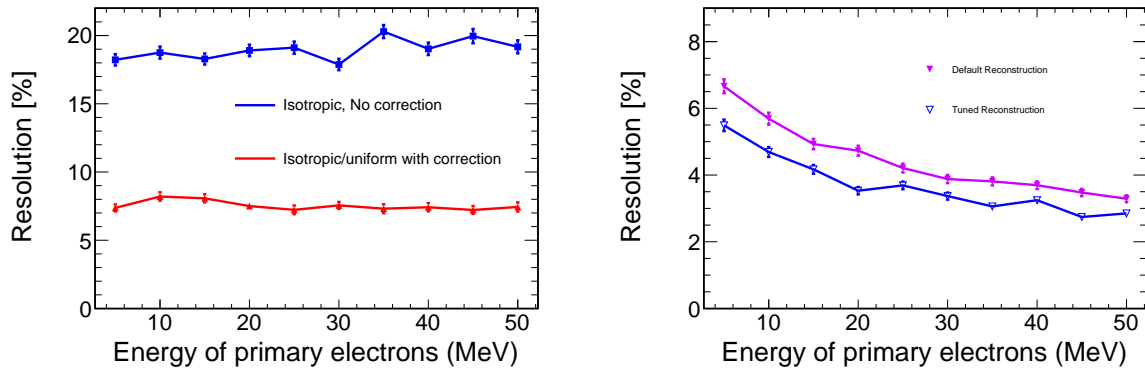


Figure 4.2: Left: Comparison of energy resolution (defined as σ/E , where σ is the spread of the collection-plane-charge-based event energy E for a monoenergetic electron), with and without electron-lifetime correction, as a function of electron energy (assumptions: 3 ms drift time, 1.63 mm/ μ s drift velocity, and 2.5 m maximum drift length). The blue curve is the energy resolution of isotropic and uniform electrons without electron-lifetime correction. The red curve is the energy resolution with electron-lifetime correction based on MC truth. Right: Comparison of energy resolution before and after tuning the reconstruction algorithm (for fixed position/direction electron events).

fig:lowe

3 data from the 35-t prototype and MicroBooNE so that realistic signal and noise modeling, which
 4 are inputs to the optimization procedures, can improve the performance modelling. The recon-
 5 struction tools are under development (see Section 8.4) and thus, physics sensitivity is currently
 6 optimized using estimates of detector performance that are input to the Fast Monte Carlo. The
 7 DUNE collaboration plans to establish a detector performance optimization task force to review
 8 various possible detector optimizations in light of the new collaboration and project organizations.
 9 This section briefly outlines the considerations and procedures that have been and will be used to
 10 optimize these parameters: the wire pitch, wire angle, wire length and maximum drift length. The
 11 wire length, angle and pitch are directly related to the APA dimensions, as discussed in Section 4.3
 12 and the APA dimensions are constrained by the needs of manufacturing, storage, transport and
 13 assembly.

14 Wire Pitch

15 The spacing between neighboring sense wires in the APAs is an optimizable parameter. In principle
 16 it is freely adjustable for all three wire planes, though to minimize the anisotropy of the detector
 17 response, similar wire pitch should be chosen in all three planes. The choice of a ~ 5 mm pitch is
 18 documented in [?]. The pitch of the grid plane wires is less important as they are not instrumented,
 19 though the grid wires do shadow the optical detectors and therefore should not be made with too
 20 fine a pitch.

21 The signal-to-noise ratio is expected to be proportional to the wire spacing, assuming that the noise
 22 on a channel is not impacted by the presence of nearby wires, and that the signal is divided among
 23 the available channels. Thermal noise and uncorrelated electronics noise satisfy these conditions.
 24 Coherent noise is a special case — filters may be applied either online or offline to reduce its

25 impact.

26 The signal-to-noise ratio requirement is set so that zero-suppression can function without elaborate
27 noise filtering. A high signal-to-noise ratio improves pattern-recognition performance, calorimetric
28 PID performance and dE/dx -based $e - \gamma$ separation. It is also important for detecting sub-MIP
29 signals, such as nuclear de-excitation photons, and it is important when adding up the energy of
30 hits on the edges of showers or on the ends of stubs initiated by supernova neutrino interactions.

31 The signal-to-noise ratio is expected to be higher in the collection plane than in the two induction
32 planes. The need to deconvolve the bipolar signals while filtering noise in the induction planes
33 means that the collection plane will be the most reliable in performing dE/dx measurements,
34 though for tracks that travel in a plane containing a collection wire and the electric field, the
1 induction planes will be critical for recovering PID efficiency. Reducing the spacing between wires
2 will have an adverse impact on the detector performance parameters that depend on the signal to
3 noise, with the effect seen more prominently in the induction-plane data.

4 The main benefit of a finer wire pitch is the ability to obtain higher resolution measurements of the
5 ionization density left by events in the detector. The spatial resolution in the plane perpendicular
6 to the electric field is also affected by transverse diffusion of the drifting electrons. It can be
7 argued that the wire spacing does not need to be much smaller than the typical width induced by
8 diffusion, though deconvolution and/or fitting techniques that combine signals from nearby wires
9 can recover some of the resolution lost to diffusion. Noise may limit the amount of resolution
10 gained using these techniques.

11 The separation of electrons from photons using the dE/dx measured in the initial part of an
12 electromagnetic shower is described in Annex 4C: *Simulation and Reconstruction*. The first 2.5 cm
13 of a shower is the most important, since subsequent showering stages have not yet taken place,
14 leaving one MIP for an electron and two for a photon conversion to two electrons, though sometimes
15 the subsequent showering starts earlier. As the first hit cannot be used to measure dE/dx (since
16 it is not known where in the volume of argon viewed by that wire the track started, the second
17 and subsequent hits must be used. But the shower can be aligned unfavorably along the wires of
18 one view or another, resulting in few usable hits. If no hits are useful, then the dE/dx method
19 cannot be used. Reducing the spacing between wires in all three views increases the precision of
20 the measurement of the initial part of the shower for $e - \gamma$ separation purposes. The current study
21 described in Annex 4C: *Simulation and Reconstruction* only uses the collection plane wires; thus
22 with a more optimal strategy, some of the efficiency that is lost with 5-mm wire spacing compared
23 with 3-mm spacing can be recovered by examining the other two views.

24 Separation of multiple close tracks is improved with more closely spaced wires. The position
25 resolution of hits is expected to be much better along the drift direction than in either of the axes
26 perpendicular to it as the sampling frequency times drift velocity is much smaller than the wire
27 spacing. As long as the tracks that should be separated from one another travel at an angle with
28 respect to the APA plane, then the fine time resolution will help with the pattern recognition even
29 if the wire pitch is large.

30 The reconstruction of short tracks, such as low-energy protons ejected by the struck nucleus at
31 the primary vertex of a neutrino scattering event, is improved with higher spatial resolution. A

reduced wire pitch also allows more precise measurements of the distance between the primary vertex and photon conversion points, which is the other component of $\pi^0 \rightarrow \gamma\gamma$ separation from electrons. Topological identification of two EM showers and their displacement from the primary vertex is expected to provide a factor of ten to twenty in NC background rejection while retaining at least 90% efficiency for ν_e CC events. A hand-scan study comparing liquid argon TPC detector performance in topological separation of NC events from ν_e CC events in a detector with 5-mm wire pitch and a detector with 10-mm wire pitch [?] showed no degradation in performance with the coarser wire pitch. Automated topological selection has yet to be developed, though it is anticipated that this finding will remain true, given that the radiation length in liquid argon is typically ~ 30 times the typical wire spacing.

The gains in physics from a finer wire pitch must be balanced against the increased cost of the electronics and online computing resources needed to read out the additional wires. In addition, the additional cold electronics components would likely create a higher heat load in the liquid and manufacturing the APAs would likely take longer due to the higher density of wires.

The spacing between the planes is customarily chosen to be similar to the spacing between the wires within the planes, though this, too, is an optimizable parameter. Narrowing this spacing improves the sharpness of the signals (in time) in both the induction and collection planes, though electronics shaping and diffusion will limit the ultimate signal sharpness. These functions can be deconvolved, though deconvolution and noise filtering produce artifacts in the signals. Studies varying the spacing between the planes can be performed to estimate the impact on two-hit time resolution.

Future studies will estimate the performance, as a function of the wire pitch, of the dE/dx -based $e - \gamma$ separation for events in which the showers are not identified topologically as candidates for having come from π^0 decay using automated tools. It is important to estimate the performance for this class of events separately because the kinematic properties of the events will correlate the performance dE/dx -based separation and topological separation.

Wire Angle

Like the wire pitch, the choice of the angles of the induction-plane wires relative to the collection plane wires affects the physics performance of the detector. Because the wires wrap from one side of each APA to the other, a discrete ambiguity is added to the continuous ambiguity of identifying where along the wire the charge was deposited.

Reconstruction of 3D objects based on 2D data (channel number vs. time) requires associating hits in one view with those in at least one other. If two wires cross only in one place, the ambiguity is removed once the hit is associated in the two views. If the wires cross more than once, three views are required in order to break the ambiguity of even isolated hits.

This association can most easily be done using the arrival time of the hits. If the time of a hit is different from that of all other hits in the event, then the association is easy. In more complex cases, where dense showers produce many hits at similar drift distances, misassociation can happen. In

15 this case, the discrete ambiguity makes it possible to displace a reconstructed charge deposition by
16 multiple meters from its true location. In the case that the U and V angles are the same and the
17 number of times a wire wraps around an APA exceeds one, then even a single, isolated hit can be
18 ambiguous. A small difference in the U and V angles breaks this ambiguity, though misassociation
19 still occurs in events with multiple nearby hits close in time. The use of clustering methods assists
1 in obtaining the correct ambiguity choices for hits in dense environments.

2 Reducing the wire angle reduces the number of crossings, but does not eliminate the possibility of
3 misassociating hits in events with multiple hits arriving simultaneously on their respective wires.
4 Reducing the angle aligns the shapes of features in the different views making it easier to correlate
5 them. The angle chosen for the DUNE far detector reference design ensures that no induction wire
6 crosses any collection wire more than once.

7 On the other hand, reducing the wire angle worsens the resolution of 3D reconstruction of hits
8 in the vertical direction. It also worsens the resolution on the measured separation between the
9 primary vertex and photon conversion points, though as pointed out above, the radiation length is
10 much longer than the wire spacing. The number of hits available for dE/dx separation of electrons
11 from photons degrades for vertically-going showers if the wire angle is reduced. A parametric study
12 of a figure-of-merit based on the measurability of the two photon-conversion lengths as a function
13 of the induction-plane wire angles is provided in [8].

14 The impact on the physics sensitivity of a small number of hits that are misreconstructed by many
15 meters from their true locations is estimated to be larger than that incurred by the degraded
16 resolution of each hit in the vertical dimension [?], though studies have yet to be performed to
17 estimate the impact on event detection efficiency, particle ID performance and energy resolution.
18 Hits with locations that are misreconstructed by large distances are not expected to contribute
19 properly to energy sums and may cause pattern recognition failures, such as missing tracks or
20 splitting of tracks into multiple pieces. Advances in algorithms to break ambiguities in complex
21 environments can allow for steeper wire angles.

22 The fact that the channel count must be an integer multiple of 128 in an APA also constrains
23 the wire angles as functions of the APA frame dimensions, though a procedure to find the proper
24 arrangement of channels that most closely approximates the optimized wire pitches and angles and
25 meets the channel count constraint may cause small deviations in the parameters.

26 Wire Length

27 The length of the collection-plane wires is determined by the APA dimensions (or vice-versa) and
28 the length of the induction-plane wires is determined by their angle and the APA dimensions.
29 The APA dimensions are largely constrained by transport and handling needs as well as stiffness
30 and production cost issues as they get larger. Capacitance and noise increase with wire length;
31 this effect would likely not be masked by electronics noise since the cold electronics is expected to
32 have very low noise. Therefore, in order to meet the signal-to-noise requirement with a finer wire
33 spacing, the wires may need to be made shorter.

34 On the other hand, longer wires lower the cost of the detector, as fewer electronics channels and
35 APA frames — and winding time and materials — are needed to instrument a given volume of
36 liquid argon.

37 It is anticipated that much of the work needed to study the impact of the wire pitch will inform
38 the wire length choice due to its impact on the signal-to-noise ratio.

39 **Maximum Drift Length**

1 The maximum drift length is another optimizable parameter. In this case, the driver for longer
2 lengths is the cost of the detector. A longer drift length assigns more liquid argon to be read out
3 by any given channel, reducing the APA count and the channel count. A longer drift length also
4 increases the fraction of liquid argon that is fiducial. Fiducial cuts will be made around the APA
5 planes to ensure containment and to minimize the impact of dead argon inside the APA planes.
6 Reducing the APA count thus reduces the amount of non-fiducial liquid argon.

7 A longer drift length, and the correspondingly longer electron lifetime, increase the likelihood that
8 the electron will attach to impurities as it drifts towards the anode plane. Once the drift length
9 has been specified, therefore, the requirements on the signal-to-noise ratio, the electron lifetime
10 and the dynamic range are coupled.

11 Increasing the drift length also degrades position resolution due to diffusion, where the spread of
12 a drifting packet of charge increases in proportion to the square root of the drift time. Charge
13 deposited near the APAs remains well measured, though charge deposited near the CPAs will
14 suffer from both attenuation and diffusion, lowering the signal-to-noise ratio. Small-signal de-
15 tection efficiencies and PID performance may decrease for events near the CPAs. Sophisticated
16 reconstruction and analysis algorithms can be used to recover resolution that is thus lost, but the
17 resolution may be limited by noise. Simulation studies in advance of CD-2 will address the impact
18 of diffusion and noise on the particle reconstruction performance.

19 **4.3 The Time Projection Chamber (TPC)**

20 **4.3.1 Overview**

21 The scope of the Time Projection Chamber (TPC) subsystem includes the design, procurement,
22 fabrication, testing and delivery of anode plane assemblies (APAs), cathode plane assemblies
23 (CPAs), the field cage and the high voltage system.

24 The TPC is the key active detector element of each DUNE far detector module. It is located inside
25 the cryostat vessel and is completely submerged in liquid argon at 88 K. The TPC is constructed of
26 modular APAs, CPAs and field-cage modules. The APAs and CPAs are assemblies of wire planes
27 and are tiled into alternating APA-CPA rows along the length of the cryostat. The resulting rows

1 are called *anode planes* and *cathode planes*, respectively. (Note the different uses of the word
 2 *plane*.) Field-cage modules enclose the four open sides between the anode and cathode planes.
 3 When proper bias voltages are applied to the APAs and CPAs, a uniform electric field is created
 4 in the volume between the anode and cathode planes. A charged particle traversing this volume
 5 leaves a trail of ionization in the ultra-pure liquid argon. The electrons drift toward the anode
 6 wire planes, inducing electric current signals in the frontend electronic circuits connected to the
 7 sensing wires. The current-signal waveforms from all sensing wires are amplified and digitized by
 8 the frontend electronics and transmitted through cold (immersed) cables and feedthroughs to the
 9 data acquisition (DAQ) system outside of the cryostat. While electrons drift toward the APAs,
 10 positive ions drift toward the CPAs at a velocity five orders of magnitude slower than that of the
 11 electrons and therefore contribute little to the signal on the wires.

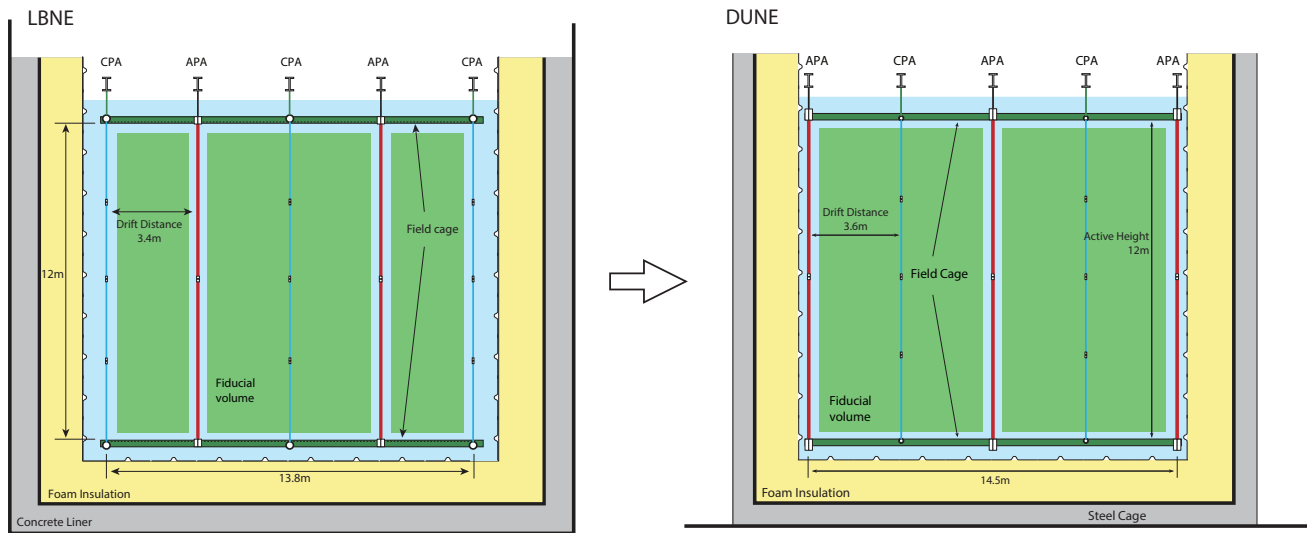


Figure 4.3: Cross sections of the LBNE 5-kt TPC (left) and the DUNE 10-kt TPC (right). The exchange of the APA and CPA positions significantly reduces the energy stored in the TPC by eliminating the two ground-facing cathode planes. This allows an increase in the detector’s fiducial volume given the same cryostat volume. The length of the DUNE TPC is 58 m along the direction of the neutrino beam (into the page).

fig:tpc-

12 The TPC active volume (Figure 4.2) is 12 m high, 14.5 m wide and 58 m long in the beam direction.
 13 Its three rows of APA planes interleaved with two rows of CPA planes are oriented vertically, with
 14 the planes parallel to the beamline. The electric field is applied perpendicular to the planes. The
 15 maximum electron-drift distance between a cathode and an adjacent anode is 3.6 m. This requires
 16 a -180 kV bias voltage on the cathode plane to reach the 500 V/cm nominal drift field. The
 17 anode plane assemblies are 2.3 m wide and 6 m high. Two 6 m modules are stacked vertically to
 18 instrument the 12 m active depth. In each row, 25 such stacks are placed edge-to-edge along the
 19 beam direction, forming the 58 m active length of the detector. Each CPA has the same width,
 20 but half the height (~ 3 m) as an APA, for ease of assembly and transportation. Four CPAs will
 21 be stacked vertically to form the full 12-m active height. Each cryostat houses a total of 150 APAs
 1 and 200 CPAs. Each facing pair of cathode and anode rows is surrounded by a field cage assembled
 2 from panels of FR-4 glass-reinforced epoxy laminate sheets with parallel copper strips connected
 3 to resistive divider networks. The entire TPC is suspended from five mounting rails under the

4 cryostat ceiling (see Figure 4.3). fig:tpc-floor-view

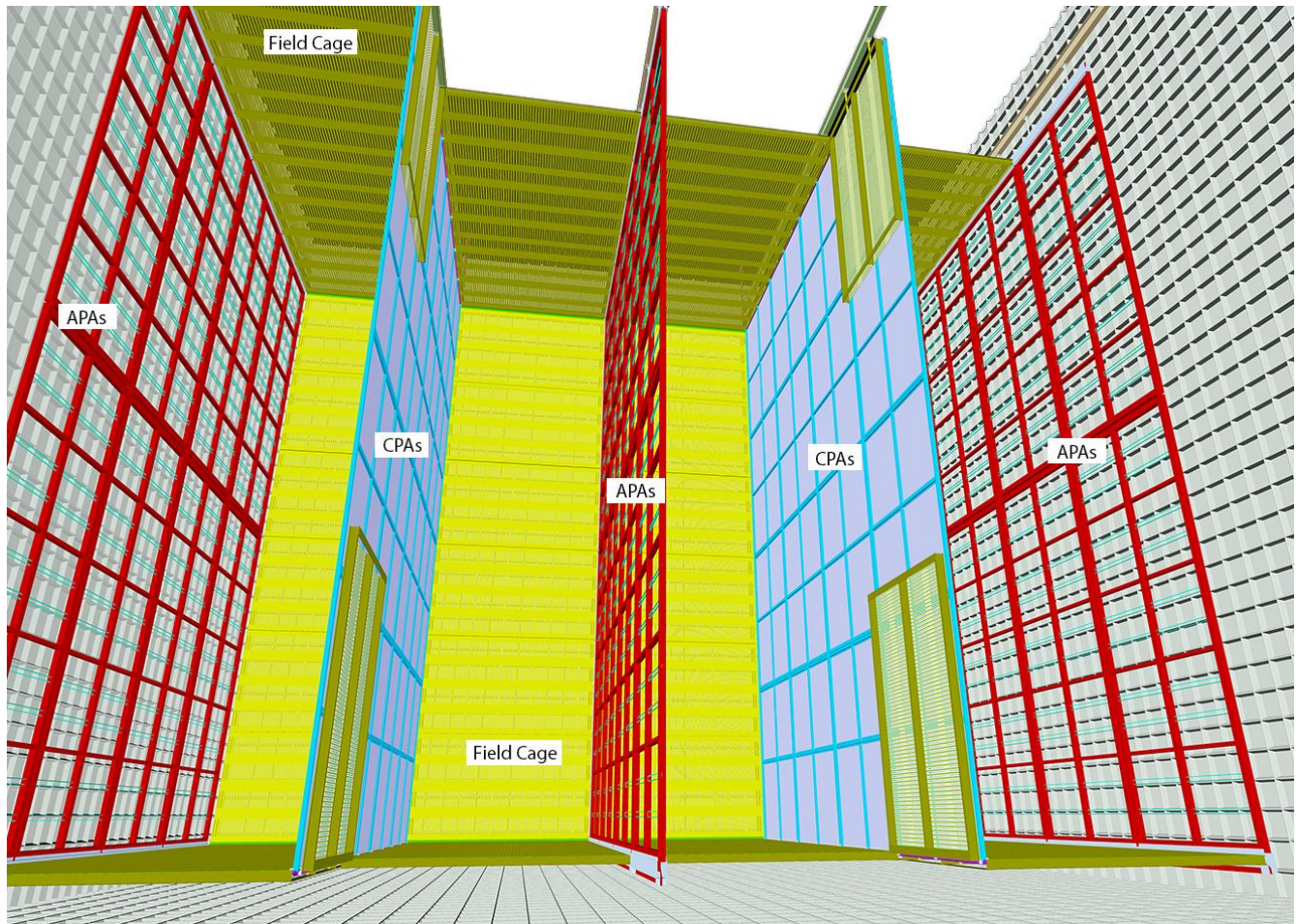


Figure 4.4: A view of the partially installed TPC inside the membrane cryostat. The APAs are shown in red, CPAs are in cyan, field-cage modules in yellow/green. Some of the field-cage modules are in their folded position against the cathode (providing aisle access during installation).

5 The units of construction of the active detector are the APAs, CPAs and field-cage modules.
 6 These are modular elements of a size optimized to simplify the manufacture, satisfy commercial
 7 highway and underground transport requirements, facilitate handling and efficient installation in
 8 the cryostat. APAs and CPAs Each element will be fully tested in LN₂ (or LAr) at the assembly
 9 site. They will be tested again at the far detector site before installation and will be monitored
 10 continuously during and after installation to detect any failures.

11 4.3.2 Anode Plane Assemblies (APA)

12 An APA is constructed from a framework of lightweight, rectangular stainless steel tubing, with
 13 four layers of wires wrapped on each side of the frame. From the outside in, the first wire layer
 14 is a shielding (grid) plane, next are two induction planes and the collection plane. The frontend
 15 electronics boards are mounted on one end of the APA frame and protected by a metal enclosure.

16 The APAs are 2.3 m wide, 6.3 m high, and 12 cm thick. The height is chosen for fabrication
 17 purposes and compatibility with underground transport limitations. The 2.3-m width is set to fit
 18 in a standard High Cube container for storage and transport with sufficient shock absorbers and
 19 clearances.

20 Wire Planes

21 APAs are strung with wire of 150 μm diameter copper beryllium (CuBe) alloy for high tensile
 22 strength, good electrical conductivity, excellent solderability and a thermal-expansion coefficient
 23 compatible with that of the stainless steel frame. The wires will be epoxied to fiberglass wire-
 24 bonding boards and then soldered to copper traces on the boards for electrical connections.

1 Four planes of wires cover each side of an APA frame as shown in Figure 4.4.

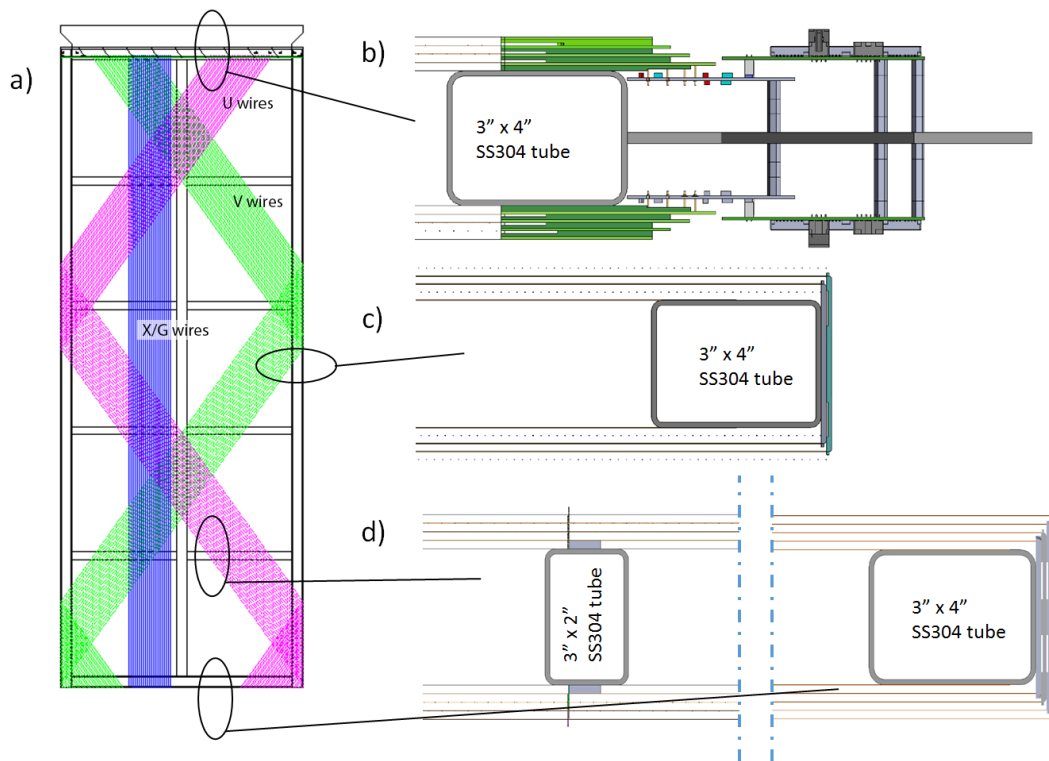


Figure 4.5: Illustration of the APA wire wrapping scheme (left), and three cross sectional views (right). At left, small portions of the wires from the three signal planes are shown in color: magenta (U), green (V), blue (X). The fourth wire plane (G) above these three, parallel with X, is present to improve the pulse shape on the U plane signals. At right, the placement of the wire planes relative to the stainless steel frame is shown for different locations on the APA. See Table 4.2 for wire plane parameters.

2 These four planes of wires are labeled, in order from the outside in: G (for grid), U, V and X.
 3 Table 4.2 summarizes the key parameters of each of the wire planes.

4 The distance between wire planes is 4.76 mm (3/16 inch, a standard printed circuit board thick-
 5 ness). Each wire plane is biased to a particular voltage such that the ionization electrons from

Table 4.2: Parameters of the four planes of wires on an APA

Label	Function	Orientation (from vertical)	Pitch (mm)	Number	Bias Voltage (volt)
G	Shield/grid plane	0°	4.79	960	−655
U	1 st induction plane	+35.7°	4.67	800	−365
V	2 nd induction plane	−35.7°	4.67	800	0
X	Collection plane	0°	4.79	960	+860

charged particle tracks will drift past the first three wire planes and be completely collected by the collection wire plane (X). The V wires are DC-coupled to the readout electronics to minimize the maximum voltage on the other wire planes. A grounded mesh plane with good optical transparency, located 4.8 mm behind the collection plane, prevents the electric field around this set of wires from being distorted by the metal frame structure and the wires on the opposite side of the frame. It also shields the sensing wires from potential EM interference from the silicon photomultipliers (SiPMs) on the photon detectors, mounted within the frame. Each wire on the U, V and X planes is connected to a front-end readout channel. The grid plane wires are not read out, but serve the important purpose of shielding the U wires from responding to distant moving charges. The total number of readout channels in an APA is 2560, for a total of 384,000 in each cryostat.

The wires on the two induction planes (U and V) are wrapped in a helical pattern around the long edges of the wire frame (Figure 4.4a). This technique makes it possible to place readout electronics only at one short edge of an APA frame, and allows tiling of the APAs on the other three sides with minimal dead space ($\sim 1.3\%$ of active area). Although wires on the induction planes are sensitive to tracks on both sides of an APA, the vertical collection-plane wires are only sensitive to one side, and therefore able to resolve this ambiguity. The upper APAs in the cryostat will have their readouts at the top edge of the frame (as shown in Figure 4.4), while the lower APAs will mount their electronics at the bottom edge. These readout electronics are located within the LAr volume but outside of the TPC active volume. On the readout end of an APA, 20 sets of front-end readout boards with 128 channels each (40U+40V+48X) are distributed on both sides of the APA, reading out the 2560 sense wires.

With the APA length and width constrained by transportation and handling limitations, the angles on the induction plane wires are chosen so that they wrap less than one full revolution around the APA. This avoids an ambiguity problem where three wires from three readout planes intersect more than once on an APA face (discussed in Section ??). Precise values of wire angle and wire pitch (see Table 4.2) were chosen to give an integral number of wires across the boards at the electronics end of the APA as well as an integral number of wire slots in the boards along the sides of the APA. A preliminary study [8] has shown that this wire layout meets the physics requirements.

The APAs facing the cryostat walls are sensitive on both sides, similar to those in the middle of the TPC. However, the negative bias voltage on their outer grid planes prevents any electrons drifting from the cryostat walls toward the sensing wires. The electronics for the outer X wire plane can be eliminated to save cost. Alternatively, these double-sided APAs can be utilized by adding another cathode plane with a small negative bias between the cryostat wall and the anode plane to form

8 a very shallow veto region.

9 **APA Frame**

10 At the nominal wire tension of 5 N, the total of 3520 wires exerts a force of ~ 7.0 kN/m on the
11 short edges of the APA, and a ~ 1.5 kN/m force on the long edges. The wire frame must be able
12 to withstand the wire tension with minimal distortion, while minimizing dead space due to the
13 thickness of the frame. The wire frame is constructed from stainless steel tubes welded in a jig.
14 Structural analysis has shown that the maximum distortion of the frame due to wire tension is
15 less than 0.5 mm. The total mass of a bare frame is ~ 260 kg.

16 All tube sections are vented to prevent the creation of trapped LAr volumes. The three long
17 tubes have slots cut in them so the photon detectors can be inserted into the APAs after the wires
18 are installed. The two long outer members of the frame are open-ended, so the photon detector
19 cables can be threaded through them to reach the signal feedthroughs on the cryostat roof. These
20 long tubes can potentially be used to carry signal and power cables from the bottom APA cold
21 electronics boards to the signal feedthroughs. This could significantly reduce the cable length
22 compared to, e.g., running the cables from the middle bottom APAs along the floor and then up
23 the wall.

24 **APA Wire Bonding and Support**

25 The wire bonding boards physically anchor the wires at the edges of an APA and provide the
26 interface between the wires and the cold electronics at the readout end of the APA. The four
27 planes of wires are attached to their respective wire bonding boards through a combination of
1 epoxy and solder. During winding of the X layer onto the APA, the wires are placed across the top
2 surface of the X wire board. The wires are then glued down with a strip of epoxy at the leading
3 edge of the board. After the epoxy has cured, the wires are soldered onto the copper pads under
4 each wire, and then the wires are cut beyond the pads. The V, U and G planes are attached on
5 top of the X boards and similarly populated with wires, one layer at a time. An array of pins is
6 pushed through holes in the stack of wire bonding boards, making electrical connections between
7 the wires and the capacitor-resistor (or CR) board, which is located between the wire boards and
8 the front-end electronics boards. The CR boards distribute the bias voltages to each wire through
9 current-limiting $20\text{ M}\Omega$ resistors, and bring the charge signal through high voltage AC coupling
10 capacitors to the cold electronics.

11 These readout boards, as described in Section [4.5](#), generate an estimated ~ 160 W of heat per
12 APA which may produce a small quantity of argon bubbles. Stainless steel covers are placed over
13 the readout boards to contain the bubbles and direct them to the gas volume of the cryostat.
14 This is particularly important for the bottom APAs where the bubbles must be contained and
15 funneled through the vertical hollow frame members to the top of the cryostat to prevent the
16 bubbles entering the TPC active volume.

17 Comb-like wire support structures (see Figure 2.9 in Annex 4A: *The LBNE Design for a Deep*
 18 *Underground Single-Phase Liquid Argon TPC*) are located on each of the four cross beams (see
 19 Figure 4.4) so that the longitudinal wires are supported every 1.2 m and the angled wires about
 20 every 1.5 m while introducing only millimeter-scale dead regions. The support structure is com-
 21 posed of strips of thin G10 sheet, with notches machined at correct intervals. These wire supports
 22 play a key role in minimizing wire deflection due to gravity and electrostatic force, enabling the use
 23 of a moderate wire tension and reducing the risk of wire breakage. They also maintain the correct
 24 wire pitch and wire plane separation even if the APA frame has a small amount of twist and warp.
 25 If a wire breaks after installation, these intermediate wire support will limit the movement of the
 26 broken wire such that it will not travel too far into the drift volume and make contact with the
 27 field cage. To further reduce the risk and impact of a broken wire, a new wire support scheme
 28 is being developed that can be applied to the outer wire planes near the bottom of the TPC to
 29 prevent a broken wire from contacting the field cage.

30 Wire-winding Machines

31 A winding machine will be constructed to lay the 3520 wires onto each APA. It has sufficient
 32 versatility that the same mechanism can wind both the angled and the longitudinal layers. Its
 33 working concepts are illustrated in Figure 4.5.

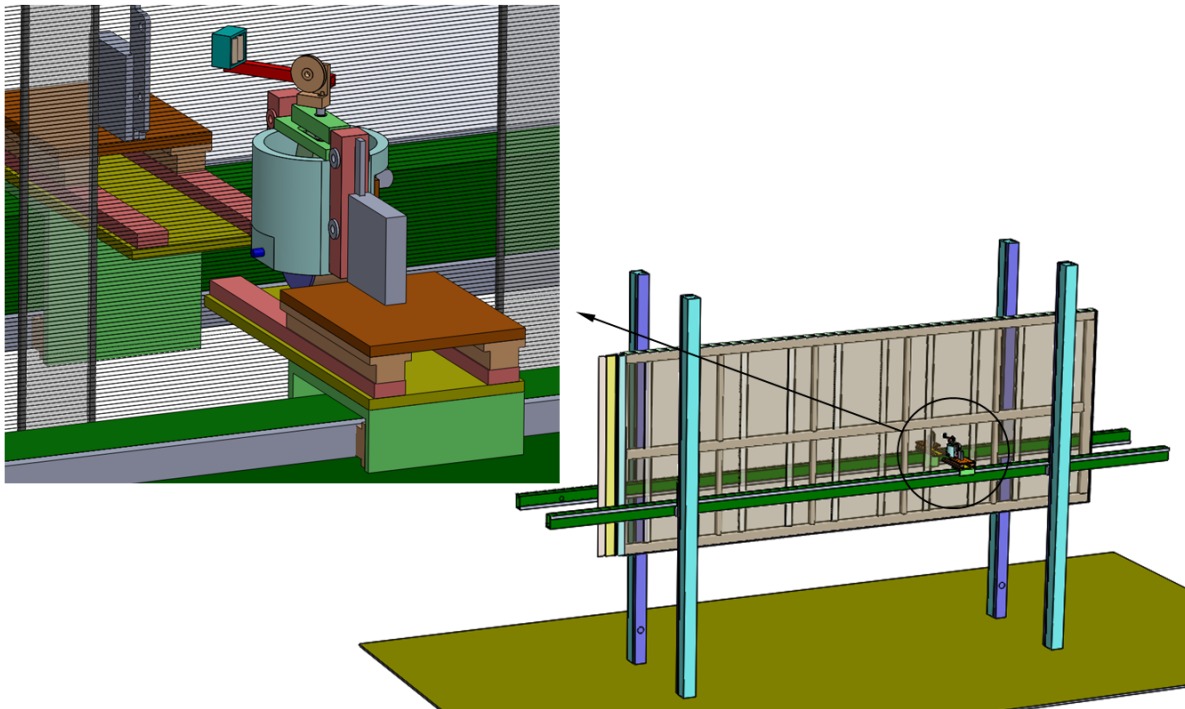


Figure 4.6: Illustration of the wire winding machine concept. The tensioner head is passed from one side of the APA to the other as it is moved around the APA to wind wire onto the APA frame. The horizontal/vertical positioning systems on each side of the APA are made of commercial linear motion components.

34 The wire tensioner is a self-contained unit that includes the wire spool. It is designed so that

35 correct wire tension is maintained, independent of the wire-feed rate and direction. The APA,
 36 oriented horizontally in the device (with one of its long edges down), is held off the ground by a
 37 couple of posts. There are X-Y positioners on either side of the APA; the tensioner is moved across
 38 the face of the APA by one of these positioners, unspooling tensioned wire as it moves. When the
 39 tensioner arrives at the edge of the APA it is passed across to the positioner on the other side
 40 of the APA while placing the wire into the appropriate slots of the edge boards. In this way the
 41 entire layer of wire can be placed on the frame.

1 Although a large part of an entire plane of wires can be wound in one continuous process, a more
 2 fault-tolerant procedure will be adopted in which the winding machine will be paused periodically
 3 to solder the last wire winding. This intermediate soldering step will prevent the unraveling of a
 4 large section due to an accidental broken wire. An automatic soldering robot will solder the wire
 5 ends after the wires have been laid down on the APA. A wire-tension measuring device will scan
 6 the newly placed wires and record the wire tension of each wire. Any wires with abnormal tension
 7 will be replaced manually.

8 4.3.3 Cathode Plane Assemblies (CPAs)

9 There are two cathode planes in each detector module. Each cathode plane is tiled from a four-
 10 unit-high by 25-unit-wide array of CPAs. Figure 4.6 shows the building blocks of a cathode
 11 plane.

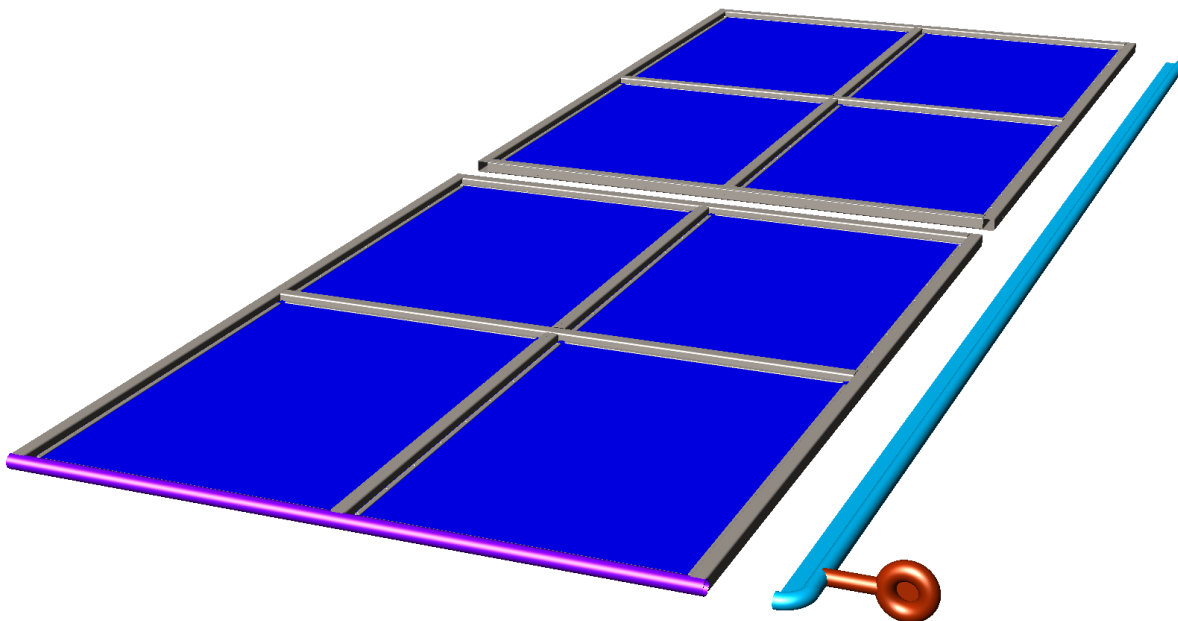


Figure 4.7: Conceptual design of the cathode plane components near a corner. Two flavors of CPAs (outer and inner unit) are used to make up the entire cathode plane; all CPAs are roughly 2.3 m wide by 3 m tall. The cathode plane is terminated at right and left ends by the end pieces (cyan colored). An HV receptacle (orange) connects with the HV feedthrough from the cryostat ceiling.

12 Each CPA is 2.3 m wide (identical to the APA width) and 3 m tall (half of APA height) for ease

of fabrication, assembly and handling. Each CPA is made of a stainless steel framework, with panels of solid stainless steel sheets mounted between the frame openings. Along each vertical column of four CPAs, there are two slightly different versions: the outer CPAs (top and bottom rows), and the inner CPAs (2nd and 3rd rows). The inner CPAs use all rectangular tubes for the frame structure, while the outer CPAs use 5 cm OD round tubes on the outside edge of the CPA facing the floor or ceiling of the cryostat to minimize the surface electric field (shown in magenta in Figure 4.6). Two sets of field-shaping end pieces are installed at the two ends (e.g., right and left) of a CPA wall to properly terminate the cathode wall with rounded edges. All CPAs are suspended from the ceiling using G10 hangers under fiberglass rails to insulate the CPAs from the cryostat.

A recent design decision exchanged the positions of the CPAs and APAs in the detector relative to the earlier LBNE reference design, placing the APAs adjacent to the cryostat wall instead of the CPAs. This change reduces the stored energy on each cathode plane by about 60%. Nevertheless, due to the enormous area of the stainless steel cathode plane, there is still nearly 100 Joules of energy when biased at 180 kV, risking physical damage to the thin membrane structure as well as to the CPA structure in the event of a high voltage discharge. In addition, in such an event, a huge voltage swing could occur on the cathode plane in tens of nanoseconds, injecting a charge pulse to the sensing wires with a large peak current that could damage the front-end electronics.

To mitigate this risk, analysis of the electrical properties of the cathode has been carried out with the goal of developing a cathode design that will substantially slow down the total energy release in case of a discharge. The best solution appears to be replacing the metallic cathode structure by non-conductive materials with a robust and highly resistive surface coating. Many choices of resistive/anti-static coating and commercially produced anti-static sheet materials are available. Studies are underway to identify a suitable coating and base material for this application. Since the electrical current feeding the field cage resistive dividers is supplied through the cathode, a special current-distribution feature must be designed to minimize voltage drop along this 58-m-long, highly resistive structure.

4.3.4 Field Cage

In the TPC, each pair of facing cathode and anode planes forms an electron-drift region. A field cage must completely surround the four open sides of this region to provide the necessary boundary conditions to ensure a uniform electric field within, unaffected by the presence of the cryostat walls.

Each 10-kt detector module requires ~ 2000 m² of field cage coverage. In the current reference design, the field cages are constructed using multiple copper-clad FR-4 sheets reinforced with fiber glass I-beams to form modules of 2.3 m \times 3.6 m in size. Parallel copper strips are etched on the FR-4 sheets using standard printed circuit board fabrication techniques. Strips are biased at appropriate voltages provided by a resistive-divider network. These strips create a linear electric-potential gradient in the LAr, ensuring a uniform drift field in the TPC active volume. Simulations have shown that the non-uniformity of the drift field quickly drops to about 1%, roughly a strip pitch away from the field-cage surface.

5 Since the field cage completely encloses the TPC drift region on four sides, while the solid cathodes
 6 block the remaining two, the field cage sheets must be perforated to allow LAr recirculation in the
 7 middle third of the TPC volume. The “transparency” of the perforation will be determined by a
 8 detailed LAr computerized fluid dynamic (CFD) study.

9 The resistor-divider network will be soldered directly onto the field-cage panels. Multiple resistors
 10 will be connected in parallel between any two taps of the divider, in order to provide fault tolerance.
 11 One end of the divider chain is connected directly to the cathode, while the other end is connected
 12 to ground at the APA through resistors of the appropriate value. A pair of field-cage modules
 13 will be pre-attached to the outer CPA modules through hinges, such that the field-cage modules
 14 can be rotated into their final position during installation, or folded back if aisle access is needed
 15 (see Figure 4.3). In addition to the resistor-divider network, surge suppressors such as varistors
 16 or gas discharge tubes will be installed between the field-cage strips to avoid the occurrence of an
 17 over-voltage condition between field-cage electrodes and the cathode in the event of a high voltage
 18 discharge.

19 The major challenge of this field-cage design is minimizing the electric field near the edges of
 20 the thin copper strips. One solution is to cover all copper edges with a thick layer of solder
 21 mask (an acrylic-based polymer with a high dielectric strength) as part of the standard PCB
 22 fabrication process. This construction is currently being implemented in the 35-t prototype TPC
 23 (see Sec 7.5 of Annex 4A: *The LBNE Design for a Deep Underground Single-Phase Liquid Argon*
 24 *TPC*). Figure 4.7 shows a section of this partially constructed field cage.

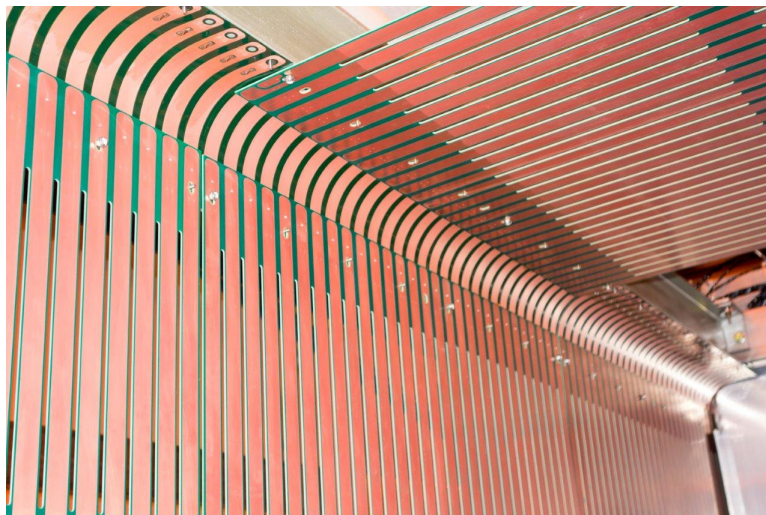


Figure 4.8: A corner of the 35-t TPC field cage during construction

25 The 35-t prototype test results will be evaluated to determine if this technique is suitable for the
 1 much larger far detector modules.

2 In the meantime, alternative concepts are being actively developed to further minimize the electric
 3 field on the field cage. One example is application of a very high-resistance coating on the outside
 4 surface of the field cage such that the surface potential distributes uniformly across the gaps
 5 between conductors and therefore eliminates the high-field region near the conductor edges. The
 6 challenge here is ventilation of this field cage surface without significantly increasing the field at

7 the edge of the perforations. Another concept is to use roll-formed metal profiles as the field-cage
 8 electrodes and support them with insulating beams. These profiles have large edge radii; this
 9 makes their surface electric field relatively low, which in turn makes it possible to place them even
 10 closer to the cryostat walls to improve the efficiency of LAr use. A sample profile is shown in
 11 Figure 4.8.

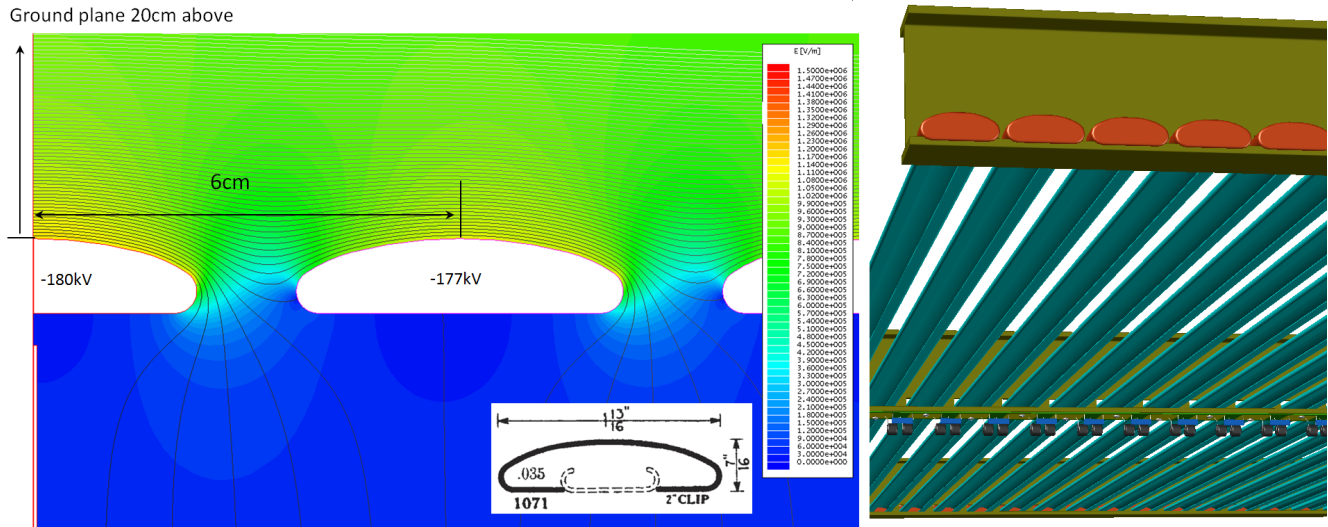


Figure 4.9: Left: electrostatic simulation of a field cage design that uses roll-formed metal profiles as the field-cage electrodes. Right: a conceptual design of a field-cage module using this profile.

12 With only a 20-cm distance separating the field cage from a ground plane, the electric field on the
 13 field cage is still under 12 kV/cm. The ends of the profiles still have high electric field, however; a
 14 possible solution is to cover the ends with UHMW polyethylene caps. This design may also cost
 15 significantly less than the reference design with PCBs.

4.3.5 High Voltage Components

1 The two cathode planes are biased at -180 kV to provide the required 500 V/cm drift field.
 2 Each cathode plane will be powered by a dedicated HV power supply through an RC filter and
 3 feedthrough.

4 The power supplies for the cathode planes must be able to provide -200 kV at 1 mA current.
 5 The output voltage ripple must not introduce more than 10% of the equivalent thermal noise from
 6 the front-end electronics. The power supplies must be programmable to trip (shutdown) their
 7 output at a certain current limit. During power on and off, including output loss (for any reason),
 8 the voltage ramp rate at the feedthrough must be controllable to prevent damage to the in-vessel
 9 electronics from excess charge injection. High-voltage feedthroughs must be able to withstand
 10 -250 kV at their center conductors in 1 atm argon gas environment when terminated in liquid
 11 argon.

2 The current candidate for the high-voltage power supplies is the Heinzinger PNC hp series, which

3 has the lowest output ripple specification. Additional filtering of the voltage ripples is done through
 4 the intrinsic HV cable capacitance and series resistors installed inside the filter box. Established
 5 techniques and practices will be implemented to eliminate micro-discharges and minimize unwanted
 6 energy transfer in case of an HV breakdown.

7 To ensure safe and reliable operation, the feedthroughs will be tested at a much higher voltage
 8 than expected in routine operation (~ 250 kV) in LAr. The feedthroughs will be mounted on the
 9 ceiling of the cryostat, their cold ends reaching through the gas ullage space and submerging into
 10 the LAr. The center conductor on the cold side of a feedthrough will be insulated and shielded by
 11 a grounded shroud at least 50 cm below the surface of the liquid to ensure bubble free operation at
 12 the tip. Figure 4.9 shows an example of the feedthrough and filter box made by the UCLA group
 13 for the 35-t prototype TPC, as well as the conceptual design of a feedthrough suitable for the far
 14 detector TPCs.



Figure 4.10: Top: The high voltage feedthrough and filter developed by the UCLA group for the 35-t TPC. The total length of the feedthrough is about 2 m, and its main body has an OD of 3.8 cm. It was tested up to 150 kV. Bottom: a conceptual design of a new feedthrough for the far detector.

4.3.6 TPC Prototyping and Tests

15 Several prototype TPC modules were constructed during the LBNE project design phase. The
 16 initial prototypes were fractional-scale or partial models of the APA and CPA. The CPA prototype
 17 was used to evaluate field-shaping electrode attachment techniques. A 40% scale APA prototype
 18 was constructed earlier on to study the placement of the wire-wrapping boards and wire-support
 19 structures. It was also used to develop the prototype winding machines. The prototypes were
 20 subjected to numerous thermal cycles down to liquid-nitrogen temperature to test the integrity of
 21 the wire-to-board and board-to-frame bonds.
 22

23 The second set of prototypes are scale models of the APA and CPA. They are being used to
 24 validate the designs and to evaluate production procedures. These functional prototypes will be
 25 installed in the 35-t prototype cryostat and are expected to be operational in 2015.

26 A TPC prototype proposed for installation in a CERN test beamline requires six full-size APAs
 27 with fully instrumented readout electronics, six full-size CPAs and complete field cage coverage.
 28 This prototype will be constructed using identical APAs, CPAs and field-cage panels as designed
 29 for the far detector. Additional features will be installed to ensure proper TPC operation given
 30 the half-height cryostat configuration. The construction and assembly of all TPC mechanical
 31 components will use the same materials and techniques as designed for the far detector, with the
 32 exception of the degree of automation for wiring the APAs, which will be reduced.

33 4.4 Data Acquisition (DAQ) System and Monitoring

34 The scope of the Data Acquisition (DAQ) system and monitoring includes design, procurement,
 35 fabrication, testing, delivery and installation of the following components (see Figure [4.10](#)):

- 36 • LArTPC detector readout
- 37 • Photon detector readout
- 1 • Computer farm
- 2 • artDAQ software toolkit
- 3 • Run Control and Slow Control
- 4 • Timing system
- 5 • Calibration system

6 The DAQ system is required to:

- 7 • collect data with a very high uptime (the goal is >99%)
- 8 • collect beam neutrino, atmospheric neutrino and proton decay candidates (generally all in-
 9 teractions with total energy deposition above about 100 MeV) with a high resolution (smart
 10 or no zero-suppression) with no dead-time.

11 It would be nice to reference a section; ‘smart’ suppression is not mentioned in the S%
 C chapter; zero supp is. How best to handle?

- 12 • collect interactions with total energy below 100 MeV with some low amount of zero-suppression
 13 loss.
- 14 • trigger at the time of the beam pulses, irrespective of how little energy is deposited in the
 15 detector.

- 16 • collect data with the most favorable zero-suppression possible over a period of >10 s (super-
17 nova trigger)
- 18 • assemble data from sub-detectors into a unified event for offline analysis.
- 19 • provide access to the shift operator and others to control and monitor the data collection and
20 detector status, view online histograms and monitor (and provide for offline use) historical
21 status of measured detector parameters.

22 This section outlines a conceptual design intended to meet the required performance for the DAQ
23 for the DUNE far detector. To reduce considerably the times when none of the DUNE far detector
24 modules are collecting data (particularly important for supernova detection); and to allow the
25 designs of the DAQ in the different 10-kt modules to be entirely different if desired, the DUNE
26 DAQ employs a decoupled design. The synchronization, triggering, data collection and run-state
27 in the different 10-kt modules are completely independent in real time and are only coupled by
28 processes running asynchronously (in the same fashion as a batch queue) in the hour or so after
29 data collection (see section 4.11 of Annex 4A: *The LBNE Design for a Deep Underground Single-
30 Phase Liquid Argon TPC*). This allows one detector module to be restarted without interrupting
31 data collection in the others.

32 The layout of the DAQ is shown schematically in Figure 4.10. fig:fddaqblock

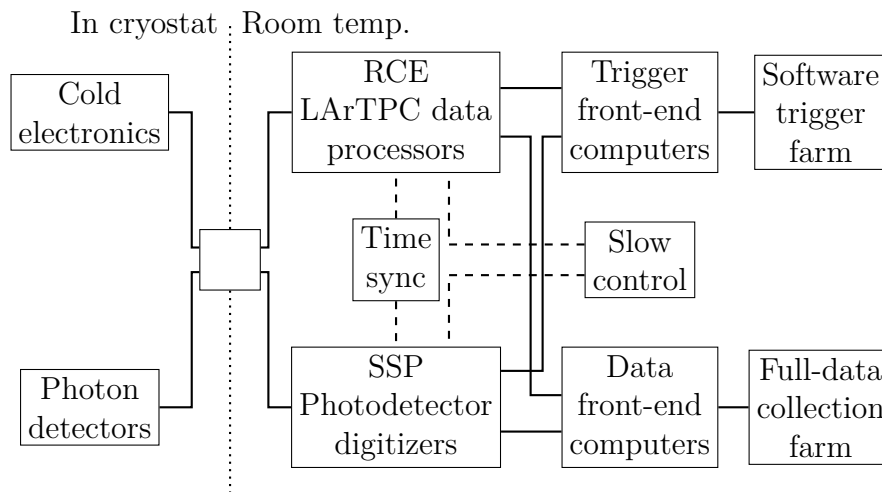


Figure 4.11: Block diagram layout of the main components of the DAQ subsystem. fig:fdda

33 To collect full detail of the most important events (deadtimeless detection of all those with energy
34 deposition of 100 MeV and above), while avoiding tricky communication to flag neighboring chan-
35 nels to those that have large hits, a model is used in which the digitized data are collected twice
36 from the initial data storage that is associated with each piece of hardware.

1 The first collection supplies a centralized software-based trigger farm continuously with zero-
2 suppressed information (a threshold on each channel detects hits above the noise level; this causes
3 the ADC samples to be kept in a time window around the hit). The second collection reads the
4 full data at the times and in the regions selected by the trigger. This is similar to the multi-level
5 triggering in a collider experiment, but with only one level of triggering. The software trigger farm

6 also records the continuous stream of zero-suppressed hits in an archival ring buffer on disk to
7 allow later analysis of supernova candidates.

8 **LArTPC detector readout** The LArTPC signals are digitized in the cold in a continuous flash-
9 ADC stream at 2 MHz, (not zero-suppressed) and serialized on 12,000 high-speed links per 10-kt
10 module that exit the cryostat. The data are received by LArTPC data processors called RCEs
11 (Reconfigurable Computing Elements) housed in industry-standard aTCA crates on COB (cluster-
12 on-board) motherboards that are designed at SLAC for a wide range of applications. The RCEs
13 are part of a network of field programmable gate arrays (FPGAs) that buffer the full raw data,
14 zero-suppress it for passing to the trigger and accept requests for data-fetching from the trigger.
15 The FPGAs in the RCEs are from the Xilinx Zynq family and contain a full Linux processor system
16 on the chip. They facilitate the high-speed data transfer from firmware into DRAM memory that
17 is accessible from Linux. A fast data-transfer network using the Ethernet protocol is used on the
18 COBs and in the aTCA crates to allow for development of more sophisticated zero-suppression
19 algorithms for improved supernova acquisition.

20 **Photon detector readout** is performed by the SiPM signal processor (SSP) described in Sec-
21 tion 4.6.1. The additional buffering required for the separate trigger and data collection paths is
22 implemented in the SSP front-end computers.

23 **Computer farm** Both the LArTPC and photon detector data are received in commodity Linux
24 computers, with no deadtime, from where the data are routed to the trigger and full-data col-
25 lection farms of computers. Although the front-end computers are logically distinct as shown in
26 Figure 4.10, one physical computer is sufficient for all the processes for each rack of APA readout
27 electronics.

28 **artDAQ software toolkit** (from Fermilab) supplies the real-time data collection functionality
29 (buffering, matching event parts, synchronization, inter-process communication, etc.) in a modern
30 design that facilitates the efficient use of multicore commodity computers running on the Linux
1 computer farms. The multicore functionality is crucial in the high data-rate environment on DUNE.
2 The detector-specific code is supplied by DUNE groups (this is centered in the UK), along with
3 detector-specific triggering (also UK). The architecture provided by artDAQ can be tailored for
4 each experiment and is entirely suitable for the “collect-twice” architecture envisioned for DUNE.

5 **Run Control and Slow Control software framework** manages the control, status display and sta-
6 tus archival of the experiment. It is based on the design of the DAQ of the ICECube experiment[?].
7 This exploits a combination of readily available, well-supported packages [message passing (ze-
8 roMQ), a web-framework (Django), databases (postgres)] to give the shift operator a unified view
9 of the status of the running experiment, and views of the monitoring data including customized
10 views and historical views. The database of slow-control measurements is exported to the host lab
11 to give access for offline programs.

12 **Timing system** To accomplish the software-based deadtimeless data acquisition in DUNE, it is
13 necessary to synchronize the clock across all readout boards. This is accomplished in two stages.
14 The main cavern-wide distribution uses the design from the NO ν A experiment, which distributes
15 a 64-MHz clock, synchronization pulses and cable-delay correction on RJ45 cables. The overall
16 clock is synchronized using a GPS receiver and transferred from the surface over optical fiber.

17 The synchronization is transferred from the COBs to the electronics in the cryostat over the same
 18 cabling as provides the data links.

19 **Calibration system** The calibration is done in three stages: (1) Pedestal and charge-injection pulser
 20 events are used to calibrate and remove drifting of the individual electronic channel responses. (2)
 21 External UV lasers are directed into the cryostat through glass-tube ports, and swivelling mirrors
 22 select the trajectories of the beams through the cryostat to provide calibration of the field non-
 23 uniformities and attenuation. (3) Cosmic-ray muons are used for the determination of the energy
 24 scale and for calibration cross-checks.

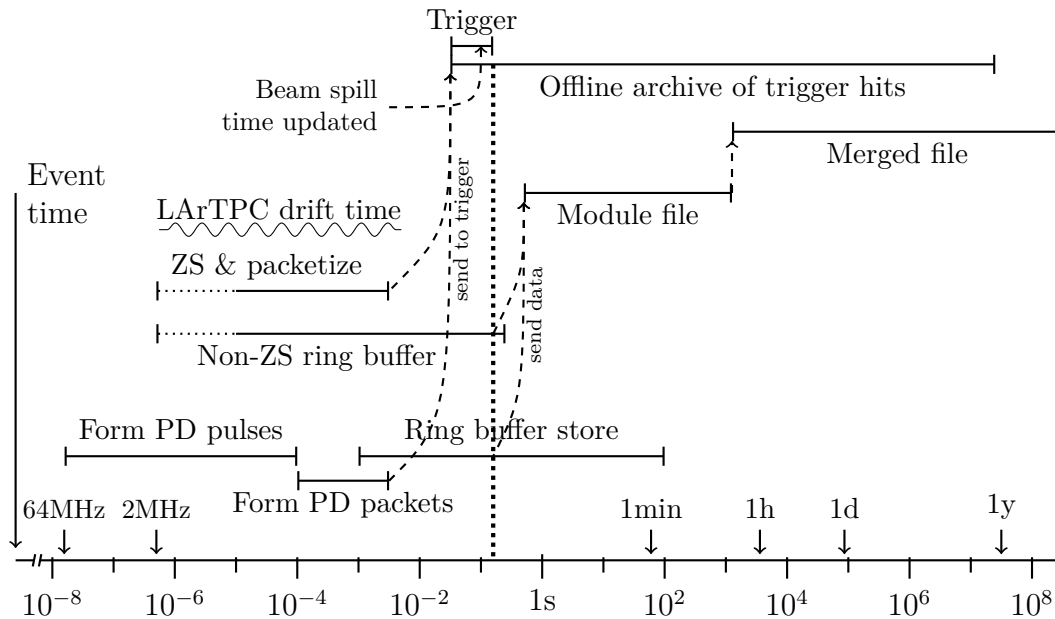


Figure 4.12: Main DAQ steps displayed relative to the event time.

fig:fdda

25 The time sequence, trigger deadlines and buffering of the readout are all shown in Figure 4.11.
 26 This figure shows time in the horizontal direction on a logarithmic scale to indicate how long after
 27 the particles appear in the detector each process can start and must finish. There is one level
 28 of triggering, with a trigger deadline (latest time a trigger decision can arrive) of 0.16s after the
 29 event has occurred, indicated by the vertical dotted line. This is long enough that in 99% of the
 30 cases, a message will arrive from the Fermilab site to update the predicted time of a neutrino spill
 31 with the actual time in order that the detector can be triggered independently of any signals in
 32 the detector. This operation has been used successfully on MINOS for many years.

fig:fddaqttime

33 As shown in Figure 4.11, prior to the trigger time and independently in each detector module,
 34 the detector readout assembles packets of data corresponding to fixed time intervals and sends
 35 them to the trigger event builders. Both the LArTPC readout and the SSP readout send zero-
 36 suppressed data, suitable for triggering, to a set of event-builder processes that run in parallel,
 37 each accepting all the data from the entire 10-kt module for a specific time interval and performing
 38 trigger algorithms on them. All time intervals are processed so that the trigger has no dead time.
 39 The data from the LArTPC and SSP are also stored in ring buffers to await collection after an
 40 affirmative trigger decision — in the case of the LArTPC, this data is not zero-suppressed. The
 41 data are built into events in a “10kt-module file” that is written to disk. About an hour later, an

42 offline process merges the data from the separate 10-kt module files and archives them at the host
43 lab.

1 To maximize data collection for a supernova, the continuous zero-suppressed trigger data is kept
2 in a large buffer area on disk. During the extended period of this event, it is desirable to collect
3 data that are cropped more gently than the zero-suppressed data stream. The non-zero-suppressed
4 ring buffers on the current design of RCEs are sufficient for 0.4 s of buffering; during a supernova,
5 the trigger farm can send instructions in the trigger messages to manage storage of data in these
6 buffers. Two possible extensions to this method are (a) extend the memory to buffer longer, either
7 on the RCEs or elsewhere in the aTCA crate, or (b) use the powerful intercommunications between
8 RCEs to ensure that information read from neighboring channels around the time of a potential
9 supernova event candidate is kept.

10 At the 4850L, the data rate in the trigger is dominated by the unwanted radioactivity from ^{39}Ar and
11 ^{85}Kr . The cosmic rays that occur about once per minute, on the other hand, are the major source of
12 events that should be collected on the data stream; the physics beam events, atmospheric neutrinos
13 and other candidate events are included in this data budget. Table 4.3 gives estimates of the rate
14 of occurrence of these events and the expected steady-state data rate (after the derandomization
15 provided by the buffering in the front-end computers).

Table 4.3: Estimated data rates in the DAQ system

Process	Rate (kHz/APA)	Data rate (MBytes/s)
Generic 2.3 ms interval	0.43	6,000
Cosmic-ray muons (4850L)	6×10^{-7}	1×10^{-5}
Radioactivity	~ 64	1.9
Electronics noise (not common mode)	~ 1	0.03

16 The requirements are met in this conceptual design by the very high throughput provided by
17 modern off-the-shelf components and the parallelism provided by artDAQ, which makes the design
18 extendable to avoid bottlenecks. The triggering allows the zero-suppression to be tuned to optimize
19 for the final level of noise, while retaining the maximum level of information for the important
20 physics events.

21 This DAQ design is being prototyped for the 35-t tests in 2015 (see Section ??), with two COBs
22 (containing 16 RCEs) and eight SSPs. The artDAQ software toolkit is being used to implement the
23 readout, event-building and triggering, although the “collect-twice” model will not be implemented
24 for the 35-t test.

25 4.5 The Cold Electronics (CE)

26 The TPC read-out electronics are mounted on the APA front-end (Figure 4.12) in LAr.

27 These electronics are therefore referred to as the “Cold Electronics” (CE) subsystem. The scope

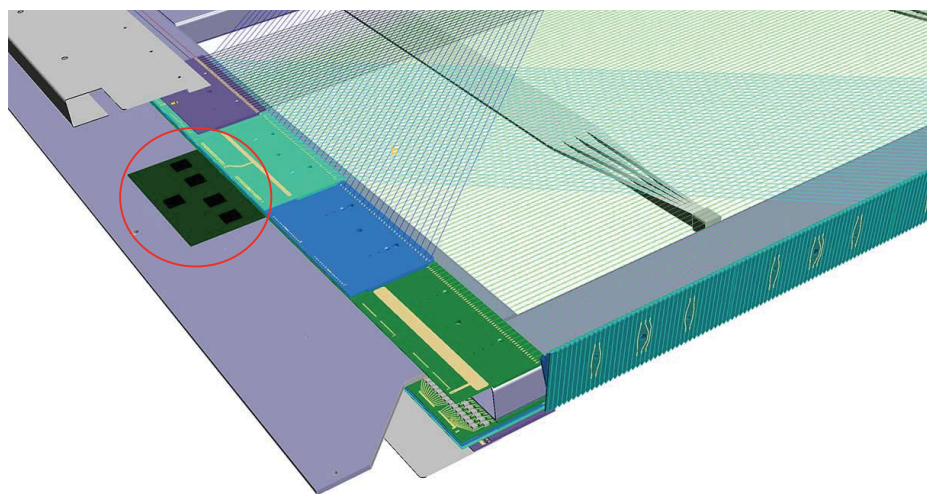


Figure 4.13: The front-end electronics, shown in the red circle, as mounted on an APA. (Note that this figure was not updated to show the current photon detection system scheme.)

fig:elec

28 of the CE subsystem includes design, procurement, fabrication, testing, delivery and installation
29 of:

- 30 • front-end electronics cards installed on the APAs;
- 31 • signal feedthroughs mounted on the cryostat;
- 32 • power supplies and cabling.

33 The following are the most significant requirements for the CE:

- 34 • minimize channel capacitance and noise
- 35 • minimize dissipated power per channel in the LAr
- 36 • read out the TPCs and transmit their data to the DAQ
- 37 • record the channel waveforms continuously without dead time
- 38 • provide sufficient precision and range to satisfy the Key Physics Parameters
- 39 • operate for the life of the facility without significant loss of function
- 40 • use only materials that are compatible with high-purity liquid argon and that have minimal
41 natural radioactivity

42 The CE are implemented as ASIC chips using CMOS technology, which performs well at LAr
43 temperatures[9], and provides amplification, shaping, digitization, buffering and multiplexing (MUX)
1 of the signals. The CE architecture is manifested in the Front End Mother Board (FEMB), a 128-
2 channel board which uses eight 16-channel Front End (FE) ASICs and eight 16-channel ADC

3 ASICs (Figure 4.13).

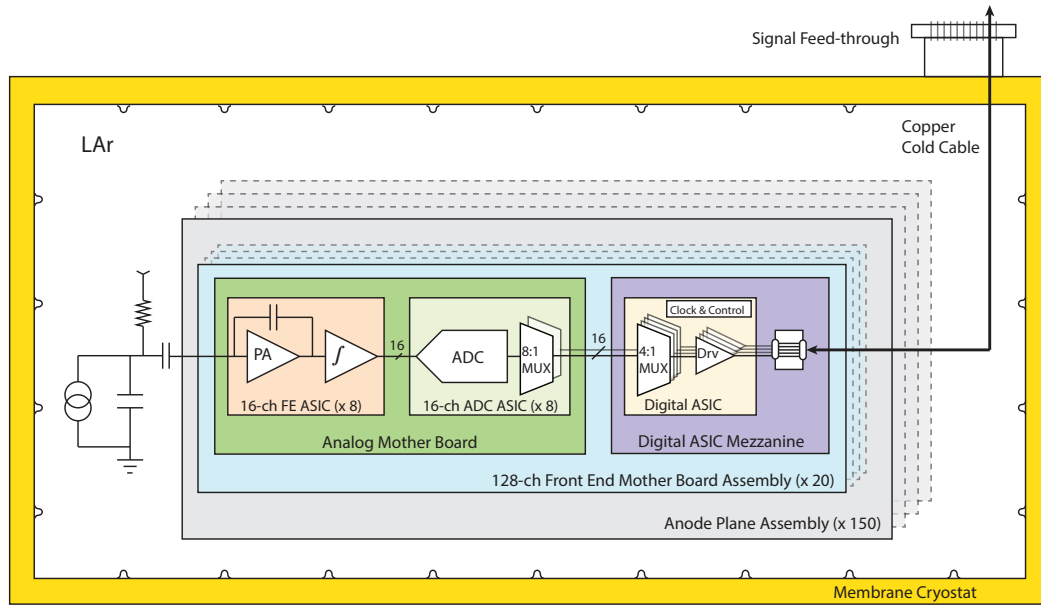


Figure 4.14: The CE architecture. The basic unit is the 128-channel FEMB. FEASIC: Front End ASIC. PA: Pre-amplifier. f : Shaper. MUX: Multiplexer. Drv: Driver.

4 The FE ASIC provides amplification and pulse shaping, while the ADC ASIC comprises a 12-bit
 5 digitizer and an 8:1 MUX stage with two pairs of serial readout lines in parallel. A Cold Digital
 6 Data (COLDATA) ASIC chip (Figure 4.14) mounted on each FEMB provides an additional MUX
 7 of 4:1 and is capable of driving the data at 1 Gb/s through 30 m of copper cable to the feedthrough
 8 and on to the DAQ. Tables 4.4 and 4.5 list the CE device counts and key parameters.

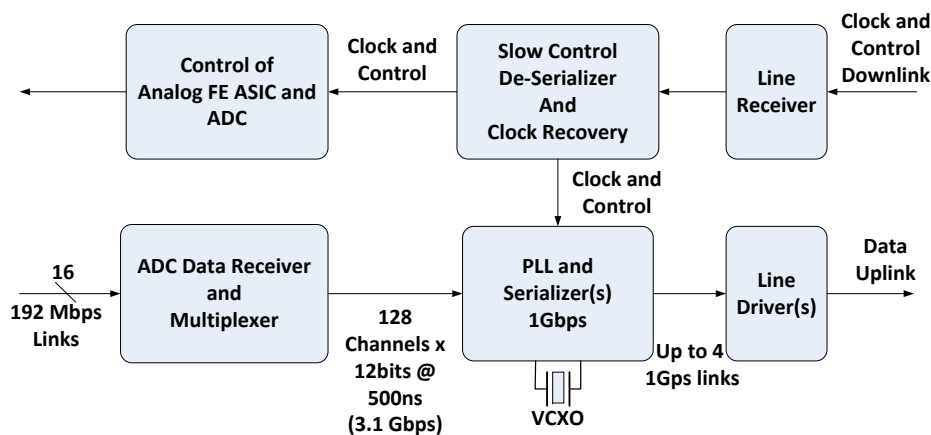


Figure 4.15: Functional block diagram of the COLDATA ASIC. PLL: Phase Locked Loop. VCXO: Voltage-Controlled Crystal Oscillator

9 An important aspect of CMOS technology is that the lifetime at cryogenic temperatures is well
 10 understood and can be well controlled, *provided that close control is maintained over the imple-*
 11 *mentation details.* This precludes the use of commercial devices, which are not intended for use
 12 in LAr, and which are produced by proprietary processes over which DUNE has no control. It is

Table 4.4: CE device counts

Parameter	per FEMB	per APA	per 10 kt Detector
Channels	128	2560	384,000
FE & ADC ASIC Chips	8	160	24,000
COLDATA ASIC Chips	1	20	3,000
FEMB	1	20	3,000
Signals-Out	4	80	12,000
APA	—	1	150

Table 4.5: CE key parameters

Parameter	Value
Signal-to-Noise (in LAr)	9:1 for 1 μ s peaking time
MUX Level	32
Sampling Frequency	2 MHz
ADC Resolution	12 bits
FE Peaking Time	0.5, 1, 2, 3 μ s (selectable)
FE Gain	4.7, 7.8, 14, 25 mV/fC (selectable)
Calibration Precision	1%
Power dissipation	11 mW/channel

13 worth noting that the FEMB, together with the FE and ADC ASIC chips, has already been proto-
 14 typed and tested using a commercial FPGA to perform the role of the COLDATA ASIC, which is
 15 currently under development. The 1-Gb/s data rate can be achieved with copper links and with-
 1 out zero-suppression or data compression. This greatly reduces the complexity of the COLDATA
 2 ASIC, with a corresponding decrease in overall risk, including risk of failure-to-implement (within
 3 a fixed schedule and budget). The COLDATA work is especially challenging, with final production
 4 not scheduled to begin until late 2019. Alternative approaches are currently under study.

5 Good reliability of cold electronics has been achieved in several previous experiments. More than
 6 8,000 cold electronics boards are used to read out \sim 180,000 channels in the ATLAS Liquid Argon
 7 Calorimeters with a failure rate of \sim 0.02% in 11 years of operation so far. The failure rate is less
 8 than 0.2% for \sim 13,000 channels of cold preamplifiers installed in the Liquid Krypton Calorimeter
 9 of the NA48 experiment for 17 years of operation. Lifetime studies of CMOS cold electronics
 10 for DUNE have been carried out to understand the aging mechanism due to channel hot carrier
 11 effects[?]. The design of the analog front end and ADC ASICs in 180-nm CMOS technology
 12 follows these design rules to secure lifetimes two orders of magnitude higher than the 30 years of
 13 experiment lifetime.

4.6 The Photon Detection System

The scope of the photon detector (PD) system for the DUNE far detector reference design includes design, procurement, fabrication, testing, delivery and installation of the following components:

- light collection system including wavelength shifter and light guides
- silicon photo-multipliers (SiPMs)
- readout electronics
- calibration system
- related infrastructure (frames, mounting boards, etc...)

LAr is an excellent scintillating medium and the photon detection system will exploit this property in the far detector. With an average energy of 19.5 eV needed to produce a photon (at zero field), a typical particle depositing 1 MeV in LAr will generate 40,000 photons with wavelength of 128 nm. At higher fields this will be reduced, but at 500 V/cm the yield is still $\sim 20,000$ photons per MeV. Roughly 1/4 of the photons are promptly emitted with a lifetime of about 6 ns while the rest have a lifetime of 1100–1600 ns². LAr is highly transparent to the 128 nm VUV photons with a Rayleigh scattering length of (66 ± 3) cm [10] and absorption length of >200 cm.³ The relatively large light yield makes the scintillation process an excellent candidate for determination of t_0 for non-beam related events. Detection of the scintillation light may also be helpful in background rejection and triggering on non-beam events.

The photon detection system reference design described in this section meets the required performance for light collection for the DUNE far detector. This includes detection of light from proton decay candidates (as well as beam neutrino events) with high efficiency to enable 3D spatial localization of candidate events. The TPC will provide supernova neutrino detection. The photon system will provide the t_0 timing of events relative to TPC timing with a resolution better than $1 \mu\text{s}$ (providing position resolution along drift direction of a couple of mm).

Alternative photon detector designs are under investigation to improve both light detection for the low-energy supernova events and their momentum resolution through determination of the event t_0 .

Figure 4.15 shows the layout for the photon detector system, which will be described in the following sections.

²Prompt and delayed photons are detected in precisely the same way by the photon detection system.

³This attenuation length requires a LN2 content of less than 20 ppm

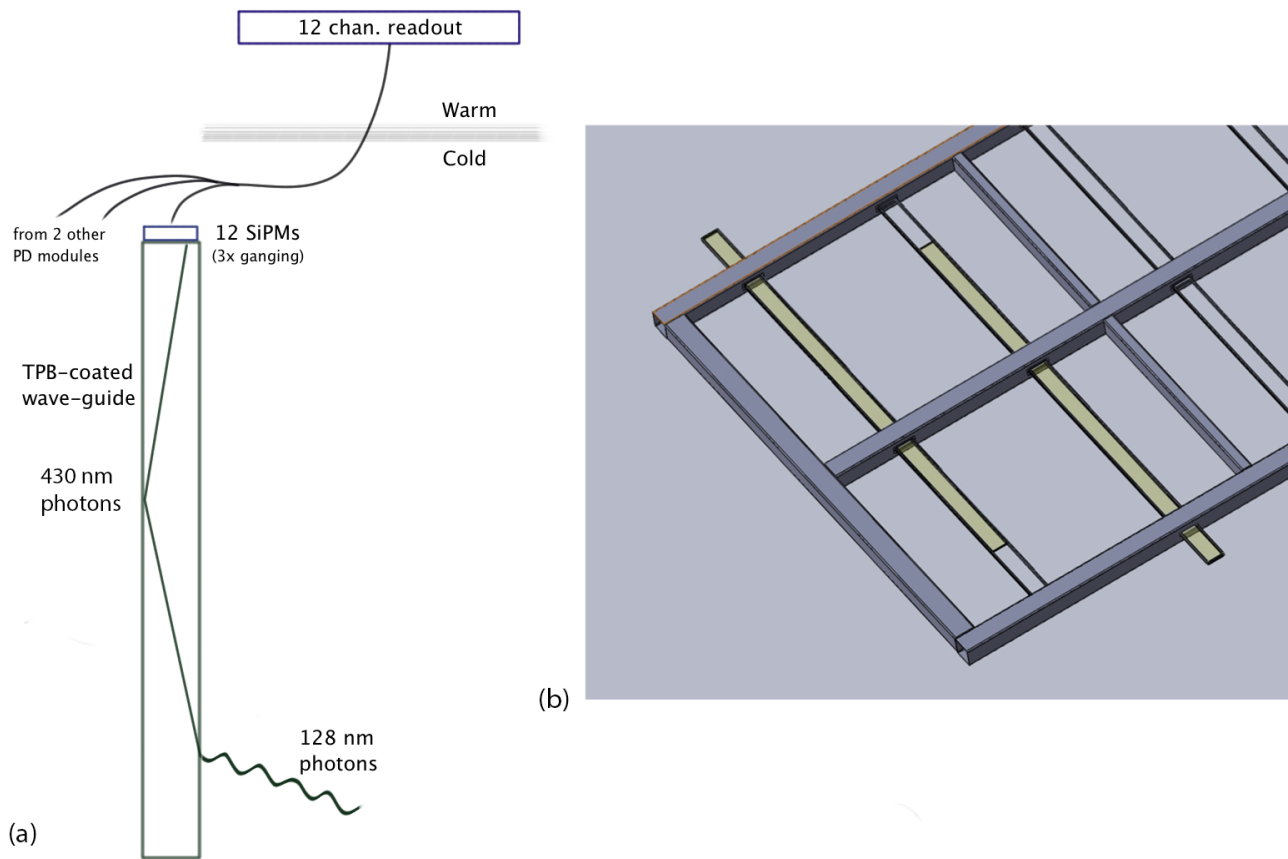


Figure 4.16: Overview of the PD system showing a cartoon schematic (a) of a single PD module in the LAr and the channel ganging scheme used to reduce the number of readout channels. Panel (b) shows how each PD module will be inserted into an APA frame. There will be 10 PDs inserted into an APA frame.

fig:PD_c

4.6.1 Reference Design

The PD system is mounted as modules on the APA frames. A PD module is the combination of one light-guide (also called a “bar” due to its shape) and 12 SiPMs, as shown in Figure 4.15 (a). To enable this, the reference design for mounting the PDs onto the APA frames calls for ten PD modules per APA, approximately 2.2-m long, 83-mm wide and 6-mm thick, equally spaced along the full length of the APA frame, as shown in Figure 4.15 (b).

The 128-nm scintillation photons from LAr interact with the wavelength shifter on the surface of the bar, and the wavelength-shifted light, with a peak intensity around 430 nm, is re-emitted inside the bar and transported through the light-guide to 12 silicon photo-multipliers (SiPMs) mounted at one end of the bar.

The wavelength shifter converts the scintillation photons striking the bar surface and directs them into the bar bulk with an efficiency of $\sim 50\%$. A fraction of the wavelength-shifted optical photons are internally reflected to the bar’s end where they are detected by SiPMs with quantum efficiency well matched to the wavelength-shifted photons. The light guides are made with a coated with TPB (1,1,4,4-tetraphenyl-1,3-butadiene). A testing program is currently underway to determine the absolute performance of the light guides in LAr.

The SiPMs used in the reference design are SensL C-Series 6 mm² (MicroFB-60035-SMT) devices. These SiPMs have detection efficiency of 41%⁴. While the C-Series SensL SiPMs are not rated for operation below -40°C their performance has been excellent for this application. At LAr temperature (89 K) the dark rate is of order 10 Hz (0.5 p.e. threshold) while after-pulsing has not been an issue. Extensive testing is underway to ensure that the SiPMs can reliably survive the stresses associated with thermal cycling in LAr and long-term operation at LAr temperature.

The SiPMs are read out using shielded twisted-pair cable, one per SiPM, but the expected final design will have three SiPMs ganged together and each readout cable will contain four individual channel cables to keep the cost and cable packing density down. During the R&D phase of the project each SiPM was read out individually in order to maximize the information gathered.

The front-end electronics reside outside of the cryostat in instrumentation racks. A custom module for receiving SiPM signals has been designed and built. The module also performs signal processing in the front-end as preprocessing for trigger and DAQ. The module is called the SiPM Signal Processor (SSP) and consists of 12 readout channels packaged in a self-contained 1U module. Each channel contains a fully-differential voltage amplifier and a 14-bit, 150-MSPS analog-to-digital converter (ADC) that digitizes the waveforms received from the SiPMs. There is no shaping of the signal, since the SiPM response is slow enough relative to the speed of the digitization to obtain several digitized samples of the leading edge of the pulse for the determination of signal timing. Digitized data is processed by a Xilinx Artix-7 Field-Programmable Gate Array (FPGA). The use of the FPGA processing allows for a significant amount of customization of the SSP operation.

Once the DUNE collaboration arrives at a refined set of physics requirements for the photon detection system a set of criteria for a calibration system will be determined. In the absence of

⁴The detector efficiency combines QE and effective areal coverage accounting for dead space between pixels.

22 such criteria two calibration systems are being explored, and will be tested in the 35-t phase-II
23 test. The first system, developed by ANL, utilizes five fiber-fed diffusers mounted on the TPC
1 CPA which uniformly illuminate the photon detectors. An alternative design is employed on the
2 IU prototypes and uses LED-driven fibers mounted alongside the waveguides.

3 4.6.2 Alternative Designs

4 Three alternative designs are currently being considered for the PD system⁵.

5 The first alternative is based on a TPB-coated acrylic panel with an embedded S-shaped wavelength-
6 shifting fiber. The Louisiana State University (LSU) group has developed prototypes based on this
7 design in an attempt to allow an increase in detector size and hence increase geometric acceptance
8 of the PD system and reduce overall system cost.

9 In this design, a single acrylic panel PD module has the same dimensions as the reference design
10 and consists of a TPB-coated acrylic panel with an embedded multi-lobed “S-shaped” wavelength
11 shifting (Y11) fiber. The fiber is read out by two SiPMs (one on the top edge, and the other on
12 the bottom edge of the plate), which are coupled to each end of the fiber and serve to transport
13 the light over long distances with minimal attenuation. The double-ended fiber readout has the
14 added benefit of providing some position dependence to the light generation along the panel by
15 comparing relative signal sizes and arrival times in the two SiPMs. The WLS fiber converts the
16 430-nm light from the TPB to light with a peak intensity of 480–500 nm, which is well-matched
17 to the peak photon-detection efficiency of typical SiPMs.

18 A prototype of a second alternative, under investigation by the Colorado State University (CSU)
19 group, is intended to address an issue with the reference design, in which the application of TPB
20 to acrylic, or other base materials, has been found to cause a significant decrease in attenuation
21 length (down to about 30 cm) of the light guide. This prototype has a thin TPB-coated acrylic
22 radiator located in front of a close-packed array of blue-green (Y11) WLS fibers. The prototype
23 is two-sided and has two identical fiber arrays and radiators mounted back-to-back with a tyvek
24 reflector between. This design allows for a reduction in the number of SiPMs required per PD
25 module. Three SiPMs per side are needed per PD module (again the same dimensions in length
26 and width as the reference design) for a total of six SiPMs per PD module.

27 The Indiana University (IU) group has advanced the CSU design and arrived at the third alter-
28 native design by replacing the Y11 fiber with a reference-design-dimensioned cast bar doped (by
29 Eljen Technology) with the same wavelength shifter as the Y11 fiber. The TPB-coated acrylic
30 radiator has also been replaced with a thin-fused silica plate coated with TPB. This prototype has
31 demonstrated an attenuation length greater than 2.5 m and early indications point to it meeting
32 the SN neutrino energy requirement. It has the highest light collection efficiency of any prototype
33 tested so far.

⁵More extensive descriptions of the alternative photon detector designs can be found in Annex 4A: *The LBNE Design for a Deep Underground Single-Phase Liquid Argon TPC*, Section 5.3.

4.6.3 Technology Selection

The alternative designs have all demonstrated the ability to detect LAr scintillation light, and development work is continuing. A testing program is underway comparing the various alternatives against the reference design. The Tall Bo large dewar at Fermilab and the cryogenic detector development facility at CSU are being used to compare the performance of full-scale and near-full-scale prototypes in LAr utilizing alpha sources and cosmic muons. Data from the 35-t prototype will also provide input into the technology decision. In Fall 2015 a decision will be made regarding which design to adopt and optimize for the first 10-kt far detector module.

4.7 Installation and Commissioning

The scope of the Installation and Commissioning (I&C) task includes the design, procurement, fabrication, labor, testing and delivery of equipment and infrastructure to support installation and commissioning of the detector at the far site. The following are included in the scope:

- detector installation planning
- installation equipment design and procurement
- construction of a full scale mockup, consisting of four APAs, two CPAs and associated field cage, to test installation operations and equipment
- procurement of support rails for the TPC
- procurement and installation of relay racks to house the electronics provided by other subsystems for detector operation
- material receipt, storage and transport to underground at the far site
- installation of the TPC, photon detection and DAQ systems at the far site (support for detector checkout will be provided by the subsystems)
- coordination of the commissioning for the detector and personnel to support detector operations

I&C will have many interfaces with LBNF, and LBNF has certain responsibilities of its own, including the following.

- Excavation and outfitting of the cavern is the responsibility of the Conventional Facilities (CF) subproject of LBNF.
- Construction and installation of the cryogenics system and cryostats is the responsibility of the cryogenics system subproject of LBNF.

6 4.7.1 Equipment and Services

7 The I&C system provides permanently installed equipment that is used by multiple detector sys-
8 tems and/or is integral to the installation process. This includes the relay racks, cable management
9 and support rails for the TPC. I&C is also responsible for several detector-specific aspects of the
10 cavern outfitting, including a clean area enclosure near the cryostat hatch to isolate the open hatch
11 and the TPC components from the cavern environment.

12 The TPC elements (APAs and CPAs, described in Section [4.3](#)), are supported by a set of five
13 support rails permanently mounted at the top of the cryostat. The rails are supported by rods
14 spaced at 5-m intervals from anchor points at the cryostat roof. The rods are installed with an
15 angle bias that allows the rails to return to a level condition after the cryostat and TPC are cooled.

16 The TPC and photon detectors require various electrical services for operation, including bias
17 voltages, power and control signal. These services follow a grounding plan (still under development)
18 discussed in Section [??](#). The electrical services pass through a total of 78 feedthrough ports located
19 on top of the cryostat, above every other APA junction. A relay rack is located adjacent to each
20 port. The rack space is shared between the TPC, photon detection system readout and power
1 supplies. For the upper APA of each pair, the cables are pre-installed and routed from the cold
2 side of the feedthrough down and along the support rail to the location where they connect to
3 their corresponding APA. For the lower APAs with the electronics near the floor of the cryostat,
4 the cables are routed from the cold side of the feedthrough down the sides of the cryostat. The
5 lower APA cables are routed in cable trays supported from the cryostat walls.

6 4.7.2 TPC Installation Process

7 Once detector components arrive at the far site they are put in a facility used for both storage and
8 testing/checkout, called an integration facility. Material is moved from the integration facility to
9 the cavern (after undergoing checkout) via the Yates shaft. As installation space in the cavern is
10 very limited, the moves will take place at the rate of installation. Most items can be transported
11 inside the Yates shaft cage, however, the APAs are too long to fit in the cage and therefore are
12 slung underneath it in a special container that holds four APAs in an internal rack. This cleaner
13 rack can be extracted from the outer container into the clean area used for installation. The
14 TPC components will have been cleaned and protected to a level suitable for installation into the
1 cryostat as part of the TPC production process, and will have arrived at the far site in clean
2 containers.

3 The clean area enclosure, in the range of class 100,000 (ISO 8 equivalent), provides an area for
4 personnel to gown with the appropriate clean-room clothing and safety shoes. A large closable door
5 is located at the drift junction where TPC storage containers can be parked to allow unloading of
6 the TPC components directly into the clean area.

7 The TPC installation process requires the temporary installation of several items in the cryostat
8 before it is filled with argon, among these:

- 9 • A lighting system with emergency backup lighting will be installed and then removed in
10 sections as the TPC installation proceeds. (This lighting will be filtered to the appropriate
11 spectrum to protect the photon detection system installed in the APAs.)

- 12 • A filtered air ventilation system with air-monitoring sensors and alarms will be installed to
13 ensure adequate air quality for work inside the cryostat. The system will also include a
14 high-sensitivity smoke-detection system that is interlocked to the power for all devices inside
15 the cryostat.

- 16 • A raised floor will be installed at the bottom of the cryostat to protect the cryostat membrane
17 and provide a flat surface above the corrugations of the cryostat. A modular design will allow
18 it to be removed in sections as the TPC installation progresses.

19 A combination of commercial and specially designed tooling will be required for TPC installation.
20 All of the detector components and equipment inside the cryostat will be inserted through hatches
1 located at one end of the cryostat. Temporary fixed scaffolds with integral stair towers will provide
2 personnel access into the cryostat. A rolling scaffold, on the cryostat raised floor, also with an
3 integral stair tower, will provide access to the top of the cryostat where the TPC connections are
4 made. Special fixtures and commercial gantry hoists are required to move APAs from a horizontal
5 orientation in storage racks to a vertical orientation at the cryostat hatches. Special platforms
6 located at the cryostat hatches will support each lower APA section while its upper APA section
7 is connected. The platform will have multiple levels to allow personnel to access the connection
8 points at the top of an APA and at the junction between an upper and lower APA. The installation
9 equipment and installation procedures will be tested with a full-height mock TPC section at a
10 suitable location at Fermilab.

11 Installation of the TPC is preceded by installation of the DAQ, including relay racks and TPC
12 cables, in order to allow immediate testing of APAs upon their placement in the cryostat.

13 The TPC installation starts with installation of the cathode planes, one row at a time, starting
14 with the top row of a plane, and progressing, one CPA at a time, from the far end of the cryostat to
15 the hatch end. As each cryostat-length row is completed, it is lifted, and the next row is attached
16 below it in the same manner; this is repeated until all four rows of the cathode plane are in place.
17 At this point, the end-wall field cage is installed at the non-hatch end of the cathode plane.

18 APA installation begins next. An APA, electronics side down, is first moved into the cryostat and
19 held temporarily in the area of the hatch. A second APA, its pair, is positioned above the first,
20 electronics side up. The two APAs are joined at the center, lifted and attached to the support rail.
1 The connected pair is moved along the support rail to its designated position and, except for the
2 first pair, connected to the previously installed adjacent stacked pair. At this point the power and
3 signal cables are connected to the APAs for testing. After proper functioning is confirmed, the field
4 cage sections between the APAs and their facing CPAs are installed and the raised floor sections
5 in that area are removed. This APA and field cage installation process is repeated progressing
6 towards the hatch end of the cryostat until the entire anode plane is in place; the field cage is
7 then installed. The process is then repeated for the other anode planes. Once TPC installation is
8 complete, the installation equipment and the scaffolding is removed from the cryostat.

9 Once the TPC is installed and all temporary equipment is removed from the cryostat, the hatches
10 are closed and all channels of the detector are tested for expected electronics noise. After successful
11 testing, the cryostat hatches are sealed and the purge proceeds, followed by a cool-down of the
12 cryostat and detector. At this point extensive detector testing will be conducted prior to filling
13 with LAr. Filling each 10-kt cryostat requires approximately six months, after which a several-
14 month-long detector commissioning phase begins.

15 **4.7.3 Grounding**

16 The detector will have approximately 300,000 channels of electronics with an intrinsic noise level
17 less than 1,000 electrons. The channels will be connected to signal collection wires that are up
1 to 7 m long, thus grounding, shielding and power distribution are critical to the success of the
2 experiment. The installation and commissioning group will develop a detector grounding plan that
3 coordinates between the CF power distribution, cryostat design and the detector systems. The
4 grounding will be configured such that each detector is on an isolated and separate detector ground
5 that is referenced to building ground through a safety saturable inductor. Dielectric breaks will be
6 used on all conductive piping/services that penetrate the cryostat. A copper ground plate under
7 the steel top plate of each cryostat will be provided as part of the cryostat and used to serve as a
8 central star ground point.

l-ground

9 Chapter 5

10 Far Detector Alternative Design: 11 Dual-Phase LArTPC

12 5.1 Overview

13 This chapter describes an alternative far detector design for DUNE. The first detector module to
14 be installed will use the reference design described in Chapter 4, however this alternative design
15 is under consideration for one or more subsequent modules. This design implements a dual-phase
16 liquid argon time projection chamber (LArTPC) augmented with a light-readout system. “Dual-
17 phase” refers to the extraction of ionization electrons at the interface between liquid and gas argon
1 and their amplification and collection in the gas phase.

2 This dual-phase design is the result of 13 years of R&D consisting of two consecutive design
3 study programs funded since 2008 by the European Union: LAGUNA and LAGUNA-LBNO. The
4 LAGUNA-LBNO design study was concluded in August 2014. In collaboration with industrial
5 partners, LAGUNA-LBNO designed an innovative, optimized and cost-effective configuration for
6 a long-baseline experiment.

7 The studies focused on the underground implementation of a very large LAr detector (GLACIER)
8 and produced many technical advances with respect to the tank, field cage and cathode, charge
9 multiplication, collection and readout, as well as advances in the areas of assembly sequencing and
10 logistics for the detector and full costing. The full design and the related technical developments
11 are described in Annex 4E: *LAGUNA/LBNO Part 2*, which was submitted to the EU at the
12 conclusion of the design study. This chapter describes the detector configuration and components,
13 and describes how the design meets the DUNE far detector physics requirements.

14 The scope of a dual-phase far detector module for DUNE includes the design, procurement, fab-
15 rication, testing, delivery, installation and commissioning of the detector components:

- 16 • Charge-Readout Planes (CRP), including extraction grid, Large Electron Multiplier (LEM)
17 and anode and readout planes

- 18 • Cathode, field cage and high voltage system
- 19 • Electronics and data acquisition
- 20 • Chimneys, isolated volumes used for electronics feedthroughs
- 21 • Slow Controls
- 22 • Light-readout system

1 The detector components and the liquid argon (LAr) will be housed in cryostats provided by
 2 LBNF, described in Volume 3: *The Long-Baseline Neutrino Facility for DUNE*. Similar to the
 3 reference design, this alternative design satisfies the performance requirements on the DUNE far
 4 detector, described in Chapter 4 for the reference design. Parameters specific to the dual-phase
 5 design are listed in Table 5.1.

Table 5.1: Performance parameters specific to the dual-phase far detector design

Parameter	Requirement	Achieved Elsewhere	Expected Performance
Gas phase gain	20	200	20-100
Electron Lifetime	3 ms	> 3 ms 35-t prototype	> 5 ms
Minimal S/N after 12 m drift	9:1	> 100:1	12:1-60:1

6 5.2 Highlights of the Design

7 This innovative dual-phase design is similar in many ways to the single-phase design, but imple-
 8 ments some unique features and offers several advantages over it, in particular:

- 9 • higher gain, leading to a larger signal-to-noise ratio (S/N)
- 10 • larger fiducial volume, enabling very long drift paths
- 11 • lower detection threshold
- 12 • finer readout pitch (3 mm), implemented in two identical collection views, x and y
- 13 • fewer readout channels (153,600 vs 384,000 for a reference design 10-kt module)
- 14 • the absence of dead material in the LAr volume

15 Following the GLACIER concept [11] (see Figure 5.1), the DUNE dual-phase LArTPC detector
 16 design has a fully homogeneous liquid argon volume, in which electrons drift upwards vertically
 17 towards an extraction grid just below the liquid-vapor interface. From there they are extracted from
 18 the liquid into the gas phase, amplified, and collected on a finely segmented anode [12, 13, 14].

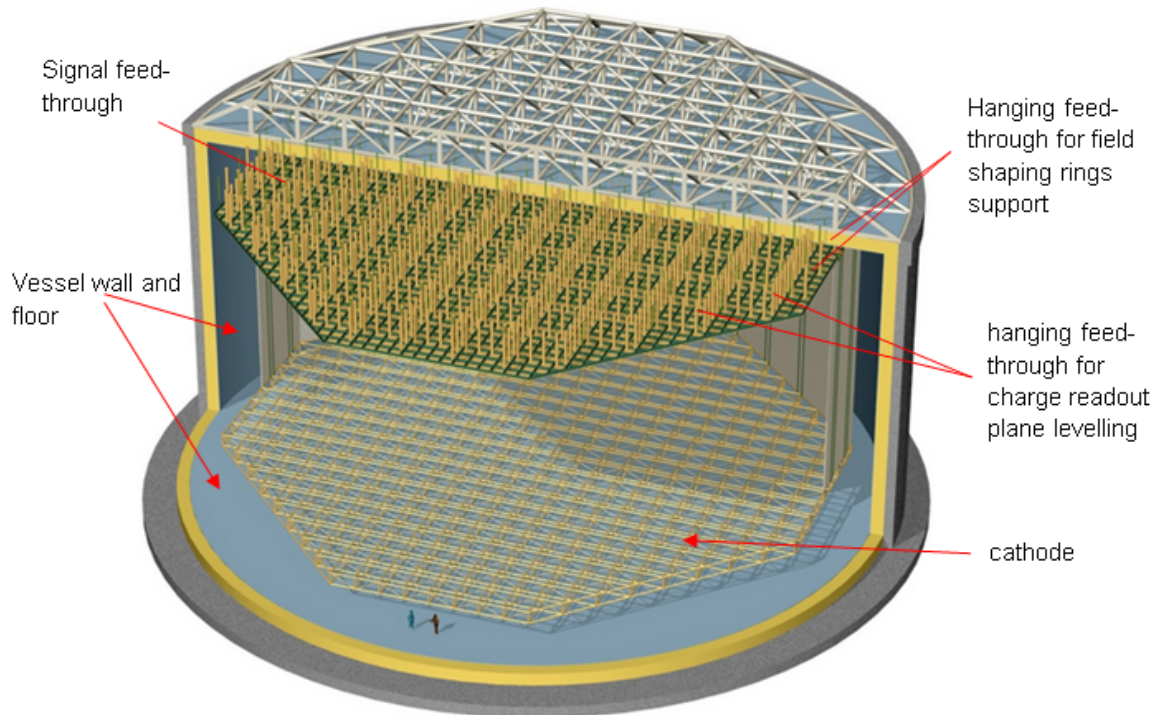


Figure 5.1: The 50-kt LBNO detector, GLACIER

fig:LBNO

19 The electron amplification in the gas phase enables a robust and tunable signal-to-noise ratio.
 20 The detector configuration is similar to a single-phase LArTPC. The features of the dual-phase
 21 design, e.g., high gain, allow achieving very long drift paths and large detector dimensions while
 22 minimizing the number of readout channels.

23 5.2.1 Charge Collection, Amplification and Readout

24 An extraction efficiency of 100% of the electrons from the liquid to the gas phase is achieved
 25 with an electric field of the order of 2 kV/cm across the liquid-gas interface, applied between an
 26 extraction grid submersed in the liquid and charge amplification devices situated in the ultra-pure
 27 argon gas.

28 These amplification devices, called Large Electron Multipliers (LEMs), are horizontally oriented
 29 1-mm-thick printed circuit boards with electrodes on the top and bottom surfaces. They are drilled
 30 through with many holes that collectively form a micro-pattern structure; when a 3-kV potential
 1 difference is applied across the electrodes the ionization electrons are amplified by avalanches
 2 (Townsend multiplication) occurring in the pure argon gas in this micro-pattern structure [16] due
 3 to the high electric field (30 kV/cm).

4 The use of avalanches to amplify the charges in the gas phase increases the S/N ratio by at least one
 5 order of magnitude with a typical gain of 20–100, significantly improving the event reconstruction
 6 quality. It also lowers the threshold for small energy depositions and provides a better resolution

7 per volumetric pixel (voxel) compared to a single-phase LArTPC.

8 The charge is collected in a finely segmented 2D (x and y) readout anode plane at the top of the
9 gas volume and fed to the front-end electronics.

10 The collection, amplification and readout components are combined in an array of independent
11 (layered) modules called Charge Readout Planes (CRPs). A CRP is composed of several 0.5×0.5 -
12 m^2 units, each of which is composed of a LEM/anode sandwich. These units are embedded in a
13 mechanically reinforced frame of FR-4 and stainless steel. The CRP structure also integrates the
14 submersed extraction grid, which is an array of x and y oriented stainless steel wires, 0.1 mm in
15 diameter, with 3.125-mm pitch. Thicknesses and possible biasing voltages for the different layers
16 are indicated in Figure 5.4.

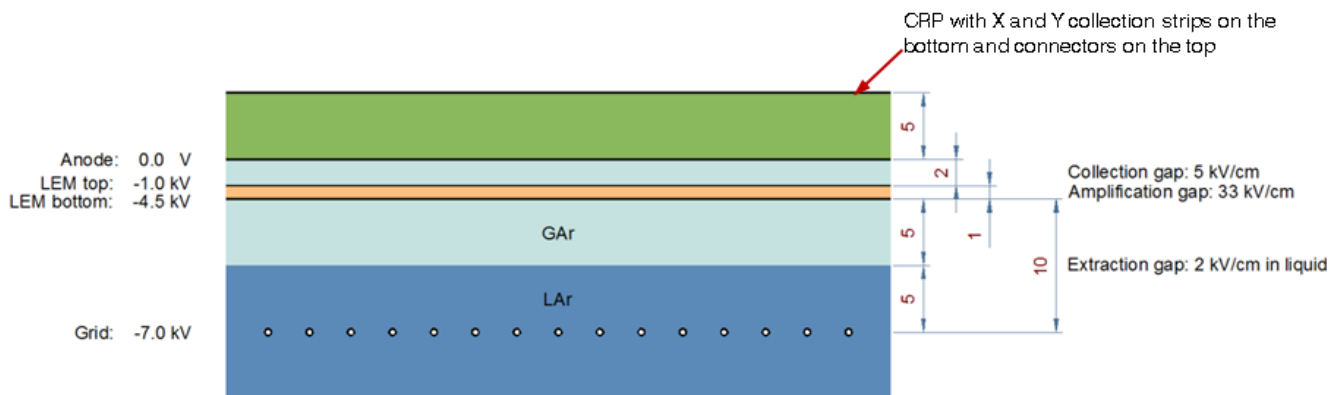


Figure 5.2: Thicknesses and HV values for electron extraction from liquid to gaseous Ar, their multiplication by LEMs and their collection on the x and y readout anode plane. The HV values are indicated for a drift field of 0.5 kV/cm in LAr.

17 Each CRP is independently suspended with stainless-steel ropes linked to the tank top deck. This
18 suspension system allows adjustment of the CRP distance and parallelism with respect to the LAr
19 surface, and keeps the extraction grid immersed.

20 Figure 5.5 shows the top of two side-by-side units and Figure 5.6 shows the x and y readout views.

21 A CRP provides an adjustable charge gain (with a minimal required gain of 20) and two independent,
22 orthogonal readout views, each with a pitch of 3.125 mm. The LEM/anode sandwiches in the
23 same CRP unit are interconnected with short flat cables so that each readout channel corresponds
24 to a total strip length of 3 m.

25 Combined with the time information coming from the LAr scintillation readout by the PMT arrays
26 (t_0), a CRP provides 3D track imaging with dE/dx information. The CRPs and their components
27 are described in Section 5.3.

28 The typical amplification achieved by this design, between 20–100, improves the S/N ratio and thus
29 compensates for the charge losses that occur along the very long drift paths due to the presence
30 of electronegative impurities. Therefore, despite the longer drift length, this design requires no

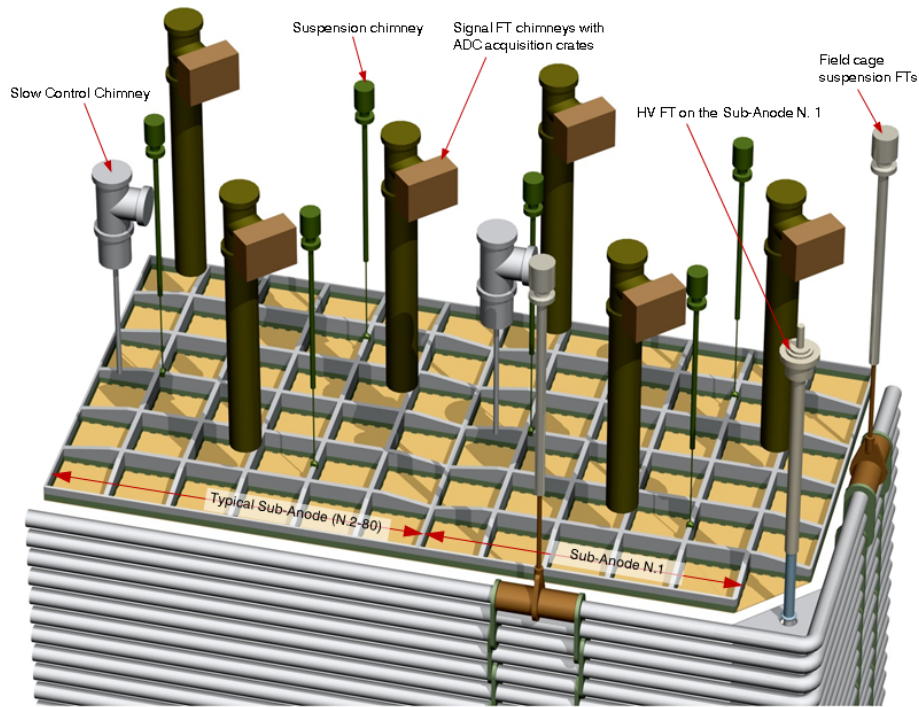


Figure 5.3: Two DUNE CRP $3\text{ m} \times 3\text{ m}$ units side by side. On the left one of the 79 equal CRP units, on the right the 1st CRP unit with a chamfered LEM/Anode Sandwich for the insertion of the high voltage feedthrough.

fig:CRP_

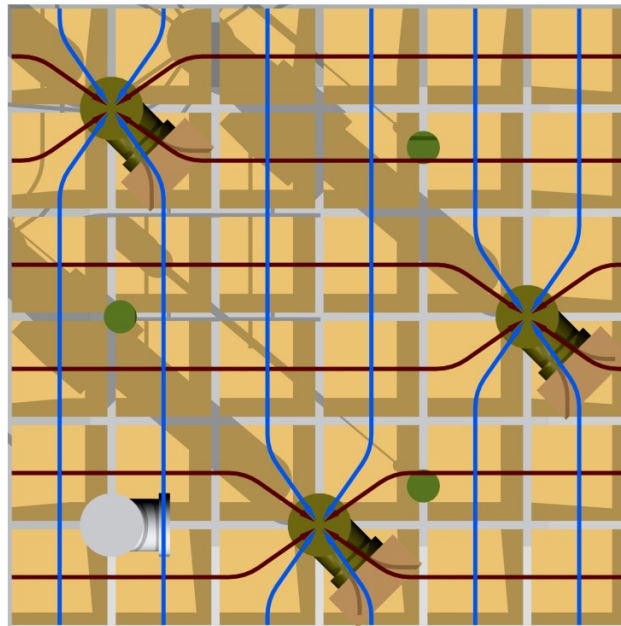


Figure 5.4: Signal collection in the x and y views of the $3 \times 3\text{ m}^2$ DUNE CRP unit by the 3 SFT chimneys.

fig:CRP_

31 higher purity of the LAr than does the reference design¹, around 0.1 ppb (or 100 ppt) of oxygen
 32 equivalent, and yields a 3-ms electron lifetime.

33 The S/N ratio can exceed 100 for a minimum ionizing particle (MIP) after a drift path of 12 m
 34 (given an electron lifetime of 3 ms, a drift field of 0.5 kV/cm and a LEM gain of 180). With the
 35 same drift field, the same electron-lifetime conditions and a LEM gain of 25, the S/N is larger
 36 than 50:1 for tracks up to 6 m from the anode; it reaches 14:1 for MIP tracks that are 12 m from
 37 the anode.

38 5.2.2 Electronics and “Chimneys”

39 The electrical signals from the collected charges are passed to the outside of the tank via a set of
 40 dedicated signal feedthrough “chimneys” (insulated volumes filled with nitrogen that pass through
 41 the top layer of insulation). The cryogenic front-end (FE) electronics cards, housed at the bottom
 42 of the chimneys, are based on analog preamplifiers implemented in CMOS ASIC circuits for high
 43 integration and large-scale affordable production. Within the chimneys, the cards are actively
 44 cooled to a temperature of about 110 K and isolated with respect to the LAr vessel by a cold
 1 feedthrough. This feedthrough is connected to the CRP via short flat cables of (0.5 m length) in
 2 order to minimize the input capacitance to the preamplifiers. Each chimney collects 640 readout
 3 channels.

4 The chimney design allows access to and replacement of the FE from the outside without con-
 5 taminating the LAr volume. The digital electronics and DAQ system are completely outside the
 6 cryostat and are housed in microTCA racks mounted on each signal feedthrough chimney.

7 Other feedthroughs are planned for the cathode HV connection, the CRPs’ suspension and level
 8 adjustment, the high voltage and signal readout of the PMTs, and the monitoring instrumentation
 9 (level meters, temperature probes, strain gauges, etc.).

10 5.2.3 Cathode, Field Cage and HV System

11 The drift field ($E \simeq 0.5$ kV/cm) inside the fully active LAr volume is produced by applying high
 12 voltage to the cathode plane at the bottom of the cryostat and is kept uniform by the field cage, a
 13 stack of 60 equally spaced field-shaping electrodes, polarized at linearly decreasing voltage from the
 14 cathode voltage to almost ground potential, reached at the level of the charged readout plane. The
 15 electrodes are rectangles made of stainless-steel tubes (diameter 140 mm, vertical pitch 200 mm)
 16 with rounded corners, running horizontally (and stacked vertically) around the active volume (see
 17 Figure 5.3). Fig: DP det2

18 The field cage is held in place by mechanical structures hung from the top deck of the vessel that
 19 also provide insulation. The cathode structure, constructed of a reinforced frame to guarantee

¹The required level of purity can be reached by starting from commercially available ppm-level bulk argon and filling a non-evacuated vessel[15]. Fig: DP det2

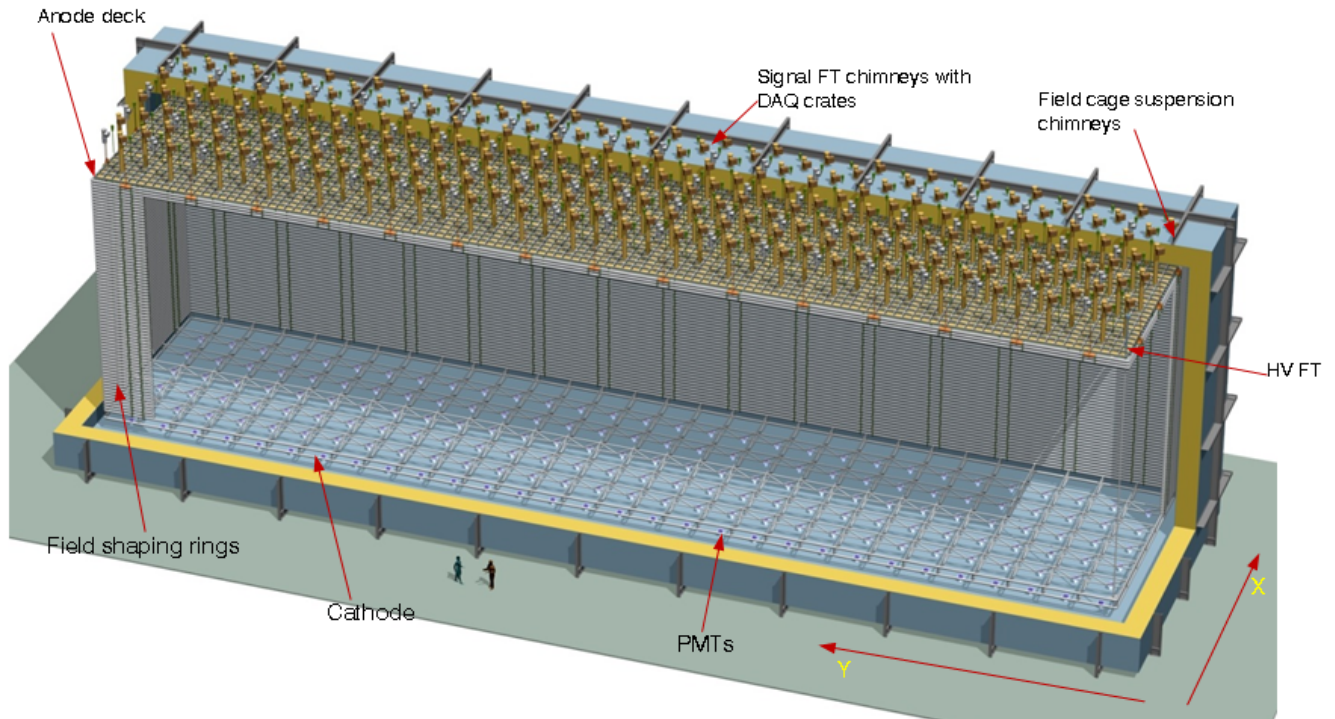


Figure 5.5: The DUNE dual-phase detector (partially open) with cathode, PMTs, field cage and anode plane with chimneys.

fig:DP_c

20 its planarity, is suspended from the field cage and hangs near the bottom of the cryostat. It is a
 21 segmented structure of tubes of different sizes arranged in a grid to minimize weight, limit sagging
 22 and avoid high electric field regions in its proximity. The segmented structure allows scintillation
 23 light to pass through and be detected by uniform arrays of photomultipliers (PMTs) mounted 1 m
 1 below it at the bottom of the tank.

2 5.3 Detector Configuration

3 The detector for the 12.1-kt active mass module is built as a single active volume 60 m long,
 4 12 m wide and 12 m high, with the anode at the top, the cathode near the bottom and an array
 5 of 180 photon detectors (PMTs, 1 per 4 m²) located at the bottom of the vessel underneath the
 6 cathode. The active volume (see Figure 5.2) is surrounded by the field cage. These components
 7 are described in Section ??.

8 The proposed design optimally exploits the cryostat volume of 14(w)×14.1(h)×62(l) m³ with an
 9 anode active area of 12×60 m² and a drift length of 12 m, corresponding to an active mass of
 10 12.096 kt of LAr (10.643 kt fiducial).

11 Do we want this many significant digits? In next pgraph, the number of sig figs doesn't even match.

12 The design is based on the 20-kt LAGUNA-LBNO design study with a CRP unit size adapted
 13 to the dimensions on the active area. The cryostat height could be increased to achieve 15-m
 14 drift, resulting in an active mass of 15.12 kt (13.444 kt fiducial). This 15.1-kt configuration, apart
 15 from the longer drift distance and field cage, would have the same characteristics of the 12.1-
 16 kt configuration, given that the covered active area is exactly the same. With these transverse
 17 dimensions, every additional meter of drift length provides a 1-kt increase in the active mass at a
 18 moderate additional cost.

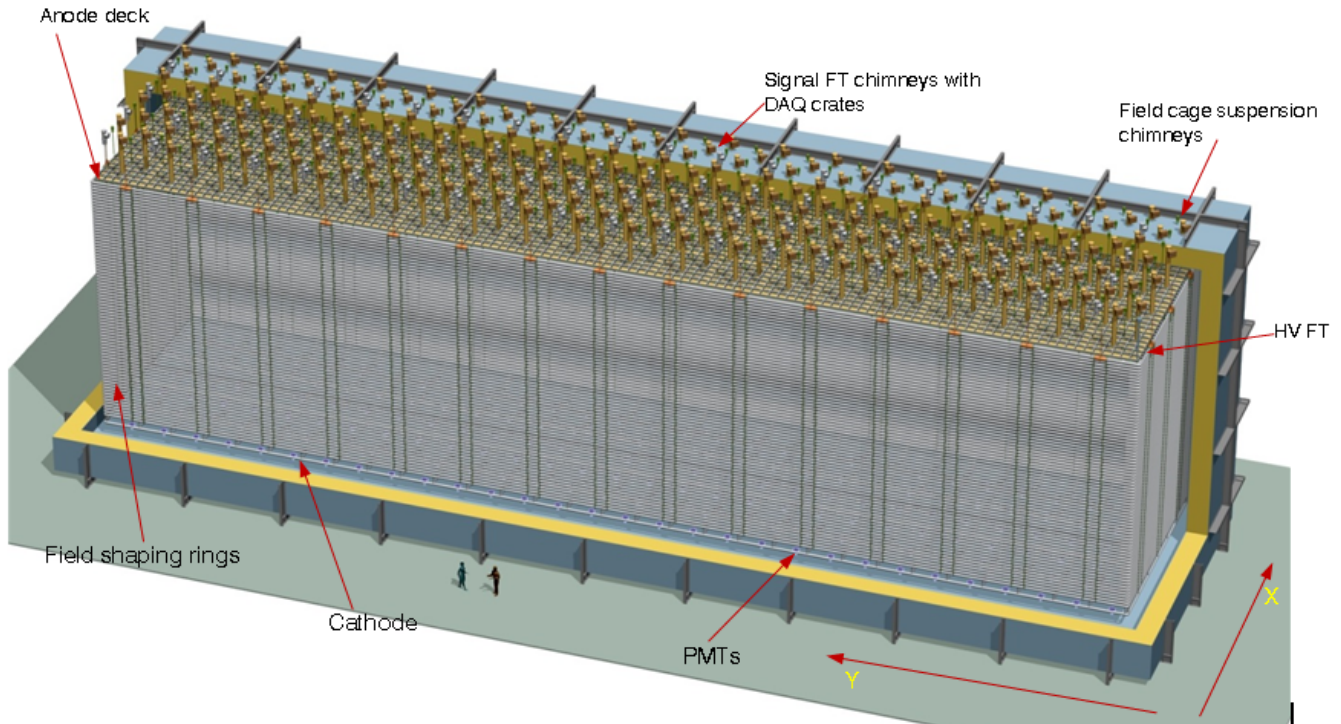


Figure 5.6: The DUNE dual-phase detector with cathode, PMTs, field cage and anode plane with chimneys.

fig:DP_d

19 The ionization electrons in the liquid phase drift in a uniform electric field towards the anode plane
 20 at the top of the active volume. This is made by by an array of 80 independent CRP modules,
 21 $3 \times 3 \text{ m}^2$ each. The extraction of the electrons from the liquid to vapor phase is performed thanks
 22 to the submersed horizontal extraction grid, integrated in each CRP structure. A CRP unit
 23 includes 36 ($0.5 \text{ m} \times 0.5 \text{ m}$) LEM/anode sandwiches, providing tunable amplification and charge
 24 collection on two independent views organized in strips of 3-m length and 3.125-mm pitch. There
 25 are 1920 readout channels for each CRP. Signals in each CRP unit are collected via three signal
 26 feedthrough chimneys hosting the the front-end cards with the cryogenic ASIC amplifiers (640
 27 channels/chimney) which are accessible and replaceable without contaminating the pure liquid
 28 argon volume. Each chimney is coupled to a microTCA crate ensuring the signals' digitization
 29 and data acquisition. These crates are connected via optical fiber links to the DAQ back-end. The
 30 total number of readout channel per 10-kt module is 153,600.

31 Each CRP unit is independently suspended by three stainless steel ropes. The vertical level of each
 32 CRP unit can then be automatically adjusted with respect to the LAr level via three suspension

33 feedthroughs, electrically operated from outside. A Slow Control feedthrough, one per CRP unit,
 34 is used for the signals readout for level meters and the temperature probes and to apply the HV
 35 bias on the two sides of the LEMs and on the extraction grid. The number of components and
 36 parameters for the 12-kt (15-kt) dual-phase LArTPC are summarized in Tables 5.2 and 5.3.

Table 5.2: Sizes and Dimensions for the 12-kt (15-kt) dual-phase LArTPC

Item	Value(s)	
Active volume width and length	W = 12 m	L = 60 m
Active volume height	H = 12 m (H = 15 m)	
Active volume/LAr mass	8,640 (10,800) m ³	12,096 (15,120) metric ton
Field ring vertical spacing	200 mm	
Field ring tube diameter	140 mm	
Anode plane size	W = 12 m	L = 60 m
CRP unit size	W = 3 m	L = 3 m
HV for vertical drift	600–900 kV	
Resistor value	100 M Ω	

Table 5.3: Quantities of Items for the 12-kt (15-kt) dual-phase LArTPC

Item	Number
Field rings	60 (75)
CRP units	4 \times 20 = 80
LEM/Anode sandwiches per CRP unit	36
LEM/Anode sandwiches (total)	2,880
SFT chimneys / CRP unit	3
SFT chimneys (total)	240
Readout channels / SFT chimney	640
Readout channels (total)	153,600
Suspension FT / CRP unit	3
Suspension FTs (total)	240
Slow Control FT / sub-anode	1
Slow Control FTs (total)	80
HV feedthrough	1
Voltage degrader resistive chains	4
Resistors (total)	240 (300)
PMTs (total)	180 (1/4 m ²)

37 A number of factors make the dual-phase TPC concept as described in this chapter well suited to
 38 large detector sizes like the DUNE far detector.

39 In this design, the charge attenuation on the long drift paths is compensated by the charge ampli-
 40 fication in the CRPs. This configuration also simplifies construction by optimally exploiting the
 1 long vertical dimensions of the cryostat, providing a large homogeneous fiducial volume free of em-
 2 bedded passive materials (effectively increasing the detector size), reducing the number of readout

3 channels, and ultimately lowering costs. The CRPs collect the charge in a projective way, with
4 practically no dead region and read the signals out in two collection views, eliminating the need
5 for induction views, which simplifies the reconstruction of complicated topologies. The tunable
6 high S/N provides operative margins with respect to the noise and electron lifetime conditions and
7 lowers the threshold on the minimal detectable energy depositions .

8 The dual-phase readout scheme has been successfully demonstrated on several prototypes through
9 R&D over a span of more than 10 years. The design of very large (20–50 kt) underground detectors
10 based on this concept has been developed in great detail in the context of the LAGUNA and
11 LAGUNA-LBNO design studies. The CERN WA105 demonstrator, described in Section 9.4, is
12 intended to prototype a full-scale implementation of this technique, as well as demonstrate other
13 technologies developed for the construction of large underground TPC detectors.

14 A complete configuration, based on the double-phase design, been optimized for the 10-kt detector
15 module of the DUNE far detector.

16 5.4 The Charge Readout System

17 In the dual-phase LArTPC concept, the ionization electrons are multiplied in avalanches occurring
18 inside detectors, the Large Electron Multipliers (LEMs), located in the argon gas phase above the
19 liquid argon level. The drift field of the TPC brings the electrons up to the liquid argon surface
20 where they can be extracted into the gas using a 2-kV/cm electric field defined across the liquid-gas
21 interface. This extraction field is applied between a submersed extraction grid (stainless steel wires
22 tensioned in both x and y directions) and the bottom side of the LEMs. The LEMs are printed
23 circuit boards oriented horizontally, with conductive layers (electrodes) on the top and bottom
24 surfaces, and many holes drilled through. The holes form a micro-pattern structure within which
25 the amplification occurs. By applying voltages across the two electrodes of the LEM, a 30-kV/cm
26 electric field region is defined in the holes [16]. Electrons transiting these high electric field regions
27 in the holes trigger Townsend multiplication in the pure argon gas.

28 The amplified charge is then collected and recorded on a 2D anode consisting of two sets of 3.125-
29 mm-pitch gold-plated copper strips that provide the x and y coordinates (and thus two views) of
30 the event.

31 Typical electric fields between each stage of the readout are illustrated in Figure 5.8. Table 5.4
32 shows the inter-stage distance and the tolerances required to obtain uniformity of gain to within
33 $\sim 5\%$.

34 The extraction grid, LEM and anode are assembled into three-layered “sandwiches” with precisely
35 defined inter-stage distances and inter-alignment, which are then connected together horizontally
36 into modular units of area 9 m^2 . These units are called Charge Readout Planes (CRPs).

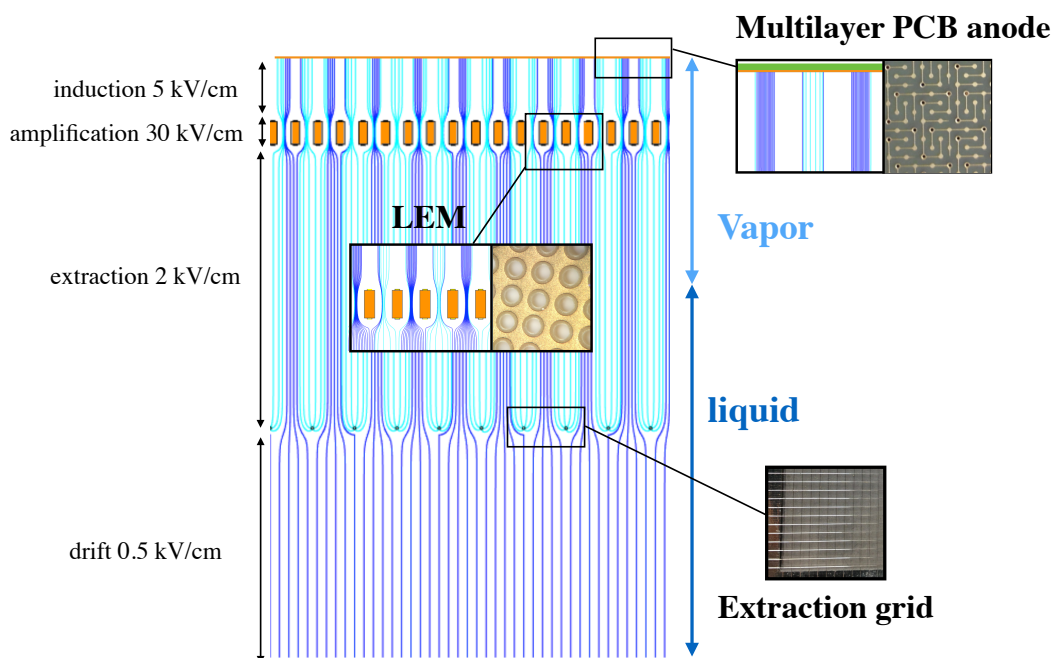


Figure 5.7: Illustration of the electric fields in the amplification region of a dual-phase LArTPC. The simulated field lines in dark blue indicate the paths followed by the drifting charges (without diffusion).

fig:setu

Table 5.4: Interstage distances and electric field settings of the dual-phase readout components.

Component	Distance [mm]	Tolerance [mm]	Electric field [kV/cm]
Anode-LEM top electrode	2	0.1	5
LEM top-bottom electrode	1	0.01	30-35
LEM bottom electrode-grid	10	1	2 (in LAr) and 3 (in GAr)

crp_dist

5.4.1 The Charge Readout Plane (CRP)

Each CRP is an independent detector element that performs charge extraction, multiplication and collection, and has its own high voltage system and independent signal feedthroughs. The entire area of the LEM and anode in a CRP is active.

The LEM and corresponding anode are pre-mounted in units of $50 \times 50 \text{ cm}^2$, called LEM/Anode Sandwich (LAS) modules, before being assembled with an extraction grid into a CRP. Each anode in a LAS is segmented in 50-cm long x and y strips. Adjacent LAS anodes are bridged together to form readout strips of the required length by connecting short flat cables to KEL connectors soldered onto the top sides of the anodes. The signals from the last anode in each strip chain are brought to feedthroughs mounted on the other side of the front-end electronics embedded inside dedicated signal-feedthrough chimneys using 50-cm-long flat cables.

The LBNO 20-kt detector design (described in Annex 4E: *LAGUNA/LBNO Part 2*) featured modularized CRPs of dimensions of $4 \times 4 \text{ m}^2$, with 2-m long anode strips. For the DUNE cryostat geometry, a size of $3 \times 3 \text{ m}^2$ with a strip length of 3 m is found to be optimal. The description in this section is based on the LBNO $4 \times 4 \text{ m}^2$ CRP.

Each CRP is independently hung from the vessel deck through its three suspension feedthroughs. It has its own high voltage system and independent signal and slow-control feedthroughs. Figure 5.9 illustrates the $4 \times 4 \text{ m}^2$ CRP; its characteristics are summarized in Table 5.5.

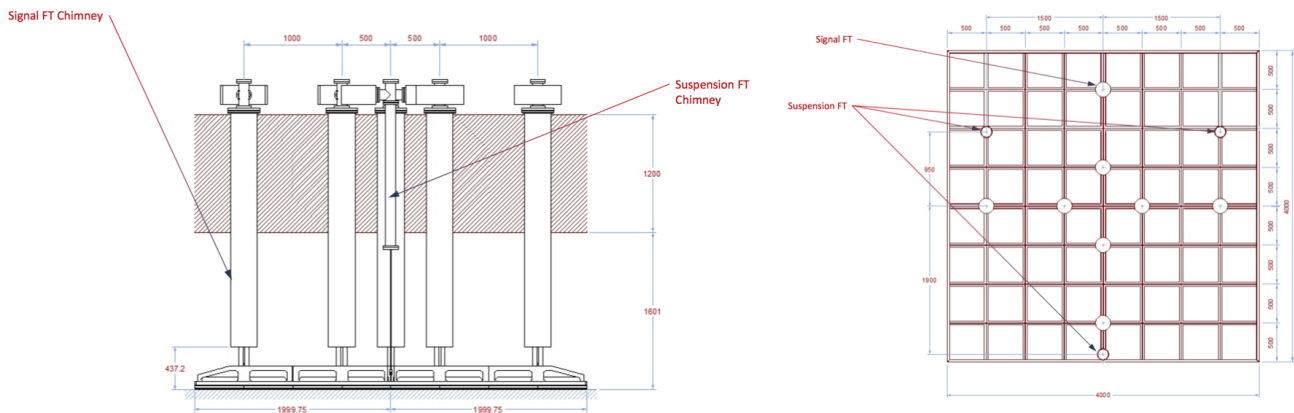


Figure 5.8: Side and top views of the $4 \times 4 \text{ m}^2$ CRP designed for LBNO (units in mm).

The entire area of the LEM and anode is active, as noted earlier, and each adjacent $50 \times 50 \text{ cm}^2$ LAS module has a gap of only 0.5 mm. Therefore, the $4 \times 4 \text{ m}^2$ area of the CRP is fully active; the 0.5-mm edge gaps occurring every 50 cm do not interfere with the charge collection in the anode, given its readout pitch of 3.125 mm.

The extraction grid consists of $100 \mu\text{m}$ diameter stainless steel wires tensioned in both x and y directions over the entire 4-m length/width of the CRP with 3.125 mm pitch. They are soldered into groups of 32 on independent wire-tensioning pads oriented perpendicularly to the side of the

Table 5.5: Numbers of components of the 4×4 m² CRP designed for LBNO

Component	Number
50×50 cm ² anode panels	64
50×50 cm ² LEM panels	64
Signal feedthroughs	8
Suspension feedthroughs	3
Readout strip length (m)	2
Number of channels	5120

21 CRP frame. Each wire-tensioning pad consists of a printed circuit board (PCB) for HV-connection
 22 that is fixed very precisely to a mechanical wire holder. The PCB has 32 soldering pads with 200-
 23 μm grooves for precise positioning of the wires. During the wire-soldering process each wire is
 24 tensioned by 150-g lead weights and positioned in a groove. (With this method better than 50 μm
 25 precision on the wire pitch, measured under the microscope, was achieved for the LBNO-WA105
 1 prototypes.) The PCB is then mounted on the wire holder and the tension of the group of 32 wires
 2 can be precisely adjusted by pushing the holder against the CRP's FR4 frame with two screws.

3 The wires, ~ 3 m long in both x and y directions, have their sags minimized to ~ 0.1 mm thanks
 4 to x and y oriented supporting comb-teeth blades (see Figure 5.7) inserted between anode planes
 5 of $1 \text{ m} \times 1 \text{ m}$ size. The array of blades penetrates the liquid surface and has the additional benefit
 6 of maintaining the liquid level still.

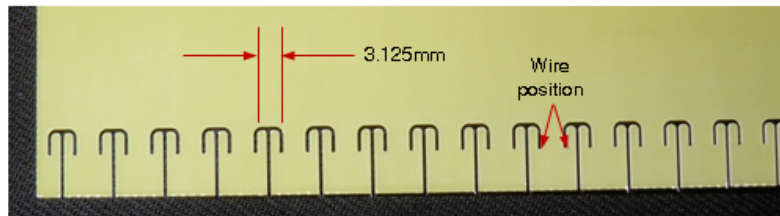


Figure 5.9: Comb for hanging extraction grid wires

7 The 4×4 m² CRP has 5120 readout channels in total. The signals from the CRP are read out
 8 through eight signal feedthroughs (SFTs) chimneys at the bottom of which the front-end electronics
 9 cards are mounted. Amplified signals are transmitted to the DAQ system located on top, outside
 10 of the vessel. Each chimney groups 640 channels.

11 The 3×3 m² DUNE CRP, is a down-sized version of the LBNO CRP; it has three signal feedthrough
 12 chimneys and 1920 readout channels.

13 Three suspension feedthroughs are arranged as an equilateral triangle whose barycenter coincides
 14 with that of the CRP; they suspend the CRP at the required position and precisely adjust the
 15 CRP level with respect to the liquid argon surface. Figure 5.10 shows a 3D view of the CRP, where
 16 the signal chimneys (discussed in Section 5.5) and the stiffening frame are visible.

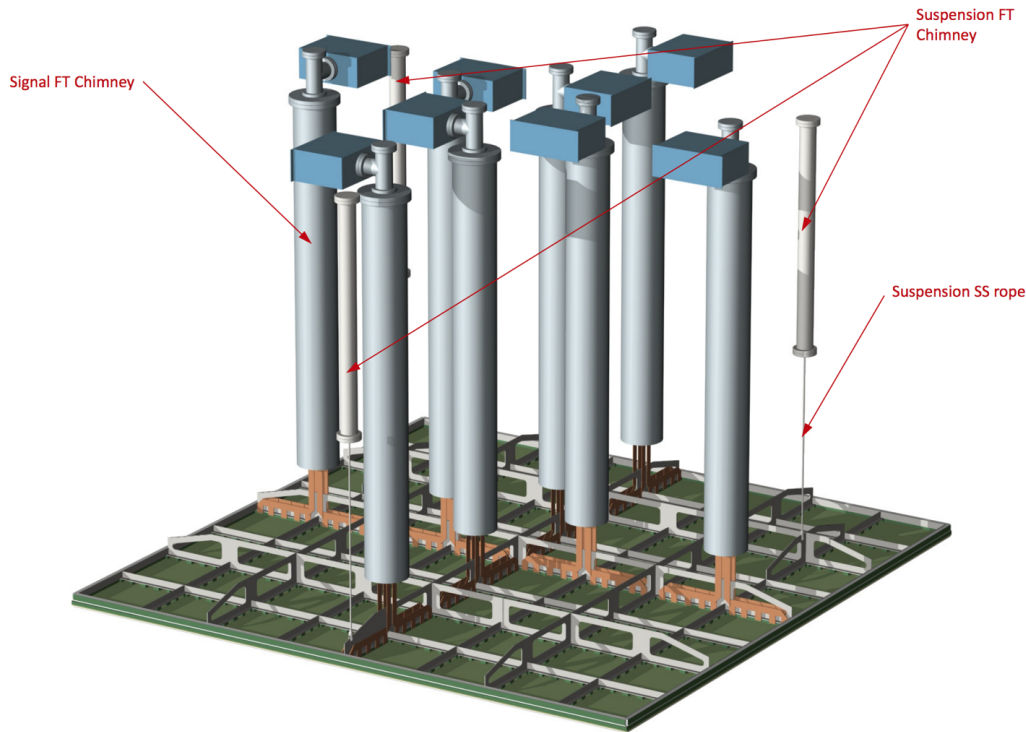
Figure 5.10: 3D view of the $4 \times 4 \text{ m}^2$ LBNO CRP.

fig:4_40

17 5.4.2 The LEM/Anode Sandwich (LAS)

18 LAS modules, the CRP building blocks composed of $50 \times 50\text{-cm}^2$ LEM-anode sandwiches, have
 19 been extensively studied as part of the ongoing CERN WA105 prototyping efforts (see 9.4). The
 20 LEMs and the anodes are produced by a PCB manufacturing company called ELTOS². Their
 21 designs are the outcome of intensive R&D effort over the last few years, aimed at maximizing the
 1 S/N ratio for the large-area readouts envisioned for use in giant dual-phase LArTPCs. Figure 5.11
 2 shows the LEMs and anodes. This section summarizes key features of the LAS.

3 **The $50 \times 50 \text{ cm}^2$ anode:** Each $50 \times 50 \text{ cm}^2$ anode is manufactured from a single multilayer Printed
 4 Circuit Board (PCB). The readout strips for both x and y views consist of a pattern of gold-plated
 5 copper tracks with a 3.125-mm readout pitch. The two views have superimposed track patterns
 6 that are electrically insulated from one another. Electrical insulation in the points where the x
 7 and y tracks would superimpose is achieved by having tracks crossing over and under each other
 8 using a system of vias between the top and bottom layers of the PCB.

9 The design of the track patterns forming the strips is such that both x and y views collect the
 10 same amount of charge, independent of the angle of charged-particle tracks with respect to the
 11 readout strip orientation. The tracks pattern should then ensure a uniform and isotropic coverage
 12 of the strip surface while minimizing the strip capacitance. These criteria have driven a thorough
 13 design optimization. Various PCB layouts were tested in order to achieve the best performance,

²www.eltos.it

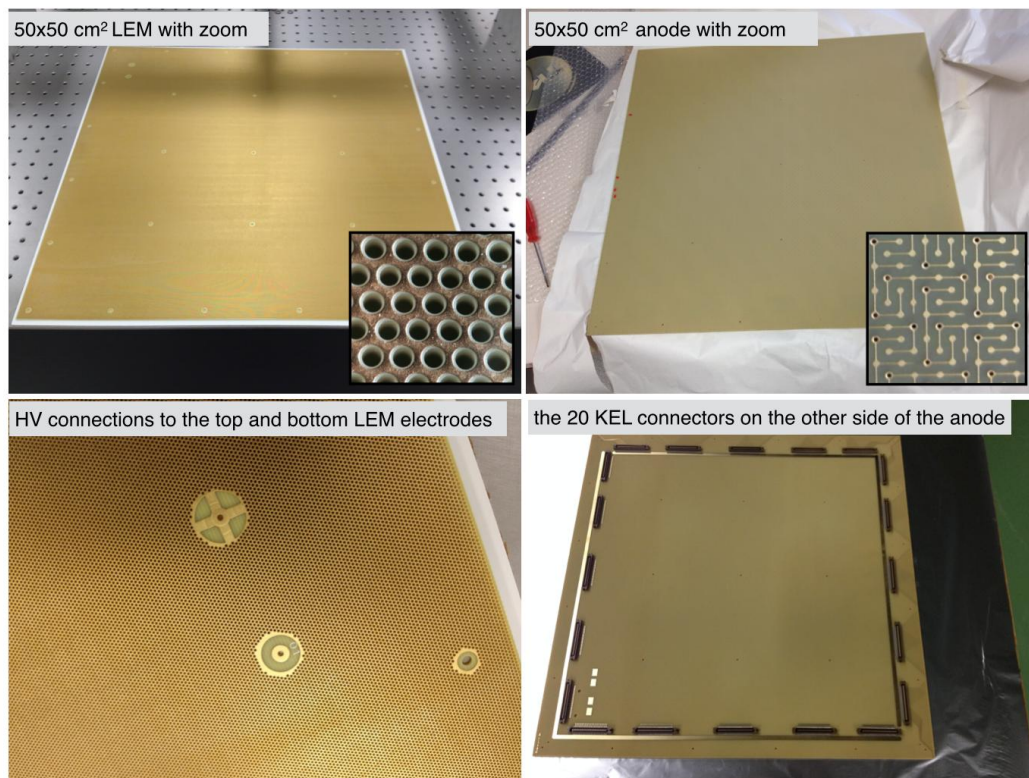


Figure 5.11: Top: pictures of the LEM and anode along with microscope views. Bottom: close up of the LEM HV connectors and back view of the anode with the KEL signal connectors to bridge to the adjacent LAS or to connect flat cables going to the signal feedthrough

fig:LEM_

as described in [17]. The final layout and schematic of the anode are shown in Figure 5.12.

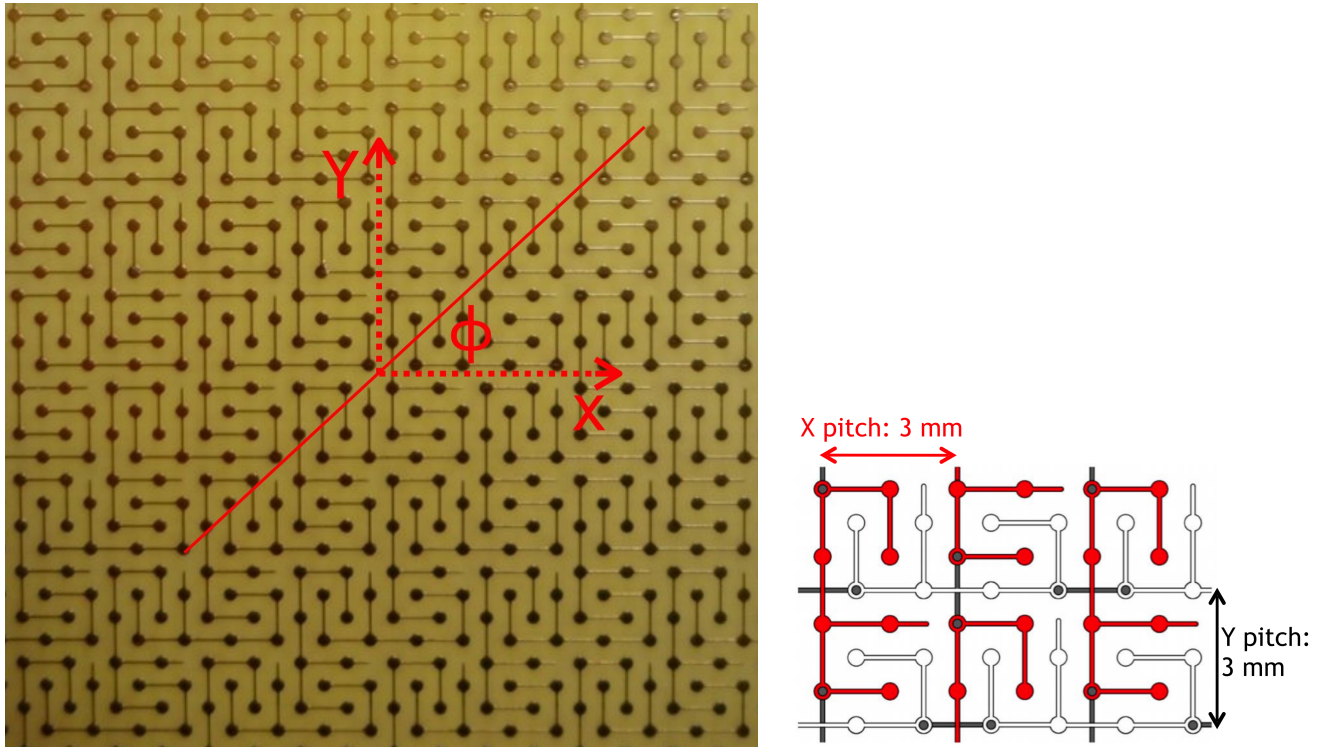


Figure 5.12: The 2D anode (left) and its schematic showing the interconnections ensuring continuity within each view while preserving insulation with respect to the perpendicular view (right). One view is filled in red and the other in white.

As result of this optimization, the electrical capacitance of the readout strips has been limited to only 150 pF/m, which translates into an electronic noise of about ~ 1000 electrons for a 2-m readout length. Figure 5.13 (right) shows that the charge-sharing asymmetry between the two views is kept within 1%. The two views can thus be treated in a completely equivalent way from the point of view of the reconstruction. The response in terms of the charge collection per unit pathlength $\Delta Q/\Delta s$ is independent of the charged-particle tracks' azimuthal angle ϕ (see Figure 5.13 left and middle).

The $50 \times 50 \text{ cm}^2$ LEM: Each LEM is built from a 1-mm-thick copper-clad epoxy PCB with $500 \mu\text{m}$ diameter holes drilled through, surrounded by a $40\text{-}\mu\text{m}$ dielectric rim. The holes are arranged in a honeycomb pattern with a pitch of $800 \mu\text{m}$, resulting in about 200 holes per cm^2 and $\mathcal{O}(500,000)$ holes over the entire $50 \times 50 \text{ cm}^2$ area. The holes provide confinement for the UV photons produced during the avalanche process and thus act as a mechanical quencher to prevent photon feedback. This property makes the LEM suitable for operation in ultra-pure argon vapor without the addition of a quenching gas.

The amplification of the drifting charges in pure argon vapor at 87 K with LEMs has been extensively demonstrated on a chamber with $10 \times 10 \text{ cm}^2$ area readout (see e.g., [18, 19]) as well as on a larger device consisting of a $40 \times 80 \text{ cm}^2$ readout. Both setups were successfully and stably operated at constant gains of at least 15, corresponding to $S/N \approx 60$ for MIPs. Recent studies

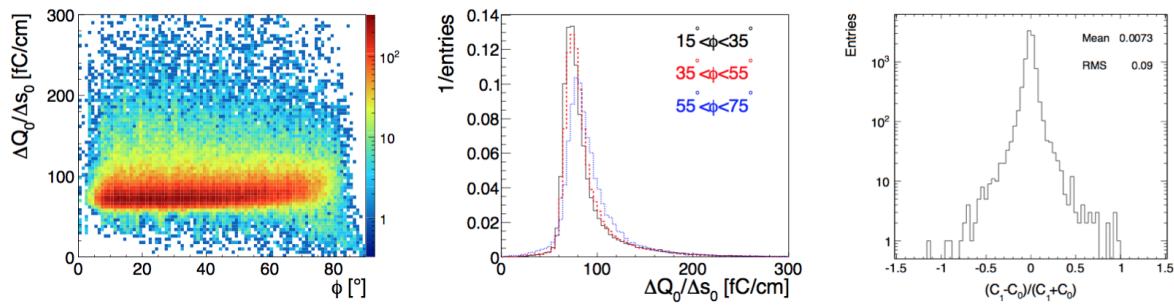


Figure 5.13: Charge deposition per unit of pathlength measured on LEM view 0 ($\Delta Q_0/\Delta s_0$) as a function of the track angle ϕ (left) and projection of the $\Delta Q_0/\Delta s_0$ distribution in three ϕ intervals (middle). The right plot shows the distribution of the difference between the total charge collected on both views normalized to their sum

fig:ano

33 systematically characterize the impact of the rim size, insulator thickness, hole diameter and hole
 34 layout on $10 \times 10 \text{ cm}^2$ area LEMs. The response in terms of maximal reachable gain and influ-
 35 ence on the collected charge uniformity, as well as the long-term stability of the gain, has been
 36 thoroughly compared for these different layouts. Some results are shown in Figure 5.14. Gains of
 37 almost 200 were reached and the LEMs could be operated at stable gains of at least ~ 15 after a
 38 charging up period of about a day.

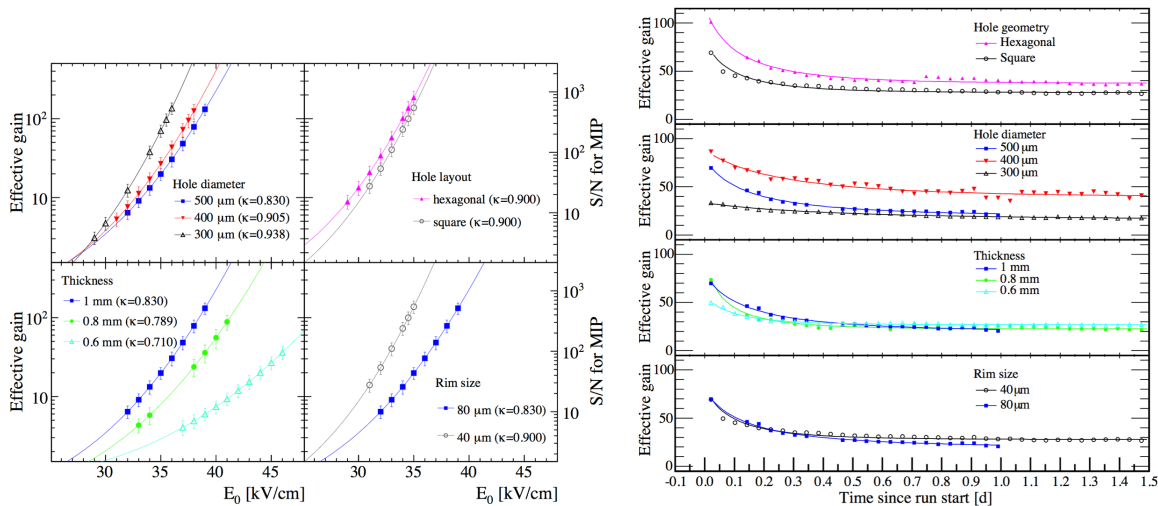


Figure 5.14: Performance of the LEMs with different geometry parameters. Left: effective gain vs. LEM electric field; right: the stabilizations of the effective gain over time.

fig:LEM

39 **LAS Assembly:** Figure 5.15 shows the LEM/anode sandwich (LAS). A LAS is fixed together
 1 with 29 M2 PEEK screws, each containing a precisely machined 2-mm-thick pillar to guarantee a
 2 constant inter-stage distance between LEM and anode on the entire $50 \times 50 \text{ cm}^2$ area. The dead
 3 zones caused by the supporting pillars and the two HV pins on the LEMs are minimized and make
 4 up less than 0.5% of the total area. The inter-stage distance between the LEM and anode in the
 5 LAS has been measured at many points. The results are shown in Figure 5.15 and are described
 6 in [21]. They indicate that the planarity is within the required tolerance of $2 \text{ mm} \pm 100 \mu\text{m}$.

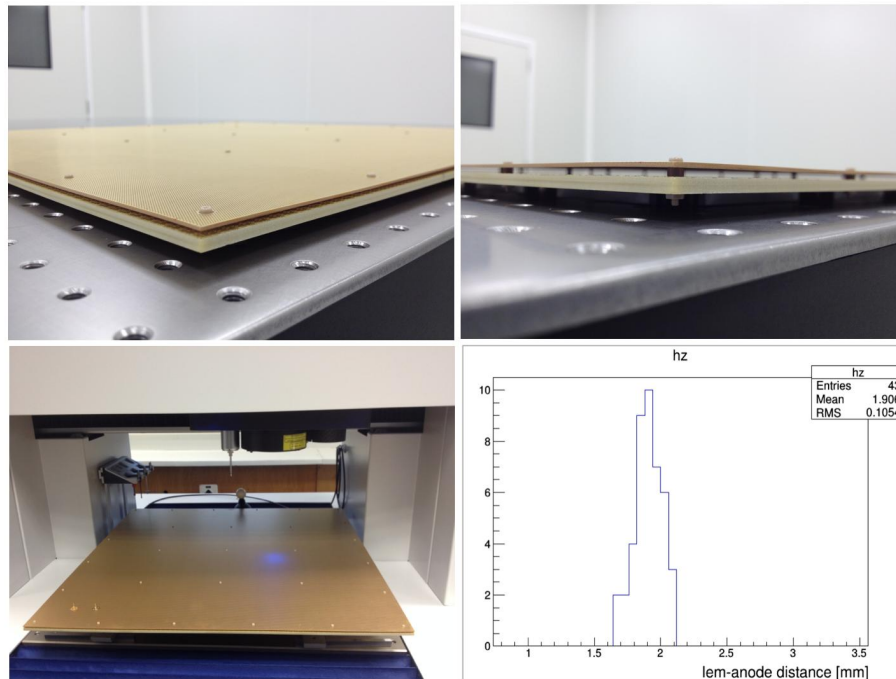


Figure 5.15: Close up pictures of the LEM/anode sandwich. The two bottom figures show a the measurement at the CERN metrology lab and a histogram illustrating the measured gap between the LEM and anode in various points. As can be seen the distribution is centered on the nominal distance of 2 mm and has an RMS of about $100\mu\text{m}$.

fig:LEM

7 The entire mounting sequence of the sandwich as well as that of the different elements of the CRP
 8 are being addressed in the WA105 prototype detectors. An example of a sandwich assembly on a
 1 $3 \times 1 \text{ m}^2$ CRP is shown in Figure 5.16.

fig:CRP_assembly

2 5.5 The Field Cage, High Voltage System and Cathode

d-alt-hv

3 This section describes the design of the high voltage system, field cage and cathode for the TPC. It
 4 is inspired by the LBNO 20-kt and 50-kt detector designs, described in Annex 4E: *LAGUNA/LBNO*
 5 *Part 2*, which can be simplified and down-sized for the DUNE detector (12 kt or 15 kt), due to the
 6 shorter drift path and the rectangular aspect ratio of the detector. The much shorter transverse
 7 dimension of DUNE's with respect to the LBNO design (12 m vs 40 m span) permits a lighter
 8 cathode structure (less sag requires less compensation) and a simpler hanging system for the drift
 9 cage and the cathode.

10 In the LBNO design the field cage is composed of equally spaced octagonal rings stacked around
 11 the active volume that create a uniform drift field; they have an intensity that is adjustable in the
 12 range 500 to 1000 V/cm. This leads to a cathode voltage of up to 2 MV when operating at the
 13 maximal field intensity of 1 kV/cm over a drift distance of 20 m.

14 Two different approaches have been developed for the drift-field high voltage generation system.

Figure 5.16: Pictures of the assembly of a $3 \times 1\text{m}^2$ CRP

fig:CRP_

15 The first one uses an external HV power supply and uses HV feedthroughs to penetrate into the
 16 detector volume. The WA105 demonstrator will use this approach for its drift of 6 m and a cathode
 17 voltage up to 600 kV. The second approach places a HV generator, the Greinacher HV multiplier,
 18 directly inside the LAr volume. It is an innovative technique, with some advantages relative to
 19 the first approach. This technique particularly suits giant-scale detectors that require a very high
 20 voltage of $\sim 1\text{--}2$ MV.

21 The DUNE detector (12-m drift) requires a voltage of 600 kV in order to operate at a field intensity
 22 of 0.5 kV/cm. This voltage is a factor of 3.3 higher than that of the reference design (Chapter 4)
 23 and it will be tested during the WA105 detector operation at 1 kV/cm over a 6-m drift.

24 The field cage designed for the LBNO 20-kt detector (20-m drift path) is composed of 99 octagonal
 25 field-shaping coils manufactured from 316L stainless-steel tubing and long radius elbows to EN
 26 10217-7 shop. The straight pipes and the elbows are assembled to form the coils by using a
 27 combination of welded and clamped joints.

1 The coils are supported by 32 off-hanging columns of G-10CR glass fibre/epoxy-laminated sheet
 2 insulating material, built in the form of chains, and suspended from the tank deck structure.

3 Each coil is designed as a series of fully welded infill tubes intended to fit between pairs of hanging
 4 support columns to form one section of the field cage. Short sections of the field-shaping coils are
 5 integrated as pins into links to assemble each chain. Longer sections and corner sections of the
 6 field-shaping coil are then fixed between the hanging columns to complete each coil (Figure 5.17).
 7 The combined assembly of 99 sets of field shaping coils within the 32 off-hanging columns provides
 8 a complete field cage.

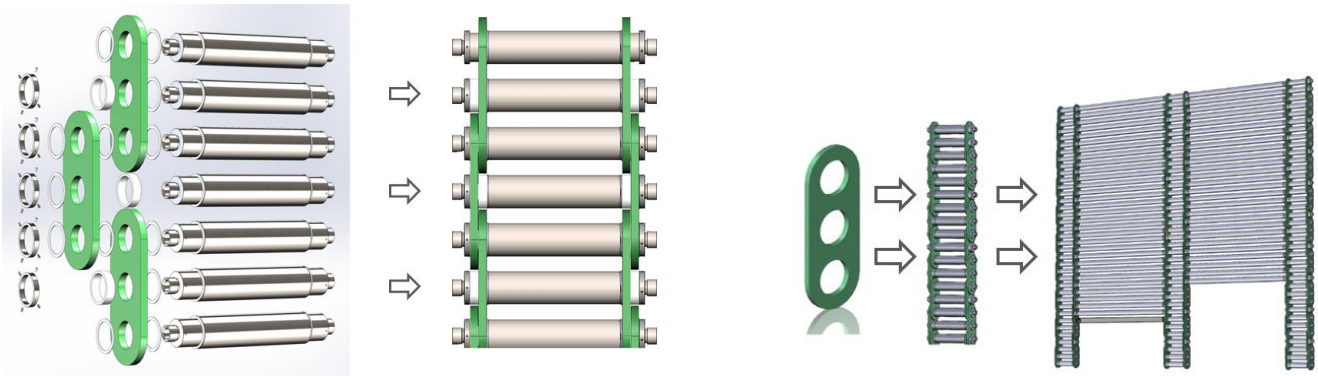


Figure 5.17: Left: assembly of the elements of a hanging chain. Right: construction of a field cage section from the hanging chains and the field shaping coil elements.

fig:LBNO

9 The infill tube specifications assume an outer tube diameter of 139.7 mm, which is common to
 10 the cathode structure. This allows a thinner wall, 1.6 mm, to be used in non-structural parts of
 11 the coils. Although a non-standard size, the total length of this tube can be manufactured as a
 12 special mill run. This will make it possible to save 21 tons of material relative to the standard
 13 tubes (wall thickness of 2.0 mm). The wall thickness of the link pins is 2.6 mm; this will provide
 14 sufficient stiffness to resist the bending torques across the link pins. All specialist preparation
 15 and welding of the link pins will be carried out in shop facilities under controlled fabrication.
 16 This includes the rough machining of the end fittings, preparation of the tube ends and the jig-
 17 welding of the complete assemblies. Further machining, after welding, will be carried out to ensure
 18 correct alignment and tolerance levels in conjunction with the hanging columns. Vent holes will
 19 be incorporated into the tubes as required to facilitate construction and to allow purging with
 20 GAr/LAr on commissioning.

21 Manufacturing, transportation and underground construction considerations were a fundamental
 22 part of the field-shaping coil design process, in collaboration with the LAGUNA-LBNO industrial
 23 partners. The requirement of construction in a clean-room environment within the completed
 24 membrane tank presented considerable challenges in terms of logistics and the development of the
 25 overall concept for fabrication. It was concluded that a modular construction approach would
 26 be required in order to (1) maximize off-site shop fabrication and minimize on-site assembly, and
 27 (2) ensure the cleanliness of construction and minimize the installation time. Each field-shaping
 28 coil is broken down into sets of three main construction modules (for more details see Annex 4E:
 29 *LAGUNA/LBNO Part 2*).

1 Although separate components, the field shaping coils and the cathode structure share identical
 2 features and dimensions. Thus, the maintenance of common interfaces is an important advantage
 3 of the overall field cage design.

4 The DUNE 12-kt detector field cage would require 60 stacked rectangular rings used to cover the
 5 12 vertical meters of drift volume.

6 The LBNO cathode design for the 50-kt detector follows an extensive review of options and analysis.
 7 The design incorporates features to minimize the static deflection of the cathode and to maximize
 8 the electrostatic performance. (To avoid regions with high electric fields, the electric field is limited

to 50 kV/cm.) Similar to the field-shaping coil, and for the same reasons, the cathode is designed as a modular structure ensuring a minimal on-site assembly time. The cathode is designed as a fully welded tubular rectangular 3D-grid structure in $2\text{ m} \times 2\text{ m}$ modules, 1 m deep in the vertical direction supported only from the periphery (Figure 5.18).

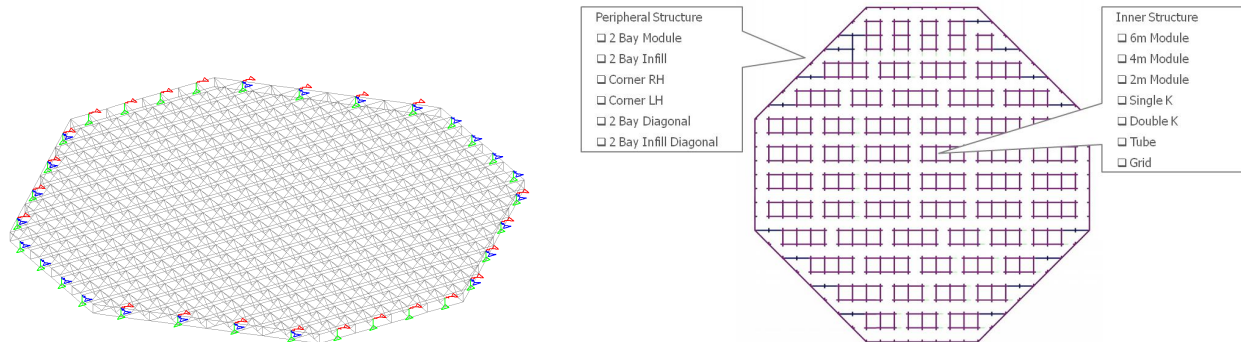


Figure 5.18: Left: cathode plane design for the LBNO detector. Right: breakdown of the cathode structure in construction modules.

The top and bottom grid structures for the cathode are manufactured from 139.7-mm OD tubes with wall thickness 2.6 mm to EN 10217-7 in 316 stainless steel. The bracing structure is manufactured from 60.3-mm OD tubes with wall thickness 2.6 mm, also to EN 10217-7 in 316 stainless steel. A grid structure comprising 10-mm OD tubes with wall thickness 1 mm, arranged in a single plane at 100-mm centers, is fitted to the top of the cathode. The maximum module size for this structure is 6 m, comprising three full $2\text{ m} \times 2\text{ m} \times 1\text{ m}$ deep modules of the cathode structure. The preparation and welding of the modules will be carried out in controlled facilities at the fabrication shop. Vent holes are incorporated into the grid structures to facilitate construction and to allow purging with GAr/LAr on commissioning. High levels of quality control will be possible with the modular construction design, and following inspection, each module will be cleaned to ISO 8 cleanliness standard and double-wrapped prior to dispatch and transportation to the site for installation and final assembly.

The cathode outer top tubular structure is identical to the bottom-most field-shaping coil; they use tubes of the same outer diameter (139.7 mm). The spans are the same (48 m for the 50-kt LBNO detector) and the vertical distance separating these components is the same as for the remaining field-shaping coils (200-mm centers). The cathode will be attached at the bottom of each hanging column by a split link in G-10CR. The cathode attachment points will also incorporate locally thickened sections of tube (as in the hanging chains) included as part of the peripheral structure nodes.

The complete assembly procedure, logistics and tooling for the field cage and cathode is described in Annex 4E: *LAGUNA/LBNO Part 2*. It is expected that the general design, adapted to the rectangular geometry, and the basic elements for the cathode construction would be similar for the 12-kt DUNE detector, but down-sized to the less challenging requirements.

5.6 The Electronics, Chimneys and DAQ

5.6.1 Overview

The LBNO 20–50-kt detector designs, developed in the LAGUNA-LBNO design study have channel counts in the range of 500,000 to 1,000,000. This large number has spawned extensive R&D over the last few years into large-scale charge-readout solutions optimized for double-phase detectors. The solutions that have been developed provide high integration levels, and significant cost reduction and performance improvement. They can be fully adopted for the DUNE far detector double-phase alternate design, which foresees 153600 channels for each 10-kt far detector module.

The R&D activities (ongoing since 2006) have focused effort on two main areas:

- development of cold front-end ASIC electronics
- development of low-cost, largely scalable data acquisition systems (DAQ) based on modern telecommunications technologies

One of the goals of the WA105 $6\times 6\times 6$ m³ demonstrator, a LArTPC with 7680 charge-readout channels described in Section 9.4, is to test the large-scale readout system developed in the LAGUNA-LBNO design study. Annex 4I: *WA105 TDR* and [22] provide detailed descriptions of the charge-readout electronics, including the cold front-end ASICs and the DAQ.

The LAGUNA-LBNO design was driven both by cost and by the particular use of the electronics for the dual-phase readout, which implies larger signals from the detector relative to single-phase, effectively releasing requirements on noise. Section 5.3 describes the charge readout system. Recall that the Large Electron Multipliers (LEMs) amplify the ionization charges by at least a factor 20, and that by adjusting its voltage, the LEM gain is tunable from there up to 200. When the charges reach the segmented anode, they are equally shared among two perpendicular collection views. The front-end amplifier connected to the anode, given the capacitance of the anode strips, would have a S/N ratio of 14 at unitary LEM gain. Considering a minimal LEM gain of 20, the amplifier provides an overall S/N ratio of 140. The S/N ratio is boosted by the LEM gain, thus implying less stringent requirements on the preamplifier noise.

The electronics consists of front-end amplifiers that are implemented as cryogenic CMOS ASICs connected to the anode with 50-cm cables; they are completely accessible from the outside while remaining very low-noise. The amplifiers must be housed in separate volumes that are completely distinct from the tank volume in order to replace them as needed without contaminating the pure argon inside the cryostat. These volumes are called chimneys.

Flat, 2-m-long cables inside each chimney connect front-end cards to digitization electronics, housed in microTCA (μ TCA) crates at the chimney exits, outside the cryostat. This design provides a way to maintain the front-end at cryogenic temperatures but keep it accessible, and maintain the digital electronics externally, at room temperature. This provides risk mitigation and significant flexibility.

38 The digitization units in the μ TCA crates are synchronized with the White Rabbit (WR) time-
39 distribution standard^[24], which was originally designed to achieve sub-ns accuracy. This built-in
40 accuracy, while not a critical aspect of the system design, is much better than what is needed
41 to align the 400-ns samples of the charge readout. WR was adopted for its practical integration
1 aspects and for cost reduction; its very high timing accuracy is a bonus. WR is also used in this
2 design as a dedicated network network for the trigger distribution.

3 The light-readout digitization electronics (see Section ^{sec:detectors-fd-alt-light}5.7) is also implemented in μ TCA and pro-
4 vides triggers from the photomultipliers (PMTs) that are distributed to the DAQ via the WR
5 network.

6 Commercial high-bandwidth and high-computing-power back-end cards are used for event-building
7 and are coupled to a farm for online processing, which is implemented for event filtering, data
8 reconstruction, calibrations and data-quality assessment.

9 5.6.2 Front-end Cryogenic Amplifiers and Chimneys

10 In the framework of the R&D related to LAGUNA-LBNO since 2006, several generations of proto-
11 types of cryogenic ASIC 0.35 microns CMOS multi-channel preamplifier chips have been developed.
12 The capability to operate at cryogenic temperatures means that cables can be shorter (in WA105
13 these cables are just 50 cm long), which reduces the associated capacitance for the connection to
14 the detector. It also makes it possible to reach an optimal amplifier S/N ratio at a temperature
15 around 110 K, which can be easily achieved in the GAr at the top of the cryostat.

16 Another significant feature of the design is the ad-hoc designed chimneys, which enable the front-
17 end electronics to remain a very short distance from the detectors in the CRP and accessible for
18 repairs without opening the cryostat. Chimneys are separate, insulated, cylindrical volumes that
19 penetrate the cryostat top, their lower half immersed in GAr, their upper half outside the tank
20 at room temperature. The front-end electronics cards are installed inside the chimneys near the
21 bottom. The chimneys are filled with inert gas and have a cooling system to keep the electronics
22 at the optimal temperature. A cold feedthrough at the bottom of each chimney isolates the cards
23 from the inner volume of the vessel and allows connection from the anode to the electronics; a
24 warm feedthrough (FT) at the top allows connection to the digitization electronics on the outside.

25 The first ASIC versions were designed principally for the readout of charge from collection and
1 induction wire planes, and could also handle bipolar signals. Since 2012 some versions of the
2 dual-phase have been developed specifically to match the dynamic range of signals coming from
3 the two collection views of the anode PCB after LEM amplification. As described in Section 5.3,
4 each collection view is instrumented with strips of 3.125-mm pitch and 3-m length (150 pF/m
5 capacitance). For this pitch, simulations of electromagnetic showers predict that a single channel
6 will collect a maximum 40 MIP. The design of the dual-phase cryogenic ASIC is based on a LEM
7 minimal gain of 20, which corresponds to 1200 fC for this maximal signal.

8 Two versions of the dual-phase ASIC chips have been produced for WA105, both with 16 readout
9 channels. The first version has a constant gain in the region 0–40 MIP. The second is characterized

10 by a double-slope gain. This second solution optimizes the resolution while preserving a large
 11 dynamic range. It is characterized by a high-gain region extending up to signals of 10 MIP, after
 12 which the gain is reduced by a factor of three in order to enable a better overall match for a dynamic
 13 range of 40 MIP. It provides the best resolution in the MIP region (dE/dx measurements) without
 14 limiting the dynamic range for showers, which can still reach up to 40 MIP (see Figure 5.19). This
 15 double-slope regime has been optimized on the basis of simulations of hadronic and electromagnetic
 16 showers. Both ASIC versions, compatible with the LEM signal dynamics, are implemented in the
 17 CMOS 0.35 μm technology; they have 16 channels, 18-mW/channel thermal dissipation or less,
 18 about 1300 electrons ENC at 250-pF input detector capacitance, and operate with this best S/N
 19 ratio at about 110 K.

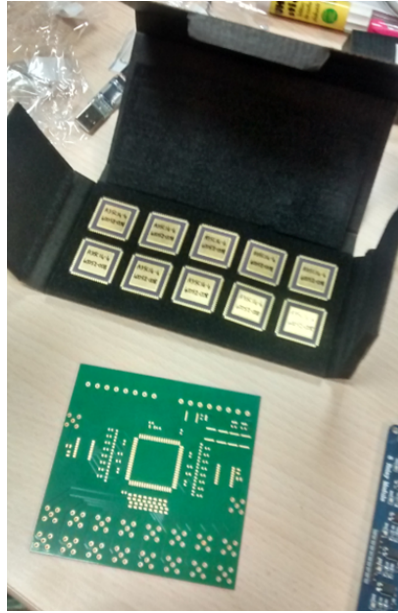


Figure 5.19: Front-end 16 channels cryogenic ASIC amplifier with the double-slope gain implementation

fig:FE_A

20 The implementation of the double-slope gain regime is obtained by replacing the feedback integra-
 21 tion capacitor of the OPAMP with a MOS capacitance, which changes its value above a certain
 22 threshold voltage. This effect is also present during the discharge phase and it can be corrected
 23 with the inclusion in the feedback loop of an additional branch with a diode and a resistor designed
 24 to keep the RC value roughly constant during discharge. This branch can be selected/deselected
 25 with an internal switch for all the channels in the ASIC (see Figure 5.20).

26 In the design under implementation in WA105 and proposed for DUNE, there are 640 channels
 27 per chimney. The 40 ASIC amplifiers needed for the readout of each group of 640 channels will be
 28 arranged on 10 pairs of front-end cards plugged into the FT at the bottom of each chimney. Each
 29 front-end card holds two ASIC chips and a few discrete components. Particular care has been taken
 30 in testing several options (Gas Discharge Tubes, Metal Oxide Varistors, double diodes) for the
 1 surge-arrestor components, which have to protect the ASICs from occasional sparks occurring in
 2 the CRP. This study was aimed at maximizing the protection efficiency, testing the components'
 3 durability for a very high number of sparks and minimizing the input capacitance seen by the
 4 pre-amplifiers. Double-diodes have been selected as the best solution given their performance and
 5 capacitance. The total dissipation of the front-end electronics will be about 11.5 W per chimney.
 6 This heat source is minor with respect to the heat conduction from the flat cables going to the

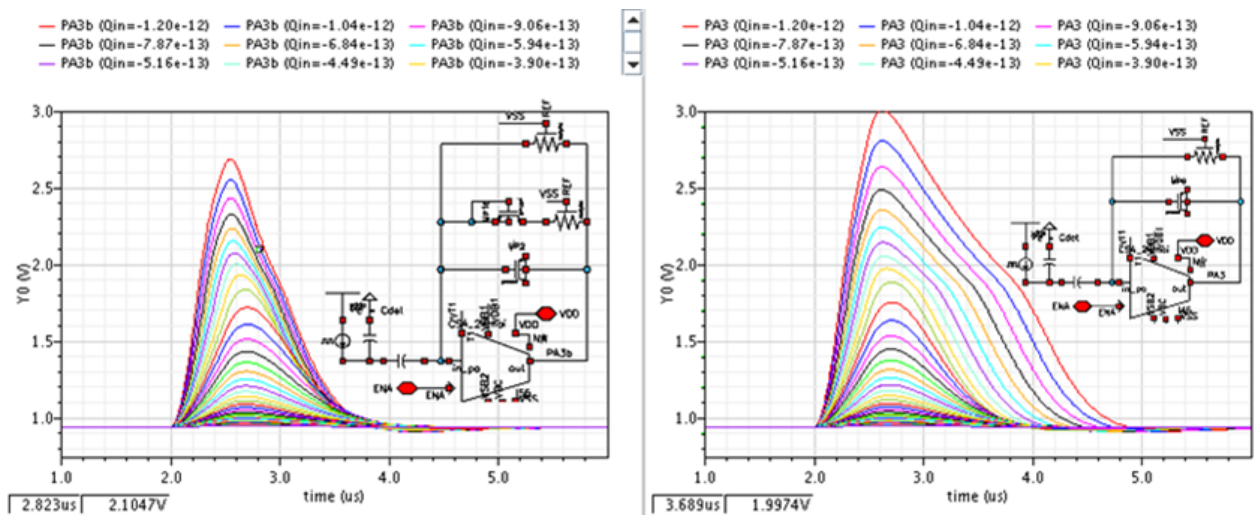


Figure 5.20: Response of the double-slope ASIC amplifier to progressively larger pulses with and without the diode/resistor feedback branch

fig:FE_c

7 digitization electronics and from the walls of the chimney. The front-end cards are kept at low
 8 temperature by a cooling system installed at the bottom of chimney that compensates for this
 9 overall heat flow. The front-end electronics is coupled to the DAQ system, described in Section ??,
 10 that is based on 12-bit ADCs, matching the needed dynamic range quite well. Figure 5.21 shows
 11 the 3D model of the signal FT chimneys hosting the cryogenic ASIC amplifiers.

sec:fd-alt-ele

fig:chimneys_scheme

12 A signal FT chimney prototype for 320 channels built for the $3 \times 1 \times 1$ m³ WA105 prototype is
 13 shown in Figure 5.22.

fig:chimneys_proto

14 Pairs of cryogenic electronics front-end cards are mounted at the end of sliding G10 blades which
 15 can be extracted from the top of the chimney. The blades, which also carry the flat cables for
 16 the connections, slide on guides mounted inside the chimney. By moving the blades, the front-end
 17 cards can be plugged/unplugged to/from connectors on the top side of the cold FT at the bottom
 18 of the chimney. This FT completely isolates the chimney from the LAr vessel. Connectors are
 19 mounted on the bottom of the FT for the 50 cm flat cables coming from the CRPs.

20 5.6.3 Digital Electronics and DAQ Architecture

elec-daq

21 The DAQ system proposed for the dual-phase DUNE detector design is based on two industrial
 22 standards:

- 23 • MicroTCA (μ TCA) standard for the distributed data network[23]
- 24 • White Rabbit (WR) standard for the distributed clock network[24]

mTCA-standard

WR-standard

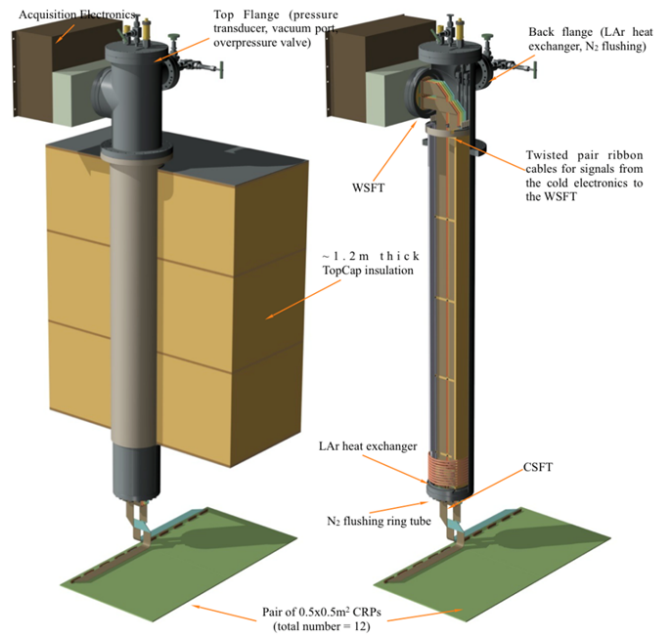


Figure 5.21: 3D model of the signal feedthrough chimneys

fig:chim

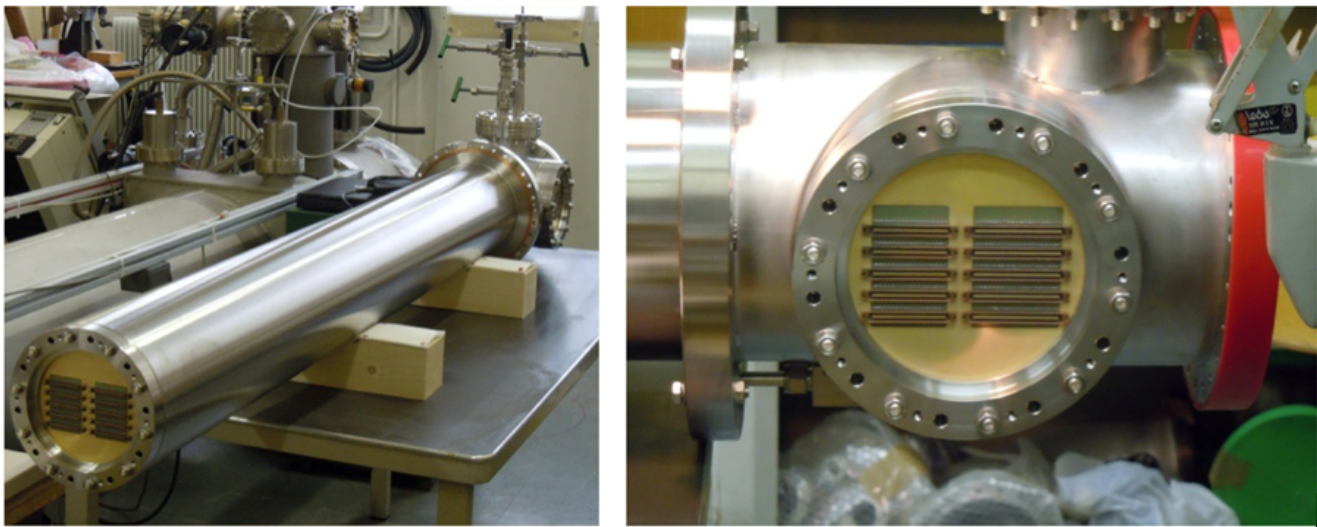
Figure 5.22: Prototype of the signal feedthrough chimney built for the WA015 3×3×1 m³ prototype

fig:chim

25 The analog electrical signals from the front-end electronics ASICs transit through the signal chim-
1 neys up to the digitization boards in the μ TCA crates (DAQ L1). The backplane of each μ TCA
2 crate (a *shelf*) is connected through a 10GbE up-link to the next level (DAQ L2). The L2 directly
3 connects the μ TCA crates to FPGA-based high-performance back-end processing boards. The
4 design calls for a lossless transmission scheme all the way down to the back-end processing board,
5 which applies all filtering algorithms and does the event building. The Huffman lossless algorithm
6 is easy to implement and typically provides a factor of 10 compression on LAr events.

7 Recorded data are sent to a local storage level where Object Storage Servers (OSS) and Meta-
8 Data Servers (MDS) are connected with the event-building workstations via a 10/40-GbE network
9 (Ethernet or InfiniBand). In parallel, signals from a high-stability common clock and time synchron-
10 ization signals are distributed (using the WR standard) to the L1 digitization cards, through a
11 dedicated, deterministic network. The WR network is also used to transmit the trigger time-stamp
12 signals, which can be generated either by the PMTs' readout electronics or by additional sources,
13 e.g., for WA105 operation in the charged particle beam, the beam trigger counters. The clock is
14 derived from a Master Clock generator connected to the WR Grand-Master switch. WA105 will
15 implement this DAQ scheme, and additional details may be found in [15].

16 5.6.4 MicroTCA Standard and Applications

17 The MicroTCA (μ TCA) standard offers a very compact and easily scalable architecture to handle a
18 large number of channels at low cost. The μ TCA or related standards — such as ATCA or xTCA —
19 are now well known in the HEP community and have been integrated into various designs at CERN
20 (e.g., LHC upgrades), DESY, etc. μ TCA fulfills requirements of the telecommunication industry
21 and offers the ability to interconnect distributed applications while providing a standard, compact
22 and robust form factor with simplified power supply management, cooling, and distribution of
23 internal clocks. The backplane of a μ TCA crate (the μ TCA shelf) accommodates high-speed
1 serial links; they are arranged in a variety of topologies to support a variety of protocols, including
2 Ethernet 1GbE or 10GbE, PCI Express, SRIO, etc. Use of Ethernet-based solutions is proposed for
3 both data and clock distribution, through the μ TCA backplanes. This choice obviously optimizes
4 the connections between the various components of the system. Constraints imposed on the data
5 transfer bandwidth point towards use of the 10GbE protocol. For the clock distribution, dedicated
6 lanes on the backplane must be defined by the user. The μ TCA standard also offers so-called *clock*
7 lanes, which distribute the timing signals to all boards hosted in the crate and which may be used
8 for any type of signal.

9 The signal digitization boards plugged into a μ TCA shelf are called Advanced Mezzanine Cards
10 (AMCs)[25]. Each AMC is connected to one or two μ TCA Carrier Hub (MCH) boards through
11 the backplane serial links. The MCH provides a central switch function allowing the AMCs to
12 communicate with each other or with external systems through an up-link access. The MCH
13 manages both the 10GbE uplink and the WR bi-directional clock distribution. Figure 5.23 provides
14 a sketch of the backplane layout and its implementation in a particular shelf type selected in the
15 design of the system.

16 The production version DAQ designed for the WA105 DAQ is based on the μ TCA.1 standard,

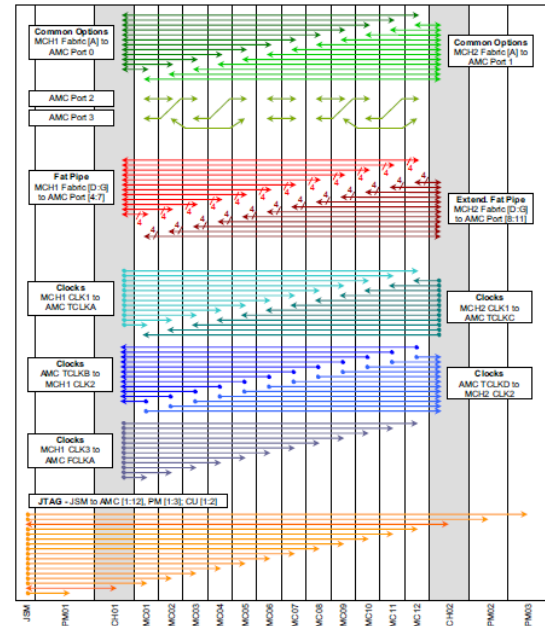
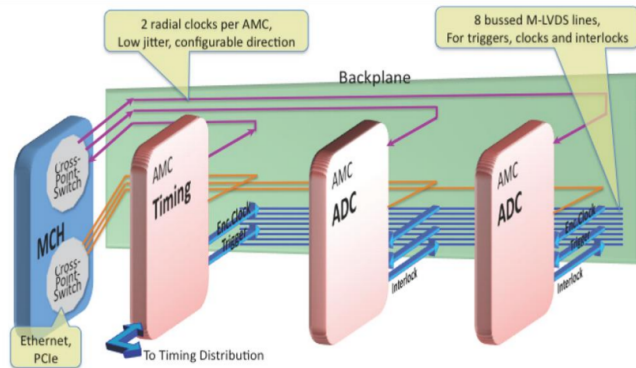


Figure 5.23: Left: global microTCA crate organization. AMCs (providing basic ADC functions) are connected to the crate controller or MCH which up-links the external systems. A dedicated AMC for the clock receives dedicated signals (master clock, trigger signals) from the timing distribution system and transcript them onto the backplane. Right: backplane layout of the Schroff 11850-015 reference.

fig:mTCA

17 with connections to the user input signals from the front side only. These connections are made
 18 with VHDCI cables in order to minimize the number of cables. One μ TCA shelf is connected to
 19 each signal chimney, reading out 640 channels corresponding to 10 AMCs.

20 Many types of μ TCA shelf are available on the market, e.g. 11850-015 8U from Schroff for μ TCA.1
 21 standard, NATIVE-R9 from NAT for μ TCA.4 standard. The cost of these items is quickly decreasing
 1 due to the fast pace of developments by the internet providers. These items all have redundant
 2 power supplies, redundant MCHs and offer different segmentations to connect the AMCs.

3 The advantage of this architecture is that it limits the DAQ electronics developments to the
 4 AMC only since that is the component that provides the functionalities for the digitization, data
 5 formatting and compression, event time-stamping and data transfer through the backplane. For
 6 WA105, the AMC is a double-size module (also compatible with μ TCA.4 standard) with a single
 7 input connector and a 10GbE link to the backplane. The input stage performs the 64-channel
 8 digitization through eight 8-channel, 14-bit ADC chips read out at a 2.5-MHz frequency. The
 9 ADC readout sequence is controlled by two FPGAs that make the data available on a double port
 10 memory. Readout of the data is performed continuously and they are stored in a local buffer.
 11 The recorded samples, each corresponding to a drift window, are selected in coincidence with the
 12 received trigger. When a trigger occurs, the samples written in the memory can be treated with
 13 compression algorithms (such as Huffman or RLE) or zero-suppression (if required) and transmitted
 14 over the network until the end of the drift window, which closes the event. These operations are
 15 managed by a third FPGA, which sends the data on the shelf backplane in order that they can
 16 be transmitted to L2. This readout scheme and hardware implementation have been validated for
 17 WA105 on a Stratix 4 prototype board, shown in Figure 5.24.

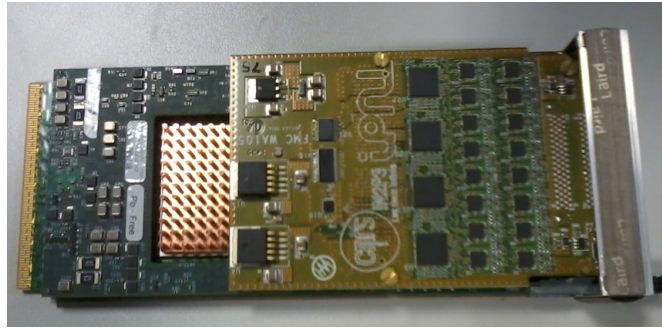


Figure 5.24: Prototype of AMC, using μ TCA.1 standard, and hosting 64 ADC channels on a mezzanine board. This prototype is used as a validation of the full and final ADC chain in WA105.

fig:AMC-

18 5.6.5 Back-end and Event Builder

19 A network hierarchical structure is implemented for the back-end and event builder in which all
 20 crates are interconnected to a dedicated back-end FPGA processing board (such as S5-PCIe-HQ,
 21 [Figure 5.25](#)).

fig:Bitware-board



Figure 5.25: FPGA processing board based on Stratix V from Altera. The board features a dual QSFPP+ cages for 40GigE or 10GigE links, 16 GBytes DDR3 SDRAM, 72 MBytes QDRII/II+, two SATA connectors and is programmable via OpenCL.

fig:Bitt

22 This kind of board is used for massive data processing in many fields (medical imaging, stock
 23 market, etc.) that require parallel processing with reduced power consumption (it dissipates only
 24 10% of the power dissipated by an equivalent CPU for a comparable number of operations). This
 25 particular board has two QSFPP+ cages to bring the data directly to the FPGA for the lowest
 1 possible latency. Upto 8×10 GbE links without data loss are available per board. The board
 2 performs further data processing, filtering and transmission to the highest level for storage. This
 3 type of board is widely used and the present generation, based on the Altera Stratix V, will evolve
 4 to the Aria X and the Stratix X. Stratix X will be probably available at the time of construction of
 5 the DUNE DAQ system. Programming of the back-end processing board is achievable through the
 6 OpenCL software suite where a kernel code, on top of a host code, allows programming the FPGA
 7 directly in a high-level language without a classical VHDL synthesis chain. OpenCL applications
 8 are transparent to the hardware used for procesing (FPGAs, CPUs, GPUs). This highly flexible
 9 feature is fully adapted to the requirements of large DAQ systems, where conditions of filtering,
 10 event building, etc., may evolve with time.

5.6.6 Timing Distribution System and White Rabbit (WR) Standard

The clock distribution will use a parallel, independent network to distribute the signal from a GPS-disciplined Master Clock down to each μ TCA shelf, through specific switches. Technically, the WR standard is based on a combination of Synchronous Ethernet (Sync-E) and Precision Time Protocol (PTP, IEEE1588), where the Ethernet clock is generated by a GPS-disciplined clock. At the level of each shelf, this high-accuracy clock is made available to each AMC through dedicated lines off the backplane. As discussed before, the μ TCA standard accommodates special lanes for clock transmission. The trigger signals (time-stamps) are encoded and sent through this dedicated WR network which has enough bandwidth for this transmission without interfering with the PTP synchronization signals. The requirements on the synchronization for the charge readout are quite loose since the typical readout frequency is of the order of a few MHz. The requirements for the PMT readout on the contrary are more stringent. The goal is to provide a nanosecond synchronization at the level of all L1 elements. This goal is typically achievable with the WR standard[24].

The WR provides an extension to the Ethernet network with Gb/s data transfer speed and allows for accurate synchronization among the different network nodes. It provides a common clock for the physical layer in the entire network, allowing sub-nanosecond synchronization accuracy and 20-ps jitter time. The WR network is designed to host up to thousands of nodes and to support distance ranges of 10 km using fiber cables. It ensures that all the Ethernet frames sent are delivered after no more than a fixed delay (controlled latency). The order of the frames should be preserved. A typical application scheme is displayed in Figure 5.26.

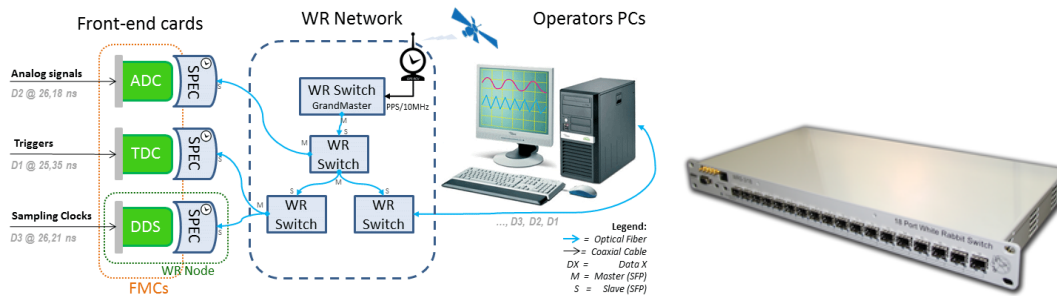


Figure 5.26: Left: general organization of a typical WR network. Right: standalone WR switch.

The WR application in the μ TCA standard is currently engineered to easily interconnect μ TCA cards. The WR switch can therefore be connected directly to its different nodes in the same rack to facilitate maintenance and limit the space occupied. The implementation scheme is based on the integration of a WR mezzanine board on the MCH of each shelf. In the future a full integration of the WR within the μ TCA DAQ system would be very powerful. The current WR implementation scheme is based on the integration of a WR mezzanine board on the MCH of each shelf. The development of this WR MCH is in progress for the WA105 demonstrator (on a MHC produced by the company NAT); the companies producing the MCH and the WR slave to be integrated show clear interest in this development.

5.7 The Slow-Control System

The slow-control system for the far detector is designed to monitor the detector operation conditions, in particular, the following physical quantities inside the tank:

- temperatures (with platinum resistors)
- pressures (with commercial piezoelectric sensors)
- LAr levels (with custom-made capacitive sensors and electronics)
- deformations of materials (with resistive strain gauges)

In addition, the slow-control system provides the hardware infrastructure needed to monitor traces of O₂, N₂ and H₂O impurities in the tank, to monitor and control the high- and low-voltage power supplies, heaters, lighting system and cryogenic video system. It will also interface to the cryogenic system and to the motorized system that adjusts the position of each Charge Readout Plane (CRP).

The design of the slow-control system is part of a continued, progressive prototyping effort aimed at developing a control system dedicated to multi-kilotonne LAr dual-phase detectors. It has been designed in the framework of the LAGUNA-LBNO design study and the WA105 experiment. WA105 represents a first, fully engineered, implementation of this design, which can be extrapolated to larger detector scales. The design also benefited from the successful example and the expertise developed in the context of the ArDM experiment [26] which is currently operating a LArTPC for dark matter searches in an underground laboratory (LSC, Spain).

The slow-control system introduces the use of National Instruments Compact RIO (Reconfigurable Input Output) modules for acquisition of all the physical quantities of interest. Figure 5.27 shows a rack prepared for the WA105 3×1×1 m³ prototype that is ready to be tested at CERN.

The entire slow-control system of the WA105 demonstrator will be managed through a single Lab-View interface [22] which will provide access to all the sensors, control the actuators and provide the platform for the video monitoring system both inside and outside the tank. Supervisory software will be implemented in the CERN UNICOS (UNified Industrial Control System) framework [27] to provide the operator interface for the monitoring of all the physical quantities and the handling of alarms.

As discussed in Section 5.1, the charge-readout system is implemented via CRP modules of 3×3 m². Each CRP is an independent detector, hence its instrumentation can also be treated as independent. A complete list of the sensors planned for use in both the 3×3 m² DUNE CRP module and the 3×1×1 m³ WA105 prototype is provided in Figure 5.28.

The number of sensors for the far detector CRP is extrapolated from the number for the prototype and is not yet final but it should be considered as an upper limit. The sensor instrumentation of the 3×1×1 m³ WA105 prototype has also led to the design of a custom Slow-Control Feedthrough (SCFT), based on the use of weldable connectors for high vacuum (see Figure 5.29). A specific

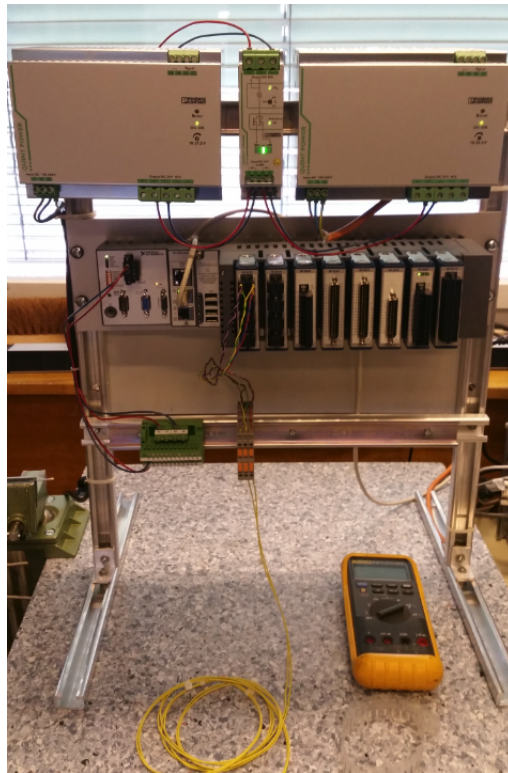


Figure 5.27: The rack is a prototype of the entire Control System; it embeds modules for resistive temperature sensors, pressure sensors, strain gauges, liquid argon level meters, control for heaters. On the upper part a redundant 24 V power supply provides fault tolerant power to the National Instrument controller and modules. Calibration of modules and sensors is ongoing.

fig:NI_p

process	measurement	sensor	range	resolution	connector to flange	LAr-Proto			Far Detector 4×4 m ² module		
						# of sensors	remote IO	# of NI modules	# of sensors	remote IO	# of NI modules
PCS											
	temperature LM	Pt 10k	85-300K	0.1 K	D-SUB	80	yes	28 (NI9219)	4	yes	1 (NI9219)
	temperature CRP	Pt 1k	85-300K	0.1 K	D-SUB	24	yes	6 (NI9219)	4	yes	1 (NI9219)
	temperature SFT	thcouple Ktype	85-300K	0.1 K	MSK-3-C16	18	yes	2 (NI9213)	24	yes	3 (NI9213)
	pressure	Keller PAA-21Y	0-2 bar	10 ⁻⁵ mbar	dedicated	8	yes	1 (NI9208)	12	yes	4 (NI9208)
	level	coax cap. filling	2 m	1 mm	SMA	2	yes	-	-	-	-
	level CRP	plate	2.5 cm	100 μm	SMA	8	no	2 (NI9203)	4	no	1 (NI9203)
	level field-cage	plate	2.5 cm	100 μm	SMA	3	no	-	-	no	-
	strain gauge	HBM full bridge	2.5 cm	gauge fact. 2	D-SUB	24	yes	6 (NI9237)	8	yes	2 (NI9237)
	trace ana N ₂	Gowmac	0-100 ppm	10 ppb	-	1	yes	-	1	yes	-
	trace ana H ₂ O	Gowmac	0-50 ppm	10 ppb	gas/liquid handling	1	yes	1 (NI9203)	1	yes	1 (NI9203)
	trace ana O ₂	AMI	50 ppb-20%	100 ppb	gas/liquid handling	1	yes	-	1	yes	-
	heaters	HS25	25 W	N/A	Caburn	20	yes	PSU + relay	20	yes	PSU + relay
	total PCS					190			79		
DCS											
	HV LEM	N/A	8 kV	N/A	SHV	24	no	CAEN PSU	128	no	CAEN PSU
	HV PMT	N/A	8 kV	N/A	SHV	5	no	CAEN PSU	16	no	CAEN PSU
	LV LEDs	N/A	24 V	N/A	D-SUB	6	no	24 DC	60	no	24 V DC
	total DCS					35			204		
DSS											
	temperature GTT	Pt 10 k	85-300 K	0.1 K	D-SUB	45	no	12 (NI9219)		no	
	cryo camera	webcam	N/A	N/A	USB	4	yes	1 (cRIO-9082)	4	no	1 (cRIO-9082)
	IR camera	webcam	N/A	N/A	USB/TCP IP	2	no	1 (cRIO-9082)	2	no	1 (cRIO-9082)

Figure 5.28: List of the slow control sensors for the 3×1×1 m³ WA105 prototype and far detectors CRP

fig:sc_s

- 1 SCFT for the DUNE $3 \times 3 \text{ m}^2$ CRP would be based on this design.

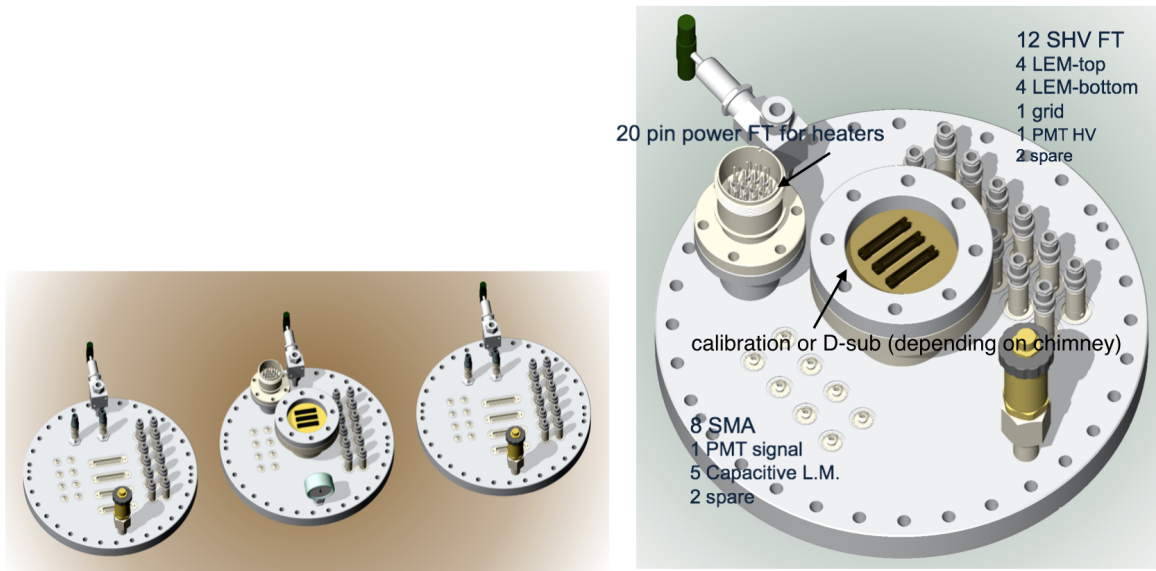


Figure 5.29: The 3 SCFTs providing weldable connectors for all the instrumentation inside the $3 \times 1 \times 1 \text{ m}^3$ WA105 tank. The number of sensors per module in the DUNE far detector will be drastically reduced with respect to this WA105 prototype.

fig:SC_f

2 5.8 The Light-Readout System

lt-light

3 The light-readout system developed in the LAGUNA-LBNO design study detects the scintillation
 4 light using 8-inch cryogenic PMTs (Hamamatsu R5912-02mod) with TPB coating. The PMTs are
 5 placed about 1 m below the cathode. The application of the TPB coating can be done at the
 6 level of the glass itself or on a transparent plate mounted over the photocathode surface. The
 7 WA105 demonstrator will use 36 PMTs R5912-02mod ($1/\text{m}^2$ of cathode surface). The mechanics
 8 for the PMTs' attachment has been carefully studied; it must counteract the PMT buoyancy while
 9 avoiding stress to the PMT glass (due to differentials in the thermal contraction between the
 10 support and the PMT itself).

11 The dual-phase LAr detectors designed for LBNO are equipped with a large number of PMTs.
 12 Depending on the size of the DUNE detector module and on the density of PMT on the detection
 13 surface, this number may be as high as 1000. The large number of photosensors called for a large
 14 integration scale solution for the front-end electronics.

15 Solutions of this kind have been studied, in the framework of the R&D program PMm2 ^{PMM2-1, PMM2-2} [28, 29],
 16 for the instrumentation of giant water Cherenkov detectors. The signal digitization is performed
 17 by grouping the PMTs in arrays of 16. Each PMT array is read out by an ASIC chip in AMS
 18 SiGe $0.35 \mu\text{m}$ technology. The ASIC, which is called PARISROC (PMT ARrray Integrated in
 19 Si-Ge Read Out Chip) ^{parisroc} [30], provides a complete readout system for triggerless data acquisition.
 20 The solution developed by this program represents an important handle for cost reduction.

21 The front-end electronics for the light readout of the WA105 demonstrator will be based on the
22 solution developed by the PMm2 R&D. The PARISROC ASIC is currently adapted to the time
23 structure of the scintillation light produced in the interactions of secondary particles in neutrino
24 interactions in LAr. The detection of the direct scintillation light (S1) that provides the absolute
25 event time is the main task of the electronics. The electronics will also process the signals from
26 the scintillation light (S2) produced by the electrons as they are extracted and amplified in the
27 gaseous phase.

28 The PARISROC chip reads the signals of 16 PMTs independently of one another. Each analog
29 channel consists of a low-noise preamplifier with variable and adjustable gain (8 bits) to compensate
30 for the relative PMT gain differences when powered by a single high voltage. The preamplifier
31 is followed by a slow channel for the charge measurement in parallel with a fast channel for the
32 trigger output. The slow channel includes a variable (50–200 ns) slow shaper followed by an analog
33 memory with depth of 2 to provide a linear charge measurement up to 50 pC; this charge is then
1 converted by a 10-bit Wilkinson ADC. The fast channel is composed of a fast shaper (15 ns)
2 followed by a low offset discriminator to auto-trigger down to 10 fC. This auto-trigger feature
3 makes the PMT array completely independent of the other PMT arrays. The threshold is loaded
4 by an internal 10-bit DAC common to the 16 channels.

5 The variable gain of each preamplifier provides the flexibility to adapt the system to the charac-
6 teristics of each PMT after it has been correctly calibrated. In the timestamping process, there
7 are two TDC ramps working in phased opposition in order to reduce the dead time (i.e., when the
8 ramp goes to zero) by selecting the other ramp that will be in its active state.

9 When an event occurs, the value of the correct ramp is digitized and inserted into the data stream
10 that includes: a 24 bit counter that goes much more slowly than the ramps in order to have a
11 coarse time measurement, a flag that indicates which ramp has been digitized, an ID of the channel
12 triggered, and the timestamp and charge information.

13 The light readout is fully integrated in the WA105 DAQ scheme. A microTCA crate housing
14 the light-readout digitization cards is naturally integrated into this architecture by taking into
15 account the common time distribution and data transmission systems. During the data-taking
16 outside the beam spills, a trigger that can be generated by the light-readout microTCA crate plus
1 its timestamp can be transmitted over the White Rabbit network similarly to the beam triggers.

2 On the light-readout front-end board there is also an ADC (AD9249 from Analog Devices) that
3 digitizes the PMT charge information on every channel independently. The charge measurement
4 can be correlated with the timing information coming from the PARISROC for better precision
5 on both quantities. A prototype of the light-readout AMC is also being developed by using the
6 Bittware development card S4AM (the same used for the LAr TPC ionization readout develop-
7 ments) and a mezzanine card including the ADC and the trigger circuit (see Figure 5.30). FIG: DAQ LRG

8 The PARISROC chip provides the timestamp at nanosecond precision and generates the trigger.
9 In parallel, an ADC AD9249 continuously digitizes all channels independently at 65 MSPS with
10 14 bits. The FPGA Stratix IV from the Bittware S4AM card controls and programs the ADC
11 and PARISROC. It also receives the data coming from both PARISROC and ADC and controls
12 which information is passed through the network to store for analysis. The charge digitization

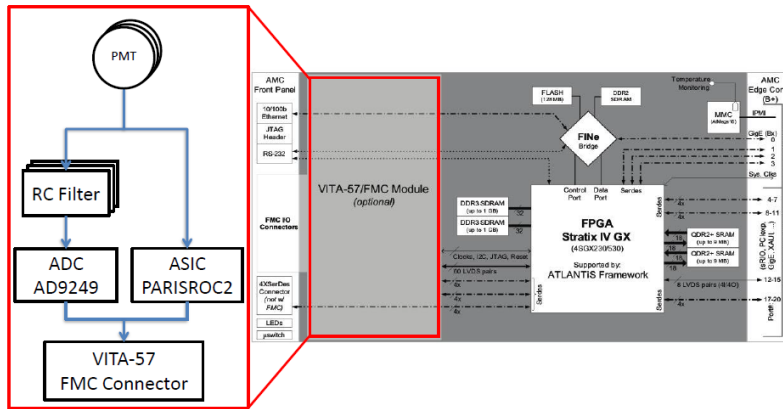


Figure 5.30: Block diagram of the light readout AMC demonstrator

fig:DAQ_

13 of the light signals is performed at 14 bits in samples of 15 ns. Considering a $5\text{-}\mu\text{s}$ light-signal
 14 duration, the digitization will produce more than 300 samples. With this amount of data it is
 15 possible to measure not only the total charge generated but also the shape of the signal and the
 16 long-component decay of the light.

17 With this light readout architecture and the White Rabbit time-distribution system, it is possible
 1 to achieve 1-ns accuracy at the level of trigger generation for the t_0 and timestamping of the events.
 2 This trigger is sent to the general DAQ and the event builder. Since the charge-readout system of
 3 the TPC runs at 2.5 MHz, the minimal time unit in the reconstruction of the drift is 400 ns.

4 5.9 Installation and Commissioning

5 5.9.1 Preparatory Work

6 Before the installation of the detector can begin, a number of preparations must be conducted and
 7 boundary conditions must be met in order to enable a safe and efficient process that minimizes the
 8 manpower required for the underground detector construction. A careful study of the installation
 9 sequence and tools and an optimization of the size and characteristics of the detector elements
 10 has been performed in order to facilitate the installation procedures. Some of the most important
 11 preparation and installation steps are listed in this section. More detailed explanation and figures
 12 are available in Annex 4E: *LAGUNA/LBNO Part 2*.

13 5.9.2 Detector Installation Sequence

14 This installation procedure has been extensively studied in the framework of the LAGUNA-LBNO
 15 design study. A construction sequence for the dual-phase DUNE LArTPC detector module instal-
 16 lation was defined based on the use of a slightly modified scaffolding arrangement with respect to

1 the LBNO design, discussed in Annex 4E: *LAGUNA/LBNO Part 2* (Design: courtesy Technodyne
2 Ltd., Eastleigh, UK). The proposed construction sequence assumes completion of the membrane
3 and insulation system installation together with completion of all tank internal pipework and cable
4 trays. At this stage, sections of the scaffolding will be removed and replaced by the Alimak-Hek or
5 similar climbing access platforms to provide increased functionality to the installation. On com-
6 pletion of the scaffolding revisions and the climbing access platform installation, the entire tank
7 and scaffolding systems will be cleaned in preparation for the detector module installation. The
8 proposed far detector module construction sequence consists of:

- 9 1. Complete installation of insulation & membrane, install cable trays from top to bottom for
10 photomultipliers (PMTs) electrical cables
- 11 2. Adjust scaffolding platforms, add Alimak-Hek platform and floor protection
- 12 3. Air purge top level installation
- 13 4. Install hanging columns for detector
- 14 5. Install lowest field shaping coil to stabilize columns, and then install first top 15 levels of
15 field shaping coils
- 16 6. Thoroughly clean top level assembly
- 17 7. Install Charge Readout (CRP) from top scaffolding platform (detailed sequences described
18 in Annex 4E: *LAGUNA/LBNO Part 2*)
- 19 8. Thoroughly clean top level assembly
- 20 9. Screen off top level to protect Anode (protective screen 1)
- 1 10. Air purge top level (allow bleed air into middle & lower levels)
- 2 11. Continue installing Field shaping coils
- 3 12. Complete installation of Field shaping coils
- 4 13. Thoroughly clean field shaping coils, remove protective screen (screen 1) to top level &
5 progressively remove all scaffolding & Alimak-Hek platforms
- 6 14. Screen off field shaping coils (incl. CRO): protective screen 2
- 7 15. Air purge top & middle levels
- 8 16. Construct Cathode from Modules. Cathode to be raised 300mm off tank bottom during
9 construction
- 10 17. Thoroughly clean cathode & space used for fabrication

- 11 18. Remove protective screen 2
- 12 19. Fit cathode to field cage using suitable jacks
- 13 20. Screen off entire detector: protective screen 3
- 14 21. Remove floor protection
- 15 22. Add cable trays, junction boxes & cables for PMTs
- 16 23. Install PMTs to tank Bottom (pre-assembled L-flanges). Check out & test PMTs
- 17 24. Clean air purge bottom level
- 18 25. Install temporary enclosure around TCO inside & outside with air lock within the enclosure
- 19 26. Remove protective screen (screen 3) using air lock system to prevent contamination of de-
20 tector
- 21 27. Close temporary construction openings
- 22 28. Thoroughly clean TCO areas
- 23 29. Remove temporary enclosures
- 24 30. Remove all tools, equipment etc. through tank roof
- 25 31. Exit via room manways
- 26 32. Close all tank roof openings

27 **5.9.3 Detector construction program and installation schedule**

28 Both the $3 \times 3 \times 1 \text{ m}^3$ prototype detector and the $6 \times 6 \times 6 \text{ m}^3$ WA105 demonstrator are planned to
29 be built in advance of the larger 4×10 -kt modules of the experiment at SURF. It is expected that
30 valuable information will be gathered from the construction of both the prototype and demonstra-
31 tor detectors that will ultimately benefit both the planning and construction forecasting for the
32 larger far detector.

33 For comparison the 20-kt LAr detector for Pyhasalmi was designed for a drift surface (roughly
34 the CRP and cathode area) of 824 m^2 in an octagonal shape with a drift length of 20 m. The
35 dual-phase DUNE LArTPC experiment at SURF has an equivalent area of $12 \times 60 = 720 \text{ m}^2$ (for
36 one module of 12 kt) with a drift length of 12–15 m (fiducial mass 1 kt / 1 m drift, total 12–15 kt).
1 The construction program calculated by Rockplan Ltd, Alan Auld Ltd and Rhyal Eng. Ltd can be
2 seen as a conservative approach for the SURF site, as most of the time corresponds more closely

3 to the instrumented surface required rather than to the drift length, but neither specific SURF
4 site-related effects nor effects of US legal procedure are taken into account in this construction
5 program.

6 The DUNE detector module installation program has been divided into three distinct (and sepa-
7 rate) stages:

- 8 1. Design
- 9 2. Manufacture/Fabrication
- 10 3. Assembly

11 The detector design must be done together with the tank deck design, as the complete detector is
12 suspended from the deck. Fabrication and manufacturing can be started while the tank construc-
13 tion is still on-going. The total time for manufacture/fabrication and construction is calculated to
14 be around six years for a DUNE far detector module, of which:

- 15 • 14 months for manufacture/fabrication off-site
- 16 • 20 months for construction/installation + testing
- 17 • 32 months total works (partially overlap)

Chapter 6

Synergies Between Far Detector Designs

-synergy

6.1 Overview

As discussed in Section [sec:detectors-strategy-FD](#) ??, two technologies for LArTPCs are being pursued. There are a number of synergies between these development efforts.

Both the reference and alternative designs for the DUNE far detector are liquid argon TPCs. The designs assume nearly identical cryostats (with some differences in the cryostat roof), in identical caverns and supported by identical cryogenic systems. The designs differ mostly in their approaches to collection and readout of the ionization signals. In the reference design, the ionization charge is measured by successive wire planes, two induction and one collection, all immersed in the LAr. In the alternative design, the charge is extracted from the liquid to the vapor and then amplified and finally collected on a 2D anode, providing two independent views.

A list of synergies between far detector subsystems designs follows:

- Interface with the cryogenics system
- High voltage
- Photon detection
- Calibration
- Underground installation strategies
- Local computing infrastructure and DAQ
- Detector modeling and simulation

1 6.2 Interface with the Cryogenics System

2 In both designs, ionization electrons have drift lengths on the order of several meters. In order to
3 reach the required millisecond scale for electron lifetime, the electronegative impurities in the LAr
4 must be maintained below the ppb level. The contamination will come primarily from impurities
5 adsorbed onto the tank and detector element surfaces. Given that the detector modules will be
6 housed in cryostats of the same design, using the same industrial LNG cryostat technology and
7 the same cryogenics systems, the process of understanding these sources and minimizing them is
8 to a great extent the same for either TPC design:

- 9 • Electronegative contamination mitigation
- 10 • Modeling contamination sources
- 11 • Contamination migration modeling
- 12 • Material properties
- 13 • Filtration
- 14 • Design of the cryogenics system
- 15 • Purity monitoring
- 16 • Roof interfaces (hatch, feedthrough, mounts)
- 17 • Grounding and Shielding
- 18 • Installation spaces and cryogenics system needs

19 For detecting interactions of beam neutrinos, the requirement for electron lifetime of >3 ms derives
20 from the minimum signal to noise ratio ($S/N > 9$) required for MIP signals on induction plane wires
21 from interactions near the cathode to be above the zero suppression thresholds. Initial studies of
22 energy resolution for supernova physics also requires an electron lifetime above 3 ms. The 3 ms
23 lifetime detector requirement is the same for both the single-phase reference design and the dual-
1 phase alternate design. As the argon purity goal is similar, work on contamination mitigation can
2 be done jointly.

3 There is much experience in the community to justify confidence that high levels of argon purity
4 can be achieved. Careful design of gas ullage and the recirculation system is vital to avoid trapped
5 pockets of gas and to minimize the mixing of the gas and the liquid at the interface. ICARUS
6 achieved a lifetime above 15 ms after modification of the cryosystem to extend the lifecycle of
7 the recirculation pump.[2] The materials test stand (MTS) at Fermilab has demonstrated that
8 contaminants in the liquid argon originate from materials in the gas space in the ullage, where the
9 warmer temperatures allow for outgassing of exposed surfaces and that materials immersed in the
10 liquid argon are not a source of contamination.[?] The MTS has measured the contamination rate

11 for many materials and is available for continued testing of additional materials. The Liquid Argon
12 Purity Demonstrator (LAPD) achieved lifetimes above 14 ms without evacuating the cryostat and
13 with a functioning TPC inside the cryostat.[?]

14 The phase-1 run of the 35-t achieved a peak 3 ms electron lifetime; however, the purity was
15 still improving when the run ended. The engineers and scientists from LBNF and both DUNE
16 detector options will work together to optimize the cryogenic design for high purity. Two examples
17 are understanding the sources of contamination in the ullage and how this contamination migrates
18 to the liquid and developing a fill procedure that preserves the purity of the incoming liquid.
19 There are several membrane cryostats that will be designed and built over the next 10 years by a
20 common engineering team: the $1 \times 1 \times 3$ m³ dual-phase prototype, Short Baseline Neutrino Detector
21 (SBND), WA105, the Single-Phase CERN Prototype (SPCP) engineering prototype as well as the
22 DUNE far detector. Each of these will learn from its predecessors and inform its successors. Based
23 on existing measurements and extrapolations to the 10 kt design a 3 ms lifetime should be readily
24 achievable.

7 6.3 High Voltage

8 Both LArTPC designs require a large HV to produce an electric field of the order of 500 V/cm
9 in the drift volume. They both thus require a HV generator, HV feedthroughs and a field cage to
10 correctly shape the electric field. While these elements differ in the two designs, they present a
11 common set of problems to solve:

- 12 • Design rules for HV
- 13 • HV generation
- 14 • HV Feedthroughs
- 15 • Field cage structure
- 16 • Arc mitigation (Stored energy and discharge)

17 6.4 Photon Detection

18 The approaches to photon detection in the two designs is different. The reference design uses
19 TPB-coated light guides instrumented with SiPMs, whereas the alternate design uses large PMTs
20 (also coated with TPB). Nevertheless, several aspects of and techniques used in the development
21 of these systems have strong synergies:

- 22 • Requirements refinement and validation

- 23 • Development and evaluation of photosensors
- 24 • Impact of background light
- 25 • Surface reflectivity
- 26 • Photon detector calibration

27 **6.5 Detector Calibration**

28 The challenging requirement on systematic uncertainties calls for a robust program of calibration,
29 which may include the use of calibration sources deployed in the detector, complementary external
30 measurements and data-driven calibration procedures. It is expected that this effort will have
31 significant synergies between the two designs:

- 32 • Active volume
- 1 • Energy scale
- 2 • Energy resolution
- 3 • PID likelihoods
- 4 • Absolute light yield

5 **6.6 Underground Installation Strategies**

6 A fundamental aspect of the detector cost optimization is related to the development of a strategy
7 for underground logistics, safety and detector installation. Dimensioning of the components to be
8 transported and assembled underground is a common issue where synergies exist. Strategies for
9 and requirements on implementing the clean rooms, additional tooling and needs for temporary
10 installations, such as scaffolding, also present opportunities for potential synergies.

11 **6.7 Local Computing Infrastructure and DAQ**

12 Once the electrical signals from the detector have been processed (e.g., by frontend preamplifiers),
13 the treatment of the digitized raw data and their compression can be strongly unified and will
14 therefore provide synergies. The online computing farm will have a very similar layout for both
15 reference and alternative designs. The software triggering and filtering algorithms will be based

16 on similar local computing architectures, offering strong synergies. Finally, the local data storage
17 and transmission to offsite tier-centers will be common.

18 **6.8 Detector Modeling and Simulation**

19 Accurate and detailed detector modeling is required. Simulations are needed for both ionization
20 electrons and scintillation photons. The basis of the synergies in this area is the common detection
21 medium of LAr:

- 22 • Charge generation and transport
- 23 • Charge diffusion and attenuation studies
- 24 • Noise and its impact on the detector performance
- 25 • Optical model and light propagation

26 **6.9 Summary**

27 A large set of possible synergies exists between the reference and alternative TPC designs. These
28 synergies will be exploited and developed within the DUNE Collaboration and the LBNF team as
29 the program of prototypes, demonstrators and other development activities continues and as the
30 detector modules and the accompanying facilities are constructed. The CERN neutrino platform,
31 in particular, will provide an excellent opportunity for joint detector development.

Chapter 7

Near Detector Reference Design

7.1 Overview

This chapter describes the reference design of the DUNE Near Detector Systems (NDS). The scope includes the design, procurement, fabrication, testing, delivery and installation of the NDS components:

- Fine-Grained Tracker (FGT) near neutrino detector (NND)
- Beamline Measurement System (BLM)
- NDS Data Acquisition system (DAQ)

Detailed descriptions of the NDS subsystems are provided in Annex 4G: *DUNE Near Detector Reference Design*.

The concept and design of the reference DUNE-ND evolved from experience with MINOS, the first generation long-baseline neutrino experiment at Fermilab, NOvA, the second generation experiment, the high resolution NOMAD detector at CERN and the T2K detector at JPARC. MINOS and NOvA employ functionally ‘identical’ detectors which fulfill the mission of these experiments, given the statistics and resolution of the respective far detectors. DUNE, the third generation experiment at Fermilab, has more ambitious goals: discovery of CP-violation, discovery of mass hierarchy, and a search for physics beyond PMNS with unparalleled precision. DUNE will have a more intense neutrino source and a higher resolution massive far detector. To meet the ultimate systematic precision needed to fulfill these goals, the ND must thoroughly characterize the beam composed of muon neutrinos/antineutrinos and electron neutrinos/antineutrinos. It must precisely measure the cross-sections and particle-yields of various neutrino processes. The particle-yields include multiplicity and momentum distributions of pions, kaons and protons produced in the hadronic jet.

17 The need to precisely quantify the neutrino source and cross-sections, including the hadronic com-
18 position, motivates a high resolution ND. The NOMAD experience suggests that a high resolution
19 detector, capable of measuring e^\pm , μ^\pm , π^{-+0} , proton and K^0 , would partially meet the challenges of
20 DUNE — the detector must be augmented to measure, and thereby precisely model, the neutrino-
21 nuclear effects. The reference DUNE-ND is a next generation near-detector concept compared
22 to the T2K experiment. Such a detector will enrich the physics potential of the DUNE/LBNF
23 program. Complementary LAr-detector(s) upstream of the high resolution ND will enhance the
24 capability of the ND complex.

25 The reference DUNE-ND, a Fine-Grained Tracker (FGT), consists of a straw-tube tracking detector
26 (STT) and electromagnetic calorimeter (ECAL) inside of a 0.4-T dipole magnet. In addition, Muon
27 Identifiers (MuIDs) are located in the magnet steel, as well as upstream and downstream of the
28 STT. The FGT is designed to make precision measurements of the neutrino flux, cross section,
29 signal and background rate at the percent level.

30 The Beamline Measurement System (BLM) will be located in the region of the Absorber Complex
31 at the downstream end of the decay region to measure the muon flux from hadron decay. The
32 absorber itself is part of the LBNF Beamline. The BLM will determine the neutrino flux and
33 spectra and monitor the beam profile on a spill-by-spill basis, and will operate for the life of the
34 experiment.

35 The Near Detector System Data Acquisition system (NDS-DAQ) collects raw data from each NDS
36 DAQ, issues triggers, adds precision timing data from a global positioning system (GPS) and builds
37 events. The NDS-DAQ is made up of three parts: NDS Master DAQ (NDS-MDAQ), Beamline
38 Measurements DAQ (BLM-DAQ) and Near Neutrino Detector DAQ (NND-DAQ).

39 7.2 The Fine-Grained Tracker

1 The scope of the DUNE Fine-Grained Tracker (FGT) near neutrino detector includes the design,
2 procurement, fabrication, testing, delivery and installation of all FGT subsystems:

- 3 • Central straw-tube tracker (STT)
- 4 • Electromagnetic calorimeter (ECAL)
- 5 • Dipole magnet (0.4-T) surrounding the STT and ECAL
- 6 • Muon identifiers (MuID): in the magnet steel and upstream/downstream of the STT
- 7 • Instrumentation for monitoring and control

8 A schematic drawing of the FGT design is shown in Figure [7.1](#). fig:STT_schematic

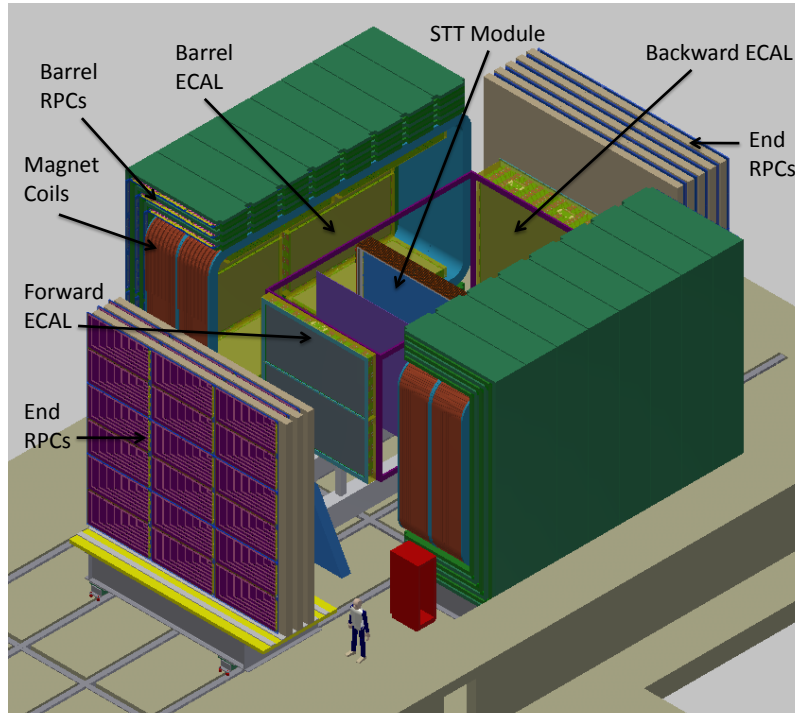


Figure 7.1: A schematic drawing of the fine-grained tracker design.

fig:STT

9 The design presented here meets the required performance for making precision measurements
 10 of neutrino fluxes, cross sections, signal and background rates for the DUNE far detector. The
 11 DUNE ND is designed to fulfill the physics program described in Chapter 6 of CDR Volume 2:
 12 *The Physics Program for DUNE at LBNF* Report [31]. The most significant requirements [32, 33]
 13 for the FGT include:

- 14 • Muon energy scale uncertainty better than 0.2% and hadronic energy scale uncertainty better
 15 than 0.5% for the low- ν flux measurements
- 16 • Magnetized detector capable of separating μ^+ from μ^- as well as h^+ from h^- , where h is a
 17 charged hadron
- 18 • Capability to to separate e^+ from e^- for absolute and relative flux measurements
- 19 • Excellent momentum (<5%) and angular (< 2 mrad) resolutions for μ^\pm , e^\pm , π^\pm and proton,
 20 and π^0/γ via decay/conversion and K_S^0/Λ produced in ν -induced interactions.
- 21 • 4π ECAL coverage to ensure accurate determination of the momentum vector of the hadronic
 22 shower
- 23 • 4π MuID coverage to identify muons with a wide range of energies and angles

- 24 • Electron/positron identification through the use of transition radiation (TR) in the entire
25 tracking detector for low-energy and/or large angle tracks (e.g. γ conversions)
- 26 • $\pi/K/p$ identification by dE/dx in the entire tracking detector
- 27 • Identification of π^0 and γ that can mimic ν_e signals at the far detector
- 28 • Use of a variety of nuclear targets, $(C_3H_6)_n$, Ar, Ca, C, Fe, etc., to quantify the impact of
29 nuclear effects in $\nu(\bar{\nu})$ -nucleus cross sections
- 30 • Provide more than 10 times the unoscillated statistics on Ar targets expected in a 40-kt far
31 detector

32 The requirements listed above imply the use of a low density, $\rho \sim 0.1 \text{ g/cm}^3$, high-resolution mag-
1 netic spectrometer. A summary of the performance requirements is given in Table 7.1 Regardless
2 of the process under study, the goal is to have the systematic error less than the corresponding
3 statistical error.

Table 7.1: A summary of the performance for the FGT configuration

Performance Metric	FGT
Dipole magnetic field	0.4 T
Average target/tracker density	$\rho \sim 0.1 \text{ g/cm}^3$
Target/tracker Volume	3.5m x 3.5m x 6.4m
Target/tracker Mass	8 t
Vertex Resolution	0.1 mm
Angular Resolution	2 mrad
E_e Resolution	5%
E_μ Resolution	5%
$\nu_\mu/\bar{\nu}_\mu$ ID	Yes
$\nu_e/\bar{\nu}_e$ ID	Yes
NC π^0 /CCe Rejection	0.1%
NC γ /CCe Rejection	0.2%
CC μ /CCe Rejection	0.01%

7.2.1 Straw-Tube Tracking Detector

Straw Tubes

6 The Straw-Tube Tracking Detector (STT) at the center of the FGT is composed of straw tubes
7 with an outer diameter of 1 cm, as well as radiators and targets that reside next to the straw tubes
8 as shown in Figure 7.2.

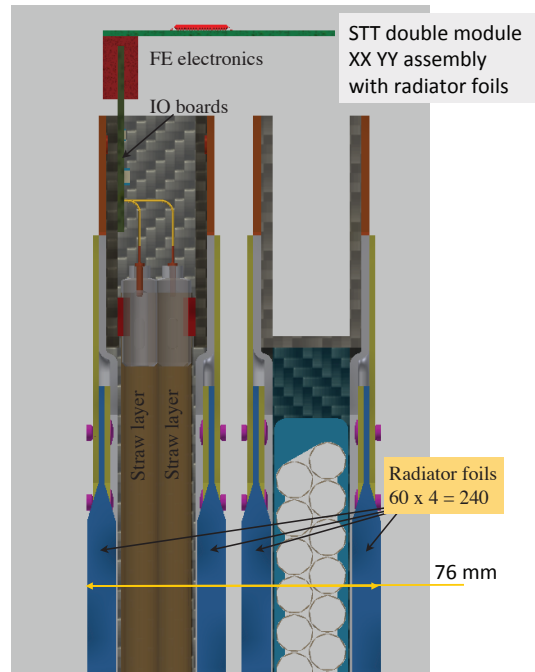


Figure 7.2: A schematic drawing of the Straw-Tube Tracking Detector (STT) design.

fig:STT_

9 The straw walls are made by winding together a film of carbon loaded Kapton XC (inner) and a
 10 film of aluminum coated Kapton HN (outer), for a total thickness of about $70 \mu\text{m}$. The anode wire
 11 is gold-plated tungsten with $20 \mu\text{m}$ diameter. Two consecutive layers of straws are staggered by a
 12 half-diameter, glued, and inserted into a carbon-fiber composite mechanical frame to form a single
 13 module. One vertical (YY) and one horizontal (XX) module are then assembled together to form
 14 a double-module (XXYY) equipped with frontend electronic readout boards. Figure 7.2 shows a
 15 schematic drawing of the STT module with four straw-tube planes and radiators. Each XXYY
 16 module equipped with radiators is equivalent to $1.45 \times 10^{-2} X_0$ ($0.2 \times 10^{-2} X_0$ without radiators),
 17 with a radiation length $X_0 \sim 5.5 \text{ m}$. The momentum measurement requires that tracks are detected
 18 in at least six straw layers. The staggered double layer design, high number of straw planes and
 19 double-end readout will contribute to resolving short track disambiguation.

20 The straw tubes will be filled with a gas mixture of either 70% Ar plus 30% CO_2 (for modules
 21 with nuclear targets) or 70% Xe plus 30% CO_2 (for modules with radiators). The dimensions
 22 of each double module in the reference design will be approximately $350 \text{ cm} \times 350 \text{ cm} \times 8.0 \text{ cm}$,
 23 including a nuclear target or four radiator planes and four straw planes. For ease of construction
 24 and transportation, each double module is made up of two modules, with two straw layers and
 25 dimensions of approximately $350 \text{ cm} \times 175 \text{ cm} \times 4.0 \text{ cm}$. Each module will have a carbon composite
 26 frame around the perimeter for support and will have an attached target or radiator.

27 The modularity of the STT provides for successive measurements using thin nuclear targets (thick-
 28 ness $< 0.1 X_0$), while the excellent angular and spatial resolution allows a clean separation of events
 29 originating in different target materials.

30 The STT will have a total of 107,520 straws — corresponding to 336 straws per plane, 1344 straws
 31 per module — and 80 modules. Both ends of the straw tubes will be read out, leading to a

- 1 total number of 215,040 electronics channels. The total mass of the STT, including targets and
 2 radiators, is approximately 8 t. Table 7.2 summarizes the main STT parameters.

Table 7.2: Straw Tube Tracker specifications

Item	Specification
Straw Tube Geometry	1 cm Diameter x 3.5 m Long
Number of Straw Tubes	107,520
Number of Straw Tubes per Plane	336
Number of Straw Tube Planes per Module	4
Number of Straw Tube Sub-Modules per Module	4
Number of Straw Tube Modules	80
Number of Straw Tube Sub-Modules	320
Length of Straw Tube Wire	376.3 km
Number of Electronics Channels	215,040
Number of Modules with Radiators	75
Radiator Thickness per Module	3.6 cm
Radiator Mass per Module	69.1 kg
Number of Modules with Nuclear Targets	10
C Mass per Target Plane	192 kg
Number of Modules with C Target Planes	2
Ca Mass per Target Plane	132 kg
Number of Modules with Ca Target Planes	1
Ar Target Geometry	5.08 cm Diameter x 3.5 m long
Number of Ar Targets per Plane	68
Ar Mass per Target Plane	112 kg
Number of Modules with Ar Target Planes	1
Fe Mass per Target Plane	96.5 kg
Number of Modules with Fe Target Planes	1

- 3 In addition to tracking charged particles and measuring Transition Radiation (TR), the STT
 4 provides dE/dx measurement to identify particles. Figure 7.3 provides a sample of pions, kaons
 5 and protons identified via dE/dx in the STT.

6 Radiator Targets

- 7 Radiators will be placed in the downstream STT modules and will serve as targets for both neutrino
 8 interactions and Transition Radiation (TR) production. Each STT module contains four radiators,
 9 where each radiator consists of 60 layers of 25- μm polypropylene (C_3H_6)_n foils, which are embossed
 10 to keep 125- μm air gaps between consecutive foils. The mass of each radiator is ~ 17 kg and the
 11 thickness is ~ 9 mm. The use of thin plastic foils regularly spaced allows the emission of transition
 12 radiation for electron/positron identification, which is detected by the Xe gas in the straws. The
 13 plastic radiators account for about 83% of the mass of each STT module and also provide the main

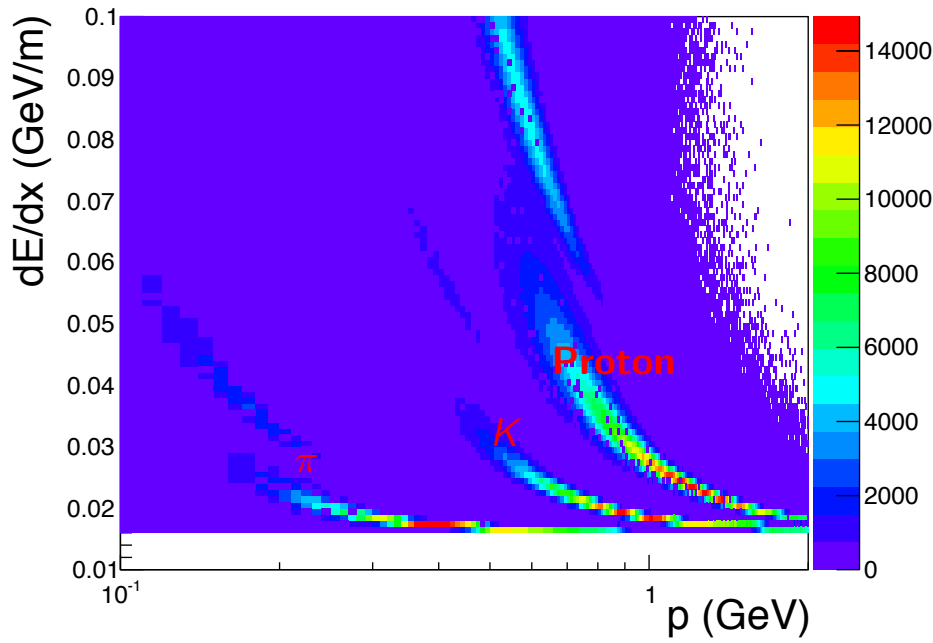


Figure 7.3: Simulated distributions of dE/dx for different particles in FGT.

fig:Part

14 (anti)neutrino target. Overall, a radiator mass of about 5 tons is required to achieve the physics
 15 sensitivity discussed in Chapter 6 of CDR Volume 2: *The Physics Program for DUNE at LBNF*
 16 and the DAE/DST Detailed Project Report[31].

17 Nuclear Targets

18 A set of different nuclear targets will be installed in front of the most upstream STT modules,
 19 which will not be equipped with radiators. The most important nuclear target is the argon target
 20 that matches the DUNE far detector. This target will consist of planes of cylindrical tubes filled
 21 with argon gas pressurized to 140 atm ($\rho = 0.233$), with sufficient Ar mass to provide ~ 10 times
 22 the unoscillated statistics expected in a 40 kt far detector. The proof of concept design consisted
 23 of 0.5-inch diameter, 3.5-m-long stainless steel tubes, with wall thickness 0.065-inch. In order to
 24 minimize the mass of the tube walls, we are investigating the use of a single plane of C-composite
 25 tubes with 2-inch diameter and a wall thickness of 0.04-inch.

26 Relevant to argon, a crucial target is calcium which has the same atomic weight ($A = 40$) as argon
 27 but is isoscalar. Since most nuclear effects depend on the atomic weight A , inclusive properties
 28 of (anti)neutrino interactions are expected to be the same for these two targets. This fact will
 29 allow the use of both targets to model signal and backgrounds in the DUNE far detector (argon
 30 target), as well as to compare DUNE results for nuclear effects on argon with the extensive data
 31 on calcium from charged lepton scattering.

32 An equally important nuclear target is carbon (graphite), which is essential in order to get
 33 (anti)neutrino interactions on free proton, through a statistical subtraction procedure from the
 34 main polypropylene target (C_3H_6)_n. The availability of such a free-proton target will allow accu-

rate flux determinations and cross section measurements, and, for the first time, a direct model-independent measurement of nuclear effects — including both the primary and final-state interactions — on the argon target relevant for the far detector oscillation analysis. The required carbon target mass is about 0.5 t (in addition to the carbon in the STT frames). The corresponding expected number of events on H target are $5.0(1.5) \times 10^6 \pm 13(6.6) \times 10^3 \nu(\bar{\nu})$ CC, where the uncertainty is dominated by the subtraction procedure.

A stainless steel target in the form of a single thin slab will provide service measurements of (anti)neutrino cross-sections for the INO experiment in India.

Finally, cylindrical tubes similar to those used for the pressurized Ar gas can be filled with standard and heavy water (H_2O and D_2O). The statistical subtraction of H_2O from D_2O will result in a quasi-free neutron.

Table [7.2](#) gives a reference configuration of the radiators and nuclear targets, listed according to their location from downstream to upstream. The final configuration of the nuclear targets will require detailed Geant4 simulations of FGT and corresponding physics sensitivity studies.

7.2.2 Electromagnetic Calorimeter

An electromagnetic calorimeter (ECAL) will surround the tracking volume on all sides and consist of three separate pieces: Forward ECAL, Barrel ECAL and Backward ECAL. The expected energy resolution is $\sim 6\%/\sqrt{E}$ for the forward ECAL. The ECAL must provide high segmentation in both the transverse and longitudinal directions to reconstruct photons from π^0 decay and electron/positrons from their Bremsstrahlung emissions. The ECAL conceptual design consists of layers of either 1.75-mm-thick (for the forward ECAL) or 3.5-mm-thick (for the barrel and backward ECAL) lead sheets and 2.5-cm-wide by 10-mm-thick plastic scintillator bars, as shown in Figure [7.4](#).

The scintillator layers for the Forward and Backward ECAL alternate as XYXYXY..., while the scintillator layers for the Barrel ECAL are all horizontal along the axis of the magnet. The Forward ECAL will consist of 60 layers of scintillator bars, where each bar has dimensions $3.2 \text{ m} \times 2.5 \text{ cm} \times 1 \text{ cm}$. The Backward ECAL will consist of 16 layers of scintillator bars, where each bar has the same dimensions, $3.2 \text{ m} \times 2.5 \text{ cm} \times 1 \text{ cm}$. The Barrel ECAL will also consist of 16 layers of scintillator bars, where each bar has the same dimensions, $3.2 \text{ m} \times 2.5 \text{ cm} \times 1 \text{ cm}$. The parameters of the ECAL design will be further optimized with the help of a full Geant simulation of FGT.

The lead sheets and scintillator bars will be assembled and glued together into complete modules of dimension $3.2 \text{ m} \times 3.2 \text{ cm} \times 81 \text{ cm}$ for the Forward ECAL and $3.2 \text{ m} \times 3.2 \text{ cm} \times 27.5 \text{ cm}$ for the Backward ECAL. For the Barrel ECAL, the module dimensions will also be $3.2 \text{ m} \times 3.2 \text{ cm} \times 27.5 \text{ cm}$. Two Barrel modules are placed end-to-end along the sides of the inner surface of the magnet (eight Barrel modules total) to provide full coverage of the barrel region. The total numbers of scintillator bars in the Forward (7680), Backward (2048) and Barrel ECAL (16384) is 26112 bars.

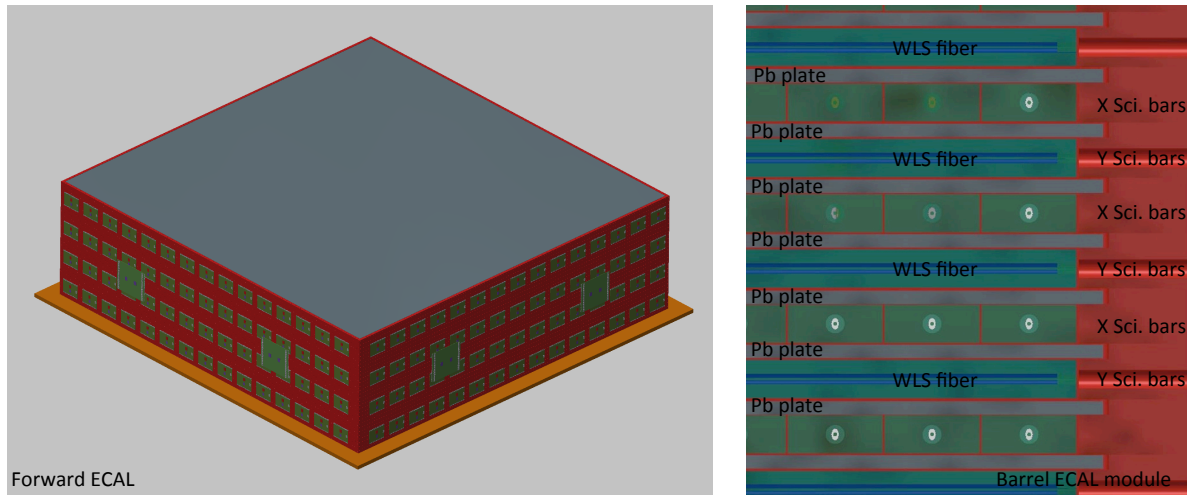


Figure 7.4: Schematic drawing of the forward ECAL equipped with the front-end and back-end readout boards (left), and a cross-section of one barrel ECAL module (right), showing the details of the assembly of alternating planes of plastic scintillator and Pb sheets.

fig:ECAL

6 The scintillator bars will be extruded with holes in the middle of each bar. The holes will then
 7 be fitted with 1-mm-diameter Kuraray wavelength-shifting (WLS) fibers. The fibers will be read
 8 out by SiPM (silicon photomultiplier) photosensors at each end. Detailed R&D studies will be
 9 performed to optimize the diameter of the scintillator hole, the fiber diameter and the proper
 10 coupling between the scintillator and the fiber for optimum light transmission.

11 The total mass of scintillator is 20.9 t, the total mass of Pb is 70.8 t, and the total number of
 12 readout channels is 52,224. Table 7.3 summarizes the specifications of the ECAL.

tab:ECAL specs

13 7.2.3 Dipole Magnet

14 The STT and ECAL modules reside inside a 0.4-T dipole magnet for the measurement of particle
 15 momentum and charge. The magnet will have inner dimensions (inside the coils) 4.5-m wide \times 4.5-
 16 m high \times 8.0-m long. The magnet has four vertical copper coils, stacked horizontally, producing a
 17 horizontal magnetic field. The return yoke will be divided into two halves along the longitudinal
 18 center line to allow the magnet to be opened to service the detector inside. shown in Figure 7.1.
 19 Each half yoke will be built from eight “C” (C-shaped) sections, and the thickness of the magnet
 20 steel will be 60 cm, consisting of 6 \times 10-cm-thick plates. The magnet power requirement with
 21 copper coils is \sim 2.4 MW, corresponding to 6 kA at 400 V. The water flow required for cooling is
 22 20 l/s. Figure 7.5 shows the B field results obtained from detailed simulations performed at the
 23 Bhabha Atomic Research Center (BARC) in India.

fig:STT schema

fig:Magnet Bfield

24 The magnet specifications are summarized in Table 7.4.

tab:Magnet specs

25 The momentum resolution is dominated by multiple scattering in the STT. The momentum reso-
 26 lution is, therefore, given by $\delta p/p = 0.053/\sqrt{(LX_0)B}$. For $B = 0.4\text{T}$, $L = 3\text{m}$, and $X_0 = 4\text{m}$, the

Table 7.3: ECAL specifications

Item	Specification
Scintillator Bar Geometry	3.2m × 2.5cm × 1cm
Number of Forward ECAL Scintillator Bars	7680
Forward ECAL Pb thickness	1.75mm
Number of Forward ECAL Layers	60
Number of Forward ECAL Radiation Lengths	20
Dimensions of Forward ECAL Module	3.2m × 3.2m × 81cm
Number of Barrel ECAL Scintillator Bars	16,384
Barrel ECAL Pb thickness	3.5mm
Number of Barrel ECAL Layers	16
Number of Barrel ECAL Radiation Lengths	10
Number of Barrel ECAL Modules	8
Dimensions of Barrel ECAL Modules	3.2m × 3.2m × 27.5cm
Number of Backward ECAL Scintillator Bars	2048
Backward ECAL Pb thickness	3.5mm
Number of Backward ECAL Layers	16
Number of Backward ECAL Radiation Lengths	10
Dimensions of Backward ECAL Module	3.2m × 3.2m × 27.5cm
Total Length of 1-mm Diameter WLS Fiber	83.6km
Total Number of Scintillator Bars	26,112
Total Number of Electronics Channels	52,224
Total Mass of Scintillator	20,890 kg
Total Mass of Pb	70,800kg

AL_specs

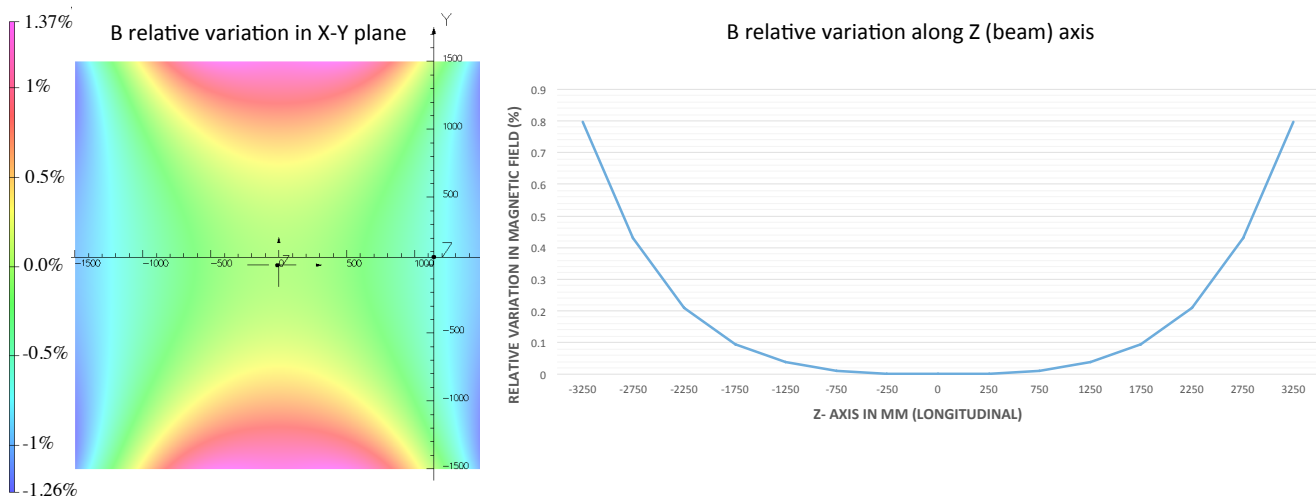


Figure 7.5: Results from the detailed simulations of the magnetic field in the dipole magnet performed at the Bhabha Atomic Research Center (BARC) in India. The plots show the deviations (in percentage) from the nominal field in the (X,Y) plane (left plot) and along the beam axis (right plot).

fig:Magn

Table 7.4: Dipole Magnet specifications

Item	Specification
Inner Dimensions	4.5 m × 4.5 m × 8.0 m
Magnetic Field	0.4 T
Number of "C" Sections	16
Thickness of Steel in the "C" Sections	60 cm
Mass per "C" Section	60 t
Number of Coils	4
Mass per Coil	40 t
Magnet Current	6 kA
Magnet Voltage	400 V
Magnet Power Requirements	2.4 MW
Water Flow for Cooling	20 l/s

27 expected momentum resolution is $\sim 3.8\%$.

28 7.2.4 Muon Identifier

29 The sides and ends of the dipole magnet will be instrumented with a muon identifier detector
 30 (MuID) that will distinguish muons from hadrons by the ability of muons to penetrate the iron
 31 without showering or interacting. The task of the MuID is to reconstruct the muon track segments
 32 and match them with the corresponding charged track reconstructed in the STT. The MuID will
 33 consist of 432 resistive plate chamber (RPC) modules interspersed between two 10-cm-thick steel
 1 plates of the dipole magnet and between 20-cm-thick steel plates at the upstream and downstream
 2 ends of the magnet as is detailed in Table 7.5.

3 The choice of RPC is motivated by the combination of low cost, ability to reach sub-mm space
 4 resolution, and existing expertise. The MuID is only meant to provide identification of the muon;
 5 the muon momentum will be measured by the STT inside the magnetic field.

6 The nominal dimensions of all RPC modules will be 1 m × 2 m with active areas of 96 cm × 196 cm.
 7 Each module has 256 X strips at 7.65-mm pitch and 128 Y strips at 7.5-mm pitch. This fine-grained
 8 pitch allows to reach spatial resolution of ~ 0.7 mm and to disentangle multiple hits resulting from
 9 events originated in the magnet iron. The modules will be grouped into trays, each containing six
 10 modules, and the trays will be sufficiently wide to allow overlapping modules. The downstream
 11 MuID will contain five steel planes of overall dimensions $6 \times 6 \times 0.2$ m³ (283.5 t) and five RPC planes,
 12 while the upstream MuID will contain three steel planes (170.1 t) of dimensions $6 \times 6 \times 0.2$ m³ and
 13 three RPC planes. The barrel MuID will contain 24 planes (three layers × eight sides) of RPCs.
 14 The RPCs will have a total thickness of 15 mm and a gap width of 2 mm. One possible gas mixture
 15 could be Ar (75%), tetrafluoroethane (20%), isobutane (4%) and sulphurhexafluoride (1%). A full
 16 scale prototype of the RPC modules was built at the Variable Energy Cyclotron Centre (VECC) in
 17 India. Figure 7.6 shows a picture taken during the assembly of the prototype and the corresponding

Table 7.5: MuID specifications

Item	Specification
Number of Barrel RPC Trays of Dimension 2.2 m × 4 m	8
Number of Barrel RPC Trays of Dimension 2.5 m × 4 m	16
Number of Barrel RPC Trays of Dimension 2.8 m × 4 m	16
Number of Barrel RPC Trays of Dimension 3.1 m × 4 m	8
Number of END RPC Trays of Dimension 2 m × 6 m	24
Total Number of RPC Trays	72
Total Number of RPC Modules	432
Mass of Downstream Steel Planes	283,500 kg
Mass of Upstream Steel Planes	170,100 kg
RPC Thickness	1.5 cm
Number of 7.65mm Pitch X Strips per Module	256
Number of 7.5mm Pitch Y Strips per Module	128
Total Number of RPC Strips and Electronics	165,888

18 efficiency measurement with a cosmic ray telescope.

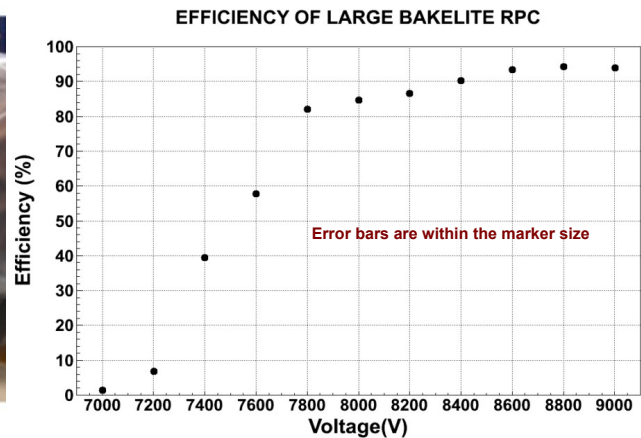


Figure 7.6: Fabrication of a large (2.4 m×1.2 m) RPC prototype at the Variable Energy Cyclotron Centre (VECC) in India (left) and corresponding efficiency tests (right).

fig:FGT_

7.2.5 Instrumentation

19 The instrumentation includes both fast readout electronics for the subdetectors and slow control
 20 of the subdetectors, involving monitoring the humidity, temperature, gas pressure, etc. There is
 21 considerable synergy in the information gathered in the STT, ECAL and MuID. Both the STT
 22 and ECAL are required to measure the total charge and the time associated with a given hit.
 23 The MuID RPCs are required to provide the position and time associated with a traversing track.
 24 Similarly, the slow control of the subdetectors share many features.
 25

26 The electronics for the three subsystems, STT, MuID, and ECAL, are all “fast” systems, i.e., all
 27 of the signals are in the few-to-10 nanosecond range. The requirements for each system are very
 1 similar: a fast output and both an ADC and a TDC on each channel. Additionally, for the STT
 2 straw tubes it is desirable to wave-form digitize the analog signal in order to enhance the ability
 3 to separate the ionization signal from the transition radiation signal. The total channel count in
 4 FGT is 433,152 channels, as shown in Table 7.6.

Table 7.6: The number of electronics channels for each of the three detector systems

Detector	# of Channels
STT	215,040
ECAL	52,224
MuID	165,888

5 Recently, an interesting new ASIC development for an upgrade to the ATLAS muon system at the
 6 LHC has come out of BNL), the VMM2 chip. It handles 64 channels and produces both fast ADC
 7 and TDC outputs. It has been fabricated and tested and should be ready by 2017, long before it
 8 will be needed for DUNE.

9 To maintain a low level of humidity and to maintain a desired temperature, both STT and ECAL
 10 subdetectors will have dry nitrogen circulating within their outer layers. Magnet coils are cooled
 11 by water, while the magnet yokes are instrumented with RPCs that must remain dry. Continuous
 12 control of humidity in all these detectors is needed. Temperature must also be continuously
 13 monitored in all of the subdetectors in order for the electronics to not overheat. Also, all power
 14 sources instrumenting the FGT and its readout need to be monitored for appropriate voltage and
 15 current.

16 Gas leaks need to be monitored in the STT and MuID. The STT will employ Xe gas, which helps
 1 with the measurement of transition radiation. Xe gas is expensive and, hence, will be recirculated;
 2 leak-monitoring is particularly important here. The requirement on leaks is less stringent for the
 3 RPCs, which have less expensive gas.

4 The water flow (pressure gradient) will be continuously monitored in order to ensure that the
 5 magnet does not overheat.

6 7.3 Matching the ND Requirements for DUNE/LBNF

7 The scope of this section addresses how the reference NND described in Section 7.2 meets
 8 the requirements of the oscillation studies described in Section 3.8.2 of Volume 2: *The Physics*
 9 *Program for DUNE at LBNF* and the short baseline precision measurements described in Sections
 10 6.1.2 and 6.1.3 of Volume 2: *The Physics Program for DUNE at LBNF*. First, we present the
 11 oscillation related systematics; the systematics affecting the precision measurements and new-
 12 physics search program follows.

7.3.1 Oscillation Analyses

The Table 3.8 in Section 3.6.2 of Volume 2: *The Physics Program for DUNE at LBNF* presents a conservative projection of systematic errors affecting ν_e appearance. The FGT measurement alleviates the systematic errors as enumerated below:

- **Beam ν_e :** The FGT will offer an event-by-event measurement of the beam ν_e via the identification of the emergent e^- in STT while rejecting the $\pi^0 \rightarrow \gamma \rightarrow e$ background via the determination of the missing- P_T vector to a high degree. In a 5-year neutrino-run (focus-positive) the FGT will accumulate 500,000 ν_e with $\simeq 55\%$ efficiency and $\geq 95\%$ purity. The resulting ν_e/ν_μ ratio will be determined to $\leq 1\%$ precision. Furthermore, by constraining the sources of ν_e (μ^+ , K^+ and K_L^0), the FGT will predict the the ratio of ν_e and ν_μ spectra at the far detector (FD) with respect to the near detector (ND) as a function of the neutrino energy, FD/ND (E_ν).
- **Beam $\bar{\nu}_e$:** Although the FD does not distinguish ν_e from $\bar{\nu}_e$, the FGT will accurately measure the beam $\bar{\nu}_e$ by identifying the emergent e^+ in the STT with efficiency and purity similar to those for ν_e . (We point out that the dominant kaonic source of $\bar{\nu}_e$ is K_L^0 ; the neutrino spectra from K_L^0 are different from those of K^+ at the FD.) In a 5-year neutrino-run, the FGT will accumulate 40,000 $\bar{\nu}_e$ and 5×10^6 $\bar{\nu}_\mu$ samples, providing a precise FD/ND prediction for the antineutrino to $\simeq 1\%$. These constraints will be even more valuable during the antineutrino run (focus-negative) where the wrong-sign backgrounds are larger.
- **Cross Sections:** First, the FGT will measure the absolute flux, via ν -e scattering, to $\simeq 2.5\%$ precision. Second, using radiator targets, the FGT will measure exclusive channels, such as quasi-elastic, resonance, coherent-mesons and the inclusive DIS channel with unparalleled precision. Since Argon is the far detector nuclear target, a set of various nuclear targets will allow translation of the cross-section measurements to ν -Ar scattering.
- **Nuclear Effects:** The FGT will employ a suite of nuclear targets including Ar-gas in pressurized tubes, a thin solid calcium target (which has the same A=40 as Ar), a C-target, etc. Specifically, the number of ν -Ar interaction will be 10 times larger than that expected in a 40 kt FD, without oscillations. Additionally, comparisons of calculations of elastic and inelastic interactions in Ar versus Ca, including FSI effects, indicate negligible differences between the two targets. Thus, the combination of the Ar and Ca targets will provide a strong constraint on the nuclear effects from both initial and final state interactions. Finally, FGT's ability to isolate ν ($\bar{\nu}$) off free-hydrogen, via subtraction of hydrocarbon and carbon targets, will provide a *model-independent* measurement of nuclear effects.
- **Hadronization:** A notable strength of FGT is to identify the yield of π^0 *separately* in neutral-current (NC) and charged-current (CC) interactions. (The estimated π^0 detection efficiency is $\simeq 50\%$.) In addition, FGT will determine the yields of π^- and π^+ , the dominant backgrounds to the ν_μ and $\bar{\nu}_\mu$ disappearance. Finally, the measurement of the composition, energy, and angle of the hadronic jet will provide a tight constraint on the overall hadronization models.

- Energy Scale:** The average density of about 0.1 g/cm^3 (close to that of liquid hydrogen) makes the STT mostly transparent to secondary particles — the entire STT length is equivalent to $\sim 1.4X_0$ including the various nuclear targets. As a result we will be able to measure accurately the 4-momenta of secondary particles as well as the missing- P_T vector in the CC processes. This redundant missing- P_T vector measurement provides a most important constraint on the neutrino and antineutrino energy scales. The capabilities of this kinematic analysis have been demonstrated by the NOMAD experiment (with similar density and B field). In addition, measurements of exclusive topologies like quasi-elastic, resonance and coherent meson production offer additional constraints on the nuclear effects affecting the neutrino energy scale (see Section 6.1.2 of Volume 2: *The Physics Program for DUNE at LBNF*). The requirements on the muon energy scale ($<0.2\%$) and total hadron energy scale ($<0.5\%$) uncertainties have been already achieved by the NOMAD experiment. The muon energy scale is calibrated with the mass constraint from the K^0 reconstructed in STT and was statistics limited in NOMAD. The total hadron energy scale is calibrated using the y_{Bj} distribution in different energy bins. Compared to NOMAD, FGT will have $\times 100$ higher statistics and $\times 10$ higher granularity.

In summary the FGT will accurately quantify all four neutrino species and predict the ratio FD/ND for them. It will measure the 4-momenta of the outgoing hadrons composing the hadronic jets in a variety of nuclear targets, in essence proving a data-driven ‘event generator’ which can be applied to the FD.

Since the FGT is based upon a different technology than the FD, it cannot account for effects of LAr reconstruction inefficiencies in the FD. The corresponding cancellation could be achieved only with an identical ND, which to some extent is an ill-defined concept due to a number of factors including size, beam profile and composition, rates etc. However, given the detailed program to calibrate LAr-detectors in test beams and multiple neutrino experiments employing LAr detectors, by the time DUNE becomes operational the reconstruction of particles in LAr will likely be well understood. Finally in Section 7.4 we outline the enhancement of the ND complex by placing complementary LAr-detector(s) upstream of the FGT.

7.3.2 Short Baseline Precision Measurements and Searches

Sections 6.1.2 and 6.1.3 of Volume 2: *The Physics Program for DUNE at LBNF* summarize a rich physics program at the near site providing a generational advance in precision measurements and sensitive searches. This short-baseline physics program and the long-baseline oscillation analyses share similar detector requirements and offer a deep synergy and mutual feedback. The reference FGT meets the requirements of the short-baseline studies as briefly outlined below:

- Resolution:** The FGT is designed to have an order of magnitude higher granularity than NOMAD, the most precise, high statistics neutrino experiment. The corresponding improvements include better tracking, electron/positron ID through TR, dE/dx measurement providing hadron-ID, 4π calorimetry, 4π muon coverage and a larger transverse area for event containment.

- **Statistics:** The 1.2 MW neutrino source at LBNF will offer a factor of 100 enhancement in statistics compared to NOMAD. The program of measuring ν and $\bar{\nu}$ interactions in a set of nuclear targets, including Ar and H, will enhance the physics potential of precision measurements and searches.

Adams:2013qkq, DPR

Sensitivity studies to the salient precision measurements and searches can be found in [34, 31].

7.3.3 Future Tasks to Quantify the Systematic Errors

We need to undertake three outstanding tasks to quantify the systematic errors in oscillation studies and precision measurement program:

- **Geant4 Simulation:** A Geant4 simulation of the FGT is needed to confirm and correct the projected systematic errors and the salient sensitivity studies.
- **Event Reconstruction:** A program to reconstruct tracks in STT and to match the information from different sub-detectors to identify secondary particles.
- **Translating ND-Measurements to FD:** A concerted effort needs to be mounted to transfer the precision measurements in ND to the LAr-FD.

The DUNE collaboration plan to pursue these issues with high priority in the coming years before CD-2.

7.4 Addition of a Liquid Argon Detector to the NND

The reference FGT ND design concept is not identical to the far detector and it is not possible to ‘cancel’ the event reconstruction errors exactly in a near to far ratio as was done in MINOS. The extent to which this lack of cancellation will limit the ultimate precision of the experiment has yet to be fully explored. However, at the international Near Neutrino Detector workshop held at Fermilab (July 2014) it was accepted that the FGT offers a sound basis for moving forward and that a LArTPC or a high-pressure gaseous-argon TPC placed upstream of the FGT would enhance the near detector capability.

The principal impediment to an identical ND — a LArTPC ND — is the event-pileup problem due to the high intensity of LBNF. Nevertheless, during the operation of LBNF/DUNE there will be periods when the accelerator is running at low intensity, for example during the initial ramp-up and during the periodic shut-downs and accelerator upgrades. A ~ 100 -t LArTPC stationed upstream of the FGT (the reference ND) would be able to accumulate tens of thousands of neutrino interactions during the low-intensity runs over the lifetime of the experiment. The FGT will act as a spectrometer for the emerging muons. In conjunction with the measurements with nuclear targets in FGT, including Ar gas, such an LAr-ND would provide a means to accurately validate

10 *in-situ* the FGT predictions for a LAr detector before the extrapolation to the FD, thus providing
11 a valuable redundancy check.

12 Furthermore, for special neutrino interaction topologies, such as neutrino-electron scattering, where
13 there is a single electron or muon in the final state, the combined LAr-ND & FGT configuration
14 could provide unique precision measurements.

15 Conceptual designs for a standalone LArTPC near detector and a gaseous argon TPC near detector
16 are under consideration and could serve as starting points for the design of this addition to the
17 FGT. Significant simulation and engineering studies are required to understand whether a liquid
18 or gas argon TPC is optimal for minimizing systematic errors in the long-baseline measurements
19 and to integrate the additional detector system with the FGT design to make a coherent near
20 detector system.

21 7.5 Beamline Measurements

22 This chapter outlines the DUNE strategy for measurements of secondary beam particles down-
1 stream of the beam absorber. These measurements are designed to provide constraints on the
2 neutrino flux at the near and far detectors, and monitor the pulse-to-pulse variation for beam
3 diagnostic purposes. The measurements and apparatus described in this chapter fall into the
4 category of equipment designed specifically for DUNE to detect muons exiting the decay tunnel.

5 7.5.1 Design Considerations

6 The requirements for the beamline measurements, as discussed in the NDC requirements
7 documentation[?], are related to how well the neutrino flux must be known. While external
8 hadron-production measurements can place constraints on the pion and kaon production in the
9 target, they do not provide any constraint on the simulation of other key features, such as the
10 horn focusing, secondary interactions, and the pion scattering and absorption in the air-filled decay
11 volume.

12 In addition to the external measurements, covered in Section 7.6, that check the simulation of
13 the thick target, horn material, decay tunnel and absorber, it is desirable to constrain the flux by
14 making independent measurements at the 4–5% level of the muons that penetrate the absorber.
15 It would not be practical to do this for all penetrating muons, but sufficient measurements at a
16 few positions can be done in a cost-effective way.

17 The primary physics goal of DUNE is to measure the transmutation of ν_μ to ν_e over the 1300 km
18 between Fermilab and SURF. It is essential for DUNE to cross-check the estimate of beam ν_e using
19 several methods. There are two dominant sources of beam ν_e : muon decays and kaon decays. The
20 muon systems are designed to directly measure the muons that penetrate absorber with an energy
21 threshold as low as possible, i.e. directly measure those muons whose decays are a major source of

22 beam ν_e . A measurement of the spectrum of those muons will translate directly into constraints
 23 on the spectrum of beam ν_e . That constraint has the advantage of being independent of poorly
 24 understood neutrino-nucleus cross sections.

25 Because muons and neutrinos come from the same parent pion and kaon decays, a measurement
 26 of the absolute muon flux, in conjunction with the energy spectrum seen in the muon monitors,
 27 can constrain the absolute neutrino flux. The goal for the DUNE muon monitors is to determine
 28 the absolute muon flux to an accuracy of 5% above a muon energy of 6 GeV (which corresponds
 1 to a neutrino energy of 1.6 GeV) in the central part of the absorber.

2 It is essential to monitor the stability of the beam direction over time. For example, above 6 GeV,
 3 the ratio of the Far Detector flux over the Near Detector flux changes by 2%. To keep the change in
 4 the neutrino beam less than 1% in all energy bins, the beam direction must be known to a precision
 5 of approximately 0.2 mrad. Because the muon monitors will be located approximately 275 m from
 6 the beam target, this requires a measurement of the muons to an accuracy of approximately 5 cm.

7.5.2 Muon-Measurement Facilities

8 The muon measurements are carried out in the region immediately downstream of the hadron
 9 absorber at the end of the decay tunnel, below the Absorber Service Building (LBNF 30). A view
 10 of the absorber area and the muon alcove is shown in Figure 7.7.

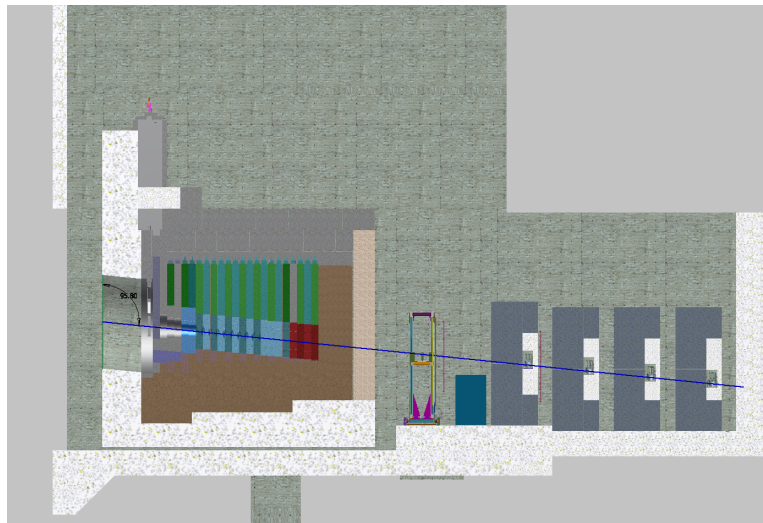


Figure 7.7: Absorber conceptual design. The figure shows the elevation view of the absorber at the end of the decay tunnel. The beam axis is shown by the blue line. The absorber is constructed of several different materials as shown: aluminum core in blue and grey, concrete (grey and tan), and steel (in brown and green).

11 The axis of the decay pipe cuts across the muon alcove at an angle and the size of the alcove
 12 is largely determined by the requirement that it contain the shadow of the four-meter-diameter
 13 decay pipe, projected through the alcove.

14 [fig:AbsorberElevationView](#)
 15 Figure 7.7 shows the downstream side of the absorber and a conceptual layout of the muon systems
 16 described in various sections of this chapter. The absorber itself is encased in concrete. The first set
 17 of muon-measurement devices, from left to right, is a variable-pressure gas Cherenkov counters,
 18 which mounted on a movable stand in order to scan across the rear surface of the absorber.
 19 Following that is an array of diamond ionization detectors and finally a set of stopped-muon
 20 counters which are interspersed between walls of steel “blue blocks”. The blue blocks are there to
 21 provide several depths at which to monitor the stopped muons as they range out in the material.
 A second array of ionization devices will also be placed farther downstream within the blue blocks.

22 [fig:AbsorberThickness](#)
 23 Figure 7.8 shows the energy lost by a horizontal muon as it traverses the absorber, as a function
 of the distance from the beam axis along a 45° line perpendicular to the beam axis.

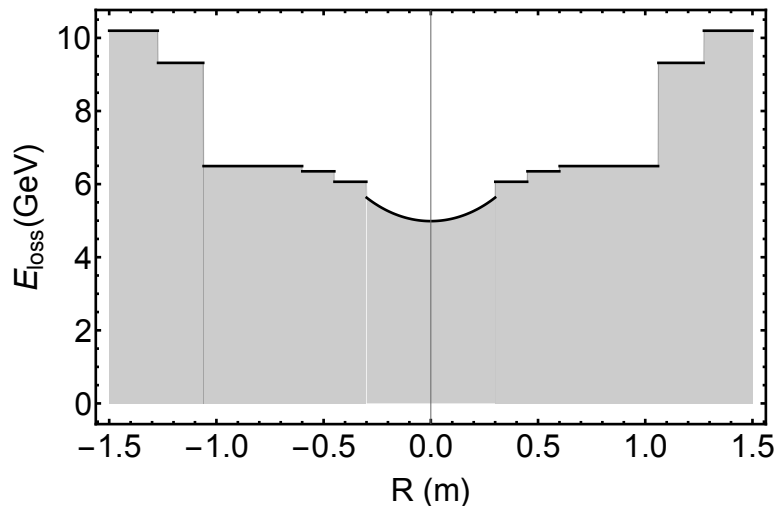


Figure 7.8: The energy loss a muon, parallel to the beam axis, experiences as it traverses the material in the absorber. The muon’s energy loss is plotted versus the distance from the beam axis, along a 45° line perpendicular to the beam axis. Muons suffer between 4.7 and 9.3 GeV of energy loss depending upon where they cross the absorber.

24 In the central region, roughly to a distance of 105 cm, the muons lose between 5.0 to 6.4 GeV, so
 25 that the lowest-energy muons leaving the absorber at that point correspond to neutrino energies
 26 of ~1.5 to 2.0 GeV. At a radius of roughly 105 cm, the full thickness of steel causes the muons
 27 10 GeV or more, corresponding to neutrino energies of ~2.6 GeV. From the perspective of the
 28 muon systems it will be desirable to lower these thresholds if possible.

29 7.5.3 Installation and Operation

30 The muon system detectors, already fully calibrated in the NuMI beam, will be installed as soon as
 31 the absorber hall (LBNF-30) is ready. Because the system will be located in a radiation-controlled
 32 environment that will not be accessible during beam operation, it is essential that the electronics
 33 and gas handling system be both robust and remotely operable. The prototype system in use at
 1 the NuMI area can be relocated for that purpose, or if desired a new system may be constructed.
 2 Periodic access will be required to the utilities area to replace gas bottles.

3 The blue blocks associated with the muon systems will be installed first. The positioned stand
4 for the Cherenkov detector system will be installed next. and then the various detectors will be
5 installed. The stopped-muon counters will be placed into the spaces between the blue-block walls
6 on support frames. There will be access to the areas between the shield blocks from the side,
7 and the stopped-muon counters will be designed so that they can be wheeled in from the side. If
8 needed, they could then be moved around to measure the stopped-muon rates across the muon
9 beam.

10 The muon systems will be operated continuously in order to insure a stable, high quality neutrino
11 beam. The muon-monitor-system data will be displayed in the control room on a spill-by-spill
12 basis to monitor the beam stability. Because the system will be located in a radiation-controlled
13 environment that will not be accessible during the beam operation, it is essential that the electronics
14 be designed for remote operation.

15 **7.6 Hadron Production Measurements**

16 **7.6.1 Introduction**

17 The technical components that would be needed to implement the strategies described in this
18 chapter are outside the scope of the DUNE NDS conceptual design. The following information is
19 included in this document because it complements the conceptual design and expands the NDS
20 capabilities to more closely meet the mission need without increasing the project cost.

21 **7.6.2 External Hadron-Production Measurements**

22 Uncertainties on hadron production will translate into uncertainties in the neutrino fluxes in the
23 DUNE Far Detector, since the neutrinos are produced by hadrons decaying in the decay pipe.
24 Precise calculations of neutrino fluxes in high-energy accelerator beams are limited at present by
25 our knowledge of hadron production cross-sections in hadron-nucleus collisions. The modeling of
26 strong-interaction cascades and hadronic yields from “thick” targets (up to a couple of interaction
27 lengths) relies on detailed knowledge of underlying physics and cross-sections, which must be
28 provided as a starting point to simulations. The resulting prediction of the flux of neutrinos,
29 produced from decays of pions, kaons, and muons emerging from a hadronic shower and beam line
30 re-interactions, is an essential part of simulations of most neutrino experiments.

31 Two-detector neutrino oscillation experiments predict the neutrino flux at the far detector by using
32 neutrino fluxes “calibrated” (or appropriately scaled) by event energy spectra measured in the
33 near detector. However, these experiments rely on beam simulations since the decay pipe (where
34 most beam neutrinos are created) provides different angular acceptance for the two detectors.
35 In addition, experiments using near and far detectors based on different detection technologies
1 further complicate the extrapolation. This chapter outlines the DUNE strategy for augmenting

2 the capabilities of the BLM with external measurements of secondary-beam particles.

3 **7.6.3 Background**

4 A complete knowledge of the momenta and decay points of the kaons, pions and muons would
5 be sufficient to predict the un-oscillated flux of neutrinos at the Near and Far Detector locations.
6 This would require knowledge of:

- 7 • the phase-space distribution of the initial proton beam
- 8 • details of all materials present in the target, horn and decay pipe areas
- 9 • the electromagnetic focusing characteristics of the magnetic horn
- 10 • the detailed development of the hadron cascade, spawned by the initial proton, that passes
11 through the target/horn/decay pipe
- 12 • the meson-to-neutrino decay rates

13 With careful engineering design and control of the materials in the target area, these items can be
14 simulated accurately except hadronic cascades in the target, horn and decay pipe. The simulation
15 of the hadronic cascade requires accurate knowledge of the hadron scattering cross sections, for
16 which there are no first-principle calculations. These cross sections must therefore rely on models,
17 which in turn require hadron-production measurements that span particle type, particle energy
18 and the various materials found in the target, horn and decay pipe.

19 At the present, a sufficient body of hadron-production measurements does not exist to achieve
20 DUNE's desired accuracy of 4-5%, as determined by the irreducible error on the statistical un-
21 certainty for the appearance-measurement background, although this is expected to improve over
22 time. A program of hadroproduction measurements has been approved as US-NA61 to run at
23 CERN.

24 **7.7 The Data Acquisition System (DAQ) and Computing**

25 The scope of the Near Detector System DAQ (NDS-DAQ) and computing includes the design,
26 procurement, fabrication, testing, delivery and installation of all the NDS-DAQ subsystems:

- 27 • NDS Master DAQ (NND-MDAQ)
- 28 • Near Neutrino Detector DAQ (NND-DAQ)
- 29 • Beamline Measurements DAQ (BLM-DAQ)

- NDS Computing

7.7.1 NDS DAQ

The Near Detector System (NDS) Data Acquisition system (NDS-DAQ) collects raw data from each NDS individual DAQ, issues triggers, adds precision timing data from a global positioning system (GPS), and builds events. The NDS-DAQ is made up of three parts, as shown in the block diagram of Figure 7.9, a master DAQ and one each for the near neutrino detector (NND, which is the FGT) and the BLM systems. The names for these are, respectively, NDS-MDAQ, NND-DAQ and BLM-DAQ.

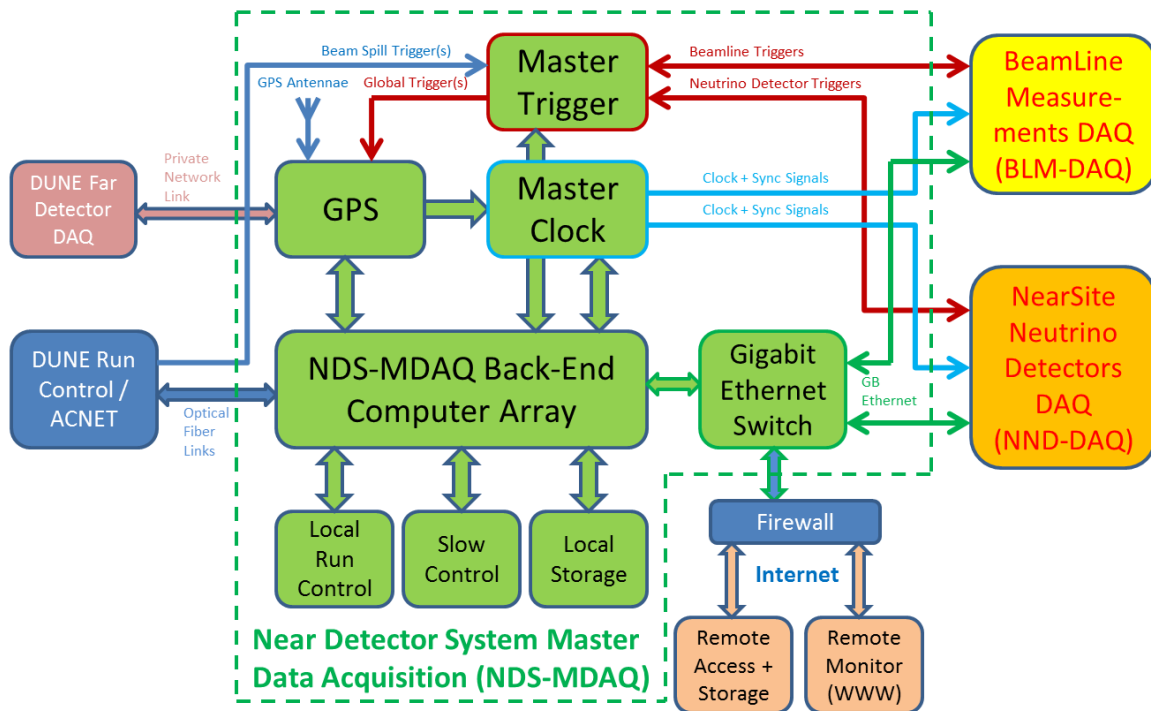


Figure 7.9: Near Detector System DAQ block diagram: The NDS-DAQ consists of the NDS Master DAQ (green blocks), the Beamline Measurement DAQ (yellow summary block) and the Near Neutrino Detectors DAQ (orange summary block). The NDS-DAQ connects to other portions of DUNE and LBNF, shown here in other colors (blue, light red, tan).

NDS Master DAQ

The NDS Master DAQ (NDS-MDAQ) is designed to provide a high-level user interface for local run control and data taking, as well as for secure remote control and monitoring. It will serve as the primary interface to the NND-DAQ and BLM-DAQ and will include the following:

- slow-control system

- 11 • online data and DAQ performance monitoring
- 12 • raw data collection
- 13 • building of events
- 14 • data storage.

15 The NDS-MDAQ includes hardware two-way triggering for both the NND-DAQ and BLM-DAQ,
 16 and GPS hardware for precision time-stamping and global clock synchronization. The design is
 17 currently based on a channel count estimate of approximately 433,000 from the near neutrino
 18 detector, plus <1,000 from the beamline detectors. Custom electronic components for the NDS-
 1 DAQ are based on existing custom designs from other experiments, e.g., T2K and ATLAS, and
 2 implement commercial components for the trigger modules, clock and timing synchronization, GPS
 3 and environmental monitoring.

4 Near Neutrino Detector DAQ (NND-DAQ)

5 The Near Neutrino Detector Data Acquisition system (NND-DAQ) collects raw data from the
 6 DAQ in each NND subdetector and connects to the NDS Master DAQ via Gigabit Ethernet. A
 7 block diagram of the NND-DAQ is shown in Figure 7.10.

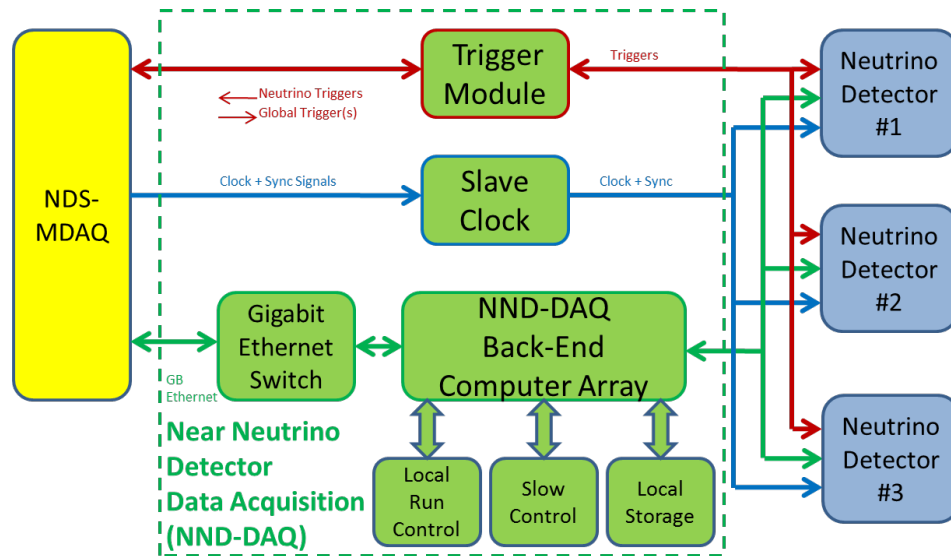


Figure 7.10: A block diagram of the Near Neutrino Detector DAQ (NND-DAQ).

8 The NND-DAQ will mainly consist of a scalable back-end computer array, interconnected to the
 9 individual subdetector DAQs via Gigabit Ethernet and specialized electronics modules for trigger
 10 processing and clock synchronization. It interfaces to the NDS-MDAQ for run control and data
 11 collection. The NND-DAQ will also have its own local run-control setup, consisting of a number
 12 of desktop workstations to allow independent local runs that include NND subdetectors only; this

13 is useful during detector commissioning, calibration runs, stand-alone cosmic runs, or other runs
14 where the beam is stopped or not needed.

15 The quantity of computers required for the NND-DAQ back-end system is highly dependent on the
16 number of channels and expected data rates of the individual neutrino detectors. One back-end
17 computer should be able to handle approximately 3,000 channels for sustainable and continuous
18 runs. Assuming a total of 433,000 channels for all NND subdetectors combined, about 150 back-end
19 computers would be needed.

20 Trigger signals from each subdetector will be collected and pre-processed by a trigger electronics
21 module, similar in design to the NDS trigger or master-clock modules of the NDS-MDAQ design.
22 Depending on the run mode, this module could feed local trigger decisions to the detector DAQs
23 for data collection, or it could forward NDS triggers from the NDS-MDAQ or higher levels to the
24 NND subdetector DAQs. A slave-clock electronics module, similar to the master-clock module in
25 the NDS-MDAQ, distributes clock- and time-synchronization signals from the NDS-MDAQ to all
26 NND subdetectors.

27 **Beamline Measurements DAQ (BLM-DAQ)**

28 The BLM-DAQ will mainly consist of a scalable back-end computer array, inter-connected to the
29 individual beamline measurement detector DAQs via Gigabit Ethernet and specialized electronics
30 modules for trigger processing and clock synchronization. It interfaces to the NDS-MDAQ for run
31 control and data collection. It will also have its own local run-control setup, consisting of a num-
32 ber of desktop workstations to allow independent local runs that include beamline measurement
33 detectors only; this is useful during detector commissioning, calibration runs, stand-alone cosmic
34 runs or other runs where the beam is stopped or not needed.

35 **7.7.2 NDS Computing**

36 The computing system encompasses two major activities: online computing with required slow-
37 control systems, and offline computing for data analysis and event simulation. The computing
38 components are based on currently available commercial computing and gigabit networking tech-
1 nology, which is likely to improve over the next years without driving costs up for the final design.

computing

2 Chapter 8

3 Software and Computing

ctors-sc

4 8.1 Overview

5 The Software and Computing effort is not part of the DUNE project and is supported from non-
6 project funds. This effort is coordinated by the DUNE collaboration and across the LBNF/DUNE
7 project. The three primary components of the effort include the computing hardware, software
8 infrastructure and reconstruction.

9 8.2 Computing Infrastructure

structure

10 There are many factors that influence the data (e.g. rates, volume, etc.) to be collected and
11 processed in DUNE. Annex 4B: *Expected Data Rates for the DUNE Detectors* describes the data
12 rates and provides a reference to the parameters and assumptions used in the estimating these
13 characteristics. The Annex contains information on both the reference design and alternative
14 design for the far detector.

15 8.2.1 Raw Data Rates

ta-rates

16 Types of data (using Supernova Burst example)

17 DUNE is a multipurpose apparatus and will pursue a variety of physics goals. This will be reflected
18 in different characteristics of data streams processed and collected in real time as well as offline
19 and different strategies and algorithms for handling these streams.

20 As one example, consider the difference between neutrino oscillation physics with beam neutrinos
21 on the one hand and the search for supernova neutrino bursts on the other. Signals produced by

22 “beam events” will be characterized by total energy in the GeV range, so that various aspects of
23 handling the signal and the data (e.g. thresholds for zero suppression etc) can be optimized for
24 minimum-ionizing particles.

25 The energy scale of signals produced by supernova neutrino burst interactions is in the range of
26 tens of MeV. For that reason, it is expected that lower thresholds will be needed while processing
27 these data in real time, which will result in considerable additional contribution from radiological
28 backgrounds. For this reason, the data rate that needs to be handled in the process of supernova
29 neutrino bursts search can be expected to be quite significant.

30 Another differentiating feature of supernova neutrino bursts is that *multiple neutrinos are expected*
31 *to arrive and interact in the detector volume* within seconds of each other, as opposed to a single
32 vertex produced by a beam neutrino (or any other localized interactions and/or decays). This opens
33 an opportunity to apply the DAQ architecture presented in 4.4 to make these data “self-triggering”,
34 i.e. to use the buffer memory in the LArTPC detector readout to detect a corresponding signature
35 in the data stream and trigger recording of the potential supernova neutrino burst event.

36 The characteristic time scale for such supernova neutrino burst data capture will be ~ 10 s. Given
37 the large amount of data arriving within this time period (see the Annex) and practical limits
1 on the bandwidth of the connection between the RCE data processors and frontend computers in
2 DAQ, local storage attached to data processors will be necessary to record the data at full-stream
3 (no zero-suppression). The buffer in the data processor will not have sufficient capacity due to
4 design and cost considerations (it can effectively buffer about 0.4 s of streaming data which is likely
5 enough for the trigger decision but not for the complete supernova event capture). Preliminary
6 estimates indicate that a storage device such as a SSD (one or two per board) will have speed
7 sufficient for this purpose. With trigger properly tuned, the number of times data are written to
8 the SSD can be kept sufficiently low so as to ensure their longevity. Once captured in this manner,
9 the data can then be transmitted to the rest of the farm within the available bandwidth.

10 The core elements of the DAQ system now exist as prototypes. The system as a whole with
11 capabilities such as described above is in the conceptual design stage and information will be added
12 to DUNE planning documents as it is developed.

13 Assumptions

14 According to the present baseline design, the Far Detector will consist of four identical modules of
15 10 kt each. For purposes of estimating data characteristics in this document the issue of possible
16 variations in the design of these modules shall not be addressed. A few basic assumptions:

- 17 • Estimates correspond to the “full detector”, i.e. is effectively normalized to 40 kt.
- 18 • Accelerator spill cycle is 1.2 s with beam expected for 0.667 of each calendar year.
- 19 • Zero-Suppression thresholds will be set at levels that preserve signals from minimum-ionizing
20 particles while effectively removing data due to electronics noise.

- 21 • The DAQ will be able to trigger based on spill times and will be able to reject isolated ^{39}Ar
22 decays on at least a per-APA basis. (for DAQ details see 4.4)

1 Far Detector LArTPC

2 The information presented below is based on the parameters listed in “Annex 4B: *Expected Data*
3 *Rates for the DUNE Detectors*”.

- 4 • TPC channel count: 1,536,000 (i.e. four times the 384,000 channel count for each 10 kt
5 module)
- 6 • Maximum drift Time: 2.25 ms
- 7 • Number of drift time windows in one DAQ readout cycle: 2.4
- 8 • ADC clock frequency: ~ 2.0 MHz
- 9 • ADC resolution (bits): 12

10 In addition to these basic parameters, there are other factors affecting data rates and volumes,
11 such as implementation of zero suppression (ZS) in the DAQ RCE processors, contribution from
12 radiological and cosmological backgrounds, and DAQ trigger configuration (cf. the case of low-
13 energy events).

14 Non-ZS maximum event size (corresponding to a snapshot of the complete TPC) can be calculated
15 as a product of the following numbers:

- 16 • Channel count
- 17 • Number of ADC samples per total drift (collection) time
- 18 • Drift time windows in one DAQ cycle
- 19 • ADC resolution

20 This results in a total of 24.9 GB worth of TPC data in one readout.

21 Zero suppression greatly reduces the event size. An overly conservative estimate (leaning to the
22 higher end of the range of values) based on a LArSoft Monte Carlo simulation of GeV-scale events
23 suggests a zero-suppressed and uncompressed event size of ~ 2.5 MB. After compression this event
1 size is expected to be ~ 0.1 MB. This particular simulation employed a less than optimal schema
2 for packing data and it is expected that with optimization these sizes can be further reduced.

3 Some of the driving zero-suppressed (ZS) and full-stream (FS) annual data volumes are summarized
4 in Table 8.1. It is important to note that the numbers in the row characterizing ^{39}Ar are given

for information only and do not represent our estimates of actual data to be committed to mass storage. Once DAQ-level rejection of isolated ^{39}Ar decay events is invoked a residual amount of data is accepted when the decay is accidentally coincident with beam- ν activity. The data required to record this background is reduced to 3% of the “with-beam- ν ” estimate of table 8.1 and is thus negligible being an order of magnitude smaller than the data associated with the beam neutrino interactions themselves.

Table 8.1: Annual data volume estimations for zero-suppressed (ZS) data from various sources. An additional full-stream (FS) data estimation is given for supernova burst (SNB).

Source	Event Rate	Event Size	Data Rate	Annual Data Volume
^{39}Ar (ZS)	11.2 MHz	150 B	1.7 GB s^{-1}	53 PB
all in-spill				159 TB
with-beam- ν				79 GB
cosmic- μ (ZS)	0.259 Hz	2.5 MB	647.4 kB s^{-1}	20 TB
beam- ν (ZS)	8770 year^{-1}	2.5 MB	0.69 kB s^{-1}	22 GB
beam- ν (FS)	8770 year^{-1}	24.9 GB	7 MB s^{-1}	218 TB
SNB cand. (ZS)	12 year^{-1}	16.7 GB	6366 B s^{-1}	201 GB
SNB cand. (FS)	12 year^{-1}	46.1 TB	17.5 MB s^{-1}	553 TB

Far Detector Photon Detector (PD)

There are variations in the basic parameters of the Photon Detector currently in the R&D stage, so the numbers presented below need to be considered as ballpark values to be made more precise at a later time:

- Readout channel count: 24,000 (i.e. four times the 6000 channel count for each 10-kt module)
- Trigger rate is uncertain at this point due to ongoing investigation; one approach assumes 1 trigger per spill cycle
- ADC resolution (bits): 12
- ADC digitization frequency: 150 MHz

It is assumed that a few dozen samples will be recorded in each channel, and there will be zero suppression of channels with signals below a chosen threshold, resulting in an order of magnitude reduction of the data volume. This results in 360 kB per spill cycle, and should be considered negligible from the point of view of requirement to data handling, compared to other data sources.

6 Near Detector Data Rates

7 The near detector is subject to an intense R&D effort and its parameters are being optimized at
8 this point. The most relevant parameters of the Fine-Grained Tracker (FGT):

- 9 • Straw Tube Tracker (STT) readout channel count: 215,040
- 10 • STT Drift Time: 120 ns
- 11 • STT ADC clock frequency and resolution (bits): 3 ns intervals, 10 bit
- 12 • ECAL channel count: 52,224
- 13 • Muon Detector Resistive Plane Chambers (RPC) channel count: 165,888
- 14 • Average expected event rate per spill: ~ 1.5

15 Since there are large uncertainties in estimates of the detector occupancy levels per event, broad
16 assumptions must be made to estimate the data rate. The current estimate (as quoted in the
17 Near Detector section of the “Expected Data Rates” Annex is $\sim 1.0 \text{ MB s}^{-1}$, which translates into
18 $\sim 30 \text{ TB year}^{-1}$.

19 8.2.2 Processed Data

20 For the purposes of this document, processed data is defined as most data which is not consid-
21 ered “raw”, i.e. it’s data derived from raw (including possibly multiple stages of calibration and
22 reconstruction) as well as data produced as a result of Monte Carlo studies.

23 There are uncertainties in anticipated quantities of all of these types of data. [Table 8.1](#) contains
1 a range of numbers reflecting limiting cases such as ZS vs FS. Depending on the exact optimum
2 readout strategy, an annual raw data volume of 1 TB to 1 PB may be collected. Assuming that the
3 data will undergo a few processing stages, one can expect the need to handle as much as $\sim 2 \text{ PB}$ of
4 data annually for reconstruction and a lesser volume for final analysis purposes.

5 For Monte Carlo, at the time of writing typical annual volume of data produced has been of the
6 order of a few tens of terabytes. Initial expectations are that the MC sample size for beam events
7 will need to be $10\text{--}100\times$ that of the data. With Collaboration growth and more detailed studies
8 (e.g. of systematics) undertaken, our expectation is that this estimate will increase.

8.2.3 Computing Model

Distributed Computing

Given the fact the Collaboration is large and widely dispersed geographically, a fully distributed approach to computing is planned, based on experience gained during the operation of the LHC experiments. This includes not only “traditional” Grid technologies in the form they were deployed during the first decade of this century, but also more recent expansion into Cloud Computing and Big Data methodology. This will allow the DUNE Collaboration to better leverage resources and expertise from many of its member institutions and improve the overall long-term scalability of its computing platform.

DUNE will operate a distributed network of federated resources, for both CPU power and storage capability. This will allow for streamlined incorporation of computing facilities as they become available at member institutions, and thus is particularly amenable to accommodate staged construction and commissioning of the detector subsystems. A modern Workload Management System will be deployed on top of Grid and Cloud resources to provide computing power to DUNE researchers.

Raw Data Transmission and Storage Strategy

FNAL will be the principal data storage center for the experiment. It will serve as a hub where the data from both the facility (e.g. beam, target and cryogenics) and the various detector systems (far and near detectors) are collected, catalogued and committed to mass storage. This will obviously require transmission of data over considerable distances (certainly for the far detector). In addition, the DAQ systems of the far detector are being designed to be located in the vicinity of the far detector (in the cavern), which results in an additional step of transmitting the data from 4850L to the surface.

Raw data to be collected from the detectors in DUNE are considered “precious” due to the high cost of operating the both the facility at FNAL and the detectors that are part of DUNE. This leads to three basic design elements in the data transmission and storage chain:

- Buffering:
 - Adequate buffers will be provided for the DAQ systems to mitigate possible downtime of the network connection between 4850L and the surface.
 - Buffers will be provided at the surface facility to mitigate downtime of the network connection between the far site and FNAL.
- Robust transmission: data transfer needs to be instrumented with redundant checks (such as checksum calculation), monitoring, error correction and retry logic.

- Redundant replicas: it is a common practice in industry and research (cf. the LHC experiments) to have a total of three copies of “precious” data, which are geographically distributed. Such geographical distribution of the replicas may include countries other than the United States, where the data will be collected. This provides protection against catastrophic events (such as natural disasters) at any given data center participating in this scheme, and facilitates rebuilding (“healing”) lost data should such event does happen.

5 Data Management

6 Data will be placed into mass storage at FNAL. Along the lines described above, additional
7 copies (replicas) will be distributed to other computing centers possessing sufficient resources. A
8 single additional copy does not necessarily need to reside in its entirety on a single data center;
9 the replicas can be “striped” across a few data centers if that becomes optimal at the time of
10 implementation of the Computing Model. For example, consideration is given to both Brookhaven
11 National Laboratory and NERSC as candidates for the placement of extra replicas.

12 Recent progress in network and storage technologies made possible *federation of storage* across
13 multiple data centers located at member institutions. In this approach, data can be effectively
14 shared and utilized via the network (cf. “data in the Cloud”). One example of an advanced system
15 of this type of XRootD.

16 For data distribution, a combination of managed data movement between sites (such as “dataset
1 subscription”, primarily for managed production), and a network of XRootD servers to cache
2 processed data and for analysis will be used. A file catalog and a Meta-Data system will be
3 required for efficient data management at scale, and an effort will be made to leverage experience
4 of member institutions in this area, making an effort to reuse existing systems or design ideas
5 where possible.

6 8.2.4 Computing Implications of the Dual-Phase Far Detector Design

7 Parameters of the alternative design of the far detector (based on the dual-phase technology) are
8 listed in Chapter 2 of the “Annex 4B: *Expected Data Rates for the DUNE Detectors*”. Here is a
9 brief summary:

- Readout channel count: 614,400 (i.e. four times the 153,600 channel count for each 10-kt module)
- Drift Time: 7.5 ms

13 For the Photon Detector in the dual-phase design:

- Readout channel count: 720 (i.e. four times the 180 channel count for each 10-kt module)

15 According to some estimates listed in the Annex, the “Full Stream” readout will produce 16.09 GB
16 of data for each candidate event. This is about 65% of the data volume in one readout cycle, in
17 the reference design. Although signal processing strategies may be implemented differently in the
18 alternative design, it can be argued that the total data rate will be of the same order of magnitude
1 or less than in the reference design.

2 8.3 Near Detector Physics Software

3 A longer description of the current status of the near detector simulation and reconstruction are
4 given in Annex 4C: *Simulation and Reconstruction* with an abbreviated summary here.

5 Two approaches are being pursued for the simulation of the DUNE near detector. The first is a
6 fast Monte Carlo based on parameterized detector responses. The GENIE[36] generator is used
7 to model the interactions of neutrinos with nuclei in the detector, and a parameterization of the
8 achieved NOMAD reconstruction performance is used to model the detector response. The second
9 approach is a full GEANT4-based simulation, which is under development. The fast Monte Carlo
10 tool is based on work done for the far detector[34] (Appendix A.3) and is capable of rapidly
11 evaluating the sensitivity of the detector design for a broad variety of analyses targeting specific
12 final states. The full GEANT4-based simulation and subsequent reconstruction chains will be used
13 to inform the parameterized responses of the fast Monte Carlo, as well as being indispensable tools
14 for simulating and extracting results from the near detector. Figure 8.1 shows the trajectory of
15 a negatively-charged muon with an initial momentum of 1 GeV propagating in the straw tube
16 tracker, as simulated using GEANT4.

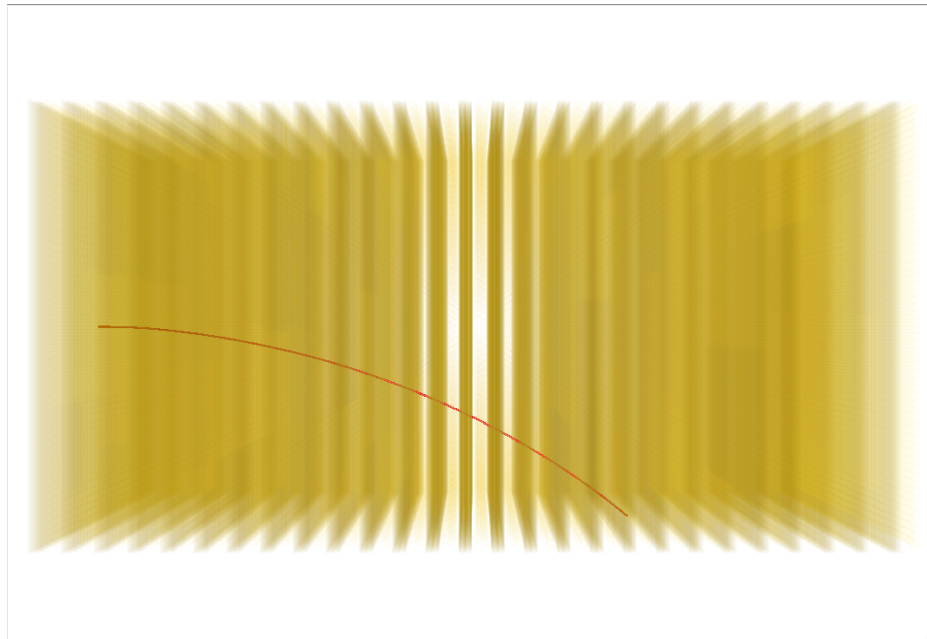


Figure 8.1: The trajectory of a 1 GeV μ^- produced by the GEANT4 simulation of the near detector's straw-tube tracker.

fig:ndev

8.4 Far Detector Physics Software

Longer descriptions of the single-phase and dual-phase far detector simulations and reconstruction are given in Annex 4C: *Simulation and Reconstruction* with an abbreviated summary here.

8.4.1 Far Detector Simulation

Detailed GEANT4-based [37, 38] Monte Carlo simulations have been developed for the single-phase and dual-phase far detector designs, incorporating both the TPC modules and the photon detection systems. These simulations provide a basis for detailed studies of detector design and performance, and also enable the development of automated event-reconstruction algorithms.

The single-phase detector simulation is implemented in LArSoft [39], which provides a common simulation framework for LArTPC experiments. LArSoft is based on the *art* framework [40], and is supported by the Fermilab Scientific Computing Division. The comparison of data from ArgoNeuT [41, 42] with LArSoft simulations gives confidence in the reliability of the detector simulation. Future data from LArIAT [43, 44], MicroBooNE [45, 46, 47], and the 35-ton prototype (Sec. 9.2) will allow further tuning of the LArSoft simulation as experience is gained. The dual-phase detector simulation and hit-level reconstruction are based on the Qscan [48] package, which has been developed over the past decade, and is currently being used for technical design and physics studies for the *Long Baseline Neutrino Observatory Demonstration (WA105)* program.

Events are generated using either the GENIE [36] simulation of neutrino-nucleus interactions, the CRY [49, 50, 51] cosmic-ray generator, a radiological decay simulator written specifically for LArSoft using the decay spectra in Ref. [52], a particle gun or one of several text-file-based particle input sources. GEANT4 simulates the trajectories of particles and their energy deposition. Custom algorithms have been developed to propagate the drifting charge and scintillation photons through the detector and to simulate the response characteristics of the TPC wires, readout electronics and photon detectors. Figure 8.2 shows some examples of simulated accelerator neutrino interactions in the MicroBooNE detector.

8.4.2 Far Detector Reconstruction

The reconstruction of particle interactions in LArTPC detectors is an active area of research that has advanced significantly in recent years. In particular, the analysis of the data from the ICARUS [53, 54, 7, 55] and ArgoNEUT experiments [43, 56, 57] required the development of a variety of new reconstruction techniques, forming the basis for precision neutrino physics measurements. Accurate reconstruction is needed not only of neutrino scattering events from the beam, but also atmospheric neutrino events, supernova burst neutrino interactions and nucleon decay events, each with its own requirements. With the advance of both single-phase and dual-phase technologies and expansion of the experimental program to include MicroBooNE [45, 58], the 35-ton prototype and the CERN test experiments, the reconstruction tools have grown in both volume and sophistication,

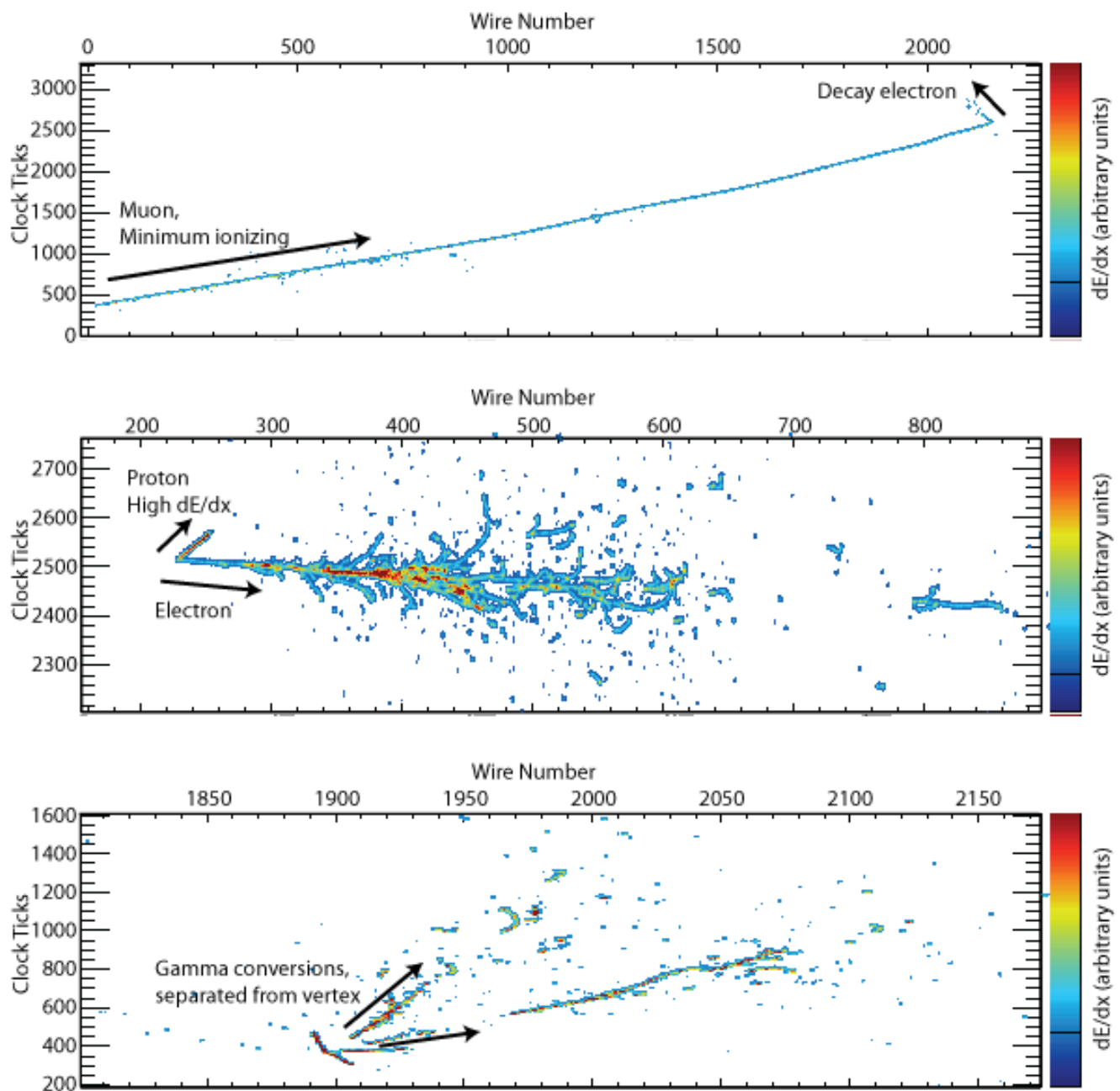


Figure 8.2: Examples of accelerator neutrino interactions, simulated by LArSoft in the MicroBooNE detector. The panels show 2D projections of different event types. The top panel shows a ν_μ charged-current interaction with a stopped muon followed by a decay Michel electron; the middle panel shows a ν_e charged-current quasi-elastic interaction with a single electron and proton in the final state; the bottom panel shows a neutral-current interaction with a π^0 in the final state that decayed into two photons with separate conversion vertices.

fig:lars

20 supported by powerful software frameworks such as LArSoft and Qscan.

21 Fully automated chains of event-reconstruction algorithms are being developed for the DUNE
22 far detector, for both the single-phase and dual-phase designs. The first stage of reconstruction
23 involves the processing of the ADC wire signals and the identification of pulses, or “hits” in the
24 two-dimensional space of wire number and charge arrival time. These hits provide the input for a
25 series of pattern-recognition algorithms, which form 2D and 3D clusters, representing individual
26 particle tracks and showers. A set of high-level algorithms is used to reconstruct the 3D vertex and
27 trajectory of each particle, identify the type of particle and determine the four-momentum. While
28 each stage of the reconstruction chain has been implemented, the algorithms – in particular those
29 addressing the higher level aspects of reconstruction such as particle identification – are rather
30 preliminary and are in active development.

31 **TPC Signal Processing, Hit Finding, and Disambiguation**

32 The signal-processing steps in the single-phase and dual-phase detectors are similar but are ac-
33 complished with separate software. Both proceed first by decompressing the raw data and filtering
1 the noise using a frequency-based filter. The single-phase signal-processing algorithm also decon-
2 volves the detector and electronics responses at this step. Both the single-phase and dual-phase
3 hit-finding algorithms then subtract the baselines and fit pulse shapes to the filtered raw data.
4 The hit-finding algorithms are able to fit multiple overlapping hits. The main parameters of the
5 hits are the arrival time, the integrated charge, and the width. A raw ADC sum is also retained
6 in the description of a hit, which often carries a better measurement of the total charge. The
7 current algorithms are found to perform well in ArgoNeuT analyses[41] for the single-phase soft-
8 ware and during several phases of R&D and prototyping on small-scale dual-phase LAr-LEM-TPC
9 setups[18, 13]. Figure 8.3 shows example event displays of the reconstructed hits in both real and
10 simulated data.

11 The wrapping of induction-plane wires in the single-phase APA design introduces an additional
12 discrete ambiguity in the data by connecting multiple wire segments to each DAQ channel. A
13 “disambiguation” algorithm is used to break the ambiguity and determine which wire segment
14 generated the charge on each hit. The algorithm forms associations between the collection and
15 induction views, identifying “triplets” of hits that have intersecting wire segments and consistent
16 arrival times. In most events, the majority of hits are associated with a single wire segment, and
17 can be trivially disambiguated. The remaining hits are then disambiguated by clustering them
18 with trivially disambiguated hits.

19 **Photon Detector Signal Reconstruction**

20 Photon detector signals are processed in similar ways to those on the TPC wires. Noise is filtered
21 out, and hits are identified as pulses above the pedestal. Hits are grouped together into clusters in
22 time, called “flashes,” for subsequent association with clusters in the TPC. Each flash has a time, a
23 total integrated charge, and a position estimate. The time of an interaction is important in order to

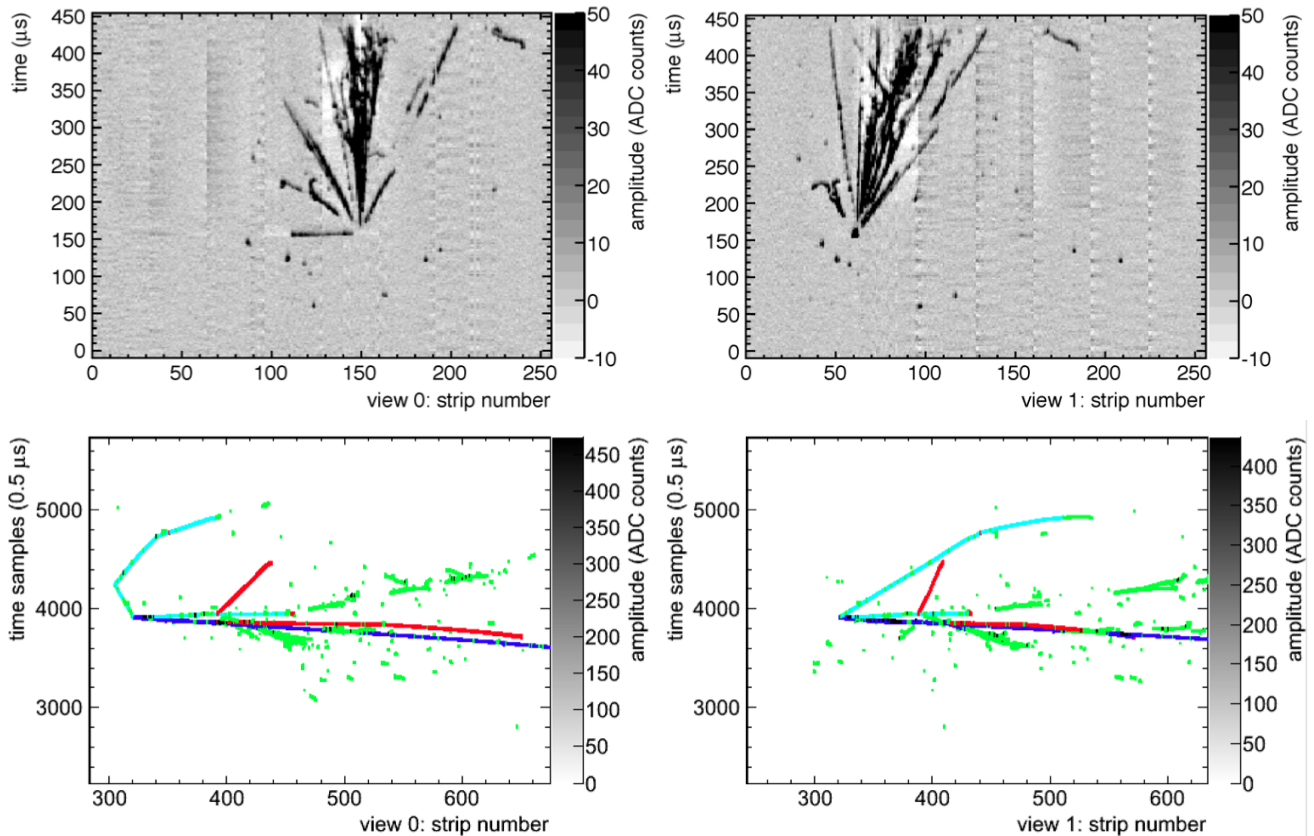


Figure 8.3: Dual-phase LArTPC-reconstructed events for data and MC. Top: Cosmic ray event displays for an hadronic shower candidate. Bottom: Reconstructed hits for a MC simulation of a 5 GeV ν_μ interaction. The secondary particles produced in the two interactions are distinguished with different colors based on the MC truth information (blue=muon, green=electron, red=proton, cyan=pion). From Ref. [13].

fig:lbnc

24 help reject cosmic-ray events and also to determine the absolute position of an event along the drift
 25 direction. This position is important in order to correct for finite electron lifetime effects for proper
 26 charge measurement, which is important for particle identification and extraction of physics results.
 27 Signal events which can be out of time from the beam include atmospheric neutrinos, supernova
 28 burst neutrinos, and proton decay interactions.

1 TPC Pattern Recognition

2 The reconstruction of particles in 3D can be accomplished either by forming 2D clusters and
 3 associating them between views, or by first associating 2D hits between views and then clustering
 4 the resulting 3D hits. The clustering of hits in LArTPC detectors is a challenging task due to
 5 the variety and complexity of event topologies. However, several automated 2D and 3D pattern-
 6 recognition algorithms have been implemented using a range of techniques.

7 One promising suite of reconstruction tools is the PANDORA software development kit[3, 4] which
 8 provides fully automated pattern recognition for both single-phase and dual-phase technologies.
 9 PANDORA implements a modular approach to pattern recognition, in which events are recon-
 10 structed using a large chain of algorithms. Several 2D pattern-recognition algorithms are first
 11 applied that cluster together nearby hits based on event topology. The resulting 2D clusters are
 12 then associated between views and built into 3D tracks and showers, modifying the 2D clustering
 13 as needed to improve the 3D consistency of the event. Vertex-finding algorithms are also applied,
 14 and neutrino events are reconstructed by associating the 3D particles to the primary interaction
 15 vertex.

16 Figure 8.4 shows the current efficiency for reconstructing the leading final-state lepton as a function
 17 of its momentum for 5 GeV ν_e and ν_μ charged-current interactions simulated in the MicroBooNE
 18 detector; the DUNE single-phase detector is expected to perform similarly, although the multiple
 19 TPC geometry with wrapped wires requires additional software effort. Figure 8.5 shows the spatial
 20 resolution for reconstructing the primary interaction vertex in these 5-GeV event samples, projected
 21 onto the x , y and z axes. An estimate of the overall vertex resolution is obtained by taking the
 22 68% quantile of 3D vertex residuals, which yields 2.2 cm (2.5 cm) for ν_μ CC (ν_e CC) events.

23 Track Fitting and Shower Measurement

1 After the pattern recognition stage, a series of high-level reconstruction algorithms is applied to
 2 the 2D and 3D clusters, which fit the trajectories of particle tracks and measure the spatial and
 3 calorimetric properties of electromagnetic and hadronic showers. Several high-level techniques
 4 have been demonstrated for use in LArTPC detectors using both real and simulated data.

5 The Kalman filter technique[59] is well-established in high-energy physics, and has been applied
 6 to 3D track reconstruction in liquid argon by ICARUS[6]. The technique incorporates the effects
 7 of multiple Coulomb scattering, enabling a scattering-based measurement of the track momentum,
 8 which is shown by ICARUS to have a resolution as good as $\Delta p/p \approx 10\%$ for the most favourable

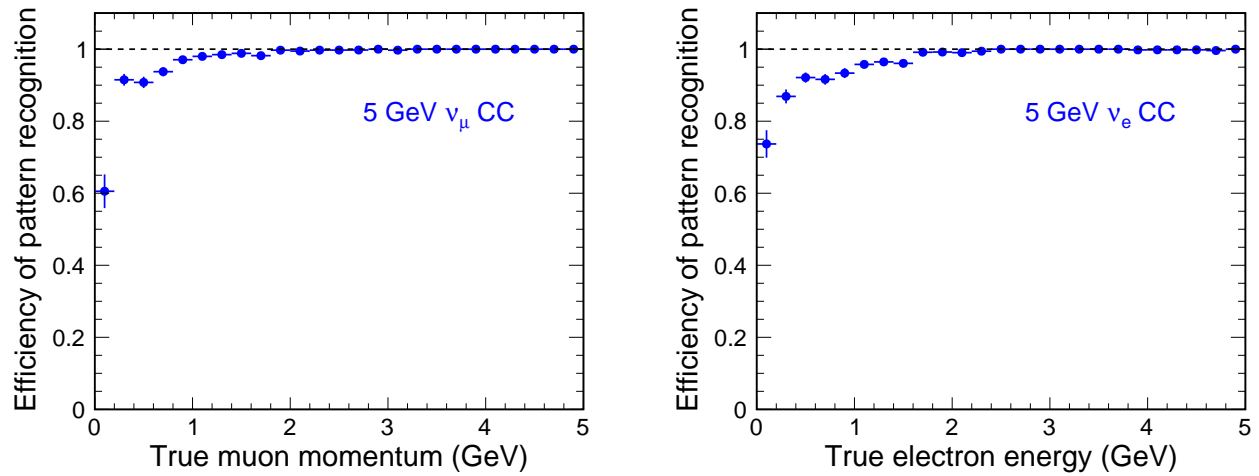


Figure 8.4: Reconstruction efficiency of Pandora pattern recognition algorithms for the leading final-state lepton in 5-GeV ν_μ CC (left) and ν_e CC (right) neutrino interactions, plotted as a function of the lepton momentum. The reconstruction performance is evaluated using the MicroBooNE detector geometry.

fig:pand

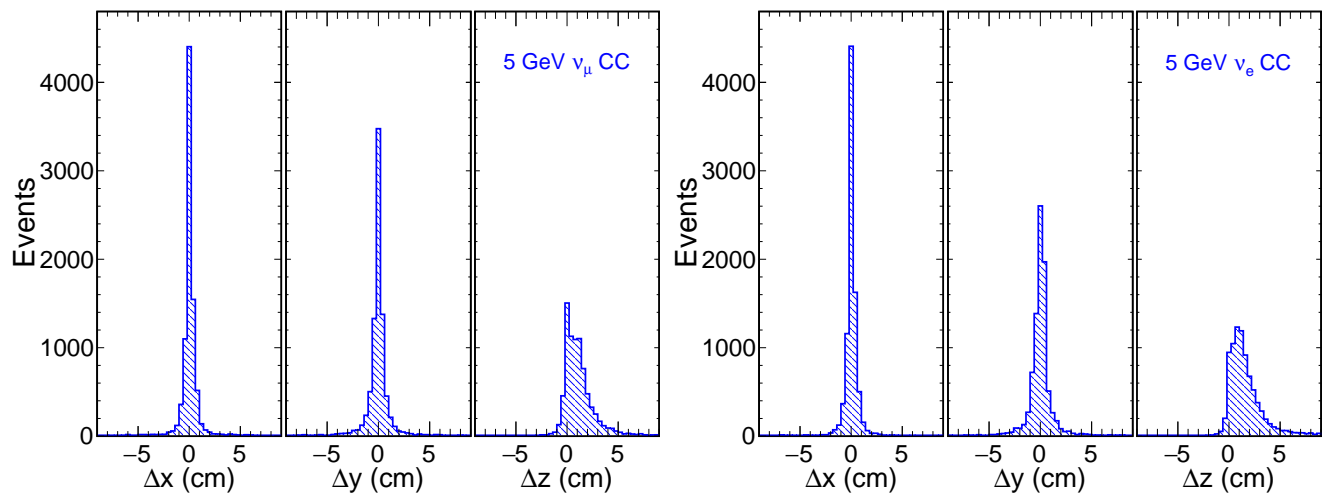


Figure 8.5: Distribution of 2D residuals between reconstructed and simulated interaction vertex for 5-GeV ν_μ CC (left) and ν_e CC (right) interactions in the MicroBooNE detector. The x axis is oriented along the drift field, the y axis runs parallel to the collection plane wires, and the z axis points along the beam direction.

fig:reco

9 track lengths. The data from ICARUS have also been used to develop a precise track reconstruc-
10 tion algorithm, which builds a 3D trajectory for each track by simultaneously optimizing its 2D
11 projections to match the observed data [55]. Another promising track reconstruction technique,
12 based on the local principal curve algorithm, has been implemented for the dual-phase detector,
13 and is shown to provide a precise reconstruction of two-body final states [60, 11].

14 A full 3D reconstruction of electromagnetic showers is currently in development. In the present
15 scheme, the first stage is an examination of clusters in terms of their 2D parameters, and a selection
16 of shower-like clusters for further analysis. The 3D start position, principal axis, and shower shape
17 variables are then reconstructed by matching up 2D hits between views. These 3D parameters,
18 combined with calorimetric information, enable a measurement of the total shower energy, as well
19 discrimination between electrons and converted photons based on the ionization energy in the
20 initial part of the shower. The kinematic reconstruction of final-state neutral pions from their
21 $\pi^0 \rightarrow \gamma\gamma$ decays can be performed by combining together associated pairs of photons.

22 Calorimetry and Particle Identification

23 The reconstructed energy of hits follows from the measured charge after corrections are made
24 for sources of charge loss. The energy of physics objects can then be reconstructed by summing
25 the energy of the associated hits and, when this is combined with reconstructed trajectory, a
26 measurement of the ionization density dE/dx can be made, which is an important input to particle
27 identification. In order to reconstruct this information, the measured charge on each hit is first
28 obtained from fits to the pulse shapes. The charge loss due to the finite electron lifetime is corrected
29 based on the time of the event, and the path length corresponding to each hit is calculated based
30 on the event trajectory. The effects of recombination, known as “charge quenching” are corrected
31 using a modified Box model [61] or Birks Law [62]. The identity of a particle track that ranges out
32 in the active detector volume may be ascertained by analyzing the ionization density dE/dx as a
33 function of the range from the end of the track, and comparing with the predictions for different
34 particle species.

1 In a liquid argon TPC, electromagnetic showers may be classified as having been initiated by an
2 electron or a photon using the dE/dx of the initial ~ 2.5 cm of the shower. Electron-initiated show-
3 ers are expected to have dE/dx of one MIP in the initial part, while photon-initiated showers are
4 expected to have twice that. Current algorithms achieve a performance of 80% electron efficiency
5 with 90% photon rejection, with a higher efficiency for fully-reconstructed showers.

6 Neutrino Event Reconstruction and Classification

7 Once the visible particles in an event have been reconstructed individually, the combined infor-
8 mation is used to reconstruct and classify the overall event. The identification of neutrino event
9 types is based on a multivariate analysis [60, 15, 11, 63], which constructs a number of charac-
10 teristic topological and calorimetric variables, based on the reconstructed final-state particles. In
11 the present scheme, a Boosted Decision Tree algorithm is used to calculate signal and background

12 likelihoods for particular event hypotheses. The current performance has been evaluated using
 13 fully reconstructed ν_e and ν_μ charged-current interactions with two-body final states, simulated in
 14 the dual-phase far detector [11]. The correct hypothesis is chosen for 92% (79%) of ν_μ (ν_e) quasi-
 15 elastic interactions with a lepton and proton in the final state, and 79% (71%) of ν_μ (ν_e) resonance
 16 interactions with a lepton and charged pion in the final state. For selected events, the neutrino
 17 energy is estimated kinematically for quasi-elastic interactions using a two-body approximation,
 18 or otherwise a calorimetric energy measurement is applied. The calorimetric reconstruction takes
 19 into account the quenching factors of the different particles, assuming that all hits not associ-
 20 ated with the primary lepton are due to hadronic activity. Figure 8.6 shows the resulting energy
 21 reconstruction for ν_e CCQE and CC $1\pi^+$ events.

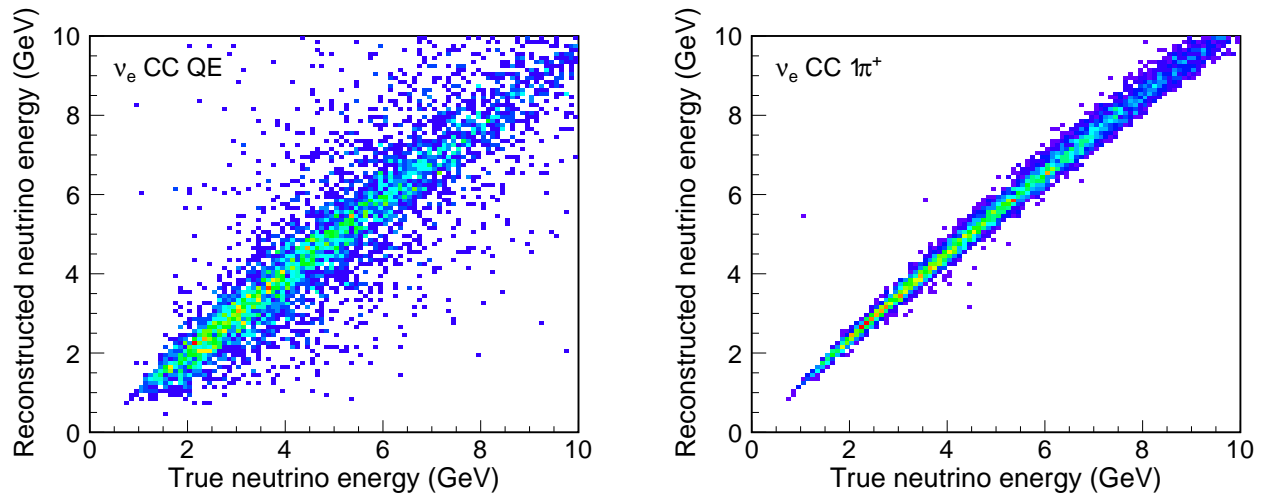


Figure 8.6: Performance of neutrino energy measurement, evaluated using the dual-phase far detector simulation. Distributions of reconstructed versus true neutrino are shown for ν_e CCQE events (left), assuming two-body kinematics, and ν_e CC $1\pi^+$ events (right), using a calorimetric energy estimation.

fig:reco

Chapter 9

Prototyping Strategy

9.1 Overview

This chapter describes the prototyping strategy for the DUNE far and near detectors and the efforts that are underway or being planned. These include:

- the 35-ton prototype at Fermilab
- the single-phase DUNE prototype at CERN
- the dual-phase LArTPC prototype at CERN known as WA105
- prototypes for the Near Neutrino Detector (NND) and Beamline Measurement (BLM) systems
- the LArTPC-based short-baseline neutrino physics program (SBN) at Fermilab

The single-phase LArTPC prototyping efforts, i.e., the 35-t at Fermilab and the DUNE prototypes at CERN, have evolved from the plans made initially for LBNE, as summarized in Chapter 7 of Annex 4A: *The LBNE Design for a Deep Underground Single-Phase Liquid Argon TPC* and fully described in the *Integrated Plan for LArTPC Neutrino Detectors in the U.S.*, a report which was submitted to the DOE in 2009. The 2009 report outlined an R&D program with the goal of demonstrating a scalable LArTPC far detector design for a long-baseline neutrino oscillation experiment. The following list of the detector development components is taken from the Executive Summary of the 2009 report (and edited to remove out-of-date information).

- Materials Test Stand (MTS) program to address questions pertaining to maintenance of argon purity
- electronics test stands at Fermilab and BNL

- 18 • the Liquid Argon Purity Demonstrator (LAPD) at Fermilab
- 19 • the ArgoNeuT prototype LArTPC
- 20 • the MicroBooNE experiment, a physics experiment that will advance our understanding of
1 LArTPC technology
- 2 • a software development effort that is well integrated across present and planned LArTPC
3 detectors
- 4 • a membrane-cryostat mechanical prototype to evaluate this technology
- 5 • an installation and integration prototype for LBNE, to understand issues pertaining to de-
6 tector assembly, particularly in an underground environment
- 7 • ~5%-scale electronics systems test to understand system-wide issues as well as individual
8 component reliability
- 9 • a calibration test stand that would consist of a small TPC to be exposed to a test beam for
10 calibration studies, relevant for evaluation of physics sensitivities

11 This detector development plan has largely been enacted. The MTS is a standard tool used to
12 assess any materials planned for use in LArTPCs. LAPD operated successfully, showing the via-
13 bility of a “piston purge” in place of evacuation to attain the desired argon purity. The membrane
14 cryostat mechanical prototype became the DUNE 35-t prototype and repeated the demonstration
15 of the piston purge in its Phase-1 operation. ArgoNeuT collected quality data in the NuMI beam
16 and helped spur the integrated reconstruction software development effort now known as LArSoft.
17 The proposed calibration test stand has become the LArIAT facility at Fermilab. The development
18 of cold electronics for LArTPCs continues, with a goal of incorporating most of the signal process-
19 ing and formatting into analog and digital ASICs. The installation and integration prototype for
20 LBNE has evolved into the 35-t Phase-2 and single-phase CERN prototypes for DUNE, described
21 in this Chapter.

22 At the time the LBNE document was written, the 35-t membrane cryostat had not yet been
23 fabricated; Section 9.2 provides a summary of the recent and near-future 35-t operations. The
24 1-kt prototype described in the LBNE document is no longer planned and has been replaced by
25 the DUNE single-phase LArTPC prototype at CERN, which is summarized in Section 9.3 and
26 fully described in Annex 4J: *CERN Single-phase Prototype Detector Proposal*. The prototyping
27 plans made for LBNE were in turn a part of a larger LArTPC detector development program at
28 Fermilab, which is also linked to the short-baseline program at Fermilab; these connections are
29 described in Section ??.

30 The dual-phase WA105 prototype detector has evolved from the European-based design studies
31 performed for LAGUNA-LBNO; the development of these is summarized in Section 5.1. The
1 WA105 detector provides a large-scale implementation of a dual-phase LArTPC as summarized in
2 Section 9.4 and fully described in Annex 4I: *WA105 TDR*. A 20-t engineering prototype of WA105,
3 also described in Section 5.1, is planned for the immediate future.

Both the single-phase and dual-phase prototypes at CERN will be operated in a test beam and calibrated with charged particles (pions, protons, muons, electrons). The data from the CERN prototypes will be combined with data from other operating LArTPCs, such as those in the Fermilab short-baseline and test beam programs and used to refine the simulations of the DUNE far detectors.

The near detector prototyping plans described in Section ?? are under development and will utilize particle test beams at CERN and Fermilab. Prototypes of certain short-baseline systems have already been operated in the NuMI beam at Fermilab.

The prototyping efforts enable the Collaboration to acquire the knowledge and skills necessary for successful construction and implementation of the DUNE detectors. They provide guidance in areas such as procurement, construction and installation techniques, in addition to refinement of technical designs and validation of cost and schedule estimates. Operation of the prototypes will provide opportunities to test data-taking and data-handling assumptions and to enhance the development of data analysis tools. Finally, the Fermilab short-baseline program offers experience with large neutrino event samples in LArTPC detectors as well as an opportunity to make detailed measurements of neutrino-argon interactions that are important for DUNE physics.

9.2 The 35-t Prototype

The 35-t (metric ton) LAr prototype was designed to demonstrate that a non-evacuatable membrane cryostat could satisfy the DUNE far detector requirement that oxygen contamination of the LAr be less than 100 parts per trillion (ppt) and stably maintain that level. In addition, construction and operation of the 35-t cryostat has also served to identify requirements for procurement of materials and services, to inform procedures for construction and to inform best practices for safe operation. Construction and operation of the 35-t membrane cryostat alone (without detector elements), now called “Phase-1,” was successfully completed in 2014.

The second phase of 35-t prototype operations (Phase-2) includes installation and operation of a small-scale, single-phase LArTPC and photon detector in this cryostat, focusing on the performance of active detector elements within the LAr volume. Phase-2 is currently under construction and plans to take data in summer 2015.

9.2.1 35-t Phase-1

The 35-t membrane cryostat was built by the Japanese company IHI, contracted by the LBNE project. Table 9.1 lists the construction materials and dimensions; more information can be found in [65].

The prototype was built in Fermilab’s PC-4 facility near the Liquid Argon Purity Demonstrator (LAPD) [64] allowing re-use of a large portion of the LAPD cryogenics-process equipment. The

Table 9.1: 35-t prototype materials and dimensions

Parameter	Value
Cryostat Volume	29.16 m ³
Liquid argon total mass	38.6 metric tons
Inner dimensions	4.0 m (L) × 2.7 m (W) × 2.7 m (H)
Outer dimensions	5.4 m (L) × 4.1 m (W) × 4.1 m (H)
Membrane	2.0 mm thick corrugated 304 SS
Insulation	0.4 m polyurethane foam
Secondary barrier system	0.1 mm thick fiberglass
Vapor barrier Normal	1.2 mm thick carbon steel
Steel reinforced concrete	0.3 m thick layer

23 proximity and size (30 t) of the LAPD vessel offers the possibility using LAPD as a partial storage
 24 vessel for LAr if it ever becomes necessary to empty the 35-t cryostat.

25 The 35-t system employs a submersible pump to move LAr from the cryostat through the filters.
 26 Figure 9.1 shows a cutaway view of the cryostat and a photograph of the interior of the completed
 27 cryostat.

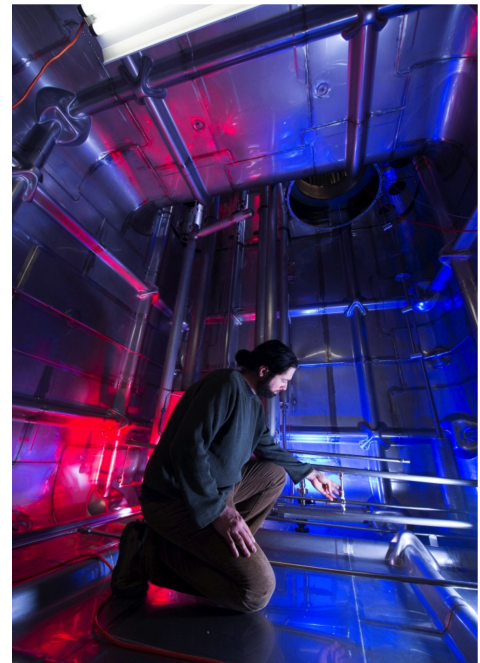
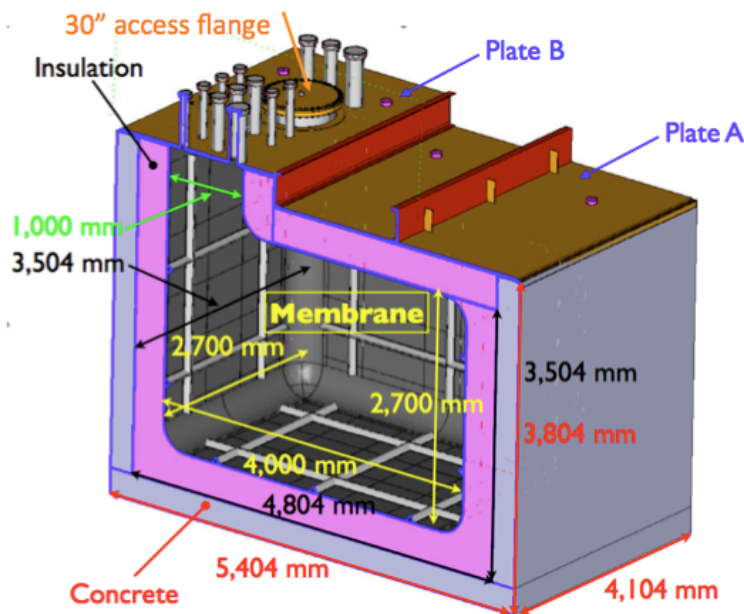


Figure 9.1: (left) Cutaway view of the 35-t prototype cryostat. (right) Interior photograph of the completed cryostat.

28 The techniques of membrane cryostat construction were demonstrated to be suitable for high-purity
 29 LArTPC operations. In particular, welding of corrugated panels, removal of leak-checking dye
 30 penetrant and ammonia-activated leak-detecting paints and post-construction-cleaning methods
 1 were tested and found to be suitable.

As was demonstrated by LAPD, initial removal of impurities within the cryostat can be achieved by purging with gaseous argon. Accordingly, this was adopted for the 35-t. Figure 9.2 graphically shows the first step of the purification process, removal of the ambient air. The initial state, $t = 0$, reflects the initial values for oxygen, water and nitrogen in the “dry air” state.

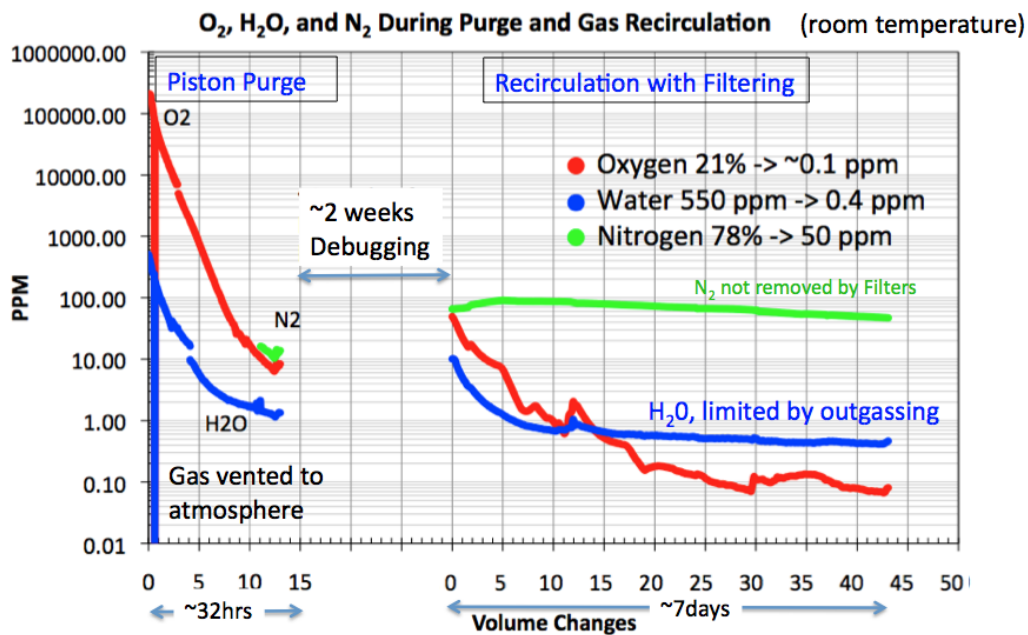


Figure 9.2: Progress of the gas argon purge as it removes impurities from the 35-t. The shown quantities are measured by various gas analyzers. The first stage of the purification is a process called the “Piston Purge”. The second stage is “Recirculation with Filtering.” The gap between the two steps was due to troubleshooting a leak.

Once the room-temperature, gas purge ceased to improve purity, the cooldown and LAr-fill stage began. A gas/liquid spray method was used to cool the cryostat. This generated a turbulent mixing of cold gas in the cryostat and cooled the entire surface. The cooldown rate was maintained within the limits specified by the cryostat manufacturer. Upon completion of the cooldown, LAr was transferred into the cryostat and purification via recirculation loop started.

During recirculation and purification, dedicated purity monitors were used to measure electron lifetime, which can be translated into equivalent oxygen contamination levels. Figure 9.3 shows the electron lifetime from the start of the LAr pump operation until the end of the Phase-1 run. In general, the electron lifetime improved as a function of pump on-time; despite several events that spoiled the lifetime, electron lifetimes of >2 ms were routinely achieved.

The 35-t Phase-1 run successfully demonstrated that there is nothing inherent to membrane cryostat technology that would preclude achieving the stated goals of the DUNE far detector. In addition, experience gained in operating the 35-t system will inform future design decisions, e.g., developing plans for replacing pumps in a way that prevents loss of purity. Future system designs could avoid the coupling of acoustical vibrations into the cryostat by locating the pumps externally; this would have the added benefit of facilitating maintenance and repair.

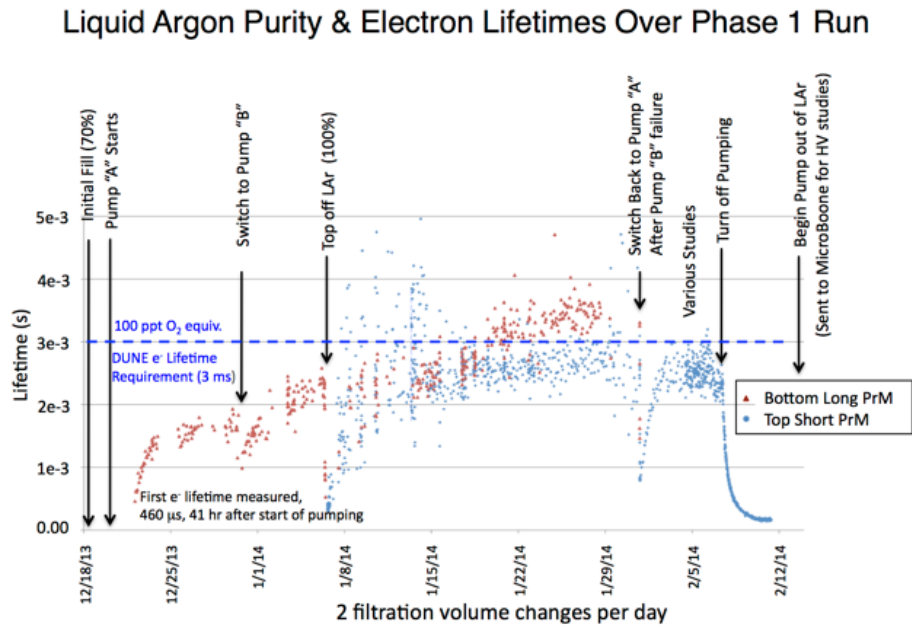


Figure 9.3: LAr electron lifetimes as measured by Cryostat Purity Monitors. Significant events are annotated on the plot. Major divisions on horizontal axis are one week periods. Equivalent purity levels are shown as dashed horizontal lines.

fig:35TP

9.2.2 35-t Phase-2

Phase-2 of the 35-t prototype includes a fully operational TPC and photon detector in the cryostat. Commissioning of the TPC is expected in August 2015 after TPC installation, purge, cooldown and LAr fill. Phase-2 operation is planned for several months of cosmic ray running. External plastic scintillator paddles placed around the cryostat will provide both the trigger and rough position measurements of the incoming cosmic rays. Figure 9.4 shows the trial assembly of the TPC outside of the cryostat along with a model of the TPC inside the cryostat.

The Phase-2 prototype incorporates many novel DUNE single-phase far detector design elements as described in previous sections of this document and allows these to be tested in an operational TPC. Some of the more important aspects are collected in Table 9.2.

As can be seen from Table 9.2, successful tests of many of the new design features will require simulation, reconstruction and analysis of 35-t data. This will be performed using the LArSoft package, which is also used to simulate and reconstruct data from ArgoNeuT, MicroBoone and LArIAT. Reuse of software developed for those experiments will greatly facilitate 35-t developments; however, the novel hardware features of the 35-t prototype necessitate new software developments, including:

- code to divide the wrapped wires into as many as five individual linear segments. A hit on a single electronic channel can, in principle, be related to a signal on any of these segments.
- “disambiguation” code to identify which of the possible wire segments was actually respon-

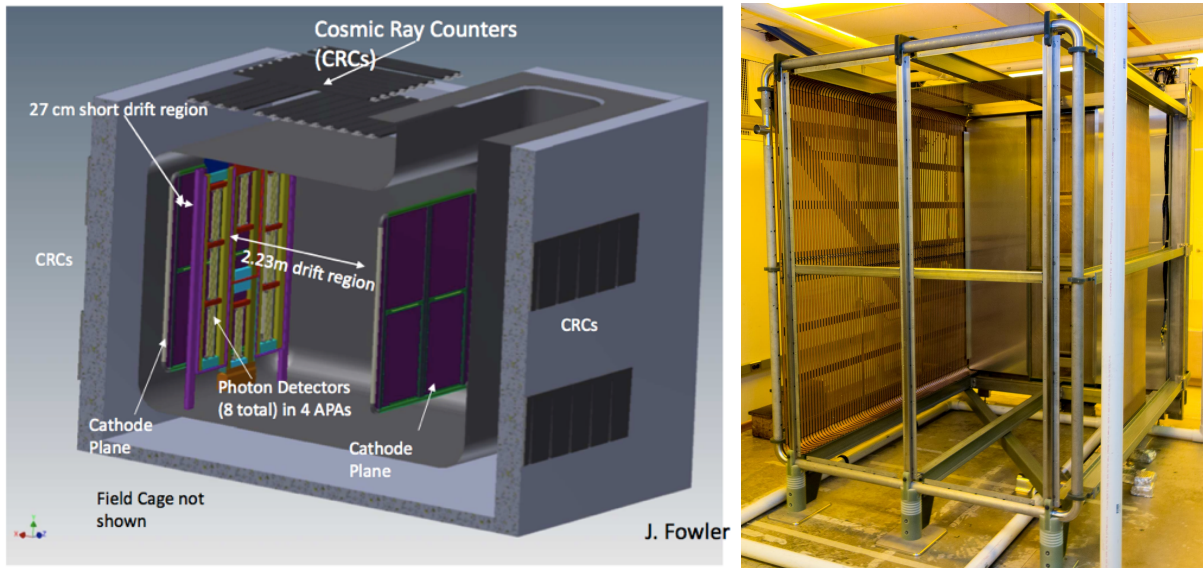


Figure 9.4: (left) Rendering of the 35-t cryostat with TPC and photon detectors installed. Note the position of the APA, which is asymmetrically located between the CPAs (purple) and splits the volume into one large and one very small separate drift regions. The length of the longer one of these is close to what is proposed for the far detector. The other has a shorter drift length due to lack of space. (right) A trial assembly of the TPC.

fig:35T

Table 9.2: 35-t Design Elements

Design Aspect	Section	How Tested
Modular APAs with wrapped wires	4.3.2	Build small-scale APA Modules with FD design
Vertical Gaps between APAs	4.3	Assemble APAs side-by-side. Study reco'd tracks that cross the gaps.
Horizontal Gaps between APAs	4.3	Build two shorter APAs and stack vertically Study reco'd tracks that cross the gaps
Field cage constructed of FR4 Printed Circuit Board	4.3	Operate at HV and measure field uniformity
APAs immersed in active volume	4.3	Study reco'd tracks that cross APAs
Cold Digital Electronics	4.5	Measure noise performance etc. <i>in situ</i>
Waveguide-style Photon Detector	4.6	Install in APAs. Measure lightyield
Triggerless-capable DAQ	4.4	Take data using multiple DAQ modes

5TDesign

2 sible for the observed hit

- 3 • code for determining the start time of the event (t_0). Since the 35-t prototype DAQ can run
4 “triggerless,” methods are needed for finding the t_0 in data. Information from the external
5 scintillator paddles as well as the internal photon detectors can be used.
- 6 • Code for “stitching” together track segments observed in different tracking volumes. Since
7 hits can come from either side of the four APAs, there are effectively eight separate tracking
8 volumes, which are treated as separate TPCs.

9 With these simulation and reconstruction tools in hand, “physics” analysis of the data can be
10 undertaken in the areas of validation of new detector design elements and analysis of basic LArTPC
11 performance. Among the highest-priority analysis tasks are:

- 12 • basic detector performance: signal/noise, purity measured with tracks, track direction reso-
13 lution, photon detector light yield
- 14 • measurement of distortions due to space charge and field non-uniformity
- 15 • identification of different types of particles: muons, protons, neutrons, pions

16 The results obtained by operating and analyzing data from the 35-t Phase-2 prototype are expected
17 to be very valuable in refining the CERN single-phase prototype design, in preparation for the first
18 10-kt DUNE far detector module.

19 9.3 The CERN Single-Phase Prototype

20 A CERN single-phase prototype detector and accompanying beam-test program is in preparation.
21 As an *engineering* prototype, it is intended to validate the construction of the components planned
22 for the first DUNE 10-kt detector module at scale and thereby mitigate risks associated with
23 extrapolating small-scale versions of the single-phase LArTPC technology to a full 10-kt detector
24 module. It is intended to benchmark the operation of full-scale detector elements and perform
25 measurements in a well characterized charged-particle beam — an essential step.

26 The prototype will incorporate components with the same dimensions and features as those for
27 the first 10-kt DUNE far detector module.

28 9.3.1 Program of Tests and Measurements

29 Besides validating the performance of the detector components, planning and constructing the
30 CERN prototype will establish and commission production sites and test the installation procedure.
1 Further, before the beam test, many basic detector-performance parameters can be established with

2 cosmic-ray muons. These data will aid in identification of potentially problematic components,
3 leading to future improvements and optimizations of the detector design. Once it is exposed to
4 a test beam of charged particles of different types and energies it will collect data that can be
5 combined with results from LArIAT and the short-baseline program at Fermilab. Together these
6 measurements will be used to validate MC simulations, and they will serve as data input to DUNE
7 sensitivity studies and allow validation and tuning of tools for event reconstruction and particle
8 identification. The following detector performance measurements are anticipated:

- 9 • characterize performance of a full-scale TPC module
- 10 • study performance of the photon detection system
- 11 • test and evaluate the performance of detector calibration tools (e.g., the laser system)
- 12 • verify functionality of cold TPC electronics under LAr cryogenic conditions
- 13 • perform full-scale structural test under LAr cryogenic conditions
- 14 • verify argon contamination levels and associated mitigation procedures
- 15 • develop and test installation procedures for full-scale detector components
- 16 • identify flaws and inefficiencies in the manufacturing process

17 The physics sensitivity of the DUNE experiment has so far been estimated based on detector per-
18 formance characteristics published in the literature, simulation-based estimates and a variety of
19 assumptions about the anticipated performance of the future detector and event reconstruction
20 and particle-identification algorithms. This engineering prototype and the test beam measure-
21 ments aim to replace these assumptions with measurements to use for full-scale DUNE detector
22 components and the algorithms and thereby enhance the accuracy and reliability of the DUNE
23 physics-sensitivity projections. The collection of beam measurements will serve both as a cali-
24 bration data set for tuning the MC simulations and as a reference data set for the future DUNE
25 detector. In order to make precise measurements, the DUNE detector will need to accurately
26 identify and measure the energy of the particles produced in the neutrino interaction with argon,
1 which will range from hundreds of MeV to several GeV.

2 More specifically, the goals of the prototype detector beam-test measurements include the use of
3 a charged-particle beam to

- 4 1. measure the detector calorimetric response for
 - 5 (a) hadronic showers
 - 6 (b) electromagnetic showers
- 7 2. study e/γ -separation capabilities

- 8 3. measure event reconstruction efficiencies as function of energy and particle type
 - 9 4. measure performance of particle identification algorithms as function of energy for realistic
10 detector conditions
 - 11 5. assess single-particle track calibration and reconstruction
 - 12 6. validate accuracy of MC simulations for relevant particle energy and orientation
 - 13 7. study other topics with the collected data sets
 - 14 (a) pion interaction kinematics and cross sections
 - 15 (b) kaon interaction cross section to characterize proton decay backgrounds
 - 16 (c) muon capture for charge identification
- 17 A detailed enumeration of the desired minimum integrated particle counts as a function of charged-
18 particle species and momentum is nearing completion. This has led to development of a run plan
19 based on realistic beam composition, particle energies and efficiency information.

20 An invited technical proposal for the CERN single-phase detector and beam-test program will
1 be submitted to the CERN SPSC in June 2015. This proposal is Annex 4J: *CERN Single-phase*
2 *Prototype Detector Proposal*. The plan includes a first beam run in 2018 before the long shutdown of
3 the LHC. Experience gained from construction, installation and commissioning of this prototype,
4 as well as performance tests with cosmic-ray data are expected to lead to an optimization of
5 corresponding phases of the DUNE single-phase far detector module(s).

6 9.3.2 Detector Configuration and Components

7 As mentioned above, the prototype detector components have the same dimensions and features
8 as those of the far detector reference design described in Chapter 4. This includes the TPC and
9 photon detector components, as well as their positioning and spacing within the cryostat.

10 TPC Configuration

11 The size of the prototype is in large part determined by the requirement to fully contain hadronic
12 showers of up to several GeV in energy. The particle containment of hadronic showers initiated
13 by charged pions or protons is a critical feature for calorimetric measurements. Simulation studies
14 indicate that showers initiated by 10-GeV primary pions and protons are contained within a volume
15 measuring 6 m in the longitudinal and 5×5 m² in the transverse directions. With the basic APA
1 unit measuring 6×2.3 m², the arrangement identified as satisfying the requirement consists of
2 two times three APAs side-by-side, a central cathode and two drift volumes each with 3.6 m drift

length. Figure 9.5 shows a view of the CERN single-phase TPC along with the field cage and a view of the TPC within the cryostat.

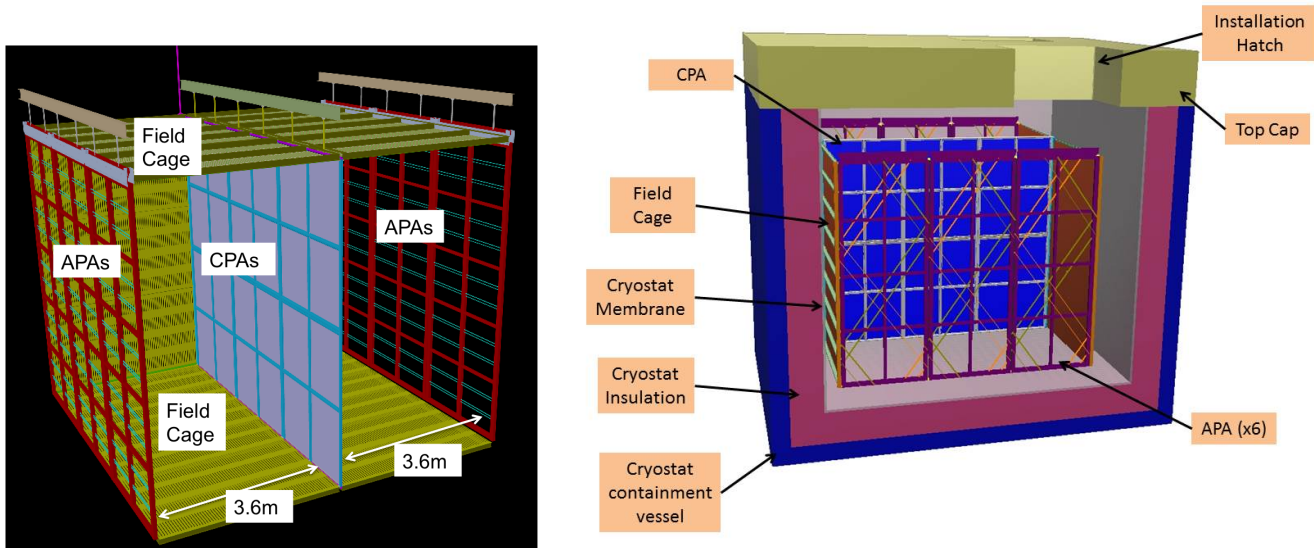


Figure 9.5: View of the CERN single-phase detector TPC (left) and inserted in the cryostat (right).

The TPC readout, photon-detection system, DAQ, slow control and monitoring, as well as the key issues of the installation procedure are described in corresponding sections of Chapter 4.

7 Cryostat

The CERN prototype uses a membrane tank technology with internal dimensions of 7.8 m (transverse) \times 8.9 m (parallel) \times 8.1 m (height). It contains 725 tons of LAr, equivalent to about 520 m³ (where the remaining volume contains the gas ullage). The active (fiducial) detector mass of LAr amounts to 400 tons (300 tons). The external cryostat dimensions are 10.6 m (transverse) \times 11.7 m (parallel) \times 10.9 m (height).

The cryostat design is scaled up from the 35-t prototype cryostat [65], described in Section 9.2. Unlike the 35-t cryostat, it uses a steel outer supporting structure with an inside metal liner. It is similar to the WA105 dual-phase prototype detector cryostat and to that for the Fermilab Short-Baseline Near Detector (SBND) [?]. The support structure rests on I-beams to allow for air circulation underneath the cryostat; this maintains the temperature within the allowable limits. A stainless-steel membrane contains the LAr within the cryostat. The pressure loading of the cryogenic liquid is transmitted through rigid foam insulation to the surrounding outer support structure. The membrane is corrugated to provide strain relief resulting from temperature-related expansion and contraction. The cryostat top cap consists of the same layers as the cryostat walls. From the inside out, the layers include the stainless-steel primary membrane, intermediate insulation layers and vapor barrier; they all continue across the top of the detector providing a leak-tight seal. The cryostat roof is a removable steel truss structure to which stiffened steel

25 plates are welded from the underside. They form a flat vapor-barrier surface onto which the roof
26 insulation attaches directly.

27 The truss structure rests on the top of the supporting structure where a positive structural connec-
28 tion between the two is made in order to resist the upward force caused by the slightly pressurized
29 argon in the ullage space. The hydrostatic load of the LAr in the cryostat is carried by the floor
1 and the sidewalls. In order to meet the maximum deflection of 3 mm between APA and CPA
2 and to decouple the detector from possible sources of vibrations, the TPCs are connected to an
3 external bridge over the top of the plate supported on the floor of the building. Everything else
4 within the cryostat (electronics, sensors, cryogenic and gas plumbing connections) is supported by
5 the steel plates under the truss structure.

6 All piping and electrical penetrations into the interior of the cryostat are made through the top
7 plate. Penetrations are clustered in one region. The top cap has two large openings for TPC
8 installation, and a manhole to allow entry into the tank after the hatches have been closed.

9 Cryogenics System

10 The main goals of the cryogenics system are to purge the cryostat prior to the start of the operations
11 (with argon gas in open and closed loops), cool the cryostat and fill it with LAr. The LAr is
12 continuously purified and the boil-off argon gas is captured, recondensed and purified. The design
13 calls for a 10-ms electron lifetime (30 ppt O₂ equivalent), a quantity that is measured by the
14 detector.

15 The LAr-receiving facility includes a storage dewar and ambient vaporizer to deliver LAr and
16 gaseous Ar to the cryostat. The LAr goes through the LAr handling and purification system,
17 whereas the gaseous Ar goes through its own purification system before entering the cryostat.
18 Studies are ongoing to standardize the filtration scheme and select the optimal filter medium for
19 both the prototype and future detectors.

20 During operation, an external LAr pump circulates the bulk of the cryogen through the LAr
21 purification system. The nominal LAr purification flow rate completes one full volume exchange in
22 5.5 days. The boil-off gas is recondensed and sent to the LAr purification system before re-entering
23 the vessel.

24 The proposed LAr cryogenics system is based on that of the 35-t prototype, MicroBooNE and
25 SBND, and the current plans for the DUNE single-phase far detector module.

26 9.4 The WA105 Dual-Phase Demonstrator

27 In recent years, two consecutive FP7 Design Studies (LAGUNA/LAGUNA-LBNO) have led to
28 the development of a conceptual design (fully engineered and costed) for a 20-kt/50-kt GLACIER-
1 type underground neutrino detector. In these studies, an underground implementation has been

assumed *ab initio* and such constraints have been important and taken into account in design choices. The LAGUNA-LBNO design study, completed in August 2014, has produced many technical developments focused on the construction of large and affordable liquid argon underground detectors addressing the complete investigation of three-flavor neutrino oscillations and the determination of their still unknown parameters. These detectors will be very powerful for non-beam studies as well, such as proton decay, atmospheric neutrinos and supernova neutrinos.

The WA105 experiment, approved in 2013, is designed to provide a full-scale demonstration of these technological developments. It will be exposed to a beam of charged hadrons/electrons/muons of 0.5–20 GeV/c to characterize the detector response to hadronic and electromagnetic showers. A detailed description of the experiment is available in the Technical Design Report of 2014, Annex 4I: *WA105 TDR*, and an up-to-date picture of technical developments can be found in the Status Report [22] submitted to the SPSC CERN committee in March 2015. These developments form the basis of the alternative far detector design, described in Chapter 5.

The WA105 demonstrator is a dual-phase LArTPC with an active volume of $6 \times 6 \times 6 \text{ m}^3$.

These dimensions are motivated by the $4 \times 4 \text{ m}^2$ Charge Readout Plane (CRP) units that are the basic readout components of the large-scale LAGUNA/LBNO 20–50-kt detectors. The $6 \times 6 \times 6 \text{ m}^3$ active volume is consistent with a fiducial volume that accommodates the CRP size and provides full containment of hadronic showers. Surface operation prohibits drift lengths above 6 m. The footprint of the active volume corresponds to 1:20 of the surface of the LBNO 20-kt detector. The active volume contains about 300 tonnes of LAr. The important parameters of the detector are presented in Table 9.3 and Figures 9.6, 9.7 and 9.8 provide a 3D drawing and two cut views.

Table 9.3: Parameters for the WA105 demonstrator

Parameter	Units	Value
Liquid argon density	t/m ³	1.38
Liquid argon volume height	m	7.6
Active liquid argon height	m	5.99
Hydrostatic pressure at the bottom	bar	1.03
Inner vessel size (WxLxH)	m ³	$8.3 \times 8.3 \times 8.1$
Inner vessel base surface	m ²	67.6
Total liquid argon volume	m ³	509.6
Total liquid argon mass	t	705
Active LAr area	m ²	36
Charge readout module (0.5 × 0.5 m ²)		36
N of signal feedthrough		12
N of readout channels		7680
N of PMT		36

The dual-phase LArTPC design drifts ionization electrons vertically through the LAr in a uniform electric field up to the liquid-vapor interface, where they are extracted from the liquid into the gas phase.

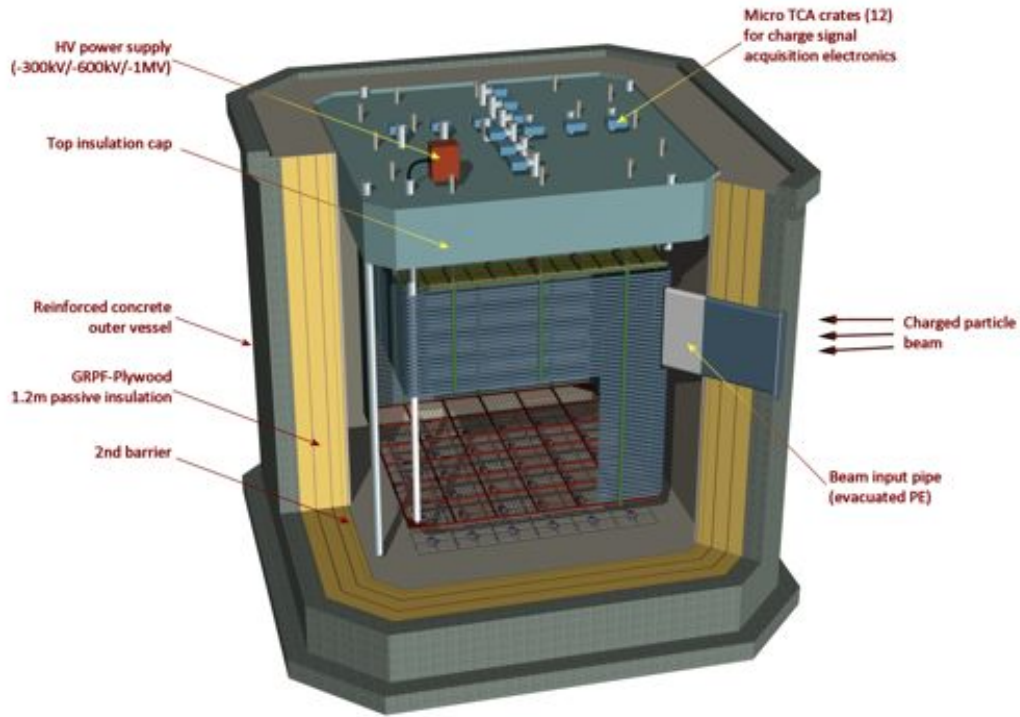


Figure 9.6: Illustration of the $6 \times 6 \times 6 \text{ m}^3$ demonstrator with the detector inside the cryostat

fig:6by6

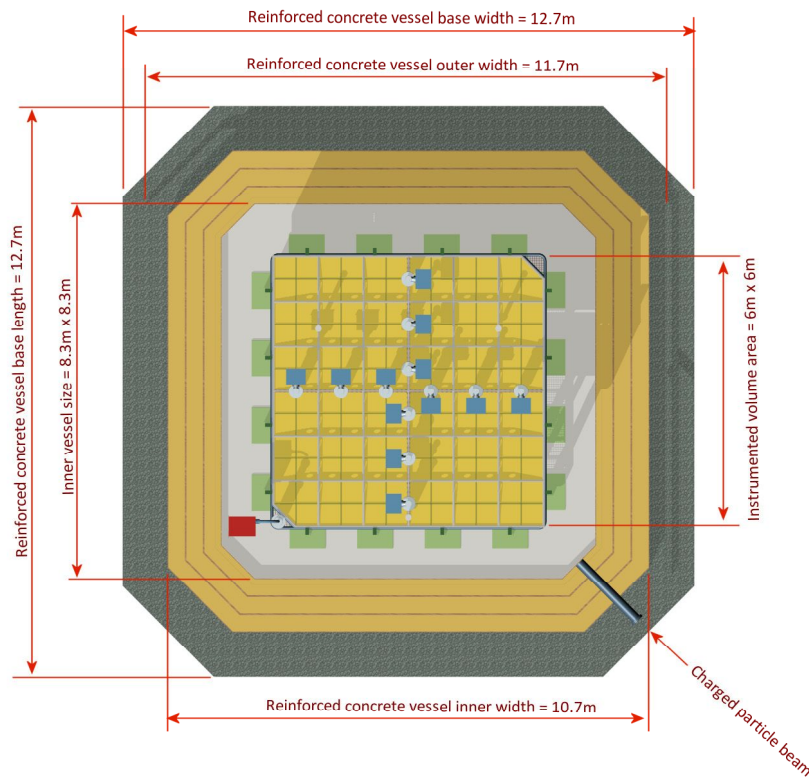


Figure 9.7: Plan view section of the $6 \times 6 \times 6 \text{ m}^3$ demonstrator

fig:6by6

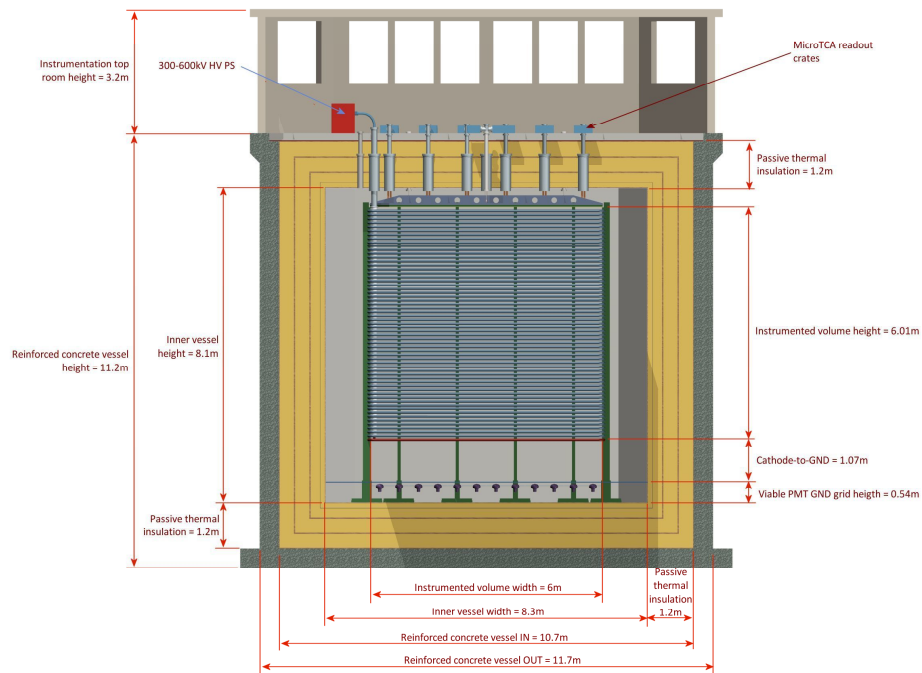


Figure 9.8: Vertical cross section of the $6 \times 6 \times 6 \text{ m}^3$ demonstrator

fig:6by6

- 26 In the gas, the Charge Readout Plane (CRP) described in Section 5.3, extracts, multiplies and
 1 collects the charge. sec:detectors-fd-alt-chg-readout
- 2 The drift path in the WA105 demonstrator reaches 6 m. The detector will operate with drift fields
 3 of 0.5 kV/cm and 1 kV/cm, corresponding to cathode voltages of -300 – 600 kV. 600 kV is the
 4 voltage also needed for the operation of the DUNE dual-phase detector module with 12 m drift
 5 at 0.5 kV/cm. The CRP has an active surface of 36 m^2 , with its anode subdivided into strips of
 6 3.125-mm pitch and 3-m length, for a total of 7680 readout channels.
- 7 The WA105 demonstrator will establish the techniques developed for the 20/50-kt LBNO detectors,
 8 in particular:
- 9 ● tank construction technique based on the LNG industry with non-evacuated vessel
 - 10 ● purification system
 - 11 ● long drift
 - 12 ● HV system 300–600 kV, large hanging field cage
 - 13 ● large area double-phase charge readout
 - 14 ● accessible cryogenic front-end electronics and cheap DAQ electronics
 - 15 ● long-term stability of UV light readout

16 Furthermore, the $6 \times 6 \times 6 \text{ m}^3$ demonstrator exposed to the test beam promises a rich physics
17 program to:

- 18 • assess detector performance in reconstructing hadronic showers; the most demanding task in
19 neutrino interactions
- 20 • measure hadronic and electromagnetic calorimetry and PID performance
- 21 • full-scale software development, simulation and reconstruction
- 22 • collect high-statistic hadronic interaction samples with unprecedented granularity and reso-
23 lution for the study of hadronic interactions and nuclear effects
- 24 • assess physics capabilities of the dual-phase versus single-phase performance, in particular:
25 high S/N, 3-mm pitch, absence of materials in long drift space, two collection views, no
26 ambiguities
- 27 • study systematics related to the reconstruction of the hadronic system (resolution and energy
28 scale), electron-identification efficiencies and π^0 rejection and particle dE/dx identification
29 for proton decay

30 The $6 \times 6 \times 6 \text{ m}^3$ WA105 detector is expected to start taking data in 2018 in the EHN1 Hall
31 extension currently under construction at CERN. The detector components are in an advanced
32 state of design/prototyping, or preproduction. Completion of the WA105 detector design and the
33 preparation of its construction have been progressing very quickly. Many technical design details
1 are benefitting from the implementation of a 20-t ($3 \times 3 \times 1 \text{ m}^3$) prototype (see Figure 9.9), which
2 corresponds to the readout cell size for the DUNE dual-phase detector module.

3 Development of this 20-t prototype has verified the complete system integration: production of
4 fully engineered prototype versions of many detector parts, including installation details and an-
5 cillary services; establishment of the Quality Assessment (QA) procedures for the construction,
6 installation and commissioning chains; establishment of the procurement processes for the major
7 detector components; and validation of the cost and schedule estimates for WA105. The $3 \times 3 \times 1 \text{ m}^3$
8 20-t prototype represents a technical test bed and integration exercise to accelerate the design,
9 procurement, QA and commissioning activities needed for the WA105 demonstrator. In particular,
10 a complete procedure for construction of GTT-licensed corrugated membrane cryostats been es-
11 tablished at CERN and a full chain for the procurement, processing, assembly and commissioning
12 of the LEM detectors and anodes has been implemented.

13 9.5 Near Detector Prototypes

14 Near detector prototypes are planned for both the neutrino detector and beamline measurements
15 systems.

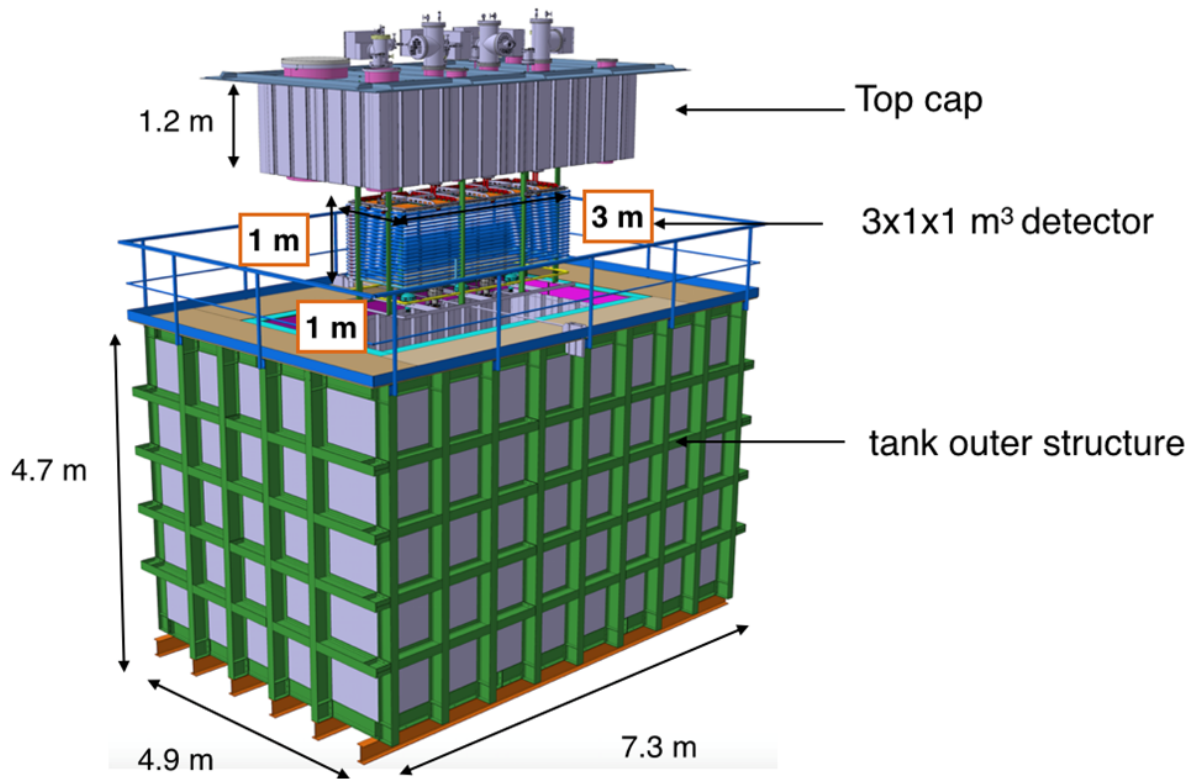
Figure 9.9: Exploded view of the $3 \times 3 \times 1 \text{ m}^3$ prototype

fig:3by1

9.5.1 Near Neutrino Detector Prototypes

The prototyping plan for the Fine-Grained Tracker (FGT) near neutrino detector, as described in Section 7.2, involves the following major steps:

- Straw-Tube Tracking detector (STT) prototyping
- ECAL prototyping
- MuID – RPC development
- Dipole magnet studies

A schematic of the FGT is given in Figure 7.1. The prototyping activity for the reference design will be developed jointly by the participating collaborators in India, with some contributions from institutions in the U.S. or other countries. The prototyping work is spread over a duration of three years. The plan is detailed below.

27 Straw-Tube Tracking Detector

28 The proposed Straw-Tube Tracking (STT) detector design provides the central active tracking of
 29 the FGT and use straws of 1-cm diameter fabricated from an inner carbon-loaded Kapton (XC)
 30 wall and a second aluminum-coated outer Kapton (HN) wall. The details of the STT design are
 1 available in Section 7.2.1. The prototype design has two layers of 60 straws each. The straws will
 2 have the same dimensions as listed in Section 7.2.1, but half the nominal length, i.e., 1.8 m. The
 3 major milestones in the STT prototyping are highlighted below.

4 The three-year STT R&D and prototyping phase will start with the 3D design of a prototype
 5 module. This will include optimization of parameters for the prototype assembly and validation
 6 of the mechanical structure using Finite Element Method (FEM) techniques. This process will be
 7 a self-feeding system with input from GEANT detector simulations. Figure 9.10 shows the STT
 8 simulation. The STT prototype will be fabricated and will undergo extensive tests both in the
 9 laboratory and in particle beams at CERN.

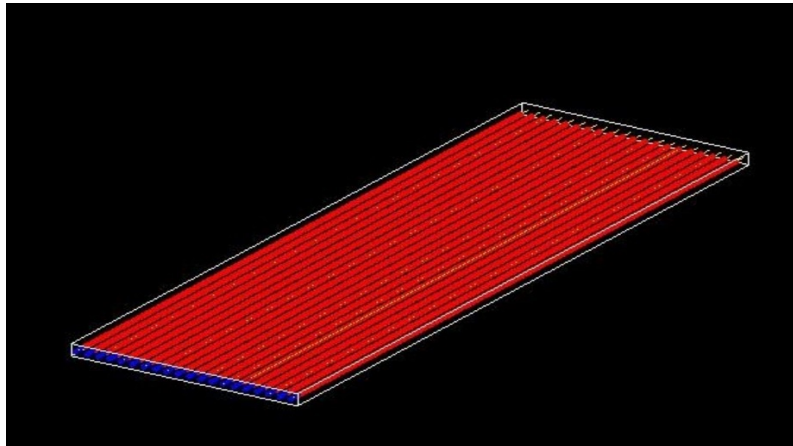


Figure 9.10: GEANT4 simulation of 1 cm straws for the STT prototype

fig:STT_

10 As described in Section 7.2.1, a key feature of the STT is the capability to integrate a series of
 11 nuclear targets for (anti)neutrino interactions. The main target is provided by the radiators that
 12 are made of thin polypropylene foils (Figure 7.2). The design of the radiator targets has been
 13 optimized with simulations of the Transition Radiation (TR) with emphasis on integration into
 14 the mechanical structure of the STT modules. The production and design of the plastic foils was
 15 discussed with vendors and a half-scale (1.8 m×1.8 m) prototype of the radiator targets will be
 16 produced to demonstrate assembly, mechanical properties and overall performance. A preliminary
 17 design has been developed for the pressurized Ar gas target (Figure 9.11), based on the use of 0.5-in
 18 diameter stainless steel tubes. Prototypes of the pressurized Ar gas tubes will be built to optimize
 19 the design of the tubes, including the tube diameter and the possibility of using carbon-composite
 20 tubes. Construction of small-scale prototypes of the Ca and C targets is also planned.

21 The straw tube sense wires were initially proposed as 30- μm diameter gold-plated tungsten, similar
 22 to the COMPASS design. In order to minimize the material budget of the mechanical frames used
 23 for the STT modules, it is important to reduce the wire tension. To this end, the prototyping
 24 includes a detailed study of the possibility of using 20- μm wires instead of the default 30- μm . The

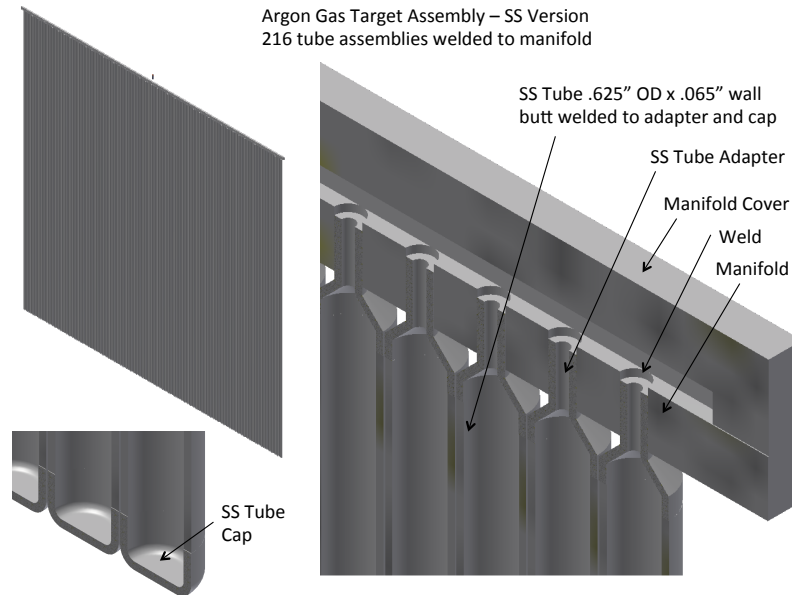


Figure 9.11: Design of the radiator target plane with pressurized Ar gas for STT

fig:STT_

25 tensile strength of these wires inside the straw tubes could affect the signal generation over a long
 26 period due to sagging; a detailed study is in progress. Figure 9.12 shows the tension measurement
 27 results for 20–30 μm wires using the induced-resonance method. The proposed tension limit on
 28 the sense wires is 70 g.

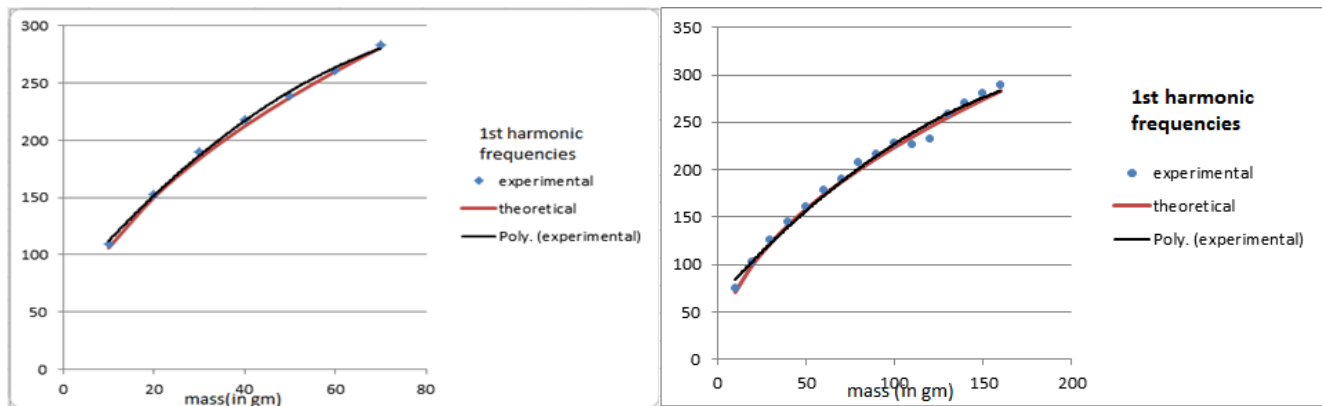


Figure 9.12: STT wire-tension measurement studies for 20 μm and 30 μm .

fig:STT_

29 A test chamber with 48 straws of the same dimensions as those for the FGT but with 1-m length
 30 has been built and is available for operational studies aimed at understanding the gas flow rates and
 31 finalizing the preamplifier selection parameters. Figure 9.13 shows a signal pulse with Ar+CO₂
 1 (80:20) gas taken with cosmic rays. The voltage versus amplitude for one of the straws is also
 2 shown in Figure 9.13 to establish the QA/QC procedure for the fabricated straws.

3 We are performing tests of prototype electronics for the signal readout. A four-channel preamplifier
 4 has been tested with the test chamber using a radioactive source and the signal has been recorded
 5 as shown in Figure 9.14.

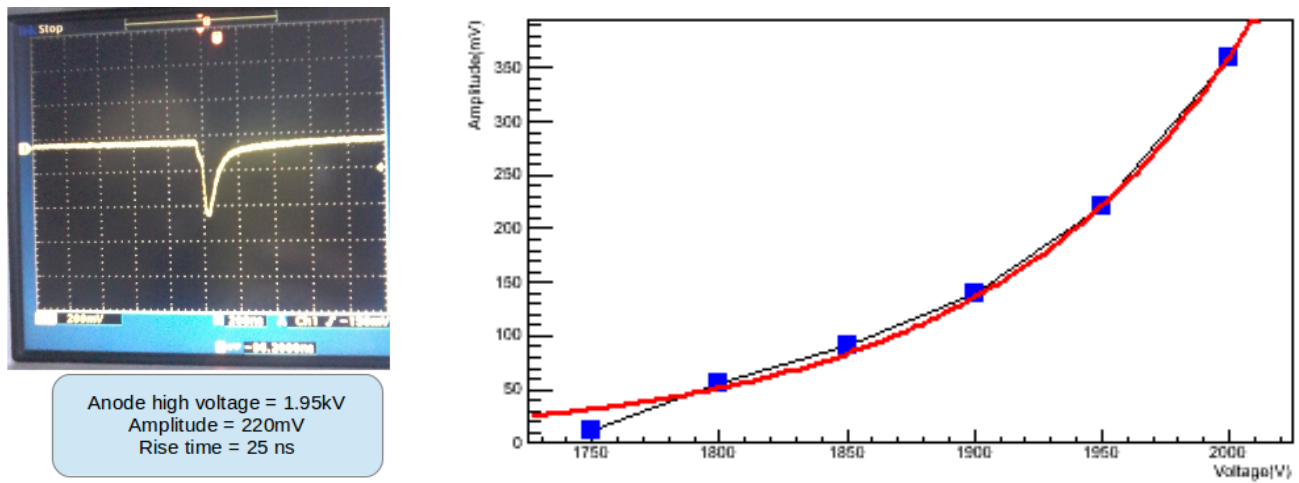


Figure 9.13: Example pulse from the test straw chamber (left) and measurement of voltage vs. amplitude for one of the straws in the test chamber (right).

fig:STT_

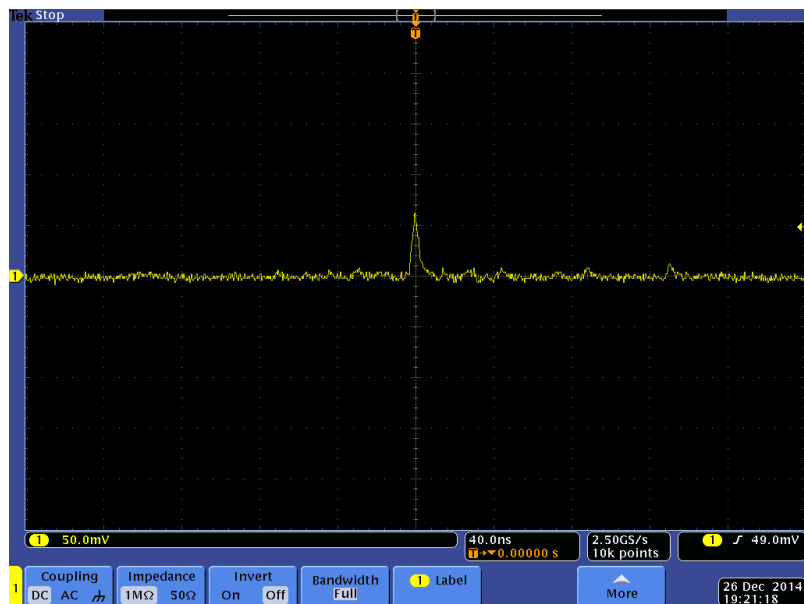


Figure 9.14: Signal from single straw using the BARC (Bhabha Atomic Research Center) preamp and source.

fig:STT_

6 The back-end DAQ is still being worked out and would follow the description in Section 7.2.5. At
7 present both CAMAC- and VME-based DAQ are available. In addition, a μ TCA-based fast DAQ
8 has also been setup.

9 Other activities are in progress. As part of the prototyping, 50 straws of 1.8 m from Lamina
10 Dielectrics Ltd. and 1 km of 30 μ m anode wire from Luma has been procured. The optical bench
11 for the fabrication of the straws has been setup. Two pre-mixed gas bottles of Ar+CO₂ have
12 been procured. The operational gas mixture of Xe+CO₂ will be added soon. Local industry and
13 vendors have been identified for manufacturing nozzles, end-plugs, wire-spacers and steel balls.
14 Local workshops are available to fabricate the mechanical structure to hold the straws in the
15 prototype design and also to fabricate a test stand for studies of efficiency and characteristics
16 with a radioactive source. Wire stringing, straw gluing and other tooling setups are still to be
17 established.

18 The final design of the STT modules will be optimized based on the results obtained from the
19 STT prototype and the related prototyping activities listed above. This task includes a detailed
3882 FEM analysis to assess the mechanical structure and the choice of final materials.

3883 **ECAL Detector**

3884 In the FGT, the ECAL detector will have 4π coverage outside the STT. The detailed description of
3885 this detector is given in Section 7.2.2. The ECAL prototype will be a 2×2 -m² module similar to the
3886 downstream-ECAL design. The half-scale downstream ECAL prototype construction, which uses
3887 Pb as the absorber and extruded scintillator with embedded fiber as the active detector system,
3888 will involve the following steps:

- 3889 • procure materials (plastic scintillator bars, WLS fibers, SiPM, Pb sheets, etc.)
- 3890 • set up mechanism to ensure the quality of the scintillator bars, fibers and Pb sheets
- 3891 • set up tools for the characterization of SiPMs
- 3892 • assemble scintillator bars in an aluminum frame for a prototype layer formation
- 3893 • undertake R&D for the coupling of the fiber to the SiPMs as well as the inserting of fiber in
3894 the scintillator
- 3895 • develop readout electronics for the prototype and set up a cosmic test stand with full DAQ
- 3896 • complete ECAL mechanical design

3897 The ECAL readout system is centered on a highly sensitive/high-gain SiPM. During the R&D
3898 phase, SiPMs from Hamamatsu, AdvanSiD and SiPM developed in India by SCL will be compared.
3899 Discussions have been started with all the vendors.

3900 Optimization of the ECAL detector geometry with GEANT4 simulations has been initiated. The
 3901 geometry in the current GEANT4 simulation includes 58 layers of alternating horizontal and
 3902 vertical scintillator layers per 1.75 mm Pb along the z -direction. In the present configuration each
 3903 scintillator layer is made of plastic scintillator bars of dimensions 4 m \times 2.5 cm \times 1 cm, resulting
 3904 in 160 bars per layer, and 9280 scintillator bars for the downstream ECAL . Figure 9.15 shows
 3905 the longitudinal view of the electromagnetic shower in the downstream ECAL by 2-GeV photons.
 3906 Figure 7.4 shows the design of the Pb-scintillator assembly configuration for the ECAL.

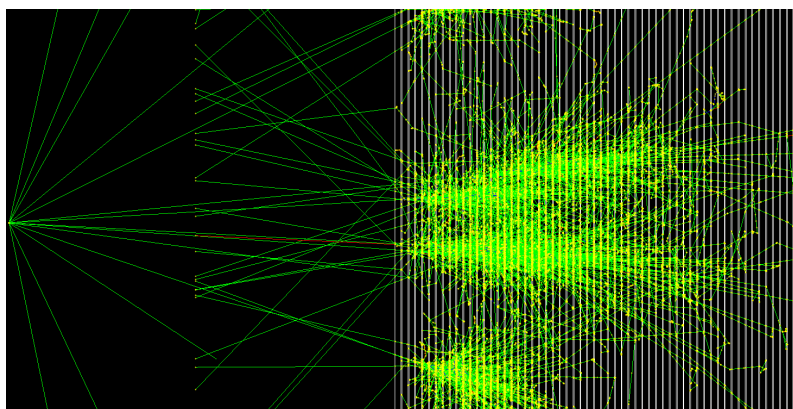


Figure 9.15: Longitudinal view of the electromagnetic shower in the downstream ECAL by 2 GeV photons.

3907 For the construction of the prototype and for the assembly of the actual detector a space of
 3908 dimension 32 m \times 12 m has been identified. Construction of a class 10,000 clean room covering a
 3909 laboratory space of 12 m \times 12 m is under consideration. Figure 9.16 shows the schematic diagram
 3910 of the laboratory refurbishment plan for the ECAL R&D and fabrication work.

3911 Dipole Magnet Development

3912 The massive dipole magnet (see Section 7.2.3) for the FGT is critical for the particle-momentum
 3913 measurements, will provide space for the MuID–RPC installation in the magnet steel and will
 3914 provide structural support for the FGT. The planned magnet prototype includes the engineering
 3915 development of the tooling and infrastructure that will be used to produce one C out of the total
 3916 eight Cs of the 8.0-m long dipole. The same C will be utilized in the final magnet assembly. In
 3917 a similar way, one of the four coils will be assembled to establish the coil winding procedure and
 3918 measure the operating characteristics. Field simulation work is very advanced (see Figure 7.5)
 3919 and the mechanical designs are being produced. (Steel dimensions are being optimized to house
 3920 the muon identification detectors.) Since it will be a closed system, access to the inner detector
 3921 systems is under extensive study.

3922 MuID–RPC Detector

3923 Muon identification is accomplished via Bakelite Resistive Plate Chamber (RPC) detectors. The
 3924 RPC mounting structure will be provided by the magnet steel (on sides and ends). Extensive

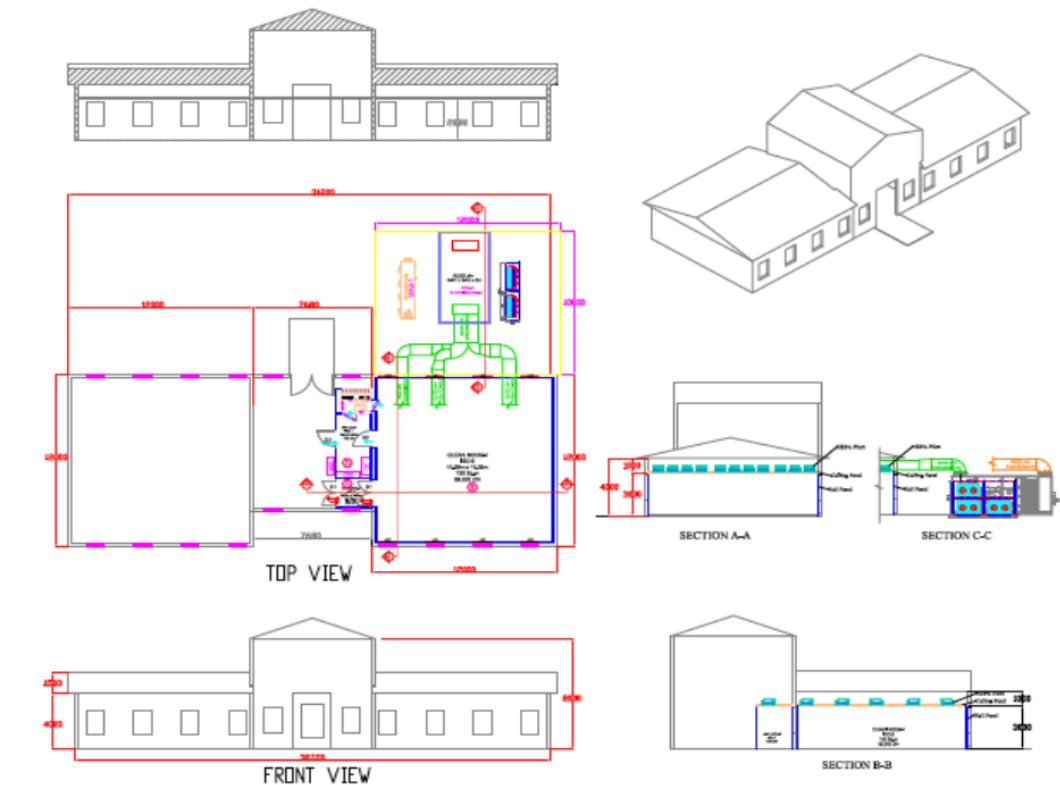


Figure 9.16: Laboratory refurbishment plan for the ECAL R&D and assembly work.

fig:ECAL

3925 R&D for RPCs is being applied to the prototyping of the muon identifiers. The size of the
 3926 FGT RPCs makes it challenging to procure the raw material from industry; however, an Indian
 3927 company has been identified and a large 2.4-m \times 1.2 m RPC prototype has been assembled (see
 3928 Section 7.2.4). The I-V characteristics obtained for these RPCs are very encouraging. More
 3929 RPCs will be fabricated during the prototyping phase and will be tested for sustained efficiency
 3930 with variation in ambient parameters, as the Bakelite is sensitive to such changes. Some of the
 3931 measured quantities are shown in Figure 9.17.

3932 The readout electronics are being developed with input from INO-ICAL detector [?] R&D. The
 3933 standard RPC gases will need to be replaced with safer ones for underground operation. An
 3934 initiative in this direction will be taken up during the prototyping phase.

3935 9.5.2 Beamline Measurement Detectors Prototyping Plan

3936 This Section describes recent and ongoing prototyping efforts for the detectors described in Sec-
 3937 tion 7.5.

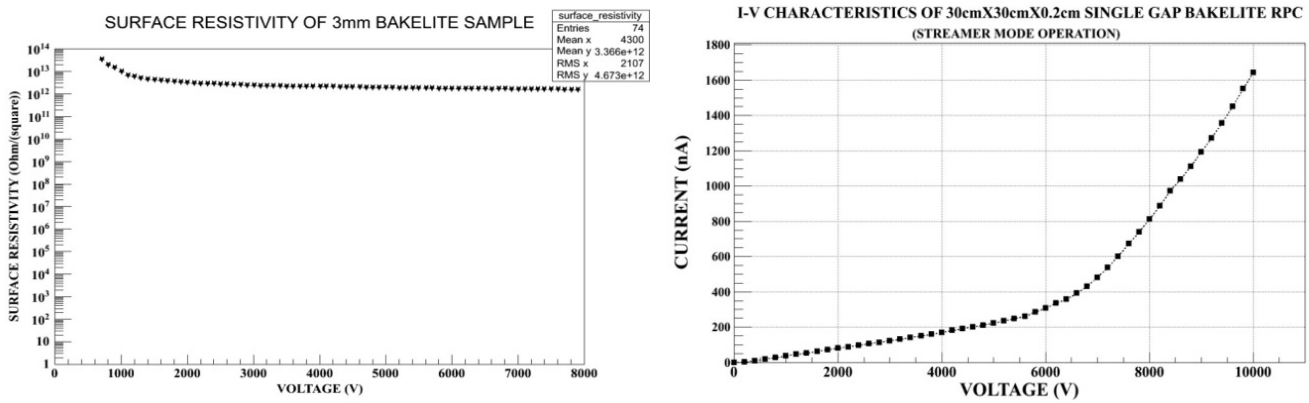


Figure 9.17: RPC characteristics measured during the prototype development.

fig:RPC_

Prototype Development for the Cherenkov and Ionization Detectors

A prototype Cherenkov counter, along with associated fully automated gas systems, HV systems, and a data acquisition system has been constructed and is undergoing testing in the NuMI neutrino beam's Muon Alcove 2. In addition, three diamond detectors [68] (from CERN) for ionization measurements have been installed in the alcove. Figure 9.18 shows the prototype detectors in the NuMI Alcove 2.

The counter has an automated gas system with an adjustable pressure that ranges from vacuum to 20 atm, corresponding to muon Cherenkov thresholds of 200 GeV/c and 1 GeV/c, respectively. When operated at vacuum, a photomultiplier tube (PMT) registers all background light unrelated to the gas, e.g., transition radiation and light from particles hitting the window and PMT glass. These contributions are observed to be very small relative to the coherent, directional Cherenkov light.

The counter is constructed with a 1-m long radiator section as shown in Figure ?? . A 20-foot extension allows the reflected Cherenkov light to travel to a sapphire pressure window viewed by a PMT.

The prototype has been fully integrated into NuMI operations and real-time waveforms can be viewed online as shown in Figure 9.19.

The top panel shows the waveform from the Cherenkov counter at 2 atm gas pressure, which corresponds to a muon momentum threshold of 3 GeV/c. The second panel shows the waveform from a 9 mm × 9 mm diamond detector mounted to the front flange of the Cherenkov radiator section, as shown in the inset of Figure 9.18.

The extracted NuMI proton beam produces a signal in the Resistive Wall Monitor (RWM) that is recorded with an identical digitizer. This allows a direct, bucket-by-bucket (individual proton pulses) comparison of the proton current onto the NuMI primary proton target. The muons are measured after the absorber with a 400-ps time resolution.

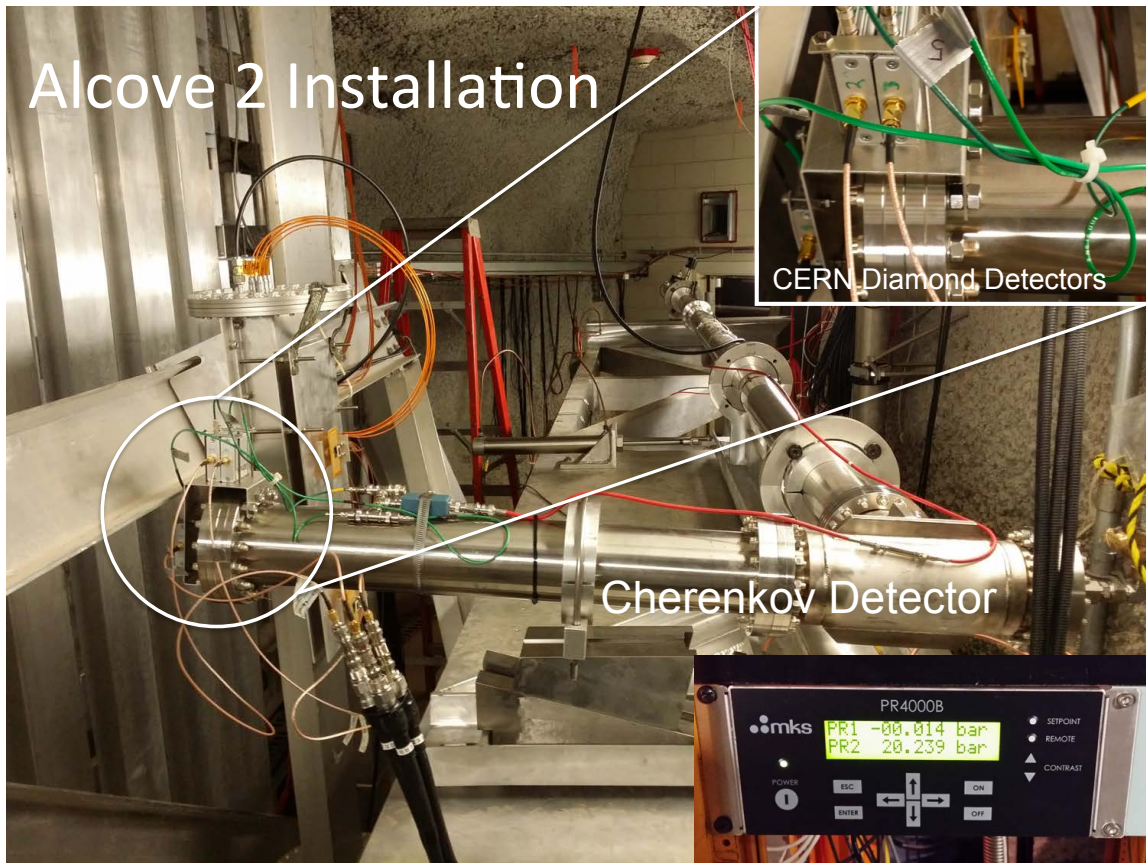


Figure 9.18: A prototype muon gas Cherenkov detector for DUNE. Muons travel through an L-shaped 4-inch Conflat pipe filled with a pressurized gas. A flat mirror mirrors directs the optical photons to a photo multiplier. The lower right inset shows the 20 bar MKS pressure reading achieved by the Cherenkov gas system, and the inset on the upper right shows the CERN/Cividec diamond detectors mounted to the Cherenkov housing.

fig:Alcove

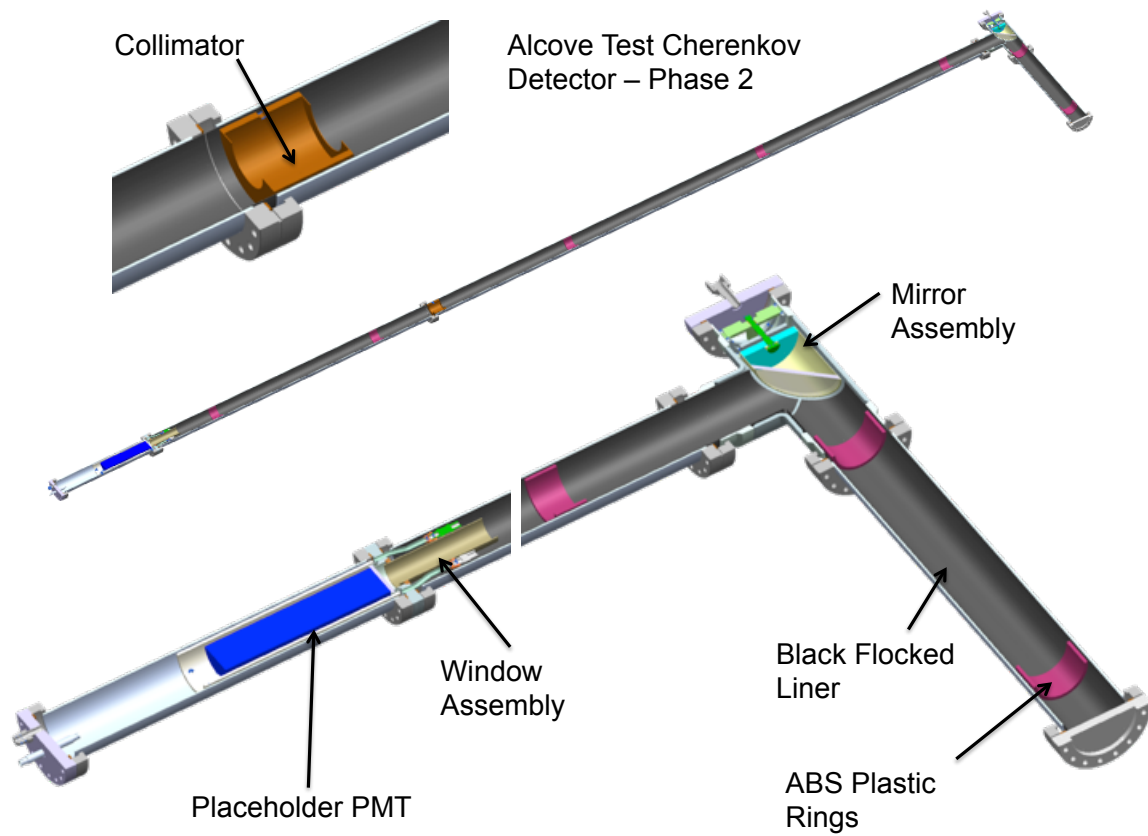


Figure 9.19: A prototype muon gas Cherenkov detector for DUNE.

fig:Cher

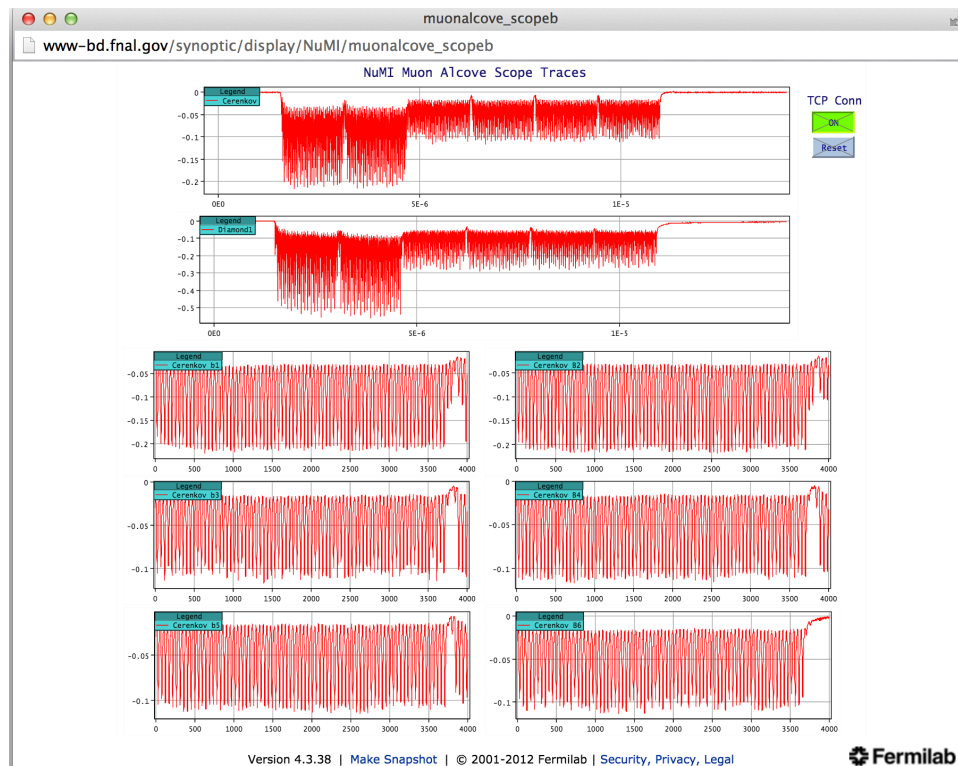


Figure 9.20: The real-time display of the muon detector prototypes in operation on the NuMI beam line. The top two panels are the Cherenkov counter and CERN diamond detector. The signals are transmitted through low-loss helix cable, then the waveform is digitized at 2.5 GHz with a 12-bit dynamic range, and is recorded onto disk storage for analysis. The signal from the muons is contained in the short beam pulse “buckets” created by the accelerator RF structure. The fast timing allows the prompt muon signal to be easily separated from potential backgrounds such as stopped-muon decays, beta decays, and neutrons.

fig:Muon

3963 **Prototype Development of the Stopped-Muon Counters**

3964 Prototype development activity for the Michel-electron detectors will be divided into studies of (1)
3965 the rate of particles and the radiation environment where the detectors will be located, and (2)
3966 development of the counters themselves.

3967 The radiation environment will be studied with Monte Carlo simulation and measurement from
3968 initial prototype detectors in the NuMI muon alcoves [69]. The prototypes will be installed in
3969 the alcoves in 2016 and 2017. Studies will be performed to determine if the photon sensors can
3970 survive the radiation environment at the location of the Michel detector. If the sensors can survive,
3971 they can be attached directly to the Cherenkov medium; if not, optical guides will have to bring
3972 the light to a lower-radiation area, to the side of the beam. Potential radiation damage to the
3973 Cherenkov radiator itself will also be studied.

3974 The detector design will focus on selecting radiator and shielding material, photon-detection tech-
3975 nology and control/readout hardware. Possible radiators include ones that use aerogel (these may
3976 be designed to be replaced periodically) and ones that use flowing liquids such as H₂O or mineral
3977 oil. Long-timescale saturation from the very high-rate environment of the beam spill could affect
3978 the photon-counting devices [70]. Thus, it will likely be necessary to design fast-switching, high-
3979 voltage circuits that turn on the photon counters in the first few microseconds after the spill is
3980 over. A similar system was developed in the 1990s for the Brookhaven Muon (g-2) Experiment [71]
3981 .

3982 A second set of muon detectors, the final DUNE design, are being constructed at this time (2015).
3983 They are being installed directly behind the NuMI proton beam dump (Muon Alcove 1), mounted
3984 on a movable stand which has undergone an engineering review at Fermilab. The entire setup,
3985 detectors and stand, will be suitable for use in the LBNF beam. The higher-radiation environment
3986 of Alcove 1 is more representative than Alcove 2 of the conditions in the eventual DUNE installa-
3987 tion, and will allow a more accurate calibration in the NuMI beam. The setup will be eventually
3988 transferred to the DUNE Absorber Hall.

3989 **9.6 Connections to the Short-Baseline Program at Fermilab**

3990 DUNE will benefit from a range of past and ongoing efforts at Fermilab. Some have been evolving
3991 in tandem with the former LBNE and present DUNE efforts. The strategy behind MicroBooNE
3992 — to incorporate some detector development aspects in an experiment with goals to investigate
3993 short-baseline neutrino physics — expanded to include detectors upstream and downstream. The
3994 Fermilab Short-Baseline Program on the Booster Neutrino Beamline now consists of the Short-
3995 Baseline Near Detector (SBND), MicroBooNE, and the ICARUS T-600; the program is fully
3996 described in a recent proposal [?]. There is significant overlap in the collaboration membership of
3997 DUNE and the three short-baseline detectors.

3998 Each of the short-baseline detectors shares some technical elements with each other and/or with
3999 the DUNE far detector prototypes e.g., cryogenic system design, argon purification techniques and

4000 cold electronics.

4001 In other aspects, e.g., the design details of the anode wire planes, the detectors are very different.
4002 The SBND is most similar to the DUNE single-phase detector design, having adopted the 35-t
4003 APA-CPA-field cage design, while the MicroBooNE TPC field cage follows the ICARUS design.
4004 The cold electronics installed on the MicroBooNE TPC represent an initial step in an ongoing pro-
4005 gram; the 35-t and the SBND implement subsequent outgrowths of cold electronics development.
4006 While commissioning its cryogenics system, MicroBooNE conducted investigations of the voltage
4007 breakdown in high-purity argon; the results prompted some design adjustments to the field cage
4008 adopted by the 35-t Phase-2 and the SBND, demonstrating the sharing and feedback of technical
4009 developments.

4010 Coordinated development of reconstruction software for LArTPC detectors is a major outcome of
4011 the 2009 *Integrated Plan*. LArSoft is fully supported by the Fermilab Scientific Computing Division
4012 and has contributors from all of the operating and planned LArTPC experiments at Fermilab.
4013 Track and shower reconstruction methods, and particle identification techniques, are already
4014 shared between ArgoNeuT, MicroBooNE, LArIAT and the 35-t. Real data from these detectors is
4015 assisting DUNE simulation efforts. The Short-Baseline experiments, starting with MicroBooNE,
4016 will develop neutrino interaction classification techniques based on the details revealed by their
4017 fine-grained tracking capabilities, and are likely to exert a strong influence on DUNE oscillation
4018 analyses.

Chapter 10

Summary of DUNE Detectors

-summary

4021 The DUNE experiment is a world-leading, international physics experiment, bringing together a
4022 global neutrino community as well as leading experts in nucleon decay and particle astrophysics
4023 to explore key questions at the forefront of particle physics and astrophysics. The massive, high-
4024 resolution near and far detectors will enable an extensive suite of new physics measurements that
4025 are expected to result in groundbreaking discoveries.

4026 The far detector will be located deep underground at the 4850L of SURF. Its 40-kt fiducial mass
4027 of LAr will enable sensitive studies of long-baseline oscillations with a 1,300 km baseline, as well as
4028 a rich program in astroparticle physics and nucleon decay searches. The far detector configuration
4029 consists of four LArTPCs. They provide excellent tracking and calorimetry performance, high
4030 signal efficiency and effective background discrimination, all of which converge to provide an overall
4031 excellent capability to precisely measure neutrino events and reconstruct kinematical properties
4032 with high resolution. The full imaging of events will enable study of neutrino interactions and
4033 other rare events to unprecedented levels.

4034 The magnetized, high-resolution near detector will measure the spectrum and flavor composition
4035 of the neutrino beam extremely precisely. It is able to discriminate neutrino flavor through particle
4036 identification and separate neutrino and antineutrino fluxes through charge discrimination of elec-
4037 trons and muons produced in the neutrino charged current-interactions. These capabilities enable
4038 DUNE to reach unprecedented sensitivity in long-baseline neutrino oscillation studies. This is the
4039 primary role of the near detector, however, its exposure to an intense flux of neutrinos will provide
4040 an opportunity to collect unprecedentedly high neutrino interaction statistics, making possible a
4041 wealth of fundamental neutrino interaction measurements, an important component of the DUNE
4042 Collaboration's ancillary scientific goals.

References

- 4043
- 4044 [1] M. Antonello, P. Aprili, B. Baibussinov, F. Boffelli, A. Bubak, *et al.*, “Operation and perfor-
4045 mance of the ICARUS-T600 cryogenic plant at Gran Sasso underground Laboratory,” 2015.
- 4046 [2] M. Antonello, B. Baibussinov, P. Benetti, F. Boffelli, A. Bubak, *et al.*, “Experimental ob-
4047 servation of an extremely high electron lifetime with the ICARUS-T600 LAr-TPC,” *JINST*,
4048 vol. 9, no. 12, p. P12006, 2014.
- 4049 [3] J. Marshall and M. Thomson, “Pandora Particle Flow Algorithm,” in *Proceedings, Interna-*
4050 *tional Conference on Calorimetry for the High Energy Frontier (CHEF 2013)*, pp. 305–315,
4051 2013.
- 4052 [4] J. Marshall and M. Thomson, “The Pandora software development kit for particle flow
4053 calorimetry,” *J.Phys.Conf.Ser.*, vol. 396, p. 022034, 2012.
- 4054 [5] D. Gibin, “Software Tools and Data Analysis,” tech. rep., FNAL, 2013. LBNE Doc 7460.
- 4055 [6] A. Ankowski *et al.*, “Measurement of through-going particle momentum by means of multiple
4056 scattering with the ICARUS T600 TPC,” *Eur.Phys.J.*, vol. C48, pp. 667–676, 2006.
- 4057 [7] A. Ankowski *et al.* *Acta Physica Polonica*, vol. B41, p. 103, 2010.
- 4058 [8] B. Baller, “TPC Wire Angle Optimization.” LBNE Doc 2836, 2010.
- 4059 [9] C. Thorn, G. D. Geronimo, A. DAndragora, S. Li, N. Nambiar, S. Rescia, E. Vernon, H. Chen,
4060 F. Lanni, D. Makowiecki, V. Radeka, and B. Yu, “Cold Electronics Development for the LBNE
4061 LAr TPC,” *Phys.Procedia*, vol. 37, p. 1295, 2012.
- 4062 [10] I. N. *et al.*, “Attenuation length measurements of scintillation light in liquid rare gases and
4063 their mixtures using an improved reflection suppresser,” *Nucl. Inst. and Meth. in Phys. Resrch*
4064 *Sec. A.*, vol. 384, pp. 380–386, 1997.
- 4065 [11] “Final report of the LAGUNA-LBNO design of a pan-European infrastructure for large ap-
4066 paratus studying Grand Unification, Neutrino Astrophysics and Long Baseline Neutrino Os-
4067 cillations (Funded by European Commission FP7 Research Infrastructures, grant agreement
4068 number: 284518),” *Annex*.

- 4069 [12] A. Badertscher, A. Curioni, U. Degunda, L. Epprecht, A. Gendotti, *et al.*, “First operation
4070 and performance of a 200 lt double phase LAr LEM-TPC with a 40×76 cm² readout,” *JINST*,
4071 vol. 8, p. P04012, 2013.
- 4072 [13] A. Badertscher, A. Curioni, U. Degunda, L. Epprecht, A. Gendotti, *et al.*, “First operation and
4073 drift field performance of a large area double phase LAr Electron Multiplier Time Projection
4074 Chamber with an immersed Greinacher high-voltage multiplier,” *JINST*, vol. 7, p. P08026,
4075 2012.
- 4076 [14] A. Badertscher, A. Curioni, L. Knecht, D. Lussi, A. Marchionni, *et al.*, “First operation of a
4077 double phase LAr Large Electron Multiplier Time Projection Chamber with a two-dimensional
4078 projective readout anode,” *Nucl.Instrum.Meth.*, vol. A641, pp. 48–57, 2011.
- 4079 [15] L. A. et al., “LBNO-DEMO: Large-scale neutrino detector demonstrators for phased per-
4080 formance assessment in view of a long-baseline oscillation experiment, The LBNO-DEMO -
4081 WA105 - Collaboration,” *CERN-SPSC-2014-013; SPSC-TDR-004*, 2014.
- 4082 [16] A. Bondar, A. Buzulutskov, A. Grebenuk, D. Pavlyuchenko, Y. Tikhonov, and A. Breskin,
4083 “Thick gem versus thin gem in two-phase argon avalanche detectors,” *JINST*, vol. 3, no. 07,
4084 p. P07001, 2008.
- 4085 [17] C. Cantini, L. Epprecht, A. Gendotti, S. Horikawa, S. Murphy, *et al.*, “Long-term operation
4086 of a double phase lar lem time projection chamber with a simplified anode and extraction-grid
4087 design,” *JINST*, vol. 9, p. P03017, 2014.
- 4088 [18] A. Badertscher, L. Knecht, M. Laffranchi, A. Marchionni, G. Natterer, *et al.*, “Construction
4089 and operation of a Double Phase LAr Large Electron Multiplier Time Projection Chamber,”
4090 2008.
- 4091 [19] A. Badertscher *et al.*, “Stable operation with gain of a double phase Liquid Argon LEM-TPC
4092 with a 1 mm thick segmented LEM,” *J. Phys. Conf. Ser.*, 2011.
- 4093 [20] C. Cantini, L. Epprecht, A. Gendotti, S. Horikawa, L. Periale, *et al.*, “Performance study of
4094 the effective gain of the double phase liquid Argon LEM Time Projection Chamber,” 2014.
4095 accepted for publication in JINST.
- 4096 [21]
- 4097 [22] "Progress report on LBNO-DEMO/WA105 (2015), G. Balik *et al.*, CERN-SPSC-2015-
4098 013/SPSC-SR-158".
- 4099 [23] "<https://www.picmg.org/openstandards/microtca/>".
- 4100 [24] "<http://www.ohwr.org/projects/white-rabbit>".
- 4101 [25] P. group, “PICMG Advanced Mezzanine Card AMC.0 Specification R2.0,” 2006.

- 4102 [26] A. Badertscher *et al.*, “ArDM: first results from underground commissioning,” *JINST*, vol. 8,
4103 p. C09005, 2013.
- 4104 [27] “UNICOS,” 2015. <http://unicos.web.cern.ch/>.
- 4105 [28]
- 4106 [29] "B. Genolini *et al.*, NIM A, vol; 610, no 1, pp. 249-252, 2009."
- 4107 [30] "S. C. Di Lorenzo *et al.*, 2009,0912.1269".
- 4108 [31] B.Chowdhary. R.Gandhi, C.S.Mishra, S.R.Mishra, J.Strait, “Detailed Project Report. Pro-
4109 posal submitted to DAE/DST.,” tech. rep., 2012. LBNE DocDB 6704.
- 4110 [32] J.Dolph, M.Diwan, R.Gandhi, S.R.Mishra, R.Petti, “Near Detector Systems Requirements
4111 Working Files.,” tech. rep., 2014. LBNE DocDB 8806.
- 4112 [33] S.R.Mishra, R.Petti, “Thoughts on the LBNE Near Detector Physics and Specifications.,”
4113 tech. rep., Univ. of South Carolina, 2014. LBNE DocDB 8850.
- 4114 [34] C. Adams *et al.*, “The Long-Baseline Neutrino Experiment: Exploring Fundamental Symme-
4115 tries of the Universe,” 2013.
- 4116 [35] “Near Detectors Requirements Documentation,” tech. rep. LBNE Doc 5579 [http://](http://lbne2-docdb.fnal.gov:8080/cgi-bin/ShowDocument?docid=5579)
4117 lbne2-docdb.fnal.gov:8080/cgi-bin/ShowDocument?docid=5579.
- 4118 [36] C. Andreopoulos *et al.*, “The GENIE Neutrino Monte Carlo Generator,” *Nucl. Instrum. Meth-*
4119 *ods*, vol. A, no. 614, pp. 87–104, 2010.
- 4120 [37] S. Agostinelli *et al.*, “GEANT4 — A Simulation Toolkit,” *Nucl. Instrum. Methods*, vol. A,
4121 no. 506, pp. 250–303, 2003.
- 4122 [38] J. Allison *et al.*, “GEANT4 developments and applications,” *IEEE Trans. Nucl. Sci.*, vol. 53,
4123 no. 1, pp. 270–278, 2006.
- 4124 [39] E. D. Church, “LArSoft: A Software Package for Liquid Argon Time Projection Drift Cham-
4125 bers,” 2013.
- 4126 [40] C. Green, J. Kowalkowski, M. Paterno, M. Fischler, L. Garren, *et al.*, “The art framework,”
4127 *J.Phys.Conf.Ser.*, vol. 396, p. 022020, 2012.
- 4128 [41] C. Anderson, M. Antonello, B. Baller, T. Bolton, C. Bromberg, *et al.*, “The ArgoNeuT De-
4129 tector in the NuMI Low-Energy beam line at Fermilab,” *JINST*, vol. 7, p. P10019, 2012.
- 4130 [42] C. Anderson *et al.*, “Analysis of a Large Sample of Neutrino-Induced Muons with the Ar-
4131 goNeuT Detector,” *JINST*, vol. 7, p. P10020, 2012.

- 4132 [43] P. Adamson *et al.*, “LArIAT: Liquid Argon TPC in a Test Beam.” FERMILAB-PROPOSAL-
4133 1034, 2013.
- 4134 [44] F. Cavanna, M. Kordosky, J. Raaf, and B. Rebel, “LArIAT: Liquid Argon In A Testbeam.”
4135 arXiv:1406.5560, 2014.
- 4136 [45] H. Chen *et al.*, “Proposal for a New Experiment Using the Booster and NuMI Neutrino
4137 Beamlines: MicroBooNE.” FERMILAB-PROPOSAL-0974, 2007.
- 4138 [46] B. J. P. Jones, “The Status of the MicroBooNE Experiment,” *PoS*, vol. EPS-HEP2011, p. 436,
4139 2011.
- 4140 [47] MicroBooNE Collaboration, “The MicroBooNE Conceptual Design Report.” [http://
4141 microboone-docdb.fnal.gov/cgi-bin/ShowDocument?docid=1821](http://microboone-docdb.fnal.gov/cgi-bin/ShowDocument?docid=1821), 2010.
- 4142 [48] D. Lussi, *Study of the response of the novel LAr LEM-TPC detector exposed to cosmic rays
4143 and a charged particle beam*. PhD thesis, ETH Zürich, 2013.
- 4144 [49] C. Hagmann, D. Lange, J. Verbeke, and D. Wright, “Cosmic-ray Shower Library (CRY),”
4145 tech. rep., Lawrence Livermore National Laboratory, 2012. UCRL-TM-229453.
- 4146 [50] C. Hagmann, D. Lange, J. Verbeke, and D. Wright, “Monte Carlo Simulation of Proton-
4147 induced Cosmic-ray Cascades in the Atmosphere,” tech. rep., Lawrence Livermore National
4148 Laboratory, 2012. UCRL-TM-229452.
- 4149 [51] C. Hagmann, D. Lange, J. Verbeke, and D. Wright. [http://nuclear.llnl.gov/simulation/
4150 main.html](http://nuclear.llnl.gov/simulation/main.html).
- 4151 [52] V. Gehman, “Intrinsic Radioactive Backgrounds in the LBNE Far Detector,” tech. rep., LBNL,
4152 2014. LBNE DocDB 8797-v2.
- 4153 [53] S. Amerio *et al.*, “Design, construction and tests of the ICARUS T600 detector,”
4154 *Nucl.Instrum.Meth.*, vol. A527, pp. 329–410, 2004.
- 4155 [54] <http://icarus.lngs.infn.it/>.
- 4156 [55] M. Antonello, B. Baibussinov, P. Benetti, E. Calligarich, N. Canci, *et al.*, “Precise 3D track re-
4157 construction algorithm for the ICARUS T600 liquid argon time projection chamber detector,”
4158 *Adv.High Energy Phys.*, vol. 2013, p. 260820, 2013.
- 4159 [56] <http://t962.fnal.gov/>.
- 4160 [57] R. Acciarri *et al.*, “A study of electron recombination using highly ionizing particles in the
4161 ArgoNeuT Liquid Argon TPC,” *JINST*, vol. 8, p. P08005, 2013.
- 4162 [58] <http://www-microboone.fnal.gov/>.

- 4163 [59] R. Kalman, “A New Approach to Linear Filtering and Prediction Problems,” *J. Fluids Eng.*,
4164 vol. 82, pp. 35–45, 1960.
- 4165 [60] J. Back, G. Barker, S. Boyd, J. Einbeck, M. Haigh, *et al.*, “Implementation of a local prin-
4166 cipal curves algorithm for neutrino interaction reconstruction in a liquid argon volume,”
4167 *Eur.Phys.J.*, vol. C74, p. 2832, 2014.
- 4168 [61] J. Thomas and D. Imel, “Recombination of electron-ion pairs in liquid argon and liquid xenon,”
4169 *Phys.Rev.*, vol. A36, pp. 614–616, 1987.
- 4170 [62] J. B. Birks, *The Theory and practice of scintillation counting*. Pergamon Press, 1964.
- 4171 [63] “FIXME,” FIXME. FIXME.
- 4172 [64] “FIXME,” FIXME. FIXME.
- 4173 [65] “FIXME,” FIXME. FIXME.
- 4174 [66] “FIXME,” FIXME. FIXME.
- 4175 [67] “FIXME,” FIXME. FIXME.
- 4176 [68] “FIXME,” FIXME. FIXME.
- 4177 [69] S. Kopp *et al.*, “Secondary beam monitors for the NuMI facility at FNAL,” *Nucl. Instrum.*
4178 *Meth.*, vol. A568, pp. 503–519, 2006.
- 4179 [70] Y. Semertzidis and F. Farley, “Effect of light flash on photocathodes,” *Nucl. Instrum. Meth.*,
4180 vol. A394, p. 7, 1997.
- 4181 [71] J. Ouyang and W. Earle, “Muon g-2 note no. 202,” tech. rep., BNL, 1994.